UNIVERSITY OF BIRMINGHAM

THE COMPLEMENTARY USE OF THEORETICAL STRUCTURE PREDICTION AND X-RAY POWDER DIFFRACTION DATA IN CRYSTAL STRUCTURE DETERMINATION

by

LIANA VELLA-ZARB

A thesis submitted to
The University of Birmingham
for the degree of
DOCTOR OF PHILOSOPHY

School of Chemistry
The University of Birmingham
September 2008

TABLE OF CONTENTS

ACKNOWLEDGEMENTS

This was one of the most important and formative experiences in my life, and I would never have done it without the help of some very special people.

First of all, my thanks and appreciation go to Maryjane for persevering with me as my tutor throughout the time it took me to complete this research and write the dissertation. Your support (and unlimited patience!) and the many conversations that clarified my thinking on this and so many other matters (from powders to grappa, and beyond!) were essential components of this journey. Thank you for your friendship and academic support - they mean a great deal to me.

I would also like to thank all the members of the CPOSS team, especially Sally Price and Panos Karamertzanis, who have generously given their time and expertise to better my work. Thank you for your contribution and good-natured support. Special thanks go to Chick Wilson for the many times he came to the rescue when I was about to give up....conferences would not have been the same without those late night pep talks!!

I want to thank my friends and colleagues in Birmingham: Adam especially, for taking on the brave task of printing out this dissertation for me and for making the office a happier place; Sam for being there from the start, even when I was almost homeless; Emma for the very special friendship; James for being like a brother to me; and all the members of Level 2 and Level 5. You've all left your footprint on my heart.

I cannot fail to mention my very dear "chemistry family" in Glasgow - Suzie, Lynne, Marc, Martin, Duncan and Andy. You guys are the true definition of friendship - thank you for being the crazy fantastic people you are. I love you all to bits and getting to know you has made this experience so much more valuable to me.

Finally, my sincere appreciation goes to my family in Malta. To Mama, who always seems to have unlimited supplies of energy, positivity, support and reassurance, and whose phonecalls helped me feel warm, safe and at home when I was going through a rough patch. Thank you for reading through all these pages, but most of all, thank you for making me feel like I was always part of a team. With you around, I will surely never walk alone. To Papinu, for all the little things he says which make a big difference to us, even though he thinks we aren't listening. You once told me "Dare to think, dare to fail, dare to act, because sometimes it's better to regret things done than things left undone". This experience would have probably just been a secret dream had it not been for those words....And lastly to my dear brother Andrew whom I missed so much while I was away. Thank you for letting me nick your laptop while I was writing up, and for putting up with my general madness. Your maturity, determination and strength of character are an inspiration to me, and I can only hope that one day I might make you as proud of me as I am of you.

ABSTRACT

The successful prediction of the crystal structure and symmetry of a material can give valuable insight into many of its properties, as well as the feasibility of thermodynamically stable polymorphs to exist. It is not uncommon, however, for numerous theoretical structures to be found within a narrow energy range, making absolute characterisation of the crystal structure impossible. The aim of this project was to investigate a number of structures from this scenario, highlighting the key differences between three potential methods for the automated comparison of predicted and experimental crystal structures.

This work was carried out by comparing the simulated powder diffraction patterns of theoretical predicted crystal structures of small organic materials with their experimental powder diffraction patterns, so that the experimentally identified structure could be automatically singled out from the many calculated. The use of traditional agreement factors (eg. R_{wp}) was compared with more sophisticated approaches namely *PolySNAP*, which uses principal-component analysis, and *Compare.x*, an algorithm based on weighted cross-correlation. Five structures were analysed, two of which had not been previously characterised. As the structure prediction calculations are carried out at 0K, and experimental data were collected over a range of temperatures (10K-293K), the effect of the resulting variations in lattice parameters on the automated processes is discussed.

In all cases, R_{wp} has proven to be a poor and unreliable discriminator in the comparison of predicted and experimental structures. The more contemporary methods based on *PolySNAP* and *Compare.x* both gave encouraging results when used to study the three known structures imidazole, chlorothalonil and 5-azauracil, and they have consequently been used in the successful solution of the two previously unknown structures adenine and guanine. A difference in sensitivity in the matching of data collected at different temperatures between the latter approaches was noted. It was found that although there is considerable overlap between the two methods, they are not absolutely interchangeable, and this distinction may be exploited in future work where more case-specific comparisons are carried out. Automated comparison techniques cannot yet replace visual comparison completely, but they reduce it drastically. Ultimately, comparisons made computationally serve as a complement to human judgement, but they may not yet eliminate it.

LIST OF TABLES

LIST OF FIGURES

1. INTRODUCTION

1.1 Background

Crystals have been objects of fascination throughout the history of mankind, with mystical, magical and even medicinal properties being attributed to them over the ages. Evidence of this are the carvings depicting their use as ornaments, amulets and charms, discovered by archaeologists in prehistoric tombs. However, crystals were not only used as ornaments in their natural form. They were also refined and used, together with sound, to produce artificial light, as the French explorer Captain Auvergne reported on his return from Tibet. This effect is also observed in New Grange in Ireland, built circa 3200BC in honour of Oenghus, god of love. Covering the facade of this temple is white quartz, a material of particular interest in the history of crystallography, since it was the first to be described as a "*crystal*". The term, which comes from the Greek word κρύσταλλοσ meaning frozen droplet, was chosen because of the icy appearance of quartz.

As crystals and their structure lie at the core of this project, a brief overview of how the study of crystals came to be the important area of solid state chemistry it is today, is due. The term "*crystallography*" derives from the two words κρύσταλλοσ and γράφιμο , the latter meaning "writing". It thus follows that documenting the description of crystals as accurately and thoroughly as possible constitutes the main focus of every crystallographer's job description.

Although crystals had been admired for their external appearance for millennia, it wasn't until 1665 that the first connection between external form and internal order was made by Robert Hooke, who suggested that the different shapes of crystals could arise from the packing together of spheres or globules[1] [Figure 1.1]. In 1669, Nicolaus Steno cut sections across quartz crystals, showing that regardless of the size of the faces on the crystals, they were always inclined to one another at constant dihedral angles[2].

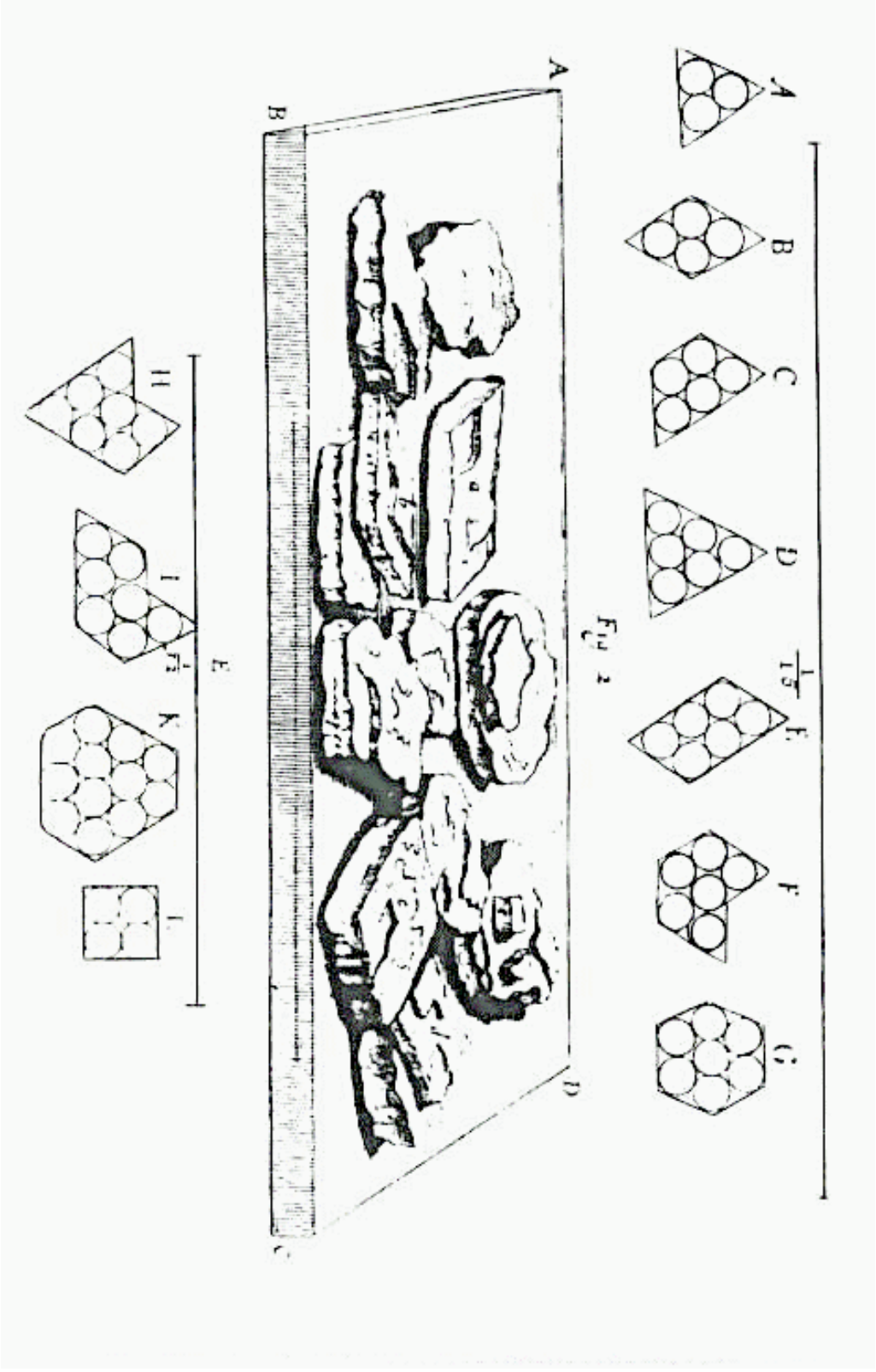

Figure 1.1. "Scheme VII" from Hooke's Micrographia, 1665, showing hypothetical crystal structures arising from packing of globules.

Later that century, Guglielmini made some observations about the constant nature of *cleavage* directions in crystals. He suggested the presence of *crystal planes* along which the crystal could be caused to split regularly, and this led him to believe that the building blocks of crystals suggested by Hooke must themselves be miniature crystals with plane faces[3]. In 1784, in his work entitled *Essay d'une théorie sur la structure des crystaux appliquée a plusieurs genres de substances crystallisées*, René Just Haüy reported experiments suggesting that continued cleavage would ultimately lead to a smallest possible unit (*molécule intégrante*), by a repetition of which the whole crystal is built[2]. If each of these units is replaced by a point, regardless of its contents, and adjacent points are joined, the resulting structural unit is a complete representation of the contents of the whole structure [Figure 1.2]. Thus Haüy, having given birth to the concept of the ***unit cell***, is deemed the "Father of Crystallography".

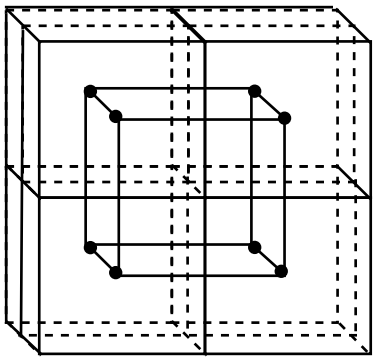

Figure 1.2. Development of the "unit cell" by replacing cubes with points.

1.2 Crystallinity and Crystal Packing

A material can be considered crystalline if its constituent molecules, atoms or ions exhibit long-range three-dimensional periodic order. This structural arrangement can be described in a complete manner by taking into consideration the repeating unit (the *unit cell*), its contents (the *structural motif*) and the manner in which the unit cell is repeated (the *symmetry*).

The unit cell can be described by three vectors *a*, *b* and *c* which are the lattice vectors and form a parallelepiped. The directions specified by these vectors can be represented by the X, Y and Z orthogonal axes respectively, while α, β and γ are the angles between them [Figure 1.3].

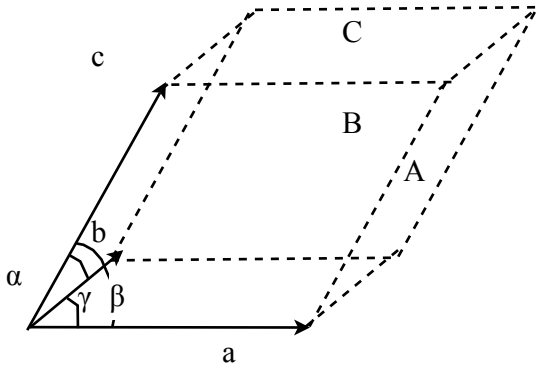

Figure 1.3 Unit cell notation. The directions of vectors a, b and c are the X, Y and Z axes.

A crystallographic plane is defined by three lattice points, or indices (*hkl*). Planes parallel to one of the three axes X, Y or Z are defined by indices of the type (*0kl*), (*h0l*) and (*hk0*) respectively, while planes parallel to faces A, B and C of the unit cell are represented by indices of the type (*h00*), (*0k0*) and (*00l*) respectively. While some crystals have a centre of symmetry illustrated by the occurrence of similar faces of the same size and shape lying in parallel pairs on opposite sides of the crystal, some others do not. Such crystals exhibit a different type of arrangement, defined by reflection, translation or rotational symmetry elements, which can only be combined together in a restricted number of ways that are consistent with each other. For a single molecule, the total collection of all its symmetry operations is called its ***point group***, and each of these point groups is characterised by a number of specific properties. Since rotation in crystal elements can only exhibit a maximum order of six, there are 32 possible ways in which symmetry factors can be combined. In order to satisfy the criterion that the unit cell must be capable of repetition in space without leaving any gaps, there is a natural limit to the types of unit cell that can be used to build a crystal. The 32 point groups give rise to only seven different unit cell shapes, and these form the basis of the classification of crystals into seven distinct groups or crystal systems [Table 1.1].

Table 1.1 The seven crystal systems.

Crystal system	*Essential symmetry*	*Restrictions on unit cell*	*Bravais lattices*
Cubic	Four three-fold rotation axes	$a = b = c$ $\alpha = \beta = \gamma = 90^o$	*P, I, F*
Hexagonal	One six-fold rotation	$a = b \neq c$ $\alpha = \beta = 90^o$; $\gamma = 120^o$	*P*
Trigonal (Rhombohedral)	One three-fold rotation	$a = b = c$ $\alpha = \beta = \gamma \neq 90^o$	*P (R)*
Tetragonal	One four-fold rotation	$a = b \neq c$ $\alpha = \beta = \gamma = 90^o$	*P, I*
Orthorhombic	Three two-fold rotations and/or mirror planes	$a \neq b \neq c$ $\alpha = \beta = \gamma = 90^o$	*P, C (A), I, F*
Monoclinic	One two-fold axis and/or mirror plane	$a \neq b \neq c$ $\alpha = \gamma = 90^o \neq \beta$	*P, C (I)*
Triclinic	None	$a \neq b \neq c$ $\alpha \neq \beta \neq \gamma$	*P*

For crystal structures showing more than just translational symmetry, a unit cell containing more than just one lattice point is chosen by convention. This is merely done for convenience, as the resultant unit cell geometry would display the symmetry more clearly. Unit cells with one lattice point are referred to as primitive (*P*), and those with more than one lattice point are called centred. The various crystal systems can exhibit different kinds of centering: side-centred, having lattice points at the centres of opposite pairs of faces (*A*, *B*, or *C* depending on which faces are centred), face-centred, having lattice points at the centres of all faces (*F*), and body-centred, having a lattice point at the centre of the cell (*I*) [Figure 1.4]. The different possible combinations of cell symmetry with primitive and centred cell geometries result in 14 lattice types, known as ***Bravais lattices***. The presence of translation coupled with the other symmetry functions, also gives rise to compound symmetry elements such as *glide planes* and *screw axes*. A glide plane is the combination of a translation with a mirror reflection, while the combination of a translation with a rotation changes the rotational axes to a screw axis. Combining all the possible symmetry operations in the solid state with Bravais lattices gives rise to 230 distinct arrangements, known as ***space groups***. Every crystal structure can be classified under one of these space groups.

The first part of a space group symbol denotes the lattice type [Figure 1.4], and is denoted by a capital letter *P*, *C* (*B* or *A*), *I* or *F*. These refer to primitive, face-centred, body-centred, and all-face-centred. The second part of the space group describes the symmetry within the unit cell. This is irreducible representation in that only the minimum symmetry is specified in order to identify the space group.

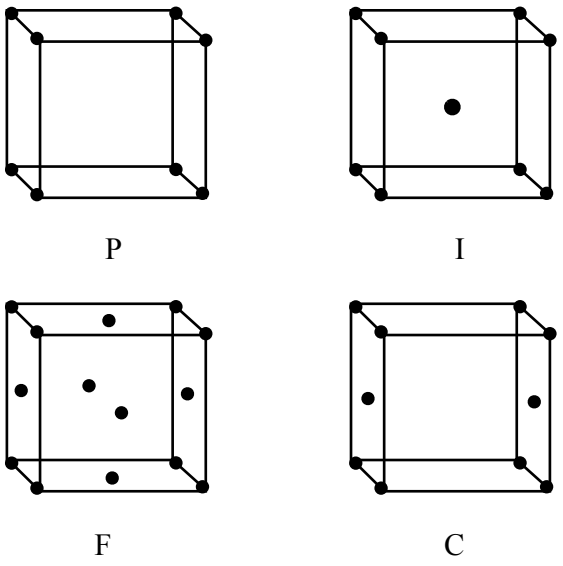

Figure 1.4 Figure illustrating the four lattice types.

In a purely translational lattice, the repeat unit of a crystal structure is either one complete unit cell (primitive cells) or a well-defined fraction of it (*A*, *B*, *C*, or *I* centering). If other symmetry elements are present, then this would relate atoms or molecules within the unit cell to each other. In this case, therefore, the unique part of the crystal structure usually corresponds to a fraction of the unit cell, and it is dependent on the amount of symmetry present. This portion is called the ***asymmetric unit*** of the structure, and by means of translation, rotation, inversion and reflection symmetry elements, it generates the entire unit cell and, consequently, the complete crystal structure.

1.3 The Importance of Structure

In this context, the term "structure" refers to the relative positions of the atoms or ions making up the material, i.e. it is a geometrical description of bond lengths, bond angles, torsion angles, non-bonded distances, etc. This enables crystallographers to represent the structure graphically, satisfying the γράφιμο part of their title. However, knowledge about the structure of crystalline materials goes beyond their pictorial importance. The structure of a crystalline system may be used to understand its physical and chemical properties, including any magnetic or optical behaviour[3], and is thus of great use. Insight into the crystal structure of materials has applications in various scientific fields: the characterisation of proteins and pigments in biology; characterisation and development of non-linear optical materials, polymers and superconductors in physics[4,5]; the reactivity and structure-energy relationships of newly-synthesised compounds in chemistry[5]; and the characterisation of drugs and bioactive materials, as well as polymorph investigation in pharmacy[6], to name a few. In the case of pharmaceuticals, most of which are administered in crystalline form, the crystal geometry of the active ingredient and its excipients directly affect the drug's bioavailability, and consequently its activity and toxicity. This particular application also raises awareness about the impact of possible polymorphs having different physico-chemical properties, both on industry, but more importantly, also in the body.

Throughout the ages, the study of the structure of crystals has made use of a wide variety of experimental tools, depending on their availability. Steno's slicing experiment, which gave rise to the notion of the constancy of angles between corresponding faces on a crystal, later prompted Rome de L'Isle (1772)[7] to take a large number of measurements using a contact goniometer (a form of protractor attached to a bar) in an attempt to prove this. It wasn't until 1809 that Wollaston[7] invented the reflecting goniometer, which enabled the measurement of interfacial angles more accurately. This subsequently led to the development of the single- and two-circle goniometers, the latter having been independently invented by Miller (1874), Fedorov (1889) and Goldschmidt (1893)[7]. The use of these tools in crystal structure determination was very popular, until Max von Laue demonstrated the diffracting properties of X-rays in 1912[8].

1.4 Diffraction

Nowadays, structure analysis relies mostly on the interaction of a material with X-rays, electrons, or neutrons, by measuring its emission or absorption of radiation. If the wavelength is fixed (a condition known as ***monochromatic*** (single-wavelength, literally meaning single-coloured) ***radiation***), the variation of intensity with direction is measured, and from these measurements it is possible to deduce the positions of the atoms in the sample. The variation in intensity, or scattering, of monochromatic radiation, results from interference effects, more commonly known as ***diffraction***. Although the diffraction theory applies to all types of radiation, only X-ray scattering is of relevance to this project, and it will therefore be discussed in further detail.

1.4.1 X-ray Diffraction

X-rays can be described as electromagnetic radiation having a wavelength of the order of 10^{-10}m (1Å). They were first described by Röntgen in 1895[7], but due to the limitations in the optical instruments available at the time, he could not perform any experiments to measure interference, reflection or refraction. It wasn't until several years later that Prof Arnold Sommerfield measured an X-ray wavelength of about 0.4Å. Inspired by discussions with Paul Ewald, who was a PhD student with Prof Sommerfield at the time, Max von Laue suggested the use of crystals as natural lattices for diffraction. W. Friedrich and P. Knipping, two of Röntgen's students, performed the experiment on a crystal of copper sulphate, and the beams were recorded photographically. Their results were published in 1912[9].

These findings stirred interest in William L. Bragg, then a student in Cambridge. He noted the geometrical shapes in Friedrich and Knipping's photographs, and believed that this diffraction could be regarded as cooperative reflections by the internal planes of the crystal. Only a year later, in 1913, Bragg and von Laue used X-ray diffraction patterns to determine the structures of KBr, KI, KCl and NaCl[10].

A simple demonstration of the method by which X-rays are generated is the standard "X-ray tube". This produces electrons by passing an electrical current through a wire filament, accelerates

them to a high velocity, and directs them onto a cooled metal target (Mo, Cu, Fe, Cr). As they hit the metal, the electrons decelerate rapidly, and this causes most of their kinetic energy to be converted to heat and lost. However, some of this energy interacts with the target metal atoms to produce X-rays. If an electron in a core atomic orbital is ionised (displaced), an electron from a higher-energy orbital will replace it, and the subsequent drop in energy will result in the emission of an X-ray photon. These particles of energy oscillate and can therefore be characterised by their wavelength (the distance between peaks), the number of peaks that pass a point per unit time (frequency) or by their energy E. If electrons in different orbitals are displaced, a difference in energy would cause the generation of a different wavelength, even though the target metal is the same, eg. In the case of Cu K_α (λ = 1.5418 Å) the transition of an electron from the 2p orbital of the L energy level to the 1s orbital on K emits α radiation, while with Cu K_β (λ = 1.3922 Å) emission of β radiation results from the transition of a 3p electron to K[11].

As an X-ray photon impinges upon a crystalline solid, it will either travel straight through it or interact with the electric field due to the electrons in the material, and thus scatter. The electron densities of all the atoms that lie in the path of an X-ray beam contribute to its scattering, causing interference (constructive or destructive) between the X-ray waves. This is X-ray interference, or ***X-ray Diffraction***.

1.4.2 Bragg's Law

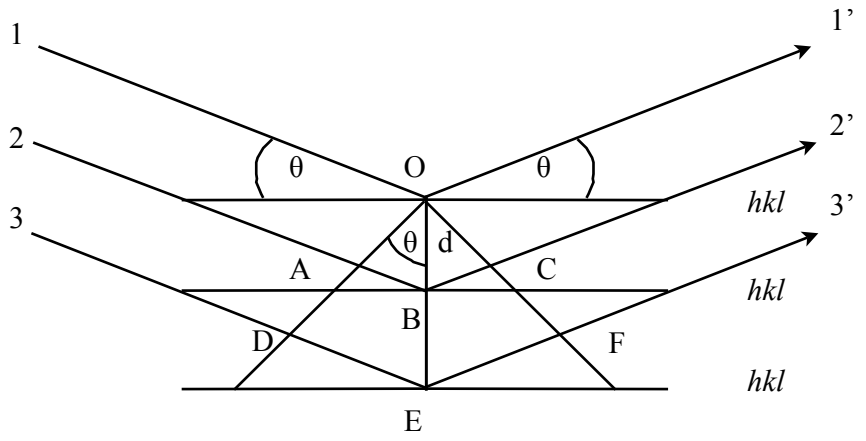

Figure 1.5 Bragg scattering of X-rays from parallel planes, with d representing interplanar spacing.

In 1913, Bragg showed that every diffracted beam that can be produced by a crystal face at a particular angle of incidence can be geometrically considered to be a reflection from sets of parallel planes passing through lattice points. This therefore requires that the angles of incidence and reflection be equal, and that the incoming and outgoing beams and the normal to the reflecting planes must themselves be in one plane [Figure 1.5]. The ***Miller Indices*** (*hkl*) are three integers that describe the orientation of a plane with respect to the three unit cell edges. The spacing d_{hkl} between successive planes is determined by the lattice geometry and is therefore a function of the unit cell parameters where V is the unit cell volume [Equation 1.1].

$$d_{hkl} = V[h^2b^2c^2\sin^2\alpha + k^2a^2c^2\sin^2\beta + l^2a^2b^2\sin^2\gamma + 2hlab^2c(\cos\alpha\cos\gamma - \cos\beta) + 2hkabc^2(\cos\alpha\cos\beta - \cos\gamma) + 2kla^2bc(\cos\gamma\cos\beta - \cos\alpha)]^{-\frac{1}{2}}$$

Equation 1.1

Diffraction from these planes will only give rise to constructive interference if the path difference between radiation scattered from adjacent planes is equal to a whole number of wavelengths. This is ***Bragg's Law***, and it can be expressed as

$$n\lambda = 2d_{hkl}\sin\theta_{hkl}$$

Equation 1.2

where λ is the wavelength of the incident radiation, $2\theta_{hkl}$ is the angle between the incident X-rays and the crystal surface and n is the order of diffraction.

The diffraction pattern of the crystal lattice is known as the ***reciprocal lattice*** owing to its reciprocal relationship with the crystal lattice: large crystal lattice spacing gives rise to small spacing in reciprocal space, and vice-versa. While direct cell parameters are usually represented by a, b, c, α, β and γ, the reciprocal lattice is denoted by $a^*, b^*, c^*, \alpha^*, \beta^*$ and γ^*. The direction of a^* is perpendicular to the directions of b and c, and its magnitude is reciprocal to the spacing of the lattice planes parallel to b and c [Figure 1.6].

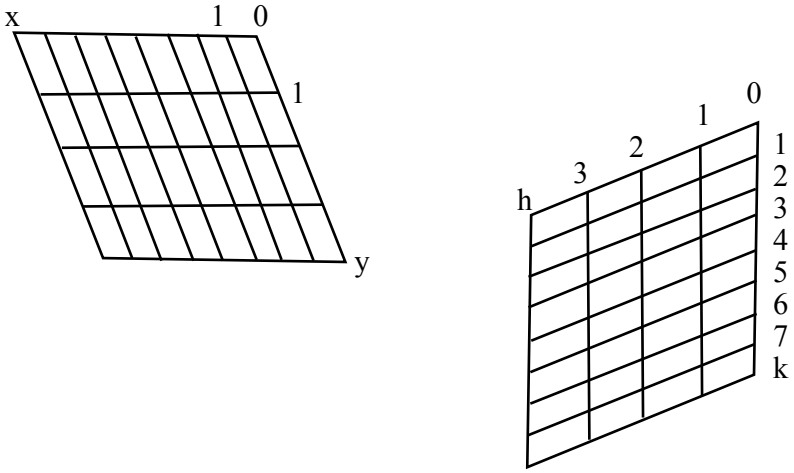

Figure 1.6 Direct lattice (left) and the corresponding reciprocal lattice (right).

The reciprocal lattice has all the properties of the real space lattice and any vectors in it represent Bragg planes which can be shown by Equation 1.3. The integers in this equation are equal to the Miller indices of the *hkl* plane.

$$d^*_{hkl} = ha^* + kb^* + lc^* \qquad \text{Equation 1.3}$$

The position of the scattering matter in the unit cell, which in the case of X-ray diffraction is electron density, determines the intensities of the diffraction pattern and is related to them by Fourier transformation: the diffraction pattern is the Fourier Transform of the electron density, which is itself the Fourier Transform of the diffraction pattern. Taking a ***scattering vector (s)*** as a point on the reciprocal lattice corresponding to a diffraction maximum defined by *hkl,* the observed intensity **I(s)** is directly related to the square of the modulus of the corresponding ***structure factor*** **F(s)**.

$$\mathbf{I(s)} \propto |\mathbf{F(s)}|^2 \qquad \text{Equation 1.4}$$

For each diffraction maximum, the electron density distribution **ρ(r)** is related to the structure factor **F(s)** of amplitude|**F(s)**|and phase **α(s)** by the equation

$$F(\mathbf{s}) = |F(\mathbf{s})| exp[2\pi i\alpha(\mathbf{s})] = \int \rho(\mathbf{r}) exp(2\pi i \mathbf{s}.\mathbf{r}) d\mathbf{r}$$

Equation 1.5

where r = $x\boldsymbol{a} + y\boldsymbol{b} + z\boldsymbol{c}$ is a vector in the direct space unit cell, (x,y,z) are fractional coordinates of the point r and integration is performed over the whole unit cell.

1.4.3 The Crystallographic Phase Problem

The reverse Fourier Transform of Equation 1.4 provides us with an expression for the electron density within the unit cell:

$$\rho(\mathbf{r}) = \frac{1}{V}\sum_{s}|F(\mathbf{s})|exp[i\alpha(\mathbf{s}) - (2\pi i\mathbf{s}.\boldsymbol{r})]$$

Equation 1.6

where V is the unit cell volume and the summation is performed over all scattering vectors **s**. The intensities measured from the diffraction data enable the calculation of an absolute value for the structure factors. However, these recorded intensities are proportional to the *squares* of the amplitudes. The square of a complex number $|F(\mathbf{s})|$ is always real, therefore information regarding the phase angles of the diffracted beam is lost. Thus although the structure factor is obtained, the absence of a phase makes structure solution unachievable. This is known as the crystallographic phase problem, a hurdle faced by many during structure determination, including Watson and Crick in the structure solution of DNA[8]. Many structure solution strategies are therefore based upon attempts to extract phase information from experimental data, in order to estimate $\alpha(\mathbf{s})$.

1.4.4 PXRD vs Single Crystal

Conventionally, a single crystal experiment involves a beam of monochromatic X-rays or neutrons, incident upon a suitably mounted and oriented single crystal. This beam is then scattered into a number of diffracted beams produced in certain directions in space. The positions and intensities of these beams are then recorded either by film, point or area detector methods, the latter being the most common. Data analysis ensues, and this can be broken down into four stages:

(1) Indexing to find the unit cell;

(2) Integration of raw images to produce a list of intensities and *hkl* values for each reflection;

(3) Structure solution (typically by direct methods or Patterson synthesis):

(4) Structure completion and refinement.

Systematic rotation of the crystal or the incident beam ensures that reflections from all sets of lattice planes are made to satisfy the diffraction condition. One of the major problems associated with single crystal experiments is the difficulty in growing a crystal of adequate proportions.

In a powder experiment, a collection of randomly oriented crystallites is exposed to the beam, rather than a single crystal. Each of these gives rise to its own diffraction pattern and individual "spots" on a detector become spread out into rings of diffracted intensity. There rings are the intersection of cones of diffracted intensity with the detector. Ring intensities can be measured by film or area detectors, but are more commonly measured by scanning a point or one-dimensional line detector across a narrow strip.

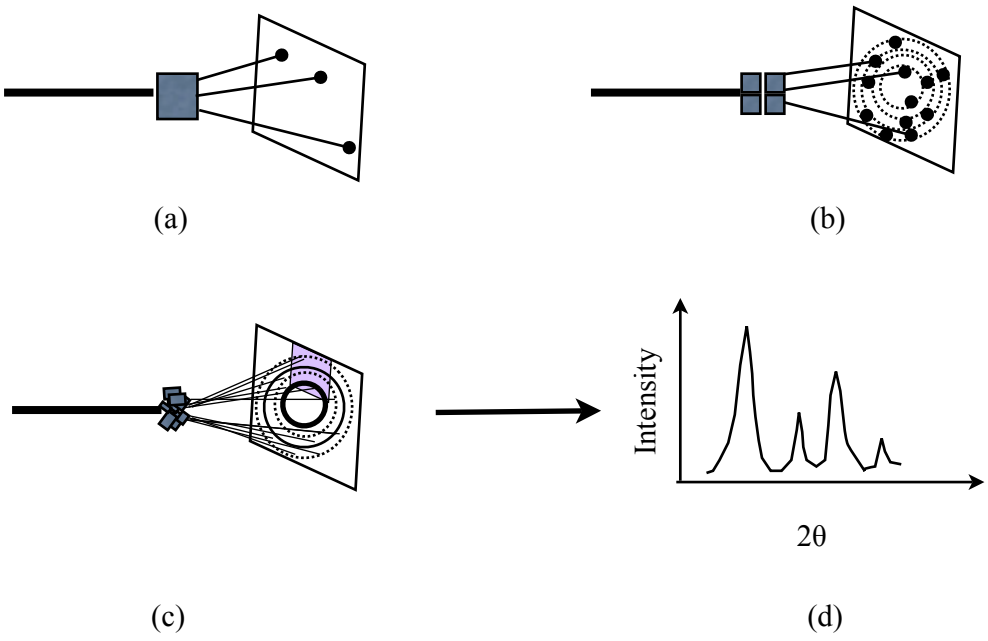

Figure 1.7 Diffraction (a) from an oriented single crystal, (b) from four crystals at different orientations with respect to the incident beam, and (c) from powder. (d) shows the pattern plotted by scanning across the purple rectangle.

The diffraction data is then represented by plotting the total diffracted intensity against the diffraction angle 2θ. As is clearly shown by Figure 1.7, one of the major problems with powder diffraction is that the three-dimensional distribution of a single crystal experiment is compressed onto the one dimensional 2θ space, leading to a vast loss of information due to peak overlap. Extraction of accurate individual reflection positions and integrated intensities, and subsequent structure factor calculations are therefore non-trivial, making structure determination from powder diffraction a very challenging procedure.

In order to minimise the effects of peak overlap as much as possible, experimental set-ups must be tailored according to the quality of the resultant peaks. Sharper and well-defined peaks provide more accurate and conclusive information about the unit cell.

1.5 Structure Determination from Powder Diffraction

Information about a material can be found in three distinct places within its powder pattern. *Peak positions* are determined by the size, shape and symmetry of the unit cell. *Peak intensities* are affected by the arrangement of scattering density (i.e. atomic coordinates) within the unit cell. *Peak shape* is the result of a combination of instrumental parameters (source, optics and detector contributions) and information about the microstructure of the material (domain size and strain).

1.5.1 Indexing

The process of structure solution of an unknown material purely from powder data basically involves the determination of the unit cell before any structure solution technique may be employed. The positions of reflections in the diffraction pattern can be used, by means of Bragg's Law [Equation 1.2] and the expression for interplanar spacing d_{hkl} [Equation 1.1], to determine a set of unit cell parameters. This process is called ***indexing***.

For simple systems, indexing can sometimes be performed by hand, but in most cases it is left to the efficiency of algorithms such as DICVOL[13], TREOR[14], and ITO[15], whose aim is to reproduce observed peaks by generating a set of trial structures and assigning figures of merit to each set of unit cell parameters. A number of such "auto-indexing" programs can be accessed via

the interface provided by software packages such as CRYSFIRE[16]. This applies a range of methods which take into consideration the measured positions of the peak maxima for a number of selected peaks.

In the case of "non-ideal" powder data, the need for more reliable indexing procedures prompted the development of new techniques over the past decade. Of particular interest are the whole-profile fitting genetic algorithm approaches in which potential unit cells are assessed against the whole profile[17], neural network approaches[18], and methods based on the traditional dichotomy approach (which is one of the features employed by CRYSFIRE[16], but that have been designed to be less sensitive to impurity peaks and large zero point errors[19, 20].

Since indexing requires accurate determination of peak positions, this step is usually the stumbling block in most attempts at solving crystal structures from powders. This is partly due to peak overlap or peak displacement, which may result in the obscuring of certain peaks crucial to the indexing process. Additional problems, such as the presence of impurities or polymorphs, a significant zero point error, or poor definition of peak positions (either due to poor sample crystallinity or poor instrumentation) can further hinder this step. Zero point errors may sometimes be overcome by the introduction of an internal standard into the sample, to quantify the correction that is to be applied. Known impurities may also be accounted for. Small crystallite size, lattice strain, and preferred orientation may also prove to be problematic to the successful indexing of a material.

1.5.2 Space Group Assignment

After determination of the unit cell is complete, a space group must be assigned to the system, and this is based on its symmetry. The symmetry within a unit cell causes the systematic absence of reflections pertaining to certain *hkl* lattices in the diffraction pattern. Assigning a space group correctly depends on the determination of which reflections are absent, followed by examination of the conditions required for these absences to occur. This process is not always straight-forward, and sometimes factors such as peak overlap preclude the resolution of a sufficient number of peaks. Space group assignment can also be complicated if the conditions for systematic absences are not unique. In this case, the next step in the process - *structure solution* -

may be carried out for each of the plausible space groups. Information regarding the presence of crystallographic symmetry within the molecule, as well as confirmation of the number of molecules present in the asymmetric unit, may, at this stage, be obtained by experimental techniques such as Solid State NMR[21].

1.5.3 Structure Solution Methods

Before refinement of a structure can be attempted, a structural model must first be obtained which will subsequently serve as a starting point in the final step of structure solution. Following unit cell and space group determination, a Pawley[22] or LeBail[23] fit is performed. These are refinement procedures similar to the Rietveld method but that do not require a structural model. They are peak-fitting routines with allowed peak positions defined by the unit cell size (which is refined), and its shape and symmetry, and they establish both the intensities of each of the diffraction maxima as well as the instrumental profile parameters. In order to ensure a reliable comparison between the experimental data and the structural information calculated for the model, it is crucial to refine unit cell parameters, zero point, peak width and peak shape. If appropriately done, this process would make the structural model a good representation of the experimental structure.

Structure solution from powder data can then be carried out using either of two method strategies, i.e. *traditional* or *direct space* approaches. In traditional methods, intensity information is extracted from the powder data and is then used in much the same way as for single crystal diffraction. In contrast, direct space methods involve the independent generation of trial structures by movement of a structural model within a pre-defined unit cell. This is solely based on the molecular structure and unit cell information, and does not take experimental data into consideration until the final step, which involves direct comparison of the powder pattern generated for the trial structure with the experimental powder pattern. Such comparison is necessary in order to assess the suitability of any given trial structure, and it is quantified by means of a crystallographic R factor or figure of merit (R_{wp} or χ^2).

Some direct space methods do involve the comparison of extracted intensities[24], but this information is only used in the final comparison stage of the structure solution process, and not to generate the structural model itself.

The trial structure having the best fit with the experimental data (i.e. the lowest R factor) is chosen as a starting point for Rietveld refinement.

1.5.4 Structure Refinement

When a suitable trial structure is selected, the structure determination process comes to its conclusive step, ***Rietveld refinement***, which aims at deriving the final crystal structure from the approximate structural model obtained during the previous steps. This process is generally done by least squares refinement of the various structure parameters present. In the Rietveld method[25], each point in the powder profile is considered as an individual intensity measurement, and it is compared to its corresponding intensity value on the calculated pattern. An optimal fit between the two patterns is obtained by the adjustment (using a Least-Squares method) of selected parameters which define both the structural model and the profile itself. The results from this point-by point comparison are then quantified by assigning a figure of merit or agreement factor, most commonly the weighted profile R factor (R_{wp}), to assess the degree of dissimilarity between the two profile patterns. GSAS[26], FULLPROF[27], TOPAS[28], and RIETAN[29], are among the most widely-used programs for Rietveld refinement.

The success of a Rietveld refinement largely depends on how accurate a representation of the true structure the initial structural model is. Factors such as preferred orientation can again play a role in hindering the successful completion of this stage of the structure determination process. However, corrections may be applied to overcome this problem.

Problems of structural instability may often arise during refinement due to insufficient accuracy or poor quality of the model. In such cases, the use of geometric restraints (soft constraints) may be necessary[30]. These restraints are based on standard molecular geometries and they bias the refinement process towards a structurally reasonable solution, impeding excess shifts in atomic positions. Generally, refinements in which soft constraints are employed allow more parameters to be refined than would be possible in unrestrained refinements[31].

The success of a refinement is assessed by the presence of three fundamental attributes: graphical representation showing a good fit, a reasonable R factor value (i.e. an R_{wp} or χ^2 close to that obtained during Pawley or LeBail fitting), and a sound final crystal structure that makes both visual and structural sense.

1.6 Thermal Expansion

One of the very important properties of materials for many technological and practical applications is ***thermal expansion***. The thermal expansion of a material can be either intrinsic or extrinsic. Intrinsic expansion, which can be isotropic or anisotropic, is of interest in this study, as it is based on the changes of the crystallographic unit cell axes with respect to temperature. Isotropic materials show the same magnitude of thermal expansion in all directions of the unit cell, and they are therefore either cubic or amorphous. In contrast, anisotropic materials have a different magnitude of thermal expansion along the different unit cell axes.

During heat transfer, the energy that is stored in the intermolecular bonds between atoms changes. When the stored energy increases, so does the length of the molecular bond. Almost all solids typically expand upon heating, as the interatomic distances increase. Some substances have a negative expansion coefficient, and will therefore expand when cooled (eg. freezing water). If the interatomic potential function is assumed to be harmonic, when temperature increases, the average distance between two atoms will not change.

In reality, however, the interatomic potential is anharmonic. Therefore as temperature increases, the average distance between two atoms also increases, and this causes thermal expansion.

As the bond between two atom groups gets stronger, the potential function becomes more symmetric and the vibrations more harmonic. If the bond is strong enough, thermal expansion may even be undetectable. This concept may be used in cases where the design of materials with low or negative thermal expansion is necessary, and therefore structures with strong bonding networks are preferred.

This response to temperature change is expressed as its coefficient of thermal expansion, which can be used in two ways: a *linear* thermal expansion coefficient, and a *volumetric* thermal expansion coefficient, defined as:

$$\alpha = \frac{1}{l}(\delta l/\delta T)_p$$

Equation 1.7

$$\alpha_v = \frac{1}{V}(\delta V/\delta T)_p$$

Equation 1.8

respectively. V is the initial volume, l is the initial length, and δV and δl are the changes in volume and length of the solid due to the temperature change δT. These are taken at a constant pressure p.

For isotropic materials, the linear thermal expansion coefficient can be approximated as being equal to one third of the volumetric coefficient. In the case of anisotropic materials, however, this is calculated as the average of the linear coefficients of thermal expansion in all axes [Equation 1.9], where α_a is the linear coefficient along a, α_b is the linear coefficient along b and α_c is the linear coefficient along c.

$$\alpha_{ave} = \frac{(\alpha_a + \alpha_b + \alpha_c)}{3}$$

Equation 1.9

The majority of work relating to the behaviour of materials with changing temperature has been carried out on inorganic solids, including AM_2O_7 (metal IV pyrophosphates) materials[32] (where A is a metal (IV cation) and M = P or V), the $Sc_2(WO_4)_3$ family[33,34], and siliceous zeolites[35]. Few examples of low temperature organic cell determination taken from this aspect exist in the literature. One such example is the determination of the anisotropic thermal expansion of glipizide[36], for which X-ray powder diffraction data were collected at temperatures between 150K and 380K, at increments of 5K. The lattice expansion of the complex molecular

crystal structure was analysed in terms of intermolecular interactions: a similar approach to that taken during earlier work on inorganic systems.

1.7 Polymorphism

As organic molecules are being developed for new materials and pharmaceuticals, the characterisation of their solid state properties is shifting the concepts on which we base our understanding of their crystallisation. Instead of a molecule having a unique crystal structure, it often appears as if the number of known solid forms, or ***polymorphs***, is proportional to the time and money spent investigating the compound. The term '***polymorphism***' (Greek: πολυ-many; μορφές-forms) is used to describe the existence of a substance in more than one crystalline form. Organic molecular crystals often display multiple polymorphs and pseudo-polymorphs (solvates and hydrates). There is a close relationship between the unique crystal structure of a compound and its properties, such that different polymorphic structures of a material often have different physical, chemical, biological and pharmaceutical properties.

The unexpected appearance of novel crystalline forms can be a scientific, industrial, or commercial disaster. The case of the protease-inhibitor ritonavir (*Norvir*®), Abbott Laboratories' anti-HIV drug, is a high-profile example of polymorphs exhibiting different properties. The drug was formulated as an encapsulated solution in ethanol and water. However, in 1998 a new crystal form appeared, first at a production plant in North Chicago, then at a plant in Italy. Ritonavir was the victim of a late-appearing polymorph with different solubility properties[37]. In contrast, the controlled use of a metastable form can offer considerable benefits when it has advantageous physical properties such as improved solubility. Another practical example is paracetamol; whereas form I is the commercially available form, form II undergoes plastic deformation and is suitable for direct compression, thus making it potentially advantageous to the pharmaceutical industry as it would eliminate the need for binders to be added during the manufacture of tablets, if its production in bulk is feasible[38]. Polymorphism has even captured the imagination of authors, in such novels as Vonnegut's critically acclaimed "*Cat's Cradle*", in which "Ice Nine", a

polymorph of ice, is found to be kinetically more stable than normal ice crystals, and converts all the water on Earth to a solid at room temperature upon contact[39].

Clearly, such discrepancies can wreak havoc in the design, preparation, formulation and marketing of new materials and in the characterisation of old ones, making polymorphism a phenomenon of great interest to several industries attempting to exercise control over the production, processing and development of organic materials in settings where a particular form is desirable over another. Exploitation of specific polymorphs requires a predictive model of how the kinetic aspects of solvents and crystallisation conditions determine which of the thermodynamically feasible crystal forms are actually observed, and this is in turn validated by additional experimentation.

The appearance of different polymorphic forms can be attributed to both kinetic and thermodynamic parameters. Polymorphs tend to convert from less stable to more stable forms, the rate of conversion depending mainly on the required activation energy and the differences in free energies between the two forms. The relative stability of these crystals as a function of conditions and the ability to produce a desired polymorph on demand are areas of great current interest. In some systems one polymorph is the stable form at all temperatures (***monotropic***) while in other systems the stable form varies with temperatures (***enantiotropic***). In addition, many organic systems display multiple metastable polymorphs.

In the ideal thermodynamic case, each polymorph is stable over its own individual range of temperatures and pressures and, when that range is exceeded, it changes into a new polymorph. These interconversions are reversible and occur at a fixed transition temperature analogous to the melting and freezing points, which separate the solid and liquid states. In actual practice, however, several polymorphs may coexist at the same temperature and pressure, in which case only one of them is thermodynamically stable. In this case the other polymorphs are said to be "kinetically metastable". The Gibbs free-energy values of the various polymorphs define the depth of each energy minimum and determine which of the various coexisting polymorphs is the thermodynamically stable form[40]. Thus, knowledge of the thermodynamic stability is important for the selection of the appropriate polymorph for pharmaceutical and chemical development.

1.8 Crystal Structure Prediction

Structure prediction aims at searching for the most thermodynamically feasible three-dimensional packing arrangement of a substance solely on the basis of its molecular structure. In the study of polymorphs, a thorough experimental solvent screen would involve the isolation and characterisation of copious amounts of crystalline samples, thus making the exercise very time-consuming, expensive, and in many cases futile. A reliable technique for the prediction of possible polymorphs would clearly be invaluable. However, one often comes across the question: are crystal structures predictable? In 1994, Gavezzotti gave a clear, uncompromising answer: No[41]. There have been several debates on the matter since[42-45], and thirteen years down the line, we can now rephrase that answer to "not yet", because the energetically feasible crystal structure of a molecule can now be predicted for an increasing range of types of molecule, as long as their relative energies are calculated accurately and an appropriate range of crystal structures is considered[46]. Crystal structure prediction can also be of significant use in the design of new materials. A range of candidate structures can be theoretically modelled to find out which one would be expected to crystallise in a form which has the desired properties.

1.8.1 Methodologies

Ab initio prediction of crystal structures involves the generation of crystal structure models without the use of any experimental data. A range of software employing various theoretical approaches has been developed[47-49], and many of the methods that are currently used have been tested in the CCDC's international blind tests of crystal structure prediction[49].

Most approaches begin with a search for the global minimum in the lattice energy. If the crystallisation is under total thermodynamic control, and the appropriate energy can be approximated by calculating the lattice energy from a model of the forces acting within the crystal, then this would result in a reliable prediction. With molecules that are sufficiently rigid, it can be assumed that they will preferentially adopt the same conformation in the crystals as in the gas phase, as modelled by an *ab initio* optimisation. The lattice energy is then obtained simply by

summing the intermolecular potential between every pair of molecules in the crystal. Most molecules are sufficiently flexible that they can change their conformation within the crystal in order to improve their intermolecular interactions and lattice energy (U_{latt}), giving an overall more stable crystal structure with lower total crystal lattice energy (E_{crys}).

$$E_{crys} = U_{latt} + \Delta E_{intra}$$

Equation 1.10

where ΔE_{intra} is the energy penalty brought about by the change in molecular conformation.

Relative crystal energies can unfortunately be very sensitive to the exact conformation especially of polar hydrogen atoms, and are therefore affected by even small changes in hydrogen bond geometry. This problem may be overcome by specifically optimising the change in lattice energy (E_{crys}) with respect to the key torsion angles as well as the otherwise rigid-body structure parameters. Shuttling between the *ab initio* and energy minimisation programs would achieve such an optimisation[50].

The effects of temperature and pressure on the relative energies of the crystal structure are totally neglected during the comparison of total lattice energies, E_{crys}. Entropically related polymorphs are common[40,51], and although enthalpy differences generally dominate entropy differences[52], ranking structures based on their free energy would place them in a different order from that obtained by lattice energy ranking[53]. Most entropy estimates are currently based on lattice dynamics calculations for rigid molecules[54], with a few studies of organic materials carried out at normal temperatures by molecular dynamics using DL_MULTI and DL_POLY[55]. In a study of the polymorphic behaviour of benzene, the free energy surface was explored by successful application of the metadynamics method[56]. These methods are, however, very computationally demanding, and although free energies at the crystallisation temperatures and pressures should be used, the total lattice energy landscape is more commonly observed as a first approximation.

Formerly, some degree of knowledge of the crystallographic attributes of the structure was used in the generation of trial structures for lattice energy minimisation in order to sample the range of possibilities effectively. Searches were therefore restricted to $Z'=1$ (where Z' is the

molecules in the asymmetric unit, compared to Z which is the number of molecules in the unit cell), and only the most common space groups for organic molecules were included. The possibility of performing more extensive searches has led to the inception of various types of simulated annealing to explore the lattice energy surface, and complete searches in specified space groups and small values of Z' became possible[57]. Recent methods[58] are proving to be capable of performing complete searches of the approximate energy surface for a wide range of specified space groups with Z'=1 or 2 for rigid molecules, as suggested by recent blind test studies[59]. These methods are very computationally-demanding, and the search effort increases rapidly with the number of conformational degrees of freedom (usually torsion angles), or molecules in the asymmetric unit, as this increases the dimensionality of the lattice energy surface.

It is therefore difficult to establish one clearly-defined method for an independent structure prediction, even in the case of closely-related structures. Even if the most theoretically accurate feasible model is used, an exhaustive search method will not necessarily predict the correct experimental structure, and the type of energy landscape obtained greatly depends on the specific molecule. Assuming that the energy gaps between the lattice minima relative to the plausible energy differences between polymorphs are qualitatively accurate, there are three possible scenarios when analysing crystal energy packing landscapes [Figure 1.8].

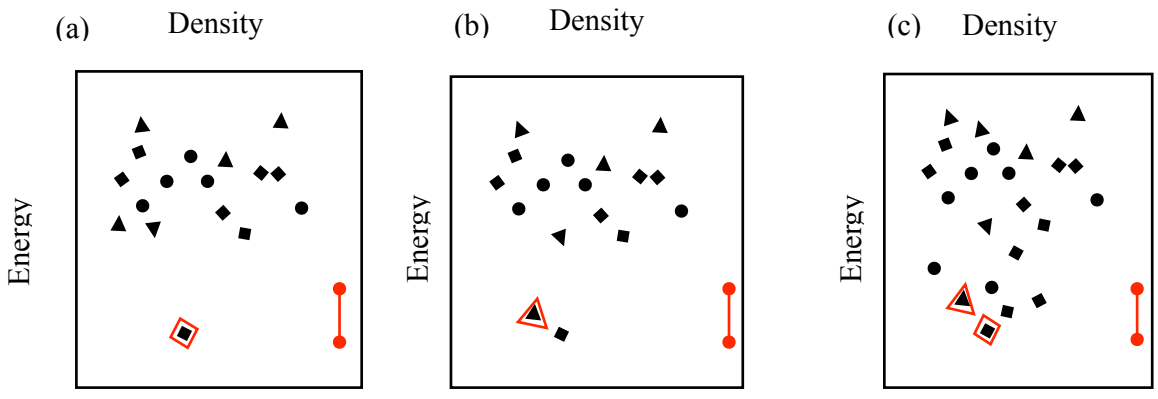

Figure 1.8 Examples of crystal energy landscapes. Each point represents a crystal structure at a local energy minimum. Different symbols denote different packing. Open symbols are the experimentally known structures. The red bar shows the energy difference that may occur between polymorphs.

(a) In an ideal case, one structure is predicted to be so thermodynamically stable that if the molecule crystallises in a structure covered by the search, it should be this structure. If this crystal structure is obtained experimentally, such an energy landscape would confirm that there are unlikely to be any polymorphs that are practically significant[60]. This energy landscape usually results when the molecules have strongly preferred directional interactions in all three dimensions, allowing them to pack densely.

(b) In the second scenario, a structure that does not correspond to the experimental structure is predicted to be more stable. This situation should prompt a thorough polymorph screen to find the predicted structure, as the existence of a form that is more stable could pose a potential hazard, economically as well as health-related in the case of products intended for human consumption. When conducting the polymorph search, prior analysis of the hydrogen bonding motifs present in the lower energy structures may help direct the search by influencing the choice of solvents required to obtain such packing[61].

(c) The third scenario that can be observed when analysing crystal energy landscapes is the one that was most-commonly encountered during this study. Sometimes, a large number of structures fall within a narrow energy range, indicating that various packing possibilities exist that are energetically competitive. A multitude of factors can influence the appearance of one of these structures experimentally, and apart from kinetic factors, temperature and pressure, these may include controllable factors[62] such as solvent, cooling rate, and initial supersaturation, as well as impurity profile[63]. For this reason, it is highly unlikely that the crystal structures which will be observed polymorphs will be selected by modelling of kinetic factors alone. Comparison with the crystal structure of related materials can provide some valuable insight, especially when combined with experimental polymorph screening.

1.9 Two-Way Relationship

Unfortunately, few molecules produce landscapes where the energy gap between the observed and other possible structures is large enough relative to the energy difference that may occur between polymorphs, and to the uncertainties in computed energies. Generally, much more accurate relative energies of the possible crystal structures are required in order to be confident of the relative ranking. Therefore the first step towards increasing the confidence that the computed crystal energy packing landscape is a realistic representation of the most thermodynamically feasible crystal structure of the molecule is the minimisation of uncertainties in the relative energies of all the possible packings in the crystal structure.

Crystal structure prediction, therefore, currently has to be treated as a complementary tool to experimental studies, sometimes providing structural data that may serve as a starting point in structure solution of data that cannot be indexed. Similarly, the coupling of experimental techniques with crystal structure prediction can serve as confirmation of the stability and/or existence of a crystal structure found during a computational search.

As discussed in Section 1.5.1, structure solution from powder diffraction is dependent on the successful indexing of the data, and failure to index powder data is not uncommon, for a multitude of reasons. The crystal structure determination of organic molecules is increasingly being tackled by the use of theoretical structure prediction coupled with experimental methods such as PXRD[64]. If neither the predicted structure nor the PXRD profile contain enough information for the characterisation of the crystal structure, structure determination may be greatly facilitated by combining the two methods.

The comparison of experimental data with that simulated from the theoretical structures is often done visually or purely on a fingerprinting basis[65,66], and there are only a few molecular cases in which the predicted structures have been used as a starting point for Rietveld refinement [64,67] both in terms of lattice parameters and crystal structure. One possible reason for the limited application of this approach is that even though the difference in lattice parameters between the experimental and calculated structures is relatively small, the variation in peak positions in the

respective patterns often makes automated quantitative comparison difficult and attempts at refinement unstable and unsuccessful.

This is partly due to the temperature differences between the two techniques: whereas routine powder data is collected at room temperature, prediction calculations search for the most energetically feasible packing at 0K, by assumption that temperature effects and zero-point energies can be neglected[60]. A reduction in temperature can significantly affect the lattice parameters and unit cell volume, although these effects are often anisotropic and hard to predict[60]. Therefore the possibility that collection of powder data at low temperatures would enable a more meaningful comparison of the simulated and calculated profiles was taken into consideration, with the added ambition of it also providing an alternative agreement factor for automatic ranking other than R_{wp}.

1.10 Project Aims

The aim of this project was primarily to evaluate a number of methods to compare X ray powder diffraction sets obtained experimentally and simulated from theoretical trial structures. Identification of a reliable comparative approach would provide an automatic numerical method to identify the "correct" predicted structure from hundreds of others.

Success in this aim could then lead to

(i) subsequent use of the "correct" predicted structure in the structure determination of crystal structures whose powder data alone was not sufficient for this purpose, and

(ii) a reliable method for screening structure prediction results and relating these results to experimental data.

With potential problems between the comparison of room temperature experimental data and low temperature prediction calculations, the suitability and effect of using data over a range of temperatures for this comparison would also be assessed.

1.11 References

1. C. Hammond, *Introduction to Crystallography*, Oxford University Press, USA, 1992

2. F. C. Phillips, *An Introduction to Crystallography*, Longmans, Green and Co., London, 1964

3. J. Pickworth Glusker and K. N. Trueblood, *Crystal Structure Analysis: A Primer*, 2nd Edition, Oxford University Press, New York, 1985

4. B. D. Cullity and S. R. Stock, *Elements of X-Ray Diffraction*, 3rd Edition, Prentice Hall, 2001

5. K. Ramakanth Hebbar, *Basics of X-Ray Diffraction and Its Applications*, I K International Publishing House, 2007

6. A. T. Florence and D. Attwood, *Physicochemical Principles of Pharmacy*, 4th Edition, Pharmaceutical Press, 2005

7. M. J. Buerger, *Contemporary Crystallography*, McGraw-Hill, USA, 1970

8. M. Laue, *Sitzber. Math.-physik. Klasse Bayer. Akad. Wiss. Munchen*, 1912, 363

9. W. Friedrich, P. Knipping and M. von Laue, *Sitz. Bayer. Akad. Wiss.,* 1912, 303

10. W. H. Bragg and W. L. Bragg, *Proc. R. Soc. London, A,* 1913, **89**, 248

11. N. Tsoulfanidis, *Measurement and Detection of Radiation*, 2nd Edition, Taylor and Francis, USA, 1995

12. J. D. Watson, *The Double Helix (New Edition)*, Longman, UK, 2001

13. A. Boultif and D. Louër, *J. Appl. Cryst.*, 1991, **24**, 987

14. P.-E. Werner, L. Eriksson and M. Westdahl, *J. Appl. Cryst.*, 1985, **18**, 367

15. J. W. Visser, *J. Appl. Cryst.*, 1969, **2**, 89

16. R. Shirley, *The CRYSFIRE System for Automatic Powder Indexing*, University of Surrey, UK, 1999

17. B. M. Kariuki, S. A. Belmonte, M. I. McMahon, R. L. Johnston, K. D. M. Harris and R. J. Nelmes, *J. Sync. Rad.*, 1999, **6**, 97

18. S. Habershon, E. Y. Cheung, K. D. M. Harris and R. L. Johnston, *J. Phys. Chem. A*, 2004, **108**, 711

19. M. A. Neumann, *J. Appl. Cryst.*, 2003, **36**, 356

20. A. A. Coehlo, *J. Appl. Cryst*., 2003, **36**, 86

21. M. Tremayne, B. M. Kariuki and K. D. M. Harris, *Angew. Chem. Int. Ed. Engl.*, 1997, **36**, 770

22. A. LeBail, H. Duroy and J. L. Fourquet, *Materials Research Bulletin*, 1988, **23**, 447

23. G. S. Pawley, *J. Appl. Cryst.*, 1981, **14**, 357

24. W. I. F. David, K. Shankland and N. Shankland, *Chem. Commun*., 1998, 931

25. H. Rietveld, *J. Appl. Cryst.*, 1969, **2**, 65

26. A. C. Larson and R. B. Von Dreele, *GSAS. General Structure Analysis System, Report No. LAUR 86-748*, Los Alamos National Laboratory, Los Alamos, New Mexico, USA, 1994

27. J-Rodriguez-Carvajal, *Abstracts of the Satellite Meeting on Powder Diffraction of the XV Congress of the IUCr*, Toulouse, France, 1990

28. A. A. Coelho, *J. Appl. Cryst.*, 2000, **33**, 899

29. F. Itzumi and T. Ikeda, *Mater. Sci. Forum*, 2000, **321**, 198

30. K. D. M. Harris and M. Tremayne, *Chem. Mater.*, 1996, **8**, 2554

31. Ch. Baerlocher, *The Rietveld Method*, R. A. Young (Ed.), International Union of Crstallography and Oxford University Press, Oxford, UK, 1993

32. V. Korthuis, N. Khosrovani, A. W. Sleight, N. Roberts, R. Dupree and W. W. Warren, *Chem. Mater.*, 1995, **7**, 412

33. J. S. O. Evans, T. A. Mary and A. W. Sleight, *J. Solid State Chem*., 1998, **137**, 148

34. J. S. O. Evans and T. A. Mary, *Int. J. Inorg. Mater*., 2000, **2**, 143

35. P. Lightfoot, D. A. Woodstock, M. J. Maple, L. A. Villaescusa and P. A. Wright, *J. Mater. Chem.*, 2001, **11**, 212

36. J. C. Burley, *Acta Cryst, B*, 2005, **61**, 710

37. J. Bauer, S. Spanton, R. Henry, J. Quick, W. Dziki, W. Porter and J. Morris, *Pharm. Res.*, 2001, **18**, 859

38. G. Nichols and C. S. Frampton, *J. Pharm. Sci.*, 1998, **87**, 684

39. K. Vonnegut, *Cat's Cradle*, Penguin Books, 1999

40. J. Bernstein, *Polymorphism in Molecular Crystals*, Oxford University Press, New York, 2002

41. A. Gavezzotti and C. Filippini, *J. Phys. Chem.*, 1994, **98**, 4831

42. A. Gavezzotti, *Cryst. Eng. Com.*, 2002, **4**, 343

43. J. D. Dunitz, *Chem. Commun,*, 2003, **5**, 545

44. J. D. Dunitz and H. A. Scheraga, *P. Natl. Acad. Sci. USA*, 2004, **101**, 14309

45. R. Desiraju, *Science*, 1997, **278**, 404

46. S. L. Price, *Cryst. Eng. Comm.*, 2004, **6**, 344

47. J. P. M. Lommerse, A. J. Stone, R. Taylor and F. H. Allen, *J. Am. Chem. Soc.*, 1996, **118**, 3108

48. W. D. S. Motherwell, *Mol. Cryst. Liq. Cryst.*, 2001, **356**, 559

49. G. M. Day et al, *Acta Cryst. B*, 2005, **61**, 511

50. P. G. Karamertzanis and S. L. Price, *J. Chem. Theory Comput.*, 2006, **2**, 1184

51. H. G. Brittain, *Polymorphism in Pharmaceutical Solids*, Marcel Dekker, New York, 1999

52. A. Gavezzotti and G. Filippini, *J. Am. Chem. Soc.*, 1995, **117**, 12299

53. J. Dunitz, G. Filippini and A. Gavezzotti, *Helv. Chim. Acta*, 2000, **83**, 2317

54. G. M. Day, S. L. Price and M. Leslie, *J. Phys. Chem.*, 2003, **107**, 10919

55. S. L. Price, S. Hamad, A. Torrisi, P. G. Karamertzanis, M. Leslie and C. R. A. Catlow, *Mol. Simulat.*, 2006, **32**, 985

56. P. Raiteri, R. Martonak and M. Parrinello, *Angew. Chem. Int. Ed.*, 2005, **44**, 3769

57. P. Verwer and F. J. J. Leusen, *Computer Simulation to Predict Possible Crystal Polymorphs*, in Reviews in Computational Chemistry Volume 12, Wiley - VCH, New York, 1998

58. P. G. Karamertzanis and C. C. Pantelides, *J. Comp. Chem.*, 2005, **26**, 304

59. B. P. Van Eijck, *Acta Cryst. B.*, 2005, **61**, 528

60. S. L. Price, *Adv. Drug Deliver. Rev.*, 2004, **56**, 301

61. N. Blagden, W. I. Cross, R. J. Davey, M. Broderick, R. G. Pritchard, R. J. Roberts and R. C. Rowe, *J. Phys. Chem. Chem. Phys.*, 2001, **3**, 3819

62. T. Threlfall, *Organic Process Res. Dev.*, 2000, **4**, 384

63. R. W. Lancaster, P. G. Karamertzanis, A. T. Hulme, D. A. Tocher, T. C. Lewis and S. L. Price, *J. Pharm. Sci.*, 2007, **96**, 3419

64. M. Tremayne, L. Grice, J. C. Pyatt, C. C. Seaton, B. M. Kariuki, H. H. Tsui, S. L. Price and J. C. Cherryman, *J. Am. Chem. Soc.*, 2004, **126**, 7071

65. A. D. Bond and W. Jones, *Acta Cryst. B*, 2002, **58**, 233

66. H. R. Karfunkel, Z. J. Wu, A. Burhard, G. Rihs, D. Sinnreich, H. M. Buerger and J. Stanek, *Acta Cryst, B*, 1996, **52**, 555

67. R. S. Payne, R. I. Roberts, R. C. Rowe and R. Docherty, *J. Comp. Chem.*, 1998, **19**, 1

2. METHODOLOGY

In the case of previously published structures, the relevant ***CIF*** (Crystallographic Information File[1]) was downloaded from the Cambridge Structural Database, and the diffraction pattern profile simulated using the Crystallographica[2] software package. These simulated patterns were then compared to the powder patterns obtained experimentally to confirm the identity and phase purity of the samples. These materials were subsequently treated as "unknowns", and were subjected to the same procedures as the previously unsolved structures.

2.1 Automated Comparison

All computational searches were conducted by collaborators at UCL, and the resulting structure files (*.res*) were passed on to us. *.res* files contain information such as lattice parameters and atomic coordinates for the predicted structure. Prior to the comparison of the predicted structure files with the data obtained experimentally, standardisation of the *.res* files had to be ensured. Due to the assorted nature of the materials under study, and the continuing evolution of novel search techniques, each set of predictions was obtained using a different search method, thus making standardisation of the structure files a more intricate and time-consuming process than was envisaged at the beginning of this project. Once the *.res* files were standardised, the experimental data were compared with the simulated data from the predicted structures using R_{wp} (GSAS) and correlation analysis (*POLYSNAP* and *Compare.x*).

2.1.1 R_{wp} Calculation

A conventional method for the comparison of calculated and experimental powder diffraction patterns involves calculating the difference plot between the two, and quantifying this dissimilarity as the sum of the differences (R_p) or the sum of the squared and weighted differences

(R_{wp}). The calculation is based on a pointwise comparison between the two powder patterns, and it is a very sensitive method.

A good agreement would, in theory, give a very low R_{wp}. Values above 20% are not considered ideal. However, R_{wp} values can often be unduly inflated by factors that do not necessarily arise from a poor structural model[3]. For two identical structures, even small discrepancies in unit cell parameters (arising, for example, from a temperature difference) would result in slight shifts in peak positions, thus increasing the dissimilarity plot between the two patterns, despite their being identical [Figure 2.1].

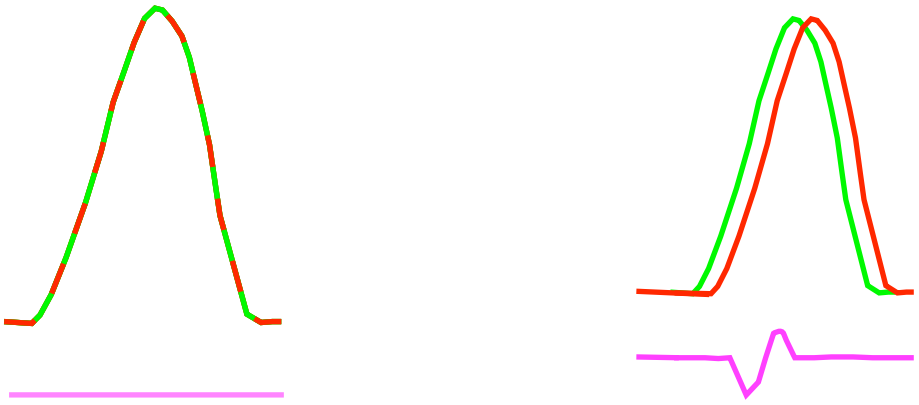

Figure 2.1 Diagram showing observed peak (red), calculated peak (green) and difference plot (pink), calculated by Rwp(obs) - Rwp(calc)[3]. Two perfectly identical peaks at exactly the same position give a straight dissimilarity line (i.e. difference = 0).

Code has been written in Fortran 77 for the automated calculation of R_{wp}, using the structural information from individual *.res* files to calculate the powder pattern that is to be compared with the experimental data [Appendix A1]. After the number of atoms present in the asymmetric unit and the number of predicted structures to be compared have been specified, the routine uses the General Structure Analysis System (GSAS[4]) software package to perform the comparison. A list of R_{wp} values in percent is then printed to an output file. To ensure that a reliable comparison was obtained between the experimental and simulated data, a LeBail fit was carried out on the experimental data (in the case of previously know structures) so that zero point, background and peak shape parameters could be modelled in the calculated data.

Optionally, the percentage expansion or contraction to be applied to the unit cell prior to R_{wp} calculation may also be specified. In this case, R_{wp} values are calculated at increments of 0.5% in unit cell length, up to the specified percentage.

2.1.2 PolySNAP

While most search-match programs available commercially use extracted *d*-spacing and intensity for each identified peak, PolySNAP[5-8] uses each data point, thus making use of all the information available within the whole profile. Data can either be imported in CIF format[1], Bruker Raw format, or *xy* format (2θ, intensity). Owing to the unavailability of CIFs in the case of previously unsolved structures, and the nature of our comparison involving theoretical structure files as well as experimental data, the format chosen for all our analyses was *xy*. Therefore all *.res* files were first used to simulate powder patterns of each theoretical structure (in the wavelength corresponding to the geometry used experimentally), before being saved as *xy* structure files. Although various formats can be read into PolySNAP, only one format may be used during any one session. After all structure files have been imported successfully, the data are then normalised to give a maximum peak intensity of 1. If necessary, the pattern is then interpolated using high-order polynomials via Neville's algorithm[9] to give increments of 0.02° in 2θ. Optional background removal then follows. This is achieved via the fitting of local n^{th}-order polynomials to the data which are then subtracted to produce a pattern with a flat baseline (the value of *n* is selected by the algorithm). The data are then smoothed using wavelets[10,11] via the *SURE* (Stein's Unbiased Risk Estimate) thresholding procedure[12,13].

Savitsky-Golay filtering[14] is employed to locate the peak positions, after which smoothing (via a digital filter) replaces each data point x_i with a linear combination of itself and a number of nearest neighbours [Equation 2.1]. This type of smoothing is distinct from the wavelet-SURE procedure, and is only used to determine peak positions.

$$g_i = \sum_{n=-n_l}^{n_r} c_n x_{i+n}$$

Equation 2.1

where g_i is any point given by the linear combination of its immediate neighbours, *n* is the order, *nl* and *nr* are the number of points taken to the left or to the right of a data point respectively, and C*n* is a coefficient determined by the least-squares fit of a polynomial of degree *M* in *i* to the values $x_{-nl}....x_{nr}$ [Equation 2.2].

$$a_0 + a_1 i + a_2 i^2 + ...a_M i^M$$

Equation 2.2

The first order derivative a_1 is required for peak location, and maxima and minima are determined by observing the gradient change. Factors such as peak width, noise and peak shape do not affect this process.

Statistical distributions are generally well-approximated in crystallography. However, the statistical methods employed by PolySNAP are non-parametric, and are based on ranks. Therefore no assumptions about the underlying data distribution are made. With non-parametric tests, the diffraction pattern must first be converted from actual data values to ranks representing those values. For a set of *n* data points in the pattern, the smallest intensity is assigned a rank of 1 [R(x) = 1], the largest a rank of *n* [*R(x) = n*], and the i^{th} largest intensity a rank of I, denoted by $R(x_i) = I$. If tied ranks exist (from data points of equal value), they are assigned a rank corresponding to the average value of the ranks they would have taken had they not been the same. The data ranks are then sorted in descending order, and this order is used, rather than the data value itself. The process of correlation therefore becomes dependent on the relationship between ranks. These statistical methods are resistant to outliers and unplanned defects[15], and in the case of powders, they overcome some problems associated with preferred orientation and peak asymmetry.

Following this pre-processing, pattern-matching is performed, optionally ***masking*** (excluding) any previously-defined regions. Noise is eliminated by setting a user-definable minimum intensity, 0.1 I_{max} by default, below which ranks are set to zero.

If a database of known phases is available, each structure file is matched with this database. In the case of a good match between an individual structure and the database, the next step is bypassed. If the resulting match is not good, indicated by pattern correlation based on all the

measured data points and using the Pearson and Spearman[5,16] correlation coefficients, quantitative analysis is carried out using singular value decomposition for matrix inversion to ensure computational stability. This is done using all the measured data points, and it results in the determination of percentage composition of the sample.

The Pearson correlation coefficient is a measure of the strength of the linear dependence, or correlation, between two variables X and Y, giving a value between +1 and −1 inclusive. It is defined as the sum of the products of the standard scores of the two measures divided by the degrees of freedom. Based on a sample of paired data (X_i, Y_i), the sample Pearson correlation coefficient can be calculated as

$$r = \frac{1}{n-1}\sum_{i=1}^{n}\left(\frac{X_i - \bar{X}}{s_X}\right)\left(\frac{Y_i - \bar{Y}}{s_Y}\right)$$

Equation 2.3

where $\frac{X_i - \overline{X}}{S_X}$, $\overline{X}$ and S_X are the standard score, sample mean, and sample standard deviation (calculated using n − 1 in the denominator).

Spearman's rank correlation coefficient ρ is a non-parametric measure of correlation. In principle, ρ is a special case of the Pearson coefficient in which two sets of data X_i and Y_i are converted to rankings x_i and y_i before the coefficient is calclated. In practice, the raw scores are converted to ranks, and the differences d_i between the ranks of each observation on the two variables are calculated.

If there are no tied ranks, then ρ is given by:

$$\rho = 1 - \frac{6\sum d_i^2}{n(n^2-1)}$$

Equation 2.4

where $d_i = x_i - y_i$ = the difference between the ranks of corresponding values X_i and Y_i, and n is the number of values in each data set (same for both sets). If tied ranks exist, Pearson's correlation coefficient has to be used instead of equation 2.4. The same rank is assigned to each of the equal values, and this is an average of their positions in the ascending order of the values.

If no database is present or quantitative analysis is not necessary, a crystallinity check then follows. This involves the estimation of the total background for each sample, followed by the integration of its intensity; the estimation of non-background intensity; the location of any diffraction peaks; and the determination of non-background to background intensity. If this ratio falls below a user-definable limit (at a default value of 3%) and if there are fewer than the default number of three peaks (which is also user-definable), then the sample is considered amorphous and treated separately during the rest of the process.

Each pattern is then matched with every other pattern including itself using a combination of Spearman[16], Pearson[5], Kolmogorov-Smirnov[17] and peak correlation coefficients. The weighted mean of these coefficients is used as an overall measure of correlation, and the user-definable weights, by default, are 0.5, 0.5, 0 and 0 respectively. This means that only non-peak-specific tests are used. A symmetric (*n x n*) ***correlation matrix ρ*** with a unit diagonal is generated, and this in turn gives rise to two more symmetric matrices ***d*** and ***s***, given by the equations

$$\boldsymbol{d_{ij}} = 0.5(1.0 - \rho_{ij}) \qquad \text{Equation 2.5}$$

$$\boldsymbol{s_{ij}} = 1.0 - d_{ij} / (d_{ij})_{max} \qquad \text{Equation 2.6}$$

where ***d*** is the ***distance matrix*** with a value $0.0 \leqslant \boldsymbol{d_{ij}} \leqslant 1.0$, and ***s*** is the ***similarity matrix***, of value $0.0 \leqslant \boldsymbol{s_{ij}} \leqslant 1.0$. Therefore for high correlations a short distance is obtained, and consequently, the shorter the distance, the greater the similarity. Any amorphous samples may, at this point, be either discarded or given a dissimilarity and distance of 1 from every other sample, and a correlation coefficient of 0. This limits the effect of the amorphous sample on the data clustering process.

Equipment settings and data collection protocols often result in shifts in 2θ between patterns, sometimes due to a change in sample height. This shift can be corrected by the following equations:

$$\Delta(2\theta) = a_0 + a_1 \cos\theta \qquad \text{Equation 2.7}$$

$$\Delta(2\theta) = a_0 + a_1 \sin\theta \qquad \text{Equation 2.8}$$

$$\Delta(2\theta) = a_0 + a_1 \sin 2\theta \qquad \text{Equation 2.9}$$

where a_0 and a_1 are constants whose maximum values are user-definable. They are refined to maximise pattern correlation using the downhill simplex method. Equation 2.7 corrects for varying sample heights in reflection mode, equation 2.8 corrects for transparency errors or for transmission geometry with constant sample-detector distance, and equation 2.9 provides transparency and thick-specimen error corrections. Singular value decomposition of the resulting correlation matrix then gives an indication on its stability for subsequent eigenanalysis and cluster analysis calculations.

PolySNAP results are usually viewed via a dendrogram [Figure 2.2], which is a two-dimensional graphical representation of the hierarchal clustering performed during data analysis. Starting from the bottom of the diagram and moving upwards, clustering follows an agglomerative methodology. Initially, each structure forms its own individual cluster (denoted by different colours), and pairs of clusters are merged as one moves up the hierarchy. Each step of the clustering process is represented by the fusion of two branches via a horizontal tie-bar. The similarity of the clustered structures depends on the position of the tie-bar on the similarity scale, which ranges from 1 at the bottom denoting 100% similarity, to 0 similarity on top. In Figure 2.2 a case of 100% similarity is shown by the red cluster to the far left of the dendrogram.

Varying degrees of similarity are shown by a cascade of tie-bars. This is illustrated by the bright blue cluster in figure 2.2, where all the experimental structures at various temperatures were clustered together with one trial structure 16. Within this cluster, there are several horizontal tie-bars denoting a degree of sub-clustering. This demonstrates the range of percentage similarity

that can exist between structures within a cluster. As the tie-bar joining the 100K and 150K cells is furthest down the cluster, these structures bear the greatest similarity (circa 75%) within the blue group. The top tie-bar in the blue cluster corresponds with the 0.5 similarity mark, showing that members of the blue cluster are at least 50% similar to eachother.

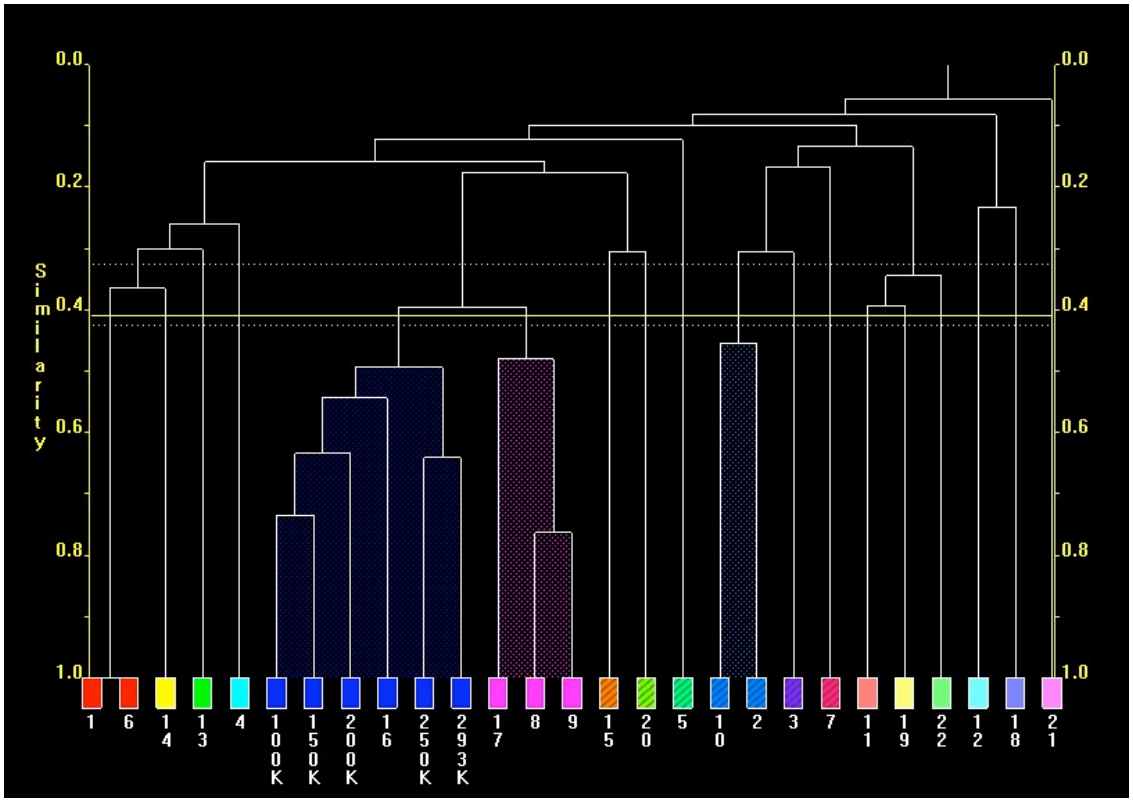

Figure 2.2 Example of a dendrogram. Different colours denote different structure clusters

2.1.3 Compare

Compare.x is an algorithm developed at UCL based on De Gelder's work[19-21]. As with some previously documented work[22,23], this algorithm does not only compare powder patterns pointwise, but it also compares a point on one pattern with the corresponding point and its neighbourhood on the other pattern and vice-versa. Text files in the same format used for PolySNAP (2θ, intensity) are used. However, these must be generated with the same 2θ range and stepsize as the experimental data, because, unlike PolySNAP, this algorithm does not perform any

interpolation of the data. Using each experimental data pattern as a reference in turn, the patterns of each computational structure are then matched with the experimental data, and their resulting correlation coefficients are printed on the screen.

Powder patterns are on an arbitrary scale, therefore the first step before assessing the similarity of patterns is to scale them. Previously[22] this was done by equalising the total number of counts (the equivalent of normalising the area under the patterns). With auto- and cross-correlation integrals, however, patterns should be scaled according to self-similarity. Although this generally leads to a similar scaling to that obtained by normalising the area, a different number of counts may be obtained for individual patterns by using this method. The correlation function describes the similarity or overlap between two patterns, and is expressed as two continuous functions *f(x)* and *g(x)* as a function of the relative shift *r* between the patterns. The interval for which patterns *f(x)* and *g(x)* are calculated determines the maximum and minimum value of *r*. For a reference pattern *f(x)*, the autocorrelation function $c_{ff}(r)$ is expressed as

$$c_{ff}(r) = \int f(x)\, f(x + r)\, dx$$

Equation 2.10

Integrating the autocorrelation function $c_{ff}(r)$ [Equation 2.11] shows that the area under the autocorrelation function is equal to the square of the area under the reference pattern *f(x)*.

$$\int c_{ff}(r)\, dr = \left(\int f(x)\, dx \right)^2$$

Equation 2.11

Similarly, equations for the autocorrelation function $c_{gg}(r)$ of the sample pattern *g(x)* can be derived

$$c_{gg}(r) = \int g(x)\, g(x + r)\, dx$$

Equation 2.12

$$\int c_{gg}(r)\, dr = \left(\int g(x)\, dx \right)^2$$

Equation 2.13

Equations 2.11 and 2.13 thus show that setting the total number of counts of the reference and sample patterns to the same number of counts results in setting the autocorrelation integrals (which express the self-similarities of the patterns) to the same value. It is therefore possible to put the autocorrelation functions for *f(x)* and *g(x)* on an absolute scale and compare them with the crosscorrelation function $c_{fg}(r)$, defined by

$$c_{fg}(r) = \int f(x)\, g(x + r)\, dx$$

Equation 2.14

$$\int c_{fg}(r)\, dr = \int f(x)\, dx \int g(x)\, dx$$

Equation 2.15

This means that the crosscorrelation integral, i.e. the area under the crosscorrelation function [Equation 2.15], is equal to the product of the areas under the patterns that are being compared, *f(x)* and *g(x)*. Normalisation of $c_{fg}(r)$ can be obtained by dividing it by the root of the product of the areas under *f(x)* and *g(x)*.

Comparison of two patterns in a pointwise manner synonymous to the method described in section 2.1.1 results in a difference criterion d_{fg} that can be defined as

$$d_{fg} = \int (f(x) - g(x))^2\, dx$$

Equation 2.16

Since this comparison does not take into account any relative shift between patterns (i.e. $r = 0$), in terms of auto- and crosscorrelation d_{fg} can be expressed as

$$d_{fg} = c_{ff}(0) + c_{gg}(0) - 2c_{fg}(0)$$

Equation 2.17

Compare.x, however, extends the pointwise approach to a neighbourhood comparison, redefining the difference criterion d_{fg} in terms of shift [Equations 2.18 and 2.19].

$$d_{fg} = \int (f(x) - g(x + r))^2 \, dx$$
$$= c_{ff}(0) + c_{gg}(0) - 2c_{fg}(r)$$

Equation 2.18

$$\int d_{fg}(r) \, dr = c_{ff}(0) + c_{gg}(0) - 2 \int c_{fg}(r) \, dr$$

Equation 2.19

Using a weighting function w that describes the neighbourhood to be adopted, the similarity s_{fg} between the two patterns may be expressed either as shown in equation 2.20, or as a function of dissimilarity [Equation 2.21].

$$s_{fg} = \frac{\int w_{fg}(r) \, c_{fg}(r) \, dr}{\left(\int w_{ff}(r) \, c_{ff}(r) \, dr \int w_{gg}(r) \, c_{gg}(r) \, dr \right)^{1/2}}$$

Equation 2.20

$$d_{fg} = s_{ff} + s_{gg} - 2s_{fg}$$

Equation 2.21

In order to include a neighbourhood in the calculation of similarity or dissimilarity, weighting functions must be defined for $r \neq 0$, and, if they are to be measured on an absolute scale, then $w_{gg}(r)$, $w_{ff}(r)$ and $w_{fg}(r)$ must be equal. The choice of the weighting function $w_{fg}(r)$ depends on the systems under comparison. For this study, a simple triangle shaped weighting function was used [Equation 2.22].

$$w_{fg}(r) = 1 - |r| / l \qquad \text{if } |r| < l$$
$$w_{fg}(r) = 0 \qquad \text{if } |r| \geqslant l$$

Equation 2.22

where l defines the width (degrees 2θ) of the neighbourhood taken into account. For this study, a range of triangle widths (varying from 0.5 to 4 degrees in 2θ, at increments of 0.5) was studied, with a default value of 2 being decided upon as it was found to give the most consistent results.

A very narrow triangle window was found to be too sensitive to peak shifts, in much a similar way as the pointwise approach. In contrast, wide triangle windows gave false high similarity values, matching peaks that bore no crystallographic relationship to each other.

Combining the functions described above, the weighted crosscorrelation function may be expressed as

$$c_{fg}^{ws} = \frac{\sum c_{fg}(\mathrm{r})\, w(\mathrm{r})}{\sqrt{\sum c_{ff}(\mathrm{r})\, w(\mathrm{r})} \quad \sqrt{\sum c_{gg}(\mathrm{r})\, w(\mathrm{r})}}$$

Equation 2.23

For identical patterns, c_{fg}^{ws} is equal to one, and the more dissimilar the patterns are, the closer its value is to zero.

2.2 Low Temperature Data

After data collection and selection of the appropriate predicted structure, LeBail fits were carried out on each data set in order to investigate the behaviour of the materials over a range of temperatures.

2.3 References

1. S R Hall, F H Allen and I D Brown, *Acta Cryst. A*, 1991, **47**, 655-685
2. T Siegrist, *J. Appl. Cryst.*, 1997, **30**, 418
3. R A Young, *The Rietveld Method*, International Union of Crystallography, Oxford University Press, Oxford, 1993, 23
4. A C Larson and R B Von Dreele, *GSAS. General Structure Analysis System*, Report No. LAUR-86-748, Los Alamos National Laboratory, Los Alamos, New Mexico, USA, 1987
5. C J Gilmore, G Barr and J Paisley, *J. Appl. Cryst.*, 2004, **37**, 231-242

6. G Barr, W Dong and C J Gilmore, *J. Appl. Cryst.*, 2004, **37**, 243-252
7. G Barr, W Dong, C J Gilmore and J Faber, *J. Appl. Cryst.*, 2004, **37**, 635-642
8. G Barr, W Dong and C J Gilmore, *J. Appl. Cryst.*, 2004, **37**, 874-882
9. W H Press, S A Teukolsky, W T Vetterling and B P Flannery, *Numerical Recipes in C*, Cambridge University Press, 1992
10. C J Gilmore, Presented at the ICDD Spring Meeting, Newton Square, Pennsylvania, USA, 1998
11. Ĺ Smrčok, M Ďurík and V Jorík, *Powder Diffr.*, 1999, **14**, 300-304
12. D L Donoho and I M Johnstone, *J. Am. Stat. Assoc.*, 1995, **90**, 1200-1224
13. R T Ogden, *Essential Wavelets for Statistical Applications and Data Analysis*, Boston: Birkhäuser, 1997, 144-148
14. A Savitzky and M J E Golay, *Anal. Chem.*, 1964, **36**, 1627-1639
15. W I Conover, *Practical Nonparametric Statistics*, John Wiley, New York, 1971
16. C Spearman, *Am. J. Of Psychol.*, 1904, **15**, 72-101
17. N V Smirnov, *Bull. Moscow Univ.*, **2**, 3-16
18. J A Nelder and R Mead, *Comput. J.*, 1965, **7**, 308-313
19. R de Gelder, R Wehrens and J A Hageman, *J. Comp. Chem.*, 2001, **22** (3), 273-289
20. E L Willighagen, R Wehrens, P Verwer, R de Gelder and L M C Buydens, *Acta Cryst. B*, 2005, **61**, 29-36
21. J A Hageman, R Wehrens, R de Gelder and L M C Buydens, *J. Comp. Chem.*, 2003, **24**, 1043-1051
22. H R Karfunkel, B Rohde, F J J Leusen, R J Gdanitz and G J Rihs, *Comp. Chem.*, 1993, **14**, 1125
23. D S Stephenson and G J Binsch, *J. Magn. Res.*, 1980, **37**, 409

3. EXPERIMENTAL

3.1 Instrumentation

The following instruments were used for X-ray powder diffraction data collection:

(i) Bruker AXS D5000 high-resolution powder diffractometer.

For each material, the sample was ground using a mortar and pestle and mounted on a flat disc between two layers of transparent tape, creating a circular area of approximately 1 cm in diameter. The powder X-Ray diffraction pattern was then recorded in transmission mode using a position-sensitive detector covering 8^o in 2θ, using $CuK_{\alpha 1}$, λ = 1.54056 Å radiation (Ge monochromated). Data were collected over the range of $5^o<2\theta<60^o$, measured in steps of 0.020343^o over a total collection time of one hour. Longer runs were carried out using the same step size over the range of $5^o<2\theta<60^o$ collected over a period of approximately 14 hours.

(ii) Bruker AXS D5005 high-resolution powder diffractometer.

Samples were ground using a mortar and pestle and placed in the low-temperature sample holder which consists of a square-shaped recess in a brass container. These data were initially collected only for 5-azauracil, chlorothalonil and imidazole. The D5005 diffractometer runs in reflection mode using $CuK_{\alpha 1,2}$ radiation (λ = 1.541838 Å), and is equipped with a Gobel mirror and a position-sensitive detector covering 8^o in 2θ. Data were collected over the range of $5^o<2\theta<55^o$, measured in steps of 0.014102^o over a total collection time of three hours. Longer runs were carried out using the same step size over the range of $5^o<2\theta<55^o$ collected over a period of approximately 14 hours. The low temperature stage was an Oxford Instruments CCC1101T stage, protected by three vacuum-sealed shields. Data sets were initially collected over a range of temperatures (75K, 100K, 125K, 150K, 175K, 200K, 225K, 250K and 293K). However, problems with transparency prompted the introduction of NaCl into the sample holder. Readings were repeated at a later date, using a thin layer of the pure material attached to the inverted sample holder by means of double-sided tape [Figure 3.3]. Data were subsequently collected over a range of temperatures (10K, 50K, 100K, 150K, 200K, 250K and 293K).

(iii) Bruker AXS D8 high-resolution powder diffractometer.

Low temperature capillary data were collected on this diffractometer in the Department of Chemistry at the University of Glasgow following observation of preferred orientation in the diffraction patterns obtained with the D5005. The samples were ground using a mortar and pestle and packed into 0.5mm glass capillary tubes to a depth of approximately 3cm. All tubes had their ends sealed before being mounted onto the capillary stage, which was then set to rotate. The powder X-ray diffraction patterns were recorded in transmission mode using a position sensitive detector covering 8^o in 2θ, using Ge monochromated $CuK_{\alpha 1}$ radiation ($\lambda = 1.54056$ Å). Data were collected over the range of $5^o<2\theta<55^o$, measured in steps of 0.014102^o over a total collection time of three hours, at various temperatures (70K, 100K, 150K, 200K, 250K and 293K) using a cryostream. Liquid nitrogen is drawn up by the action of the diaphragm pump from an unpressurised supply vessel into the cryostream coldhead, where it then passes through a heater so that most of the liquid is turned into vapour at the boiling point of liquid nitrogen. This vapour is then dried with a line drier unit to ensure there is no moisture in the gas. The flow rate of the gas from the pump is regulated by a variable flow controller as the gas flows back into the cryostream coldhead where it is recooled. A heater and a sensor regulate the temperature of the vapour before it enters the nozzle of the cryostream. The gas then flows along the isothermal nozzle and out over the sample.

3.2 Sample Effects

Powder data for all samples were collected on the D5000 at room temperature. Low temperature data collection was initially carried out on the D5005 with its original sample cell set-up. ***Transparency*** and ***sample contraction*** issues then prompted the use of an internal inorganic standard, NaCl, introduced into the sample in the ratio 1:2. However, analysis of the resulting powder patterns and problems with Rietveld refinement revealed a substantial degree of ***preferred orientation*** in some of the samples, thus inspiring the use of a capillary set-up rather than a flat sample holder in cases where preferred orientation was observed.

The analysis of the NaCl mixture to correct for transparency caused unstable and unsatisfactory refinements. Consequently, further attempts at overcoming transparency issues were made using the D5005 instrument in Birmingham. After several discussions, a decision was made to mount the sample on the reverse side of the sample holder by means of double-sided tape. This set-up, whilst eliminating the problems linked with transparency, gave rise to the issue of ***sample displacement***. However, this was addressed by applying a significant zero point error to the data obtained with this method. The sample effects mentioned above will now be discussed in further detail.

3.2.1 Transparency and Sample Contraction

Transparency errors are encountered when X-ray photons penetrate into the specimen, thus lowering the effective diffraction surface and causing a discrepancy in peak positions [Figure 3.1]. This error bears a direct relationship with the absorption of the X-ray beam by the material, i.e. the linear attenuation coefficient, and may be quantified by:

$$\Delta 2\theta = \frac{\sin 2\theta}{2\mu R}$$

Equation 3.1

where μ is the linear attenuation coefficient for the specimen at a particular wavelength, R is the radius of the focusing circle, and 2θ is expressed in radians[1]. The greater the absorption (i.e. high values of μ), the smaller the error ($\Delta 2\theta$).

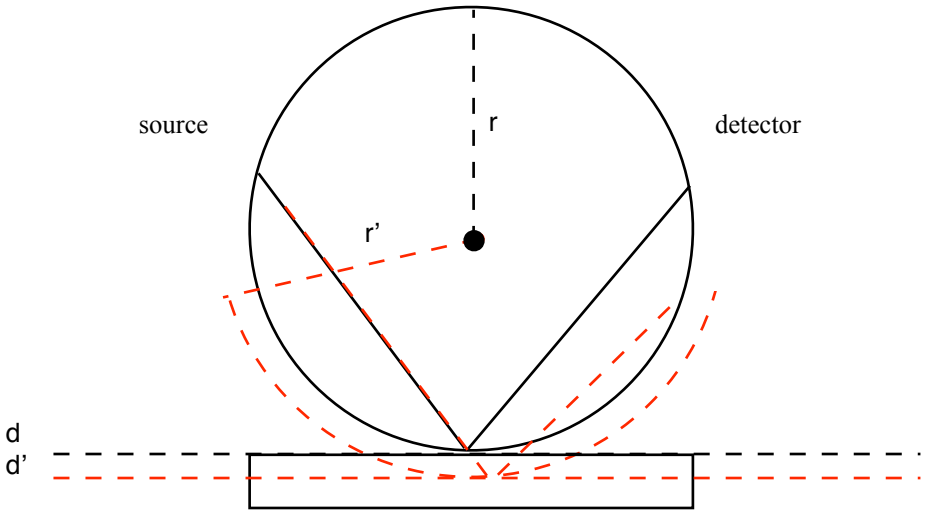

Figure 3.1 Diagram showing the effect of specimen transparency or specimen displacement on the radius of the focusing circle. r = radius of focusing circle, r' = effective radius, d = diffraction surface and d' = displaced diffraction surface[1]. Red lines denote displacement scenario.

In the case of organic and other low-absorbing materials, the attenuation coefficients are very small, therefore transparency is not an uncommon problem, especially with the systems under consideration in this project.

Another sample effect having similar consequences to those described above is sample contraction. As the environment of the crystallites gets colder, the unit cell volume of the sample decreases and the material contracts within the holder, lowering the diffraction surface and altering the zero point. In such cases, the error may again be calculated using Equation 3.1 since the direct consequence of sample contraction is displacement of the effective diffraction surface [Figure 3.2 (c)].

The low temperature set-up on the D5005, which operates in reflection mode, is such that the surface of the sample holder is at the position from which it is assumed X-rays are diffracted. Figure 3.2 illustrates the effects of transparency and sample contraction on this arrangement.

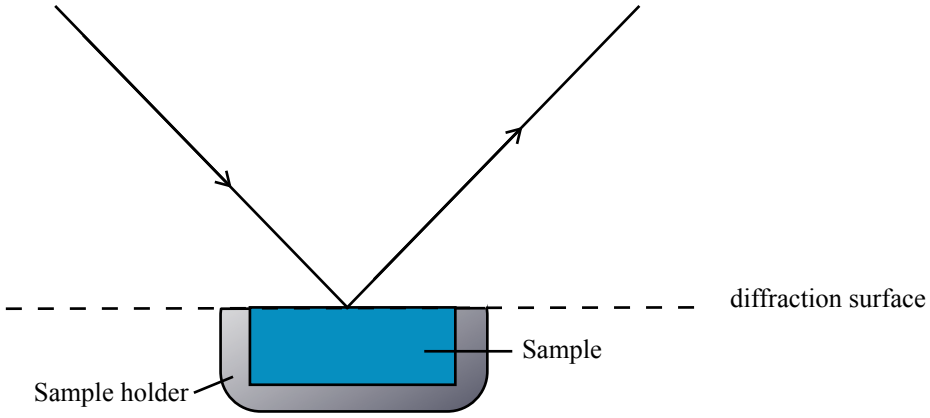

(a) Sample exhibiting no transparency or contraction

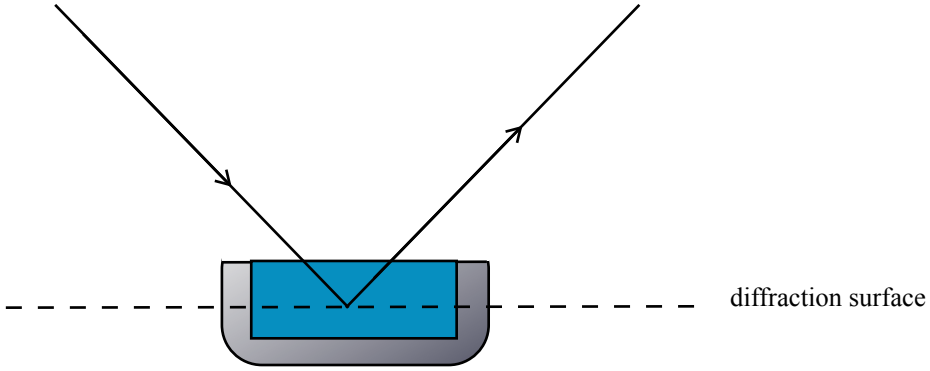

(b) Sample transparency

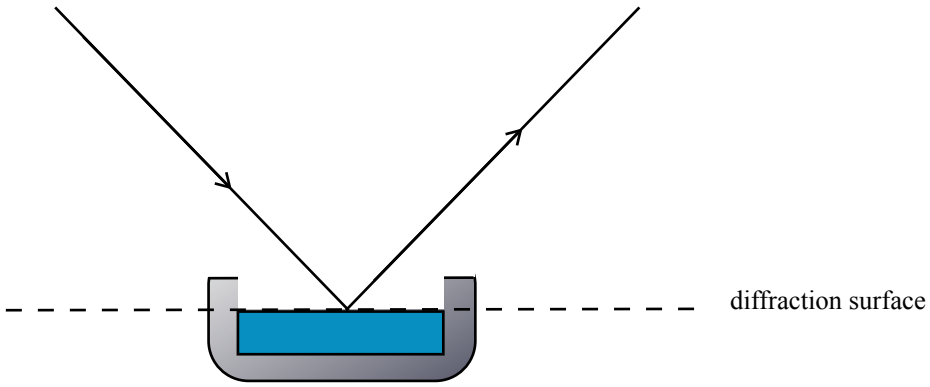

(c) Sample displacement (or sample contraction)

Figure 3.2 Diagram showing the effect of specimen transparency and specimen displacement on diffraction surface.

To monitor the effects of sample transparency, an inorganic material not prone to transparency effects was added to the sample. NaCl was selected as its lattice parameters and behaviour over a range of low temperatures are well-documented[2], and it is unreactive with the materials of relevance to this project. For more accurate LeBail analysis, the cell parameters for NaCl must take thermal contraction into account. A thermal expansion coefficient was therefore applied to the NaCl structure, and peak positions calculated for the salt peaks over the range of temperatures studied [Table 3.1].

*Table 3.1. Calculated peaks for NaCl with a change in temperature at different wavelengths (*Coefficient of thermal expansion for NaCl = -40.5 × 10^{-6} Å/K)[2]*

Temperature	Corrected *a*	Cu-Kα			Cu-Kα_1		
(K)	(Å)	Peak 1	Peak 2	Peak 3	Peak 1	Peak 2	Peak 3
250	5.6385	27.397	31.739	45.500	27.374	31.712	45.461
225	5.6375	27.402	31.745	45.509	27.379	31.718	45.469
200	5.6365	27.407	31.751	45.517	27.384	31.724	45.478
175	5.6355	27.412	31.756	45.526	27.389	31.730	45.486
150	5.6345	27.417	31.762	45.535	27.394	31.735	45.495
125	5.6335	27.422	31.768	45.543	27.399	31.741	45.503
100	5.6324	27.427	31.774	45.552	27.404	31.747	45.513
75	5.6314	27.432	31.780	45.561	27.409	31.753	45.521

3.2.2 Sample Displacement

A more efficient method of data collection which avoids sample transparency and reduces contraction errors involves mounting a fine layer of the sample on the reverse side of the sample holder using double-sided tape. By this method, the sample height is slightly displaced from its original position, thus causing a zero point error [Figure 3.3]. This error is constant and can therefore be calculated prior to the refinement stage [Equation 3.1].

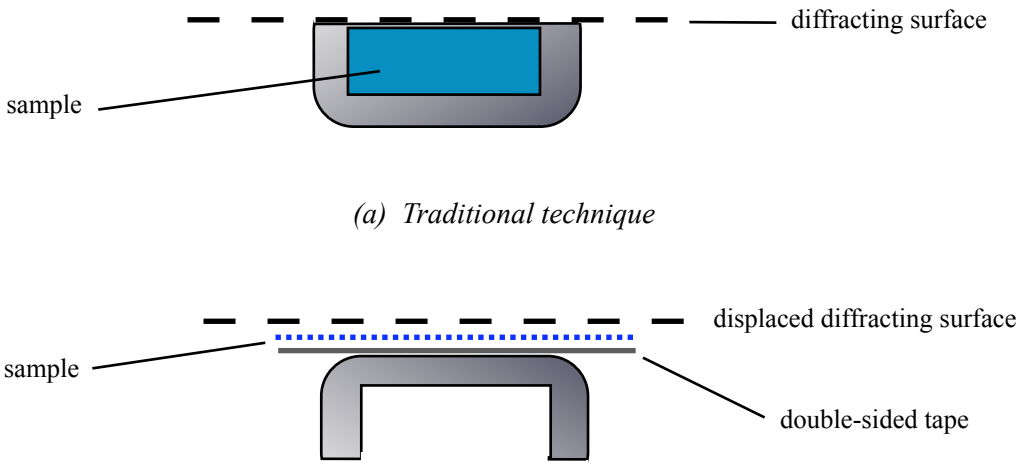

(a) Traditional technique

(a) Modified technique

Figure 3.3 Diagram showing the techniques used to mount the sample onto the sample holder for collection of low-temperature data on the D5005.

3.2.3 Preferred Orientation

In an ideal powder sample, the crystallites are oriented completely randomly and independently from the direction of the beam. This gives each crystal orientation the same probability of reaching the diffraction condition. Preferred orientation is a property arising when the crystallites in a sample have a stronger tendency to be oriented in one way rather than another.

For sample identification and fingerprinting purposes, preferred orientation is often not critical as it does not affect the positions of the peaks observed. It does, however, affect the relative peak intensities within a pattern, thus hindering reliable intensity extraction and consequently structure solution and refinement. The type and extent of preferred orientation is often dependent on the crystal habit of the material. Anisotropic crystallites, eg. long needles or flat platelets, tend to exhibit preferred orientation and pack preferentially in certain directions rather that others.

When a material is packed into a flat sample holder (and sometimes backed with a glass slide), as in the case of the D5005 low temperature original set-up, preferred orientation of the crystallites can sometimes be encouraged. The cleavage (or growth faces) of the material, which are all of the same crystallographic type, align themselves mostly parallel to the direction of the packing, with only a small proportion perpendicular to the surface. The direction that lies

perpendicular to the flat sides of the surfaces is the preferred orientation axis, and the intensities of reflections from planes perpendicular to this axis will be enhanced, while those from the parallel planes will be suppressed.

Since preferred orientation produces systematic distortions of the reflection intensities, mathematical models can be used to correct for this effect during refinement. However, this is not so reliable in cases of structure solution. It is believed that few powder patterns are completely free from this phenomenon[3], and it has consequently become routine practice to incorporate corrections for preferred orientation in Rietveld refinement processes.

Attempts at forcing a material to take up random orientation may often prove futile, as preferred orientation is a problem that, if present, can generally be reduced but not eliminated completely by experimental measures. Care when preparing and mounting the sample is important in avoiding this bias, as excess compression or sliding the backing glass can encourage the alignment of anisotropic crystallites. Consequently, the use of capillaries rather than flat sample holders may sometimes address this issue. Other experimental techniques which may be employed to mimic the random orientation of more isotropic materials include mixing the sample with an amorphous material, spray-drying and grinding.

3.2.4 Sample Loss

Additional problems were encountered through sample loss during initial data collection on the D5005. The design of the low-temperature apparatus is such that a high vacuum is created around the specimen chamber, to allow such extreme temperatures to be reached. Any gaps arising between these chambers cause a pressure difference that may lead to a change in orientation of the powder particles, or (as in the case of imidazole) to some of the more volatile samples being vacuumed out of the sample holder. The consequences are similar to those observed with transparency and sample displacement. In the case of the D5005, use of the reverse side of the sample holder avoided this problem.

3.3 Materials

With the exception of the data collected on the D5005 using the internal standard, all samples were used in their original form, as received from the supplier or originator. The following table illustrates the materials used and the data sets collected at various settings.

Table 3.2 List of data sets collected for each material studied.

	D5000	D5005 (original)	D5005 (mixed with salt)	D8 (capillary)	D5005 (thin film on reverse side)
Adenine	✓			✓	✓
5-Azauracil	✓	✓	✓		✓
Chlorothalonil	✓	✓	✓	✓	✓
Guanine	✓				✓
Imidazole	✓	✓	✓	✓	✓

3.4 References

1. R Jenkins and R L Snyder, *Introduction to X-Ray Powder Diffractometry*, Wiley Interscience, New York, 1996.
2. P D Pathak and N G Vasavada, *Acta Cryst. A*, 1970, **26**, 655
3. E Sturm and W Lodding, *Acta Cryst. A*, 1968, **24**, 650

4. IMIDAZOLE

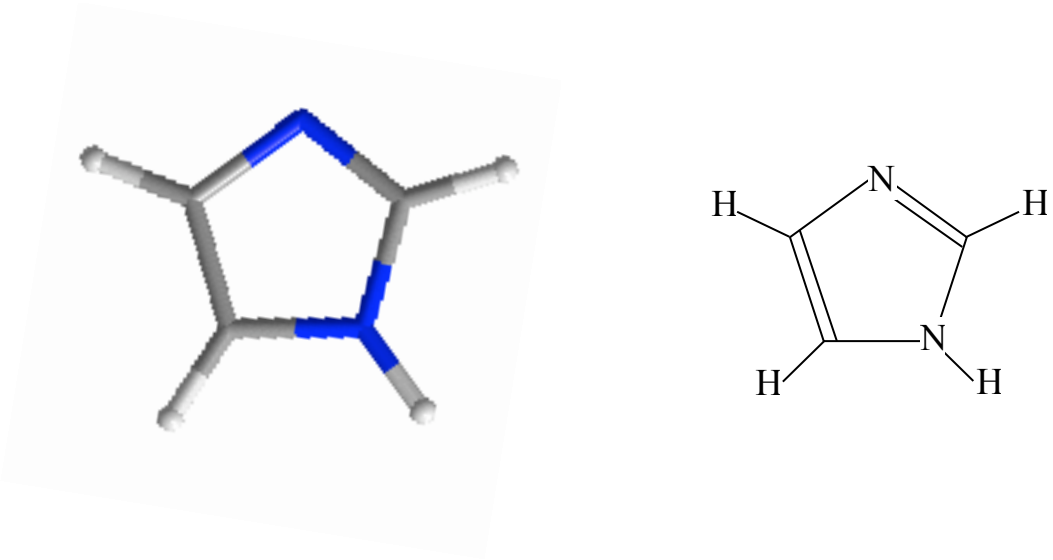

Figure 4.1. Imidazole (1,3-diaza-2,4-cyclopentadiene)

4.1 Background

The simplest member of the imidazole family is imidazole itself: a colourless to pale yellow crystalline solid with a weak amine-like odour. Whilst being generally poorly soluble in water, its derivatives dissolve in organic solvents such as chloroform, propylene glycol and polyethoxylated castor oil. They are antimetabolites and inhibitors of histamine, and are commonly used as insecticides.

The imidazole molecule has a high propensity for side-chain substitution, and the composition of such chains is accountable for the activity of the material, as well as its degree of toxicity. Thus, imidazole compounds have various commercial uses, ranging from topical antimycotics (e.g. clotrimazole, miconazole and ketoconazole)[1] to industrial fungicides (e.g. imazalil). Some also exhibit antibacterial, antiprotozoal and antihelmintic activity (e.g. metronidazole, tinidazole and mebendazole respectively)[1]. Imidazole and its derivatives are also widely used as intermediates in the synthesis of organic compounds including pharmaceuticals, agrochemicals, dyes, photographic chemicals, corrosion inhibitors, epoxy curing agents, adhesives and plastic modifiers.

4.1.1 Crystal Structure

The crystal structure of imidazole was determined by single crystal neutron diffraction at 103K, with additional studies carried out at 108K, 113K, 123K and 293K [2] [Table 4.1]. Imidazole has a monoclinic ($P2_1/c$) lattice, with Z = 4, and has not yet been shown to exhibit polymorphic behaviour. It has polar hydrogen atoms that form hydrogen bonds to the lone pairs on the nitrogen atom. These form twisted chains that run parallel to the *c* axis [Figures 4.2 and 4.3].

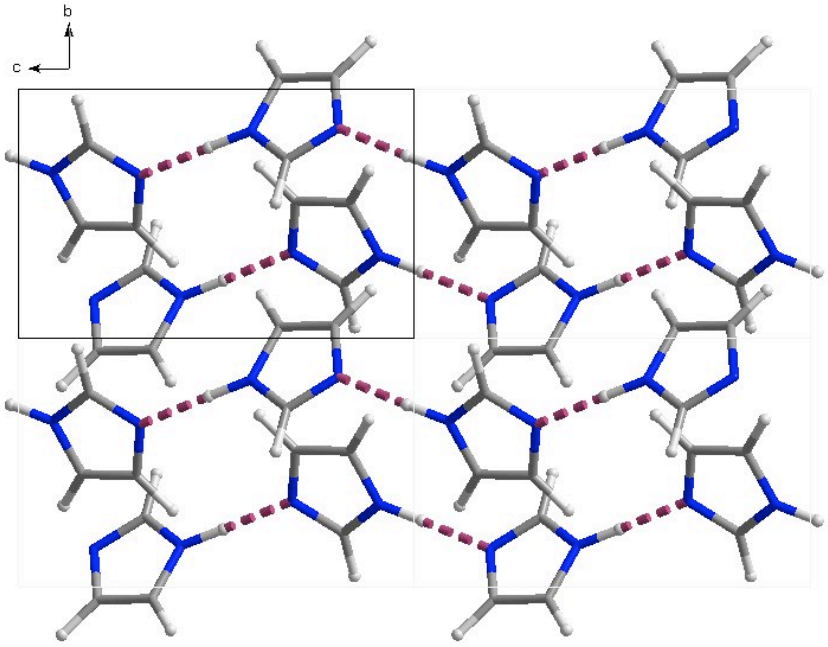

Figure 4.2. Imidazole molecules forming chains parallel to the c axis. Dotted lines denote NH···N hydrogen bonds

Adjacent molecules in the chains are twisted by about 60° with respect to each other, and these chains are joined by short N-H····N contacts (H.....Acceptor distance of 1.8085Å). The hydrogen bonds, forming a network through the crystal, result in dominant electrostatic interactions, giving an estimated electrostatic contribution of about 60% of the total lattice energy[3].

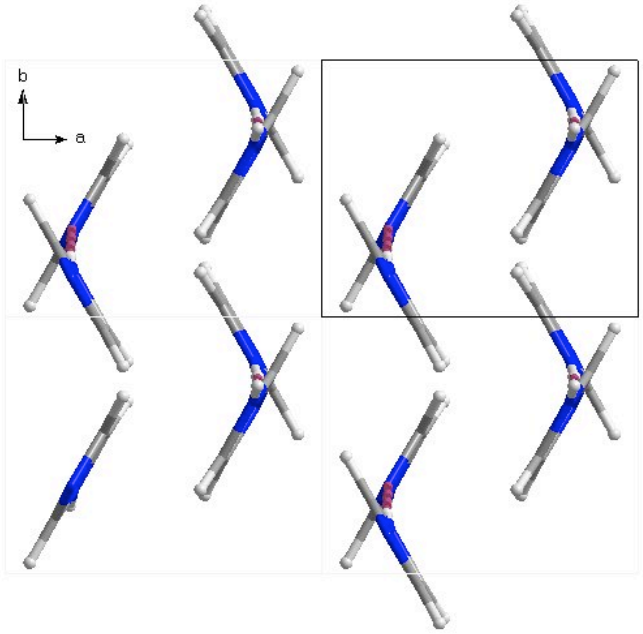

Figure 4.3. A view down the c axis

4.1.2 Crystal Structure Prediction

Imidazole represents an "ideal" system for structure prediction studies[4], given that it is a rigid structure. This means that the frequencies of the low energy k=0 (where k is the kinetic energy) intermolecular lattice vibrations obtained by lattice energy minimisation are a close representation of the experimental system[4]. At a temperature of 0 K, the system is thermodynamically most stable. The computational search resulted in a total of 65 theoretical structures for imidazole, many of which vary only slightly in density, and lie within 7 kJ mol^{-1} of the global minimum[4] [Figure 4.4].

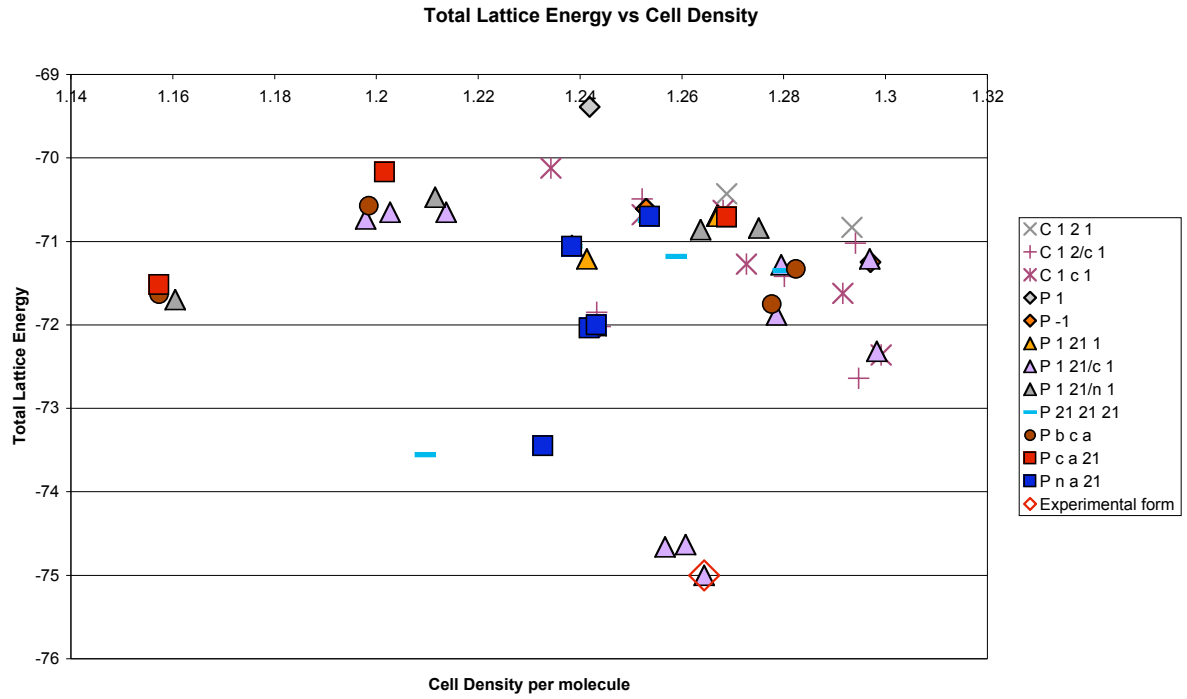

Figure 4.4 The distribution of low energy structures found in the search for minima in the lattice energy of imidazole. The minimum corresponding to the known crystal structure (ExpMinOpt) is denoted by the open red diamond[4]. [Permission for reproduction granted by the author of reference 4.]

Variations from the known crystal structure are observed on comparison of the low energy structures, and although the structures are very similar, comparison of the powder patterns reveals their differences. Although the global minimum corresponds to the known crystal structure, there are structures within 2 kJ mol^{-1} in which the hydrogen-bonded molecules are coplanar, and others lying within 3.5 kJ mol^{-1} which differ in the arrangement of the hydrogen-bonded chains. However, all the low energy crystal structures are based on the same hydrogen bonding network and they favour the anti-parallel stacking of chains[4].

The experimental and *ab initio* optimised molecular structures exhibit only minor differences, and the most thermodynamically stable predicted structure at 0K corresponds with the known crystal structure[4]. Although other structures are thermodynamically feasible, the same hydrogen bonding motif is dominant, thus making manipulation of crystallisation conditions unlikely to give a kinetic advantage in the nucleation and growth of a long-lived polymorph.

4.2 Results

4.2.1 Low Temperature Data

When compared to the published data [Table 4.1], the unit cell parameters of the lowest energy predicted structure were similar to those of the published single crystal structure obtained at 108K. Hence the unit cell parameters from this predicted structure were used as a starting point for a LeBail fit on the 150K data. The unit cell parameters from this initial fit were then used as a starting point for a LeBail fit on the 50K and 200K data. Subsequent LeBail fits on the remaining temperature data sets followed the same "stepwise" methodology.

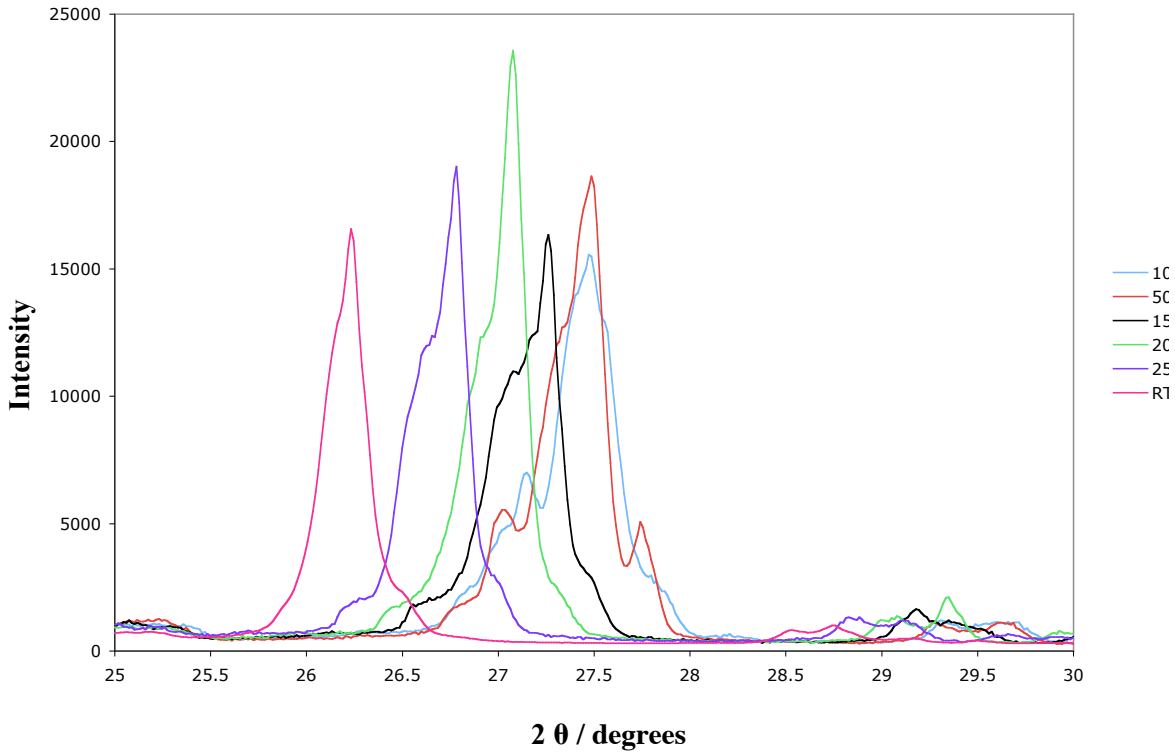

Figure 4.5 Section of superimposed powder diffraction data at all temperatures (D5005) showing the selected peaks (012) shifting towards the right with decreasing temperature.

The powder diffraction pattern indicates a clear contraction in the unit cell with decreasing temperature, as indicated by the clear shift in peak position (012) towards the right [Figure 4.5]. At lower temperatures, additional peaks are resolved indicating peak overlap at higher

temperatures. This overlap is reduced as the structure contracts anisotropically, thus exhibiting a difference in shift between peaks representing distinct reflections. The effect of changing temperature over the entire diffraction pattern from 10 to 45 degrees along 2θ is shown in Appendix A2.1.

The percentage differences in *a*, *b*, *c*, *β* and volume with varying temperature were calculated and, as expected, the volume increases as higher temperatures are reached, while *a*, *b*, *c* and *β* change accordingly to accomodate this expansion [Table 4.1 and Figure 4.6].

Table 4.1 Unit cell parameters of lowest energy predicted structure and determined from experimental data, and published unit cell dimensions for imidazole with changing temperature. The numbers in brackets denote the percentage change with respect to those values obtained from the 10K data.

Temperature (K)	***a (Å)***	***b (Å)***	***c (Å)***	***β(°)***	***Volume (Å³)***
Single Crystal Values[2]					
103	7.569 (1)	5.366 (1)	9.785 (2)	119.08 (1)	347.32
108	7.572 (2)	5.368 (1)	9.782 (2)	119.03 (1)	347.65
113	7.577 (2)	5.373 (1)	9.777 (3)	118.93 (2)	348.36
123	7.583 (1)	5.375 (1)	9.779 (2)	118.92 (1)	348.87
Predicted values[4] (0K)	7.57	5.37	9.78	119.1	347.3
10	7.537 (1) (0.00)	5.078 (2) (0.00)	9.410 (1) (0.00)	120.83 (2) (0.00)	309.26 (0.00)
50 ***(% change)***	7.476 (1) (-0.81)	5.238 (3) (+3.14)	9.571 (2) (+1.72)	119.55 (3) (-1.06)	326.06 (+5.43)
150 ***(% change)***	7.561 (2) (+0.31)	5.335 (2) (+5.06)	9.762 (1) (+3.74)	120.09 (1) (-0.61)	340.71 (+10.17)
200 ***(% change)***	7.612 (1) (+0.99)	5.349 (3) (+5.34)	9.823 (1) (+4.39)	118.60 (1) (-1.85)	351.17 (+13.55)
250 ***(% change)***	7.749 (3) (+2.82)	5.358 (2) (+5.51)	9.712 (2) (+3.22)	119.15 (3) (-1.39)	352.22 (+13.89)
293 ***(% change)***	7.742 (2) (+2.73)	5.382 (3) (+5.97)	9.646 (1) (+2.51)	117.76 (1) (-2.54)	355.67 (+15.01)
293 (D5000)	7.569 (1) (+0.43)	5.366 (1) (+5.66)	9.779 (2) (+3.93)	119.10 (1) (-1.43)	347.04 (+12.23)

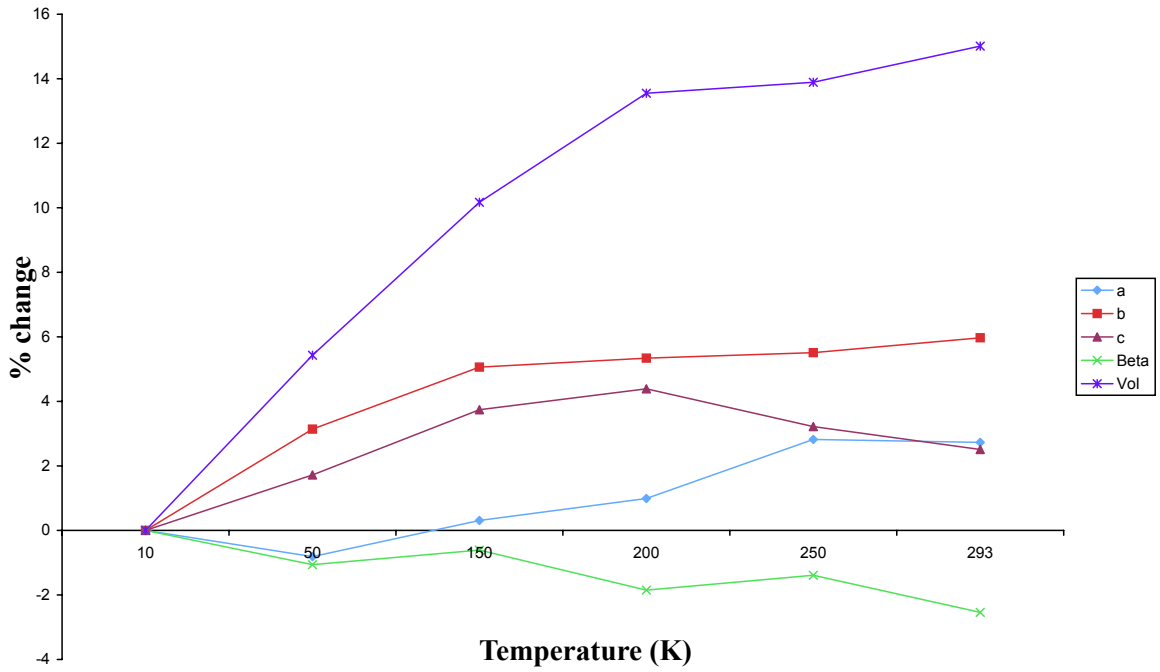

Figure 4.6 Graph showing the percentage change in unit cell dimensions with temperature.

Over the range of temperatures, the unit cell volume would be expected to increase as a result of thermal expansion. In the case of imidazole, *a* and *b* were found to increase overall with temperature, while *c* and *β* showed irregular behaviour. Although atypical, these changes in the lattice parameters still resulted in an overall expansion of the unit cell, as indicated by the increase in volume. This anisotropic behaviour will be due to relative hydrogen bond strengths and sterics in each direction. However, the LeBail fits used here may show a significant correlation of lattice parameters during fitting, making these results unreliable. Hence these results will not be interpreted further in this work.

4.2.2 Automated Comparison

4.2.2.1 R_{wp}

The 65 predicted structures were each compared, using R_{wp}, with the experimental data collected at each temperature. The outcome of these comparisons was non-discriminatory, with none of the 65 structures singled out as being significantly similar to any of the experimental data. R_{wp} values ranging from 51.83% to 79.94% were obtained, although in most cases, no significant discrimination was found [Table 4.2, Figures 4.7 and 4.8]. In addition, only one of the predictions (ai35) was ranked as the best fit to data recorded at two different temperatures. The correct predicted structure (ak34) was not identified by R_{wp} as having a similar powder pattern to the data collected at any of the temperatures. The simulated patterns for all predicted structures shown in the table and the corresponding experimental patterns are found in Appendix A2.2.

Table 4.2. Structures with lowest R_{wp} identified at each temperature. The difference is that between the R_{wp} for the top ranked structure [$R_{wp}(x)$] and the correct prediction [$R_{wp}(ak34)$] at each temperature. Black numbers denote the correct structure being ranked top, while red numbers denote incorrect structures ranked as the best.

Temperature (K)	***Top ranked structure***	***R_{wp} (x) (%)***	***R_{wp} (ak34) (%)***	***Difference (%) [$R_{wp}(x)$ - $R_{wp}(ak34)$]***
10	ca61	66.5	71.5	-5.0
50	ca34	66.5	68.5	-2.0
150	ai35	52.9	67.6	-14.7
200	de38	51.8	72.2	-20.4
250	ai35	59.3	65.0	-5.7
293	am36	56.5	59.9	-3.4
293 (D5000)	am44	70.7	71.7	-1.0

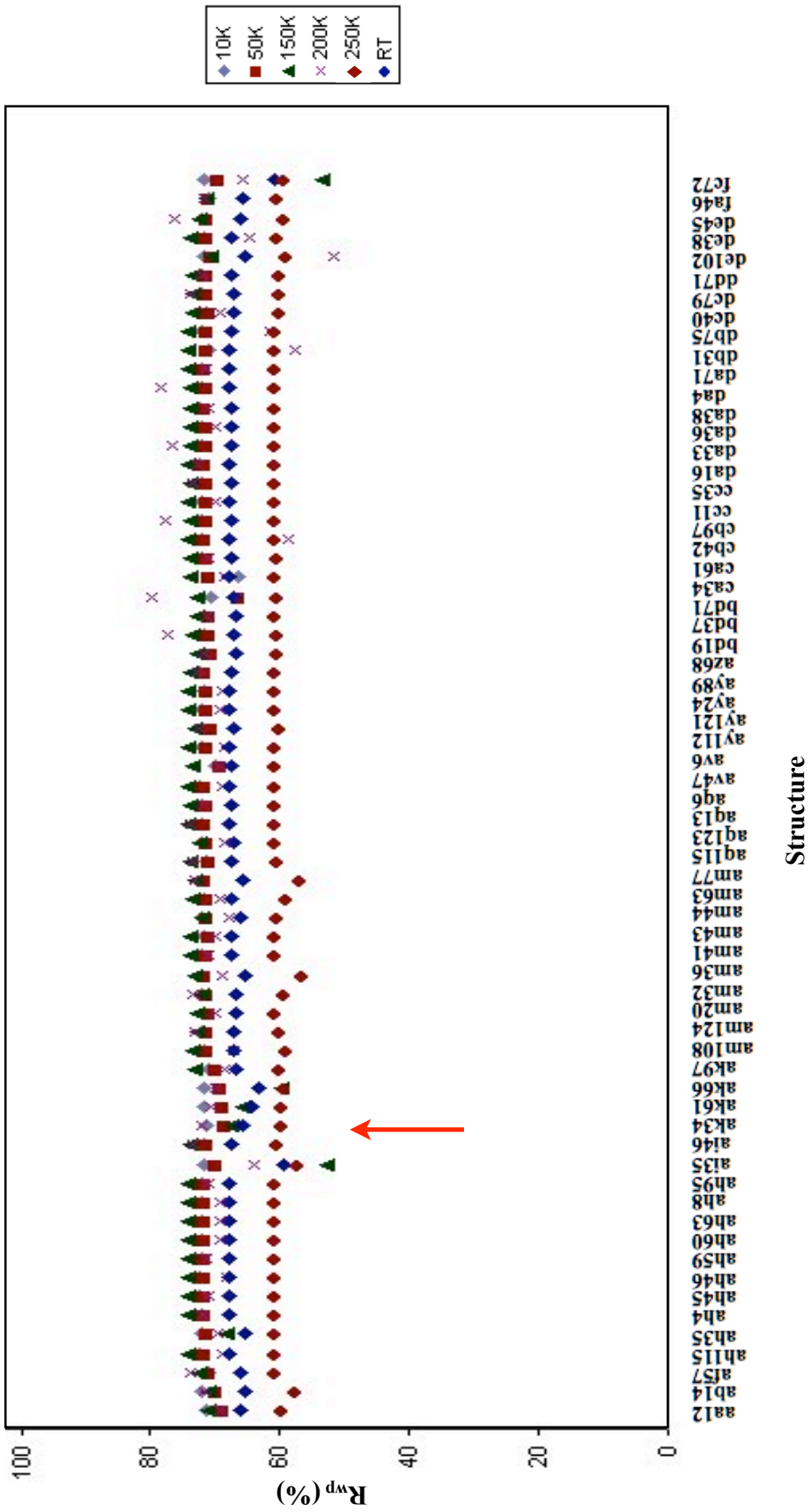

Figure 4.7 R_{wp} values for each predicted structure at each temperature. The arrow indicates structure ak34.

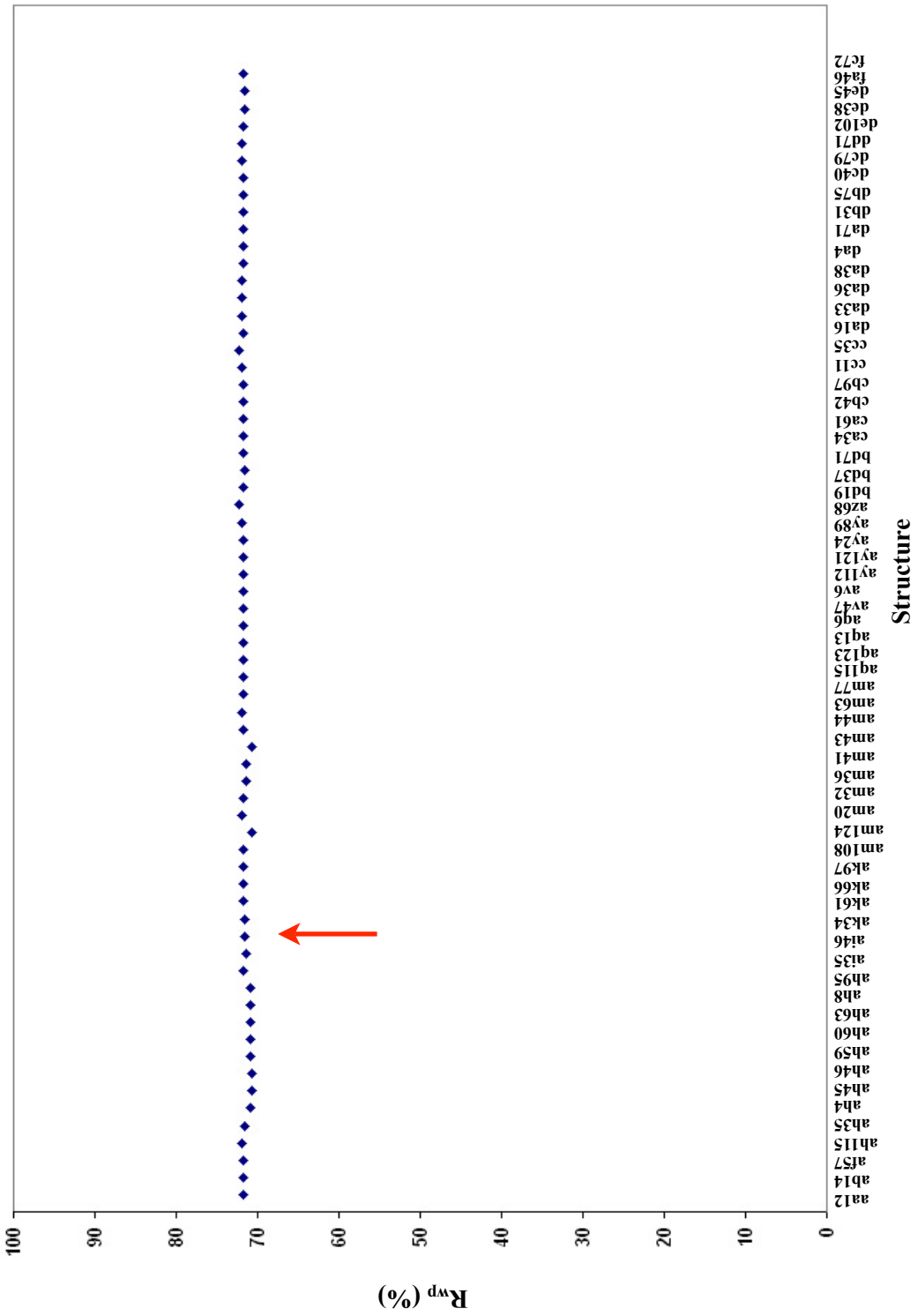

Figure 4.8 R_{wp} values for each predicted structure against the D5000 data at room temperature. The arrow indicates the correct structure ak34.

4.2.2.2 PolySNAP

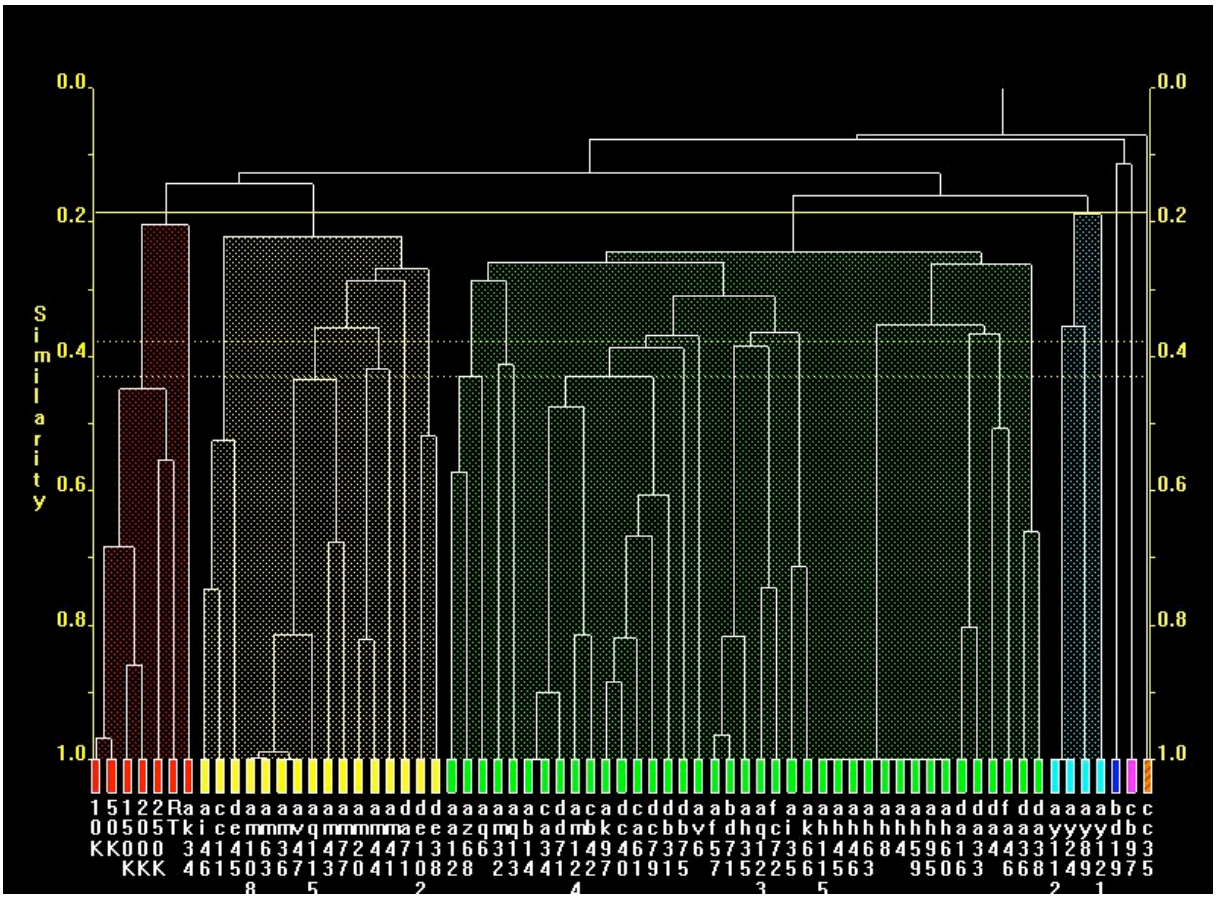

Figure 4.9. Dendrogram showing similarity clusters for imidazole predicted and experimental powder patterns

For PolySNAP analysis, the data collected on the different diffractometers were analysed separately due to the difference in wavelength between the two setups. In the dendrogram comparing all 65 predicted structures with the D5005 data [Figure 4.9], structure ak34, which corresponds to the published structure, was grouped with the entire set of experimental data at all temperatures (cluster marked in red). Although all experimental data were grouped together, it was interesting to note that within this cluster were paired subsets, with the lower temperature data pair being ranked as more similar to each other than the next pair up. Taking each temperature separately and looking at the structure with the highest correlation in each case, structure ak34 was the top ranking structure at all temperatures above 150K [Table 4.3].

Table 4.3. Structures with highest correlation coefficient [P(x)] at each temperature, and the difference to the value obtained for the correct structure [P(ak34)]. If P(ak34) = P(x), then the difference between P(ak34) and the next best stucture is taken. Black numbers denote cases where the correct structure was identified, the difference was positive. An incorrect match gave a negative difference, as shown by the values in red.

Temperature (K)	***Top ranked structure***	***Correlation coefficient of top ranked structure***	***Correlation coefficient***	***Difference [P(ak34) - P(x)]***
10	am32	0.356	0.330 (ak34)	-0.026
50	am32	0.358	0.321 (ak34)	-0.037
150	ak34	0.412	0.368 (ak61)	+0.044
200	ak34	0.419	0.382 (ak61)	+0.037
250	ak34	0.539	0.378 (fc72)	+0.161
293	ak34	0.722	0.491 (dd71)	+0.231
293 (D5000)	ai35	0.299	0.151 (ak34)	-0.148

On analysis of the corresponding correlation coefficients at the higher temperatures, two other structures (dd71, with a correlation value of 0.4912, and de102, with 0.4236 both at 293K) could be considered to be placed significantly higher than the rest, though not as high as structure ak34 [Figures 4.10 and 4.11]. However, on visual comparison of the respective powder diffraction patterns it was clear that neither of these two patterns bear a great similarity to the experimental data or ak34 [Figure 4.12]. The structures having the highest correlation coefficients when compared with the experimental data at the lower temperatures 10K and 50K, and with the D5000 data, (am32 and ai35 respectively), were also assessed visually and their powder patterns found to differ significantly from the respective experimental data [Appendix A2.3].

It is evident from the correlation plot [Figure 4.10 and Table 4.3] that the degree of similarity between the predicted structure ak34 and the experimental data increases with temperature. Although the overall trend is retained as temperature varies, the discrimination between the highest ranking structure and the structure with the second highest correlation coefficient also increases with temperature, as indicated clearly by the values in the table.

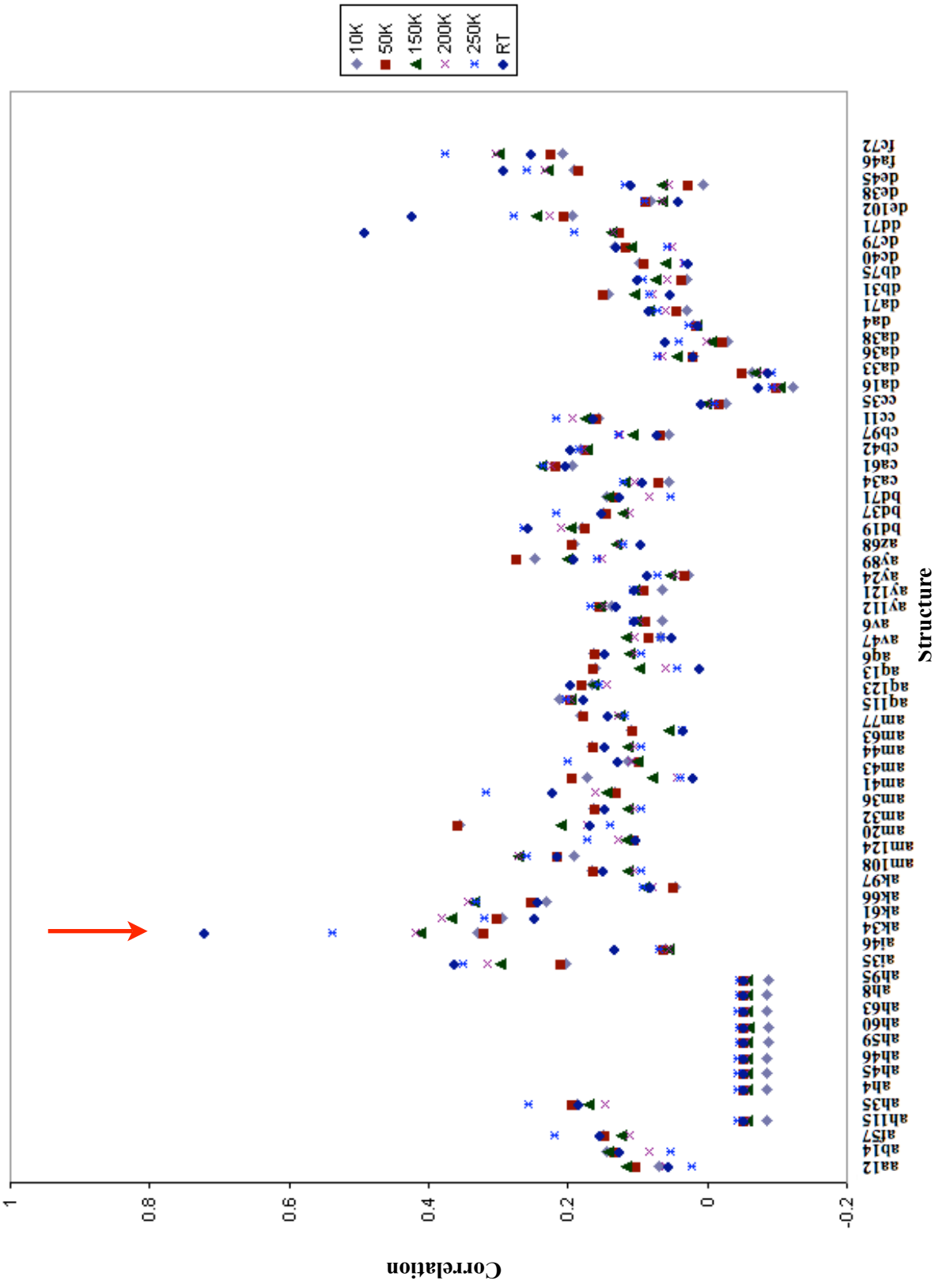

Figure 4.10 Correlation coefficients of all 65 structures at each temperature. The arrow indicates structure ak34

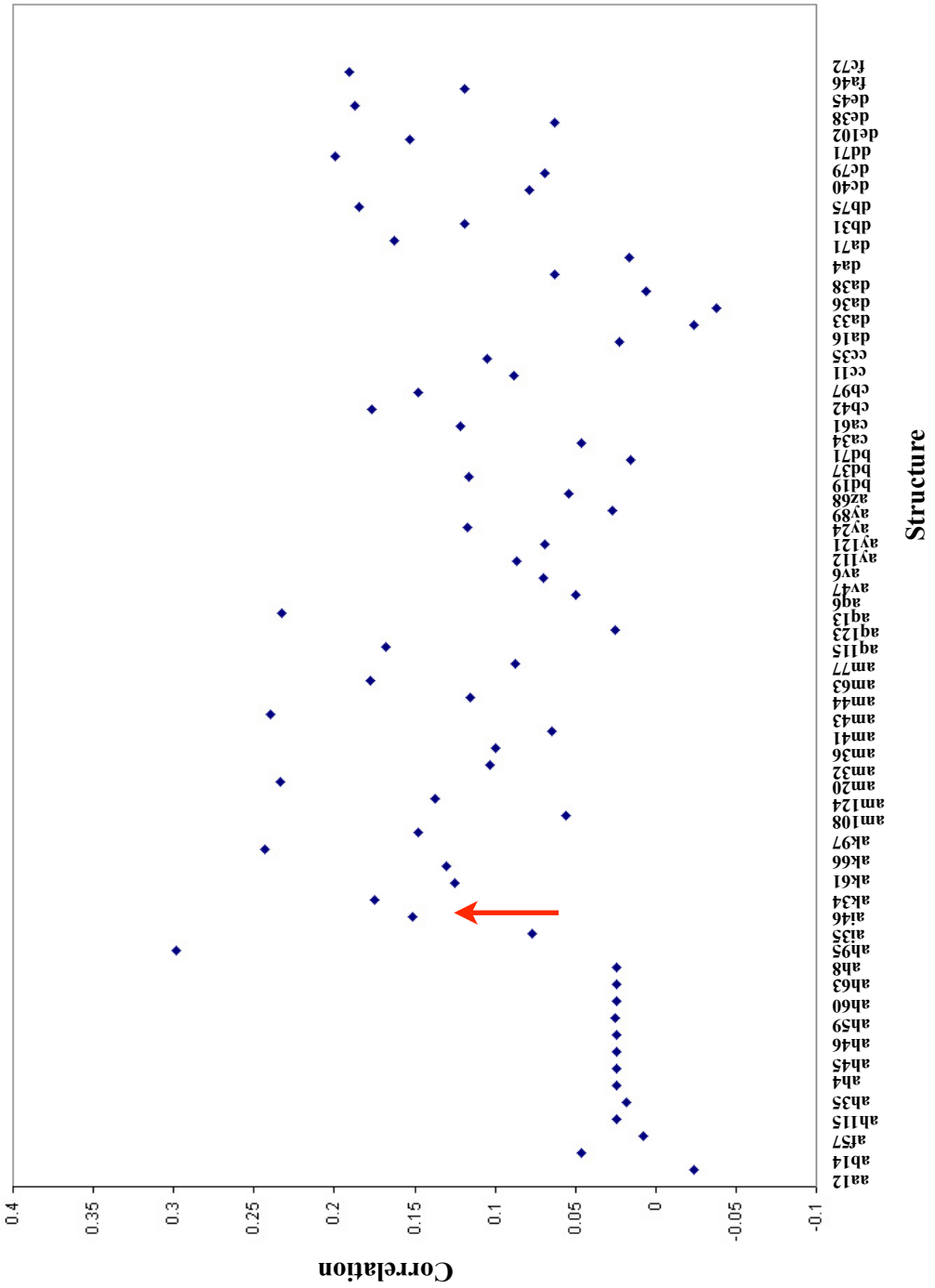

Figure 4.11 Correlation coefficients of all 65 structures against the D5000 data. The arrow indicates structure ak34

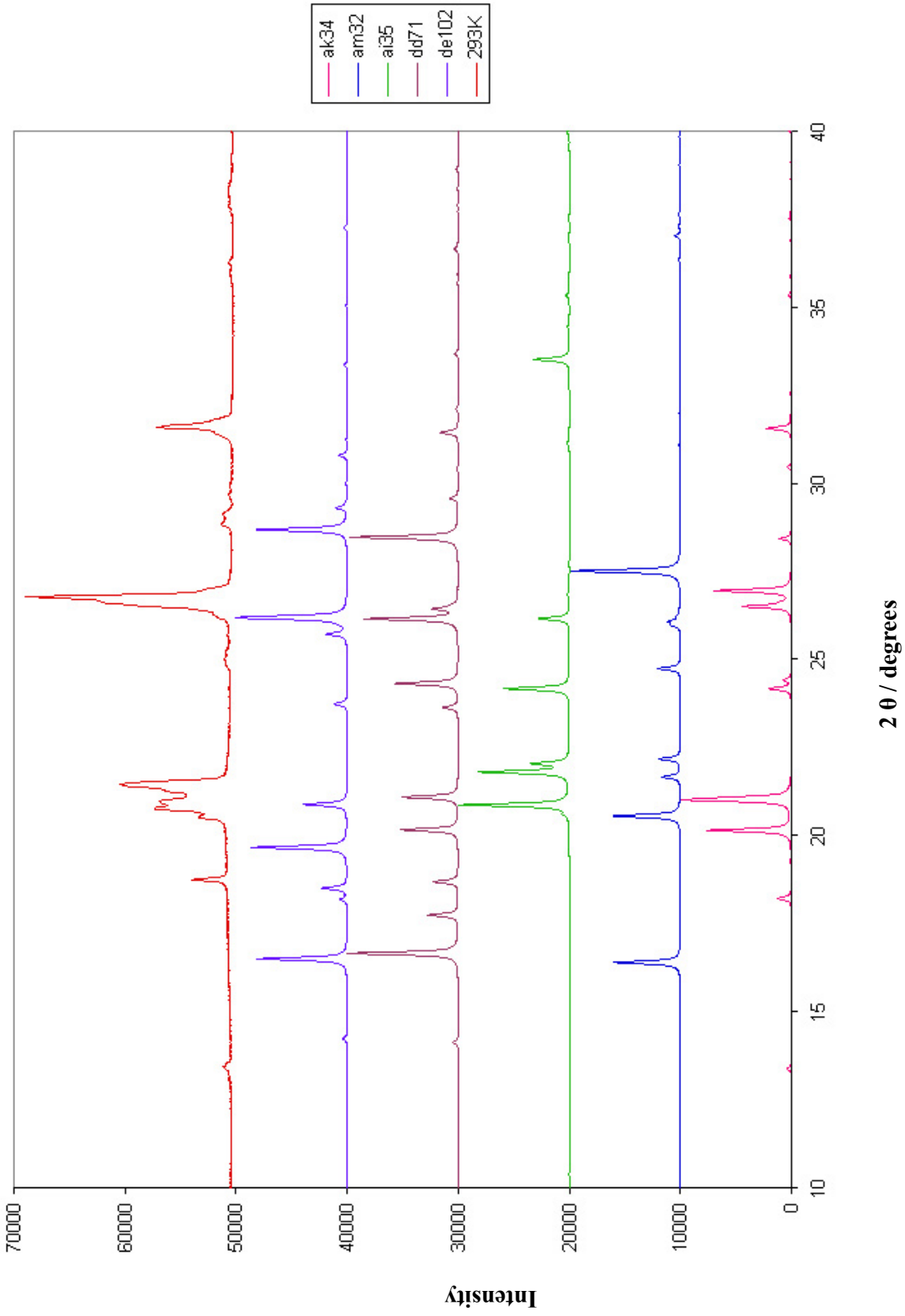

Figure 4.12 Powder diffraction patterns for five selected predicted structures and the experimental structure at room temperature (D5005).

4.2.2.3 Compare.x

Using the default triangle window value of 2, *Compare.x* identified the correct structure ak34 at the three intermediate temperatures 150K, 200K and 250K. As with *PolySNAP*, at lower temperatures, *Compare.x* selected structure am32, while structure ai35 had the highest correlation ranking at room temperature [Table 4.4, Figures 4.13 and 4.14]. On visual comparison their powder patterns differed significantly from the corresponding experimental data [Appendix A2.4].

Table 4.4. Structures with highest correlation coefficient [C(x)] at each temperature, and the difference to the value obtained for the correct structure [C(ak34)]. Black numbers denote cases where the correct structure was identified, the difference was positive. An incorrect match gave a negative difference, as shown by the values in red and blue. Blue denotes ak34 being ranked second, while values in red correspond to ak34 being ranked third or lower.

Temperature (K)	***Top ranked structure***	***Correlation coefficient of top ranked structure***	***Correlation coefficient***	***Difference [C(ak34) - C(x)]***
10	am32	0.869	0.818 (ak34)	-0.051
50	am32	0.880	0.833 (ak34)	-0.047
150	ak34	0.895	0.887 (ak61)	+0.008
200	ak34	0.895	0.881 (ak61)	+0.014
250	ak34	0.910	0.890 (ak66)	+0.020
293	ai35	0.894	0.862 (ak34)	-0.032
293 (D5000)	ai35	0.893	0.859 (ak34)	-0.034

Although the default triangle window value of 2 was selected for this work, a variety of triangle windows ranging from 0.5 to 4.0 in increments of 0.5 were tested using this data [Appendix A2.4-tables A2.4.1-A24..8]. As expected, narrow windows did not allow enough flexibility, thus resembling a more pointwise approach. When wider triangle windows were used, higher correlation values resulted due to too much flexibility within the comparison parameters. A wider window gives a higher probability of finding peaks within the 2θ range stipulated by that window. For a window at any given point, multiple peaks found within the stipulated 2θ range give an erroneous cumulative correlation. Thus, falsely high correlations resulted from using too wide a window.

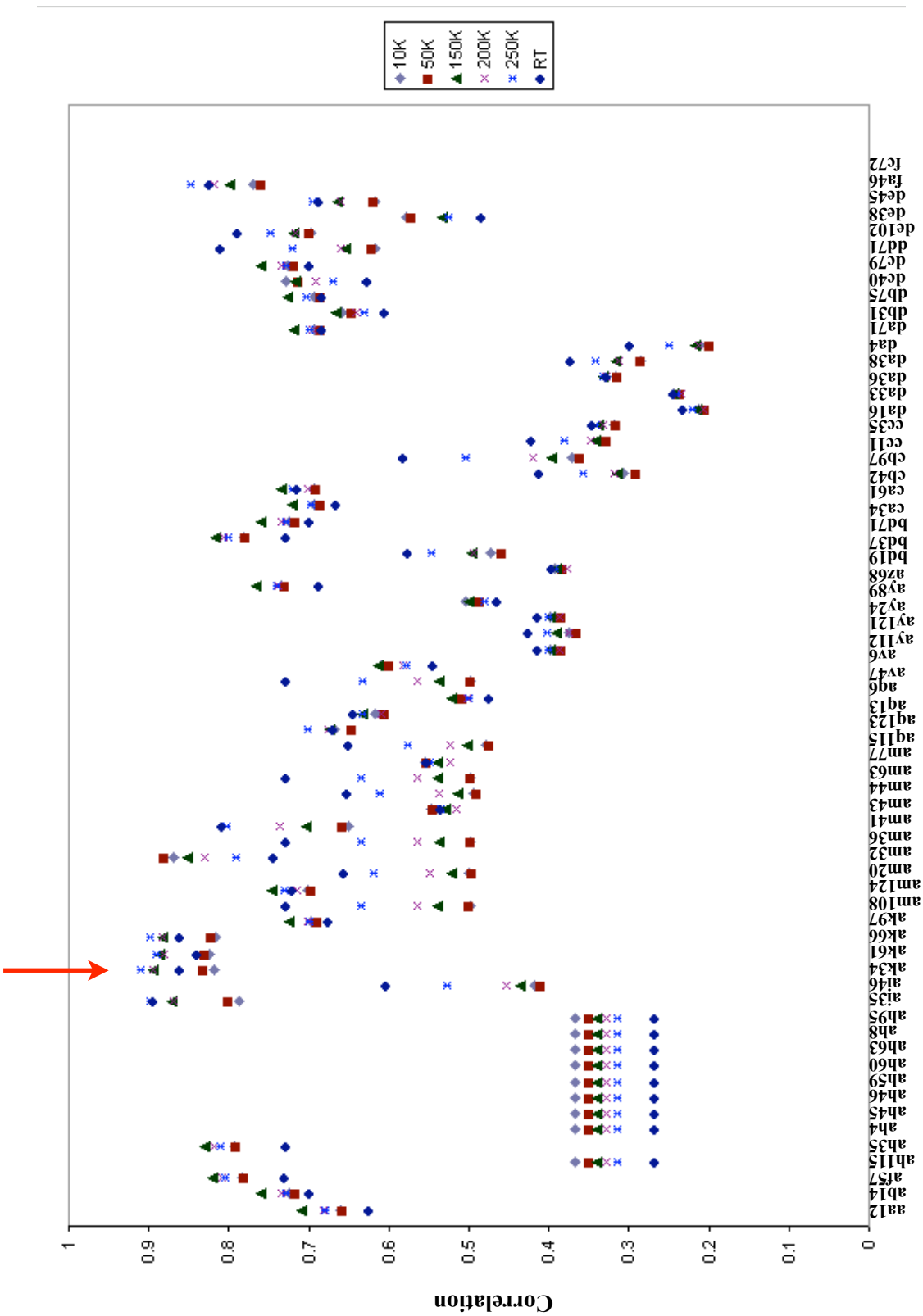

Figure 4.13 Correlation coefficients of all 65 structures at each temperature (D5005). The arrow indicates structure ak34.

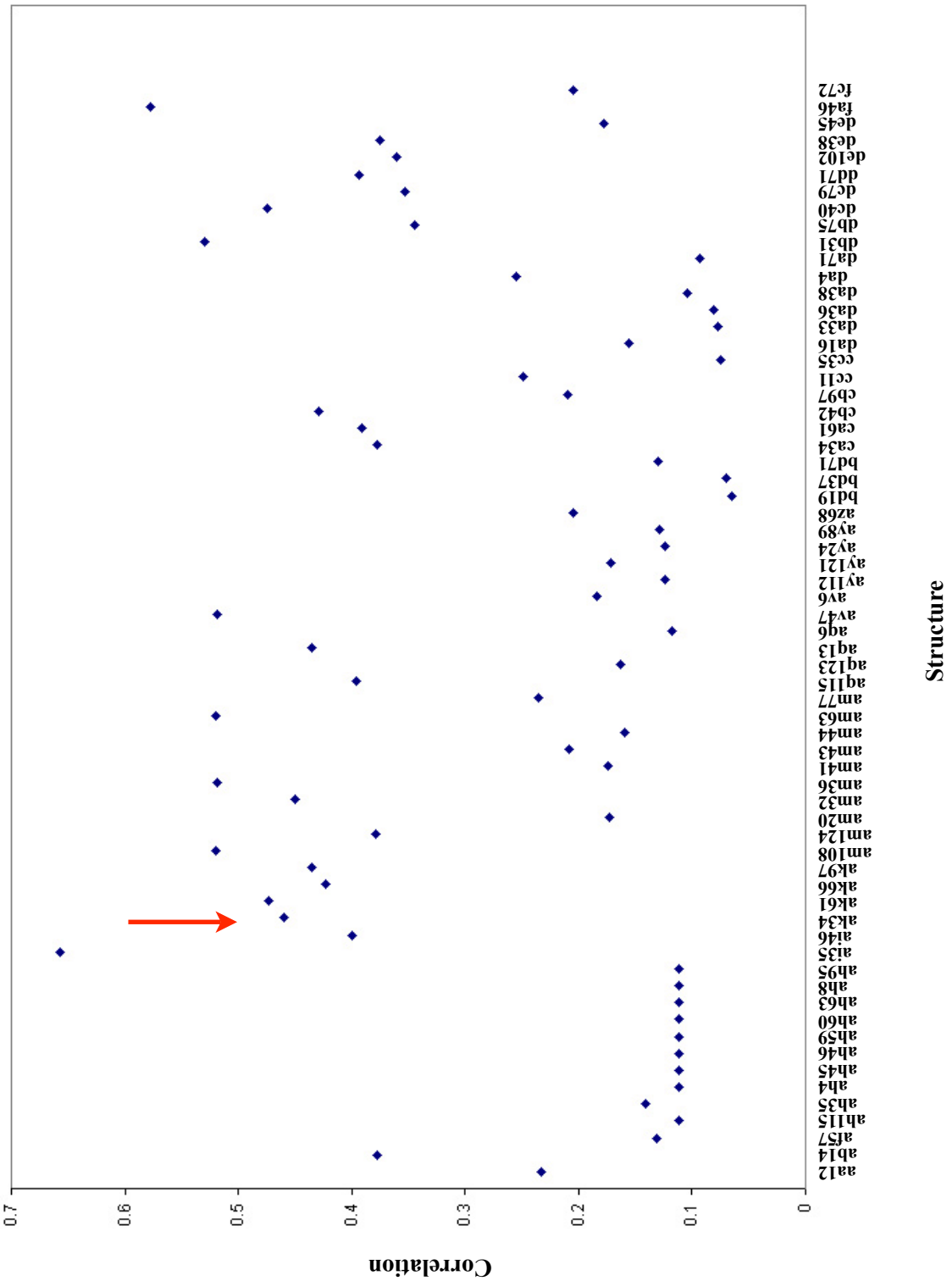

Figure 4.14 Correlation coefficients of all 65 structures against the D5000 data. The arrow indicates structure ak34.

4.3 Discussion

Table 4.5. Comparison of the ability of the three methods in the automated identification of the correct predicted structure. Values in red denote the modulus of the difference between the correct structure and the structure ranked first. If the correct structure is ranked first, values denote the difference between the correct structure and the next best (shown in black).

Temperature	R_{wp}	*PolySNAP*	*Compare*
10	5.0	0.026	0.051
50	2.0	0.037	0.047
150	14.7	0.044	0.008
200	20.4	0.037	0.014
250	5.7	0.188	0.020
293	3.4	0.231	0.032
293 (D5000)	1.0	0.148	0.034

With all three methods, higher temperatures generally demonstrated a greater degree of similarity with the correct predicted structure. The reason behind this could possibly be brought down to zero point error. This would also explain why, in all three scenarios, the room temperature data obtained by transmission geometry did not exhibit the same degree of similarity with the theoretical structure as its reflection geometry counterpart.

Despite the fact that predictions are carried out at low temperatures, with both *PolySNAP* and *Compare*, the experimental data that best matched the predicted structure were at room temperature and 250K respectively. This implies that a zero point error correction may be needed in future work. It is interesting to note that both methods picked the same three structures, albeit at different temperatures. Due to time restrictions, this has not been investigated further. However, with the understanding gained through this project, a zero-point error that can be measured reliably can be pre-defined in *PolySNAP* prior to running a comparison. This would possibly result in the correct structure being identified at temperatures close to the predictions' temperature, and ideally also at all other temperatures making for a more direct and meaningful comparison. *Compare*, having shown to be more stable over a range of temperatures, would be the method of choice in the case of a non-defineable zero-point error. In comparison with

PolySNAP, *Compare* gave higher overall correlation coefficients. However, although the discrimination between the highest ranking structure and the structure with the second highest correlation coefficient increased with temperature there was less discrimination between the data when compared with the values obtained from the *PolySNAP* analysis [Figure 4.15]. This could suggest that the *PolySNAP* correlation is more sensitive to changes in temperature (and the resulting shifts in 2θ) as opposed to *Compare*.

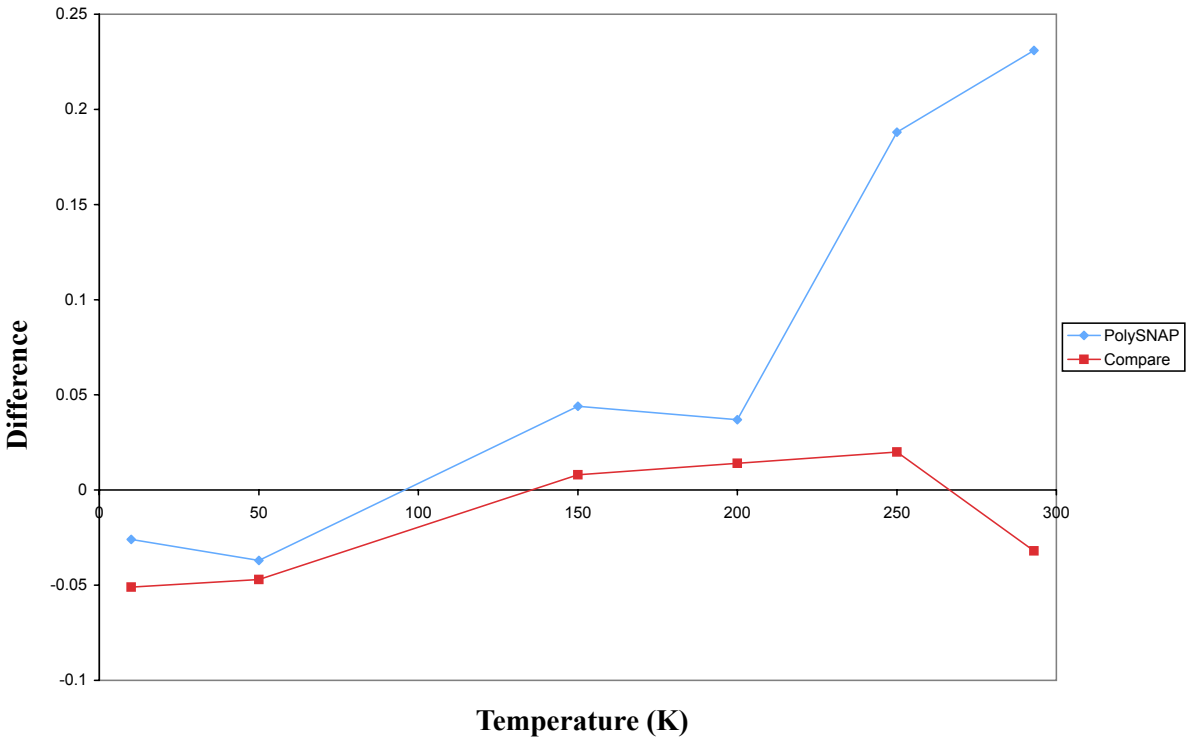

Figure 4.15 Difference in correlation coefficients between ak34 and the structure with the next highest correlation. In cases where ak34 was not ranked first, the difference between ak34 and the structure with the highest correlation is shown.

4.4 References

1. British National Formulary, Pharmaceutical Press, Edition 1, **54,** Sept. 2007, 319
2. R K Mc Mullan, J Epstein, J R Ruble and B M Craven, *Acta Cryst. B.*, 1979, **35**, 688-691
3. G Day, S L Price, M Leslie *J Phys Chem B* (2003) **107**, 10919-10933
4. S L Price, B Patel, P Pridhanani-Jethani and A Torrisi, *ACA Trans,* 2004 **39**, 2-13

5. CHLOROTHALONIL

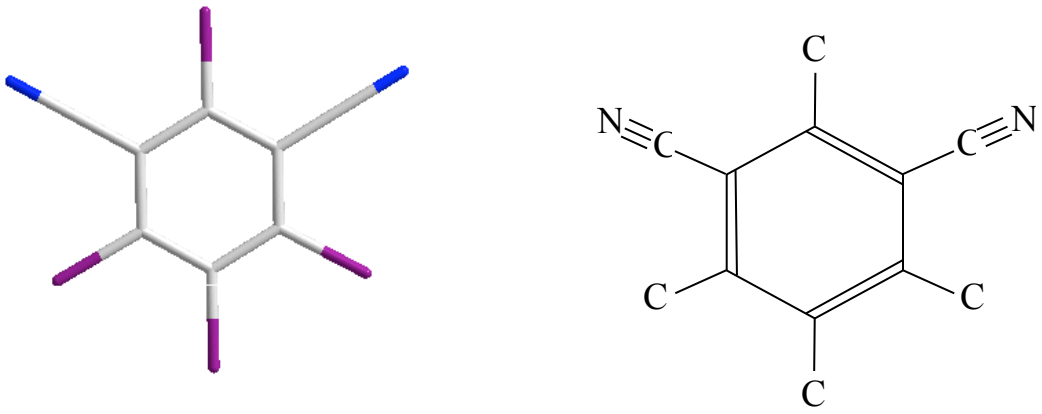

Figure 5.1. Chlorothalonil (2,4,5,6-tetrachloro-1,3-benzenedicarbonitrile)

5.1 Background

Chlorothalonil is an aromatic halogen compound which forms part of the chloronitrile family. It is a non-corrosive gray to colourless crystalline material, commonly known as a general-use pesticide under the trade names Bravo® or Daconil 2787®. Chlorothalonil is also used as a broad-spectrum fungicide, particularly on horticultural crops[1] as well as in home gardens, and it may also be encountered in paints and wood preservatives where it acts as a biocide.

Chlorothalonil acts by inhibiting enzyme systems in fungi and it persists on the surface of plant foliage, thus helping to prevent fungal disease in plants. A significant application of this material is in the control of fungal diseases in nurseries, seed orchards, Christmas plantations and greenhouses, targeting fungal blights, needlecasts and cankers on conifer trees. Peanuts, tomatoes, potatoes, onions and celery are frequently treated with this fungicide.

There are three known polymorphs of chlorothalonil reported to date[2], all of which have been predicted successfully within the constraints of prediction techniques. Form I is the polymorph that is commercially available and is the form under primary consideration in this study. It remains stable over long time-periods.

5.1.1 Crystal Structure of Form I

The single crystal structure of chlorothalonil Form I has been determined by Britton[3] at room temperature, while Forms II and III were first characterised by Tremayne *et al*[2] during a simultaneous experimental and computational search for polymorphs [Table 5.1]. Form I has a monoclinic ($P2_1/a$) lattice, with Z = 4. The structure consists of infinite molecular chains linked into antiparallel ribbons [Figures 5.2 and 5.3].

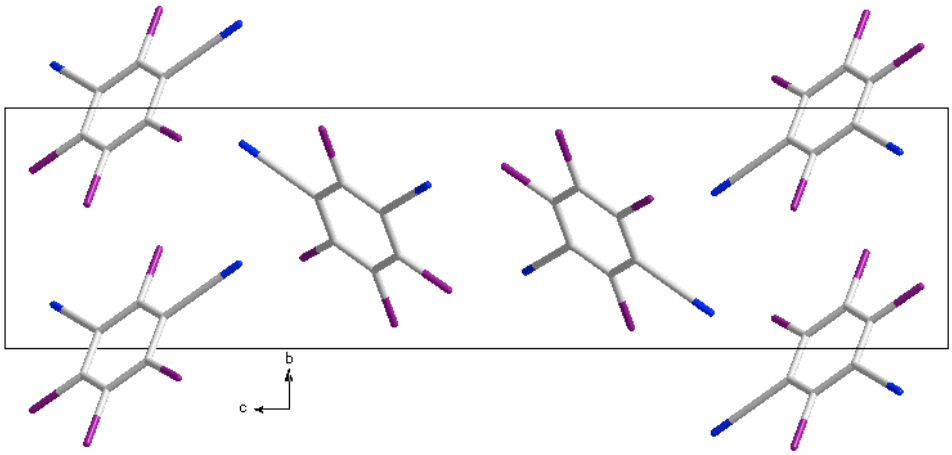

Figure 5.2. A view of the crystal structure of Form I of chlorothalonil in projection down the a axis.

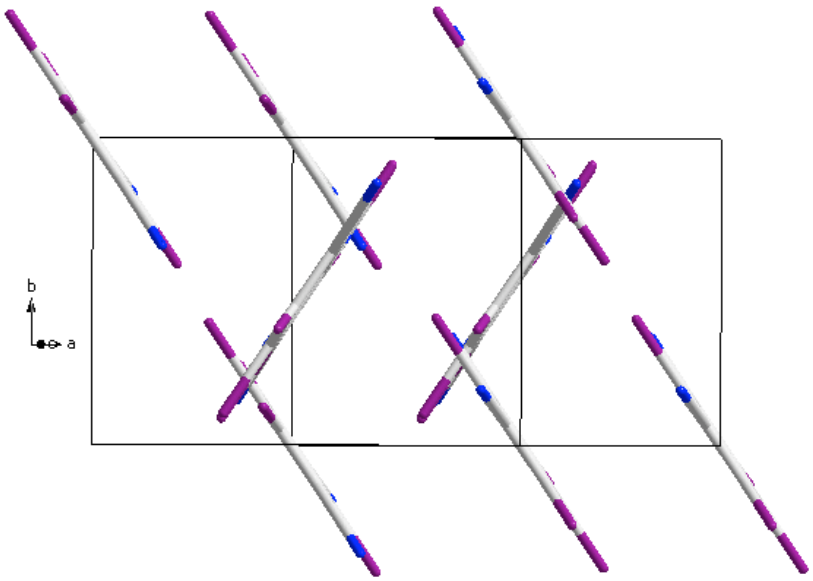

Figure 5.3. Packing diagram showing the herringbone structure

5.1.2 Crystal Structure Prediction

In contrast with imidazole, chlorothalonil is a more challenging molecule with respect to crystal structure prediction. This is due to its dominant Cl----N interactions being directional[4]. Although not widely discussed, these short cyanohalide interactions are commonly found where X is Cl or Br, and they arise due to halogen polarizability[5]. The computer modelling was based on a rigid chlorothalonil molecule, using a molecular geometry obtained by *ab initio* optimisation of the SCF (Self-Consistent Field, now better known as Hartree-Fock) wave function.

Initially, the computational search generated dense packings of the *ab initio* molecular structure of chlorothalonil in 29 different crystal geometries. This resulted in a total of 1304 starting structures, which were then used as starting points in the lattice energy minimization calculations, carried out using the FIT potential[6] [Figure 5.4].

The 27 structures found within 5 kJ mol^{-1} of the global minimum, i.e. the most energetically favourable structures, were then reminimised using the ANI potential[6]. Some reordering of the relative lattice energies was observed with the change in potential, and the number of distinct structures was reduced to 22. This is due to the fact that some structures that were distinct minima with FIT converged to the same minima for the ANI potential surface, lowering the symmetry in some of the cases. For both potentials, however, the global minimum in the search corresponded with Form I.

Out of the 22 theoretical structures, 18 were found to have a Z'=1, and the remaining 4 structures had Z'=2. The unit cell parameters of the 5 lowest energy structures are shown in [Table 5.1]. Most of the theoretical structures were also found to have plate-like morphologies, with the largest dimension up to ten times the thickness. When structures with such anisotropic behaviour are predicted, this may indicate a possibility of preferred orientation being encountered during subsequent analysis by powder diffraction. In such cases, this warning could suggest the adoption of capillary geometry during powder diffraction data collection.

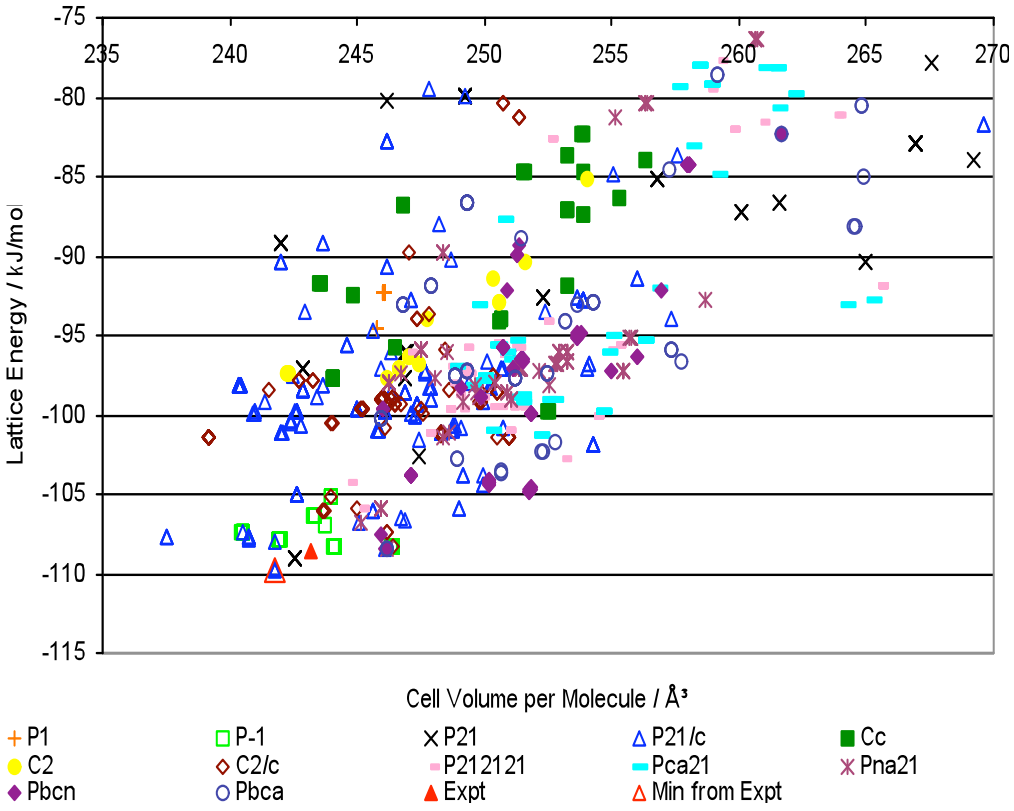

Figure 5.4 The distribution of some of the lower energy structures found in the search for minima in the lattice energy of chlorothalonil. The minimum corresponding to the known crystal structure of Form I (Min from Expt) is denoted by the open red triangle[7]. [Permission for reproduction granted by the author of reference 7.]

Table 5.1. The unit cell parameters of the five lowest energy structures for Chlorothalonil minimised using the ANI potential[2].

	Space Group	E_{latt} (kJmol^{-1})	Cell Vol (Å^3)	*a* (Å)	*b* (Å)	*c* (Å)	*α* (deg)	*β* (deg)	*γ* (deg)
exp	$P2_1/a$	-98.79	243.180	24.753	6.226	6.340	90.00	95.41	90.00
min[a]	$P2_1/a$	-99.40	243.246	24.840	6.272	6.288	90.00	96.65	90.00
	Structures in search			Reduced cell parameters					
FC45	$P2_1/c$	-99.40	243.243	24.839	6.288	6.272	90.00	96.65	90.00
AB15	*P*-1	-99.39	238.424	6.482	7.774	10.166	91.31	106.80	102.50
AI44	$P2_1/c$	-99.31	243.379	12.750	12.309	6.228	90.00	95.12	90.00
AF18	$P2_1$	-99.02	243.922	12.486	6.302	6.235	90.00	95.31	90.00
AB3	*P*-1	-98.16	243.514	6.077	6.350	12.727	94.53	94.72	92.96

5.2 Results

5.2.1 Low Temperature Data

The unit cell parameters of the predicted structure are similar to those of the published single crystal structure obtained at room temperature. For this reason, the unit cell parameters from the published single crystal structure were used as a starting point for a LeBail fit on the 293K data. The unit cell parameters obtained from this initial fit were then used as a starting point for a LeBail fit on the 250K data. Subsequent LeBail fits on the lower temperature data sets followed the same "stepwise" methodology.

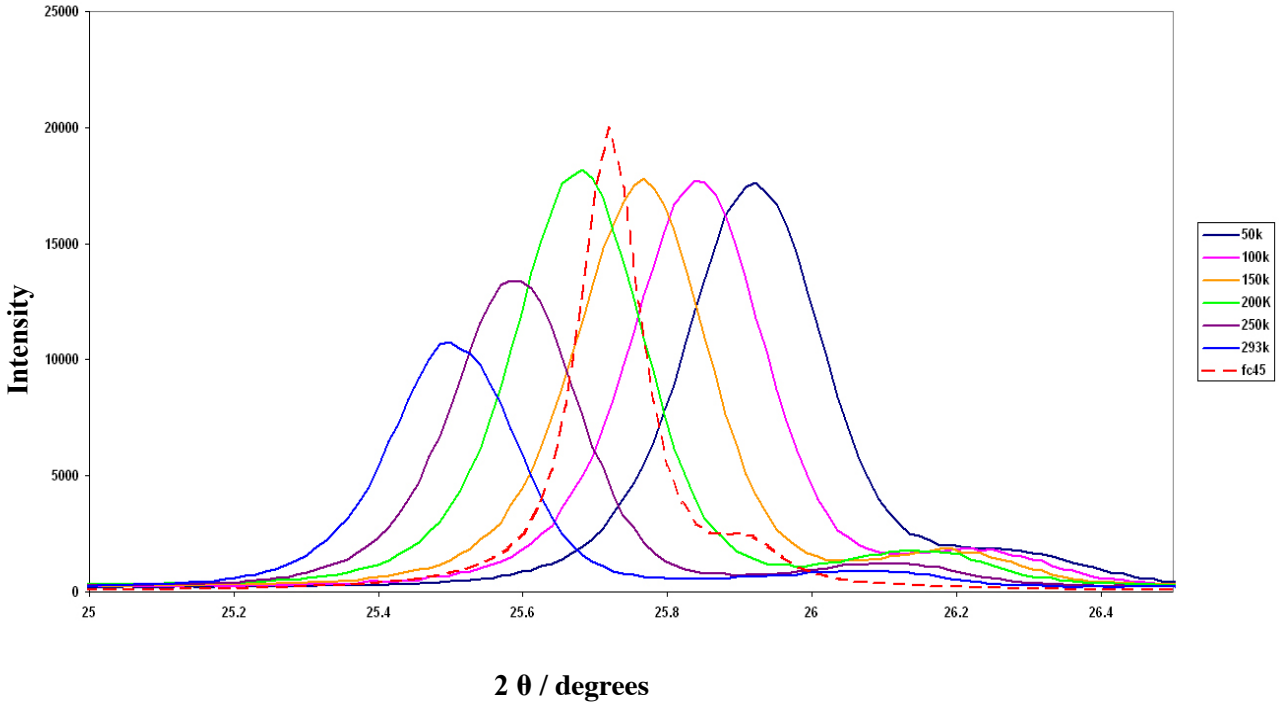

Figure 5.5 Section of superimposed powder diffraction data at all temperatures showing peak (112) shifting towards the right with decreasing temperature.

The powder diffraction pattern again illustrates a contraction in the unit cell with decreasing temperature, as indicated by the clear shift in peak position (112) along 2θ [Figure 5.5] and across the diffraction pattern from 5 to 45 along 2θ [Appendix A3.1].

The percentage differences in *a*, *b*, *c*, *β* and volume with varying temperature were calculated and, as expected, the volume increases as higher temperatures are reached, while *a*, *b*, *c* and *β* change accordingly to accomodate this expansion [Table 5.2 and Figure 5.6].

Table 5.2 Unit cell parameters of the lowest energy predicted structure, those determined from experimental data, and published unit cell dimensions for chlorothalonil with changing temperature. The numbers in brackets denote the percentage change with respect to those values obtained from the 100K data.

Temperature (K)	***a (Å)***	***b (Å)***	***c (Å)***	***β(°)***	***Volume (Å³)***
Single Crystal Values[3]	24.753(1)	6.226(1)	6.340(2)	95.41(3)	972.719
Predicted values[2] (0K)	6.272(2)	6.288(1)	24.839(1)	96.65(1)	975.247
100	24.552 (1)	6.183(2)	6.351(3)	96.18(2)	958.589
(% change)	(0.00)	(0.00)	(0.00)	(0.00)	(0.00)
150	24.623(1)	6.175(2)	6.351(3)	95.89(2)	960.534
(% change)	(+0.29)	(-0.13)	(-0.01)	(-0.29)	(+0.20)
200	24.705(1)	6.225(1)	6.325(4)	95.85(3)	967.743
(% change)	(+0.62)	(+0.67)	(-0.39)	(-0.34)	(+0.95)
250	24.687(1)	6.231(1)	6.328(2)	95.62(2)	968.687
(% change)	(+0.55)	(+0.77)	(-0.36)	(-0.58)	(+1.05)
293	24.739(2)	6.233(3)	6.328(3)	95.34(1)	971.612
(% change)	(+0.76)	(+0.80)	(-0.36)	(-0.87)	(+1.36)
293 (D5000)	24.749(3)	6.228(2)	6.337(1)	95.40(2)	972.363
(% change)	(+0.80)	(+0.72)	(-0.23)	(-0.81)	(+1.44)

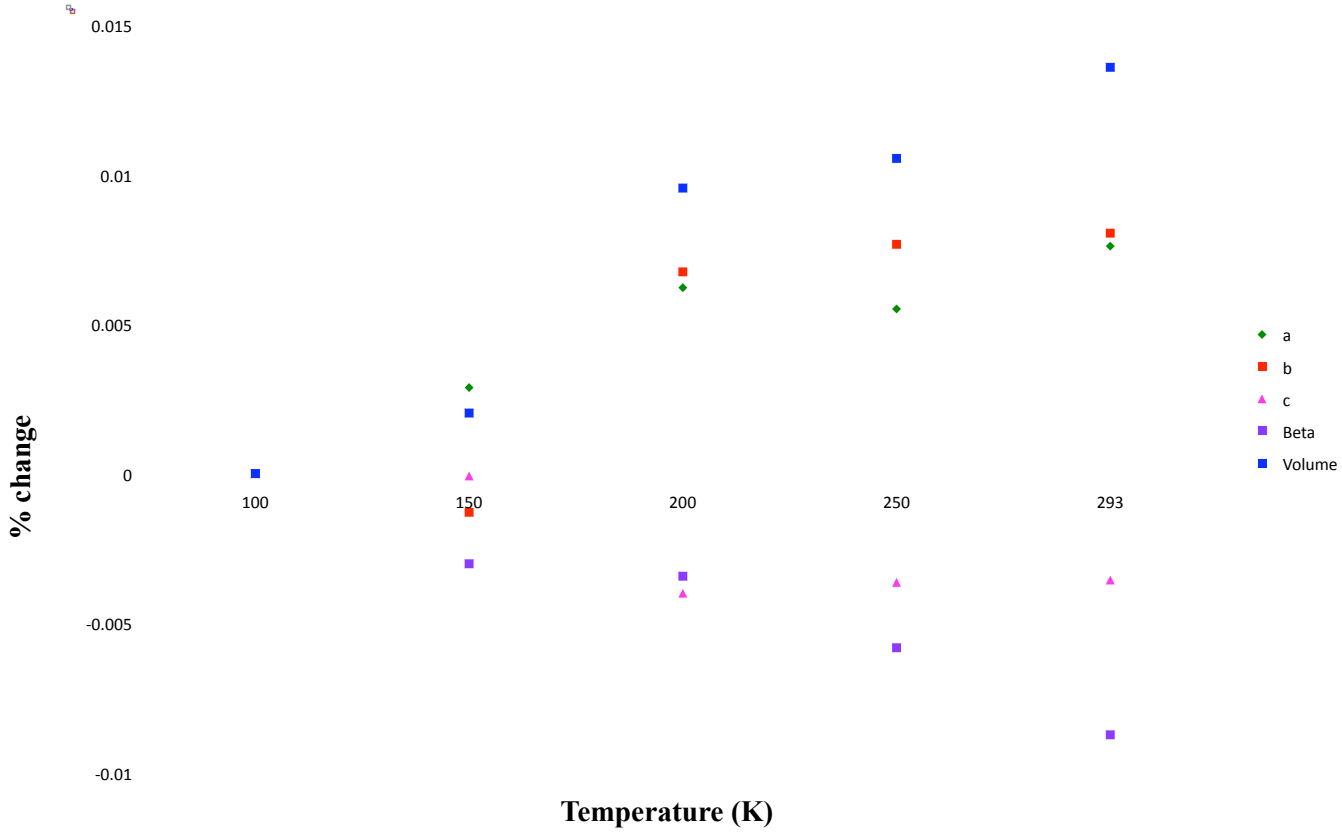

Figure 5.6 Graph showing the percentage change in unit cell dimensions with temperature.

Over the range of temperatures, *a* and *b* increase overall while *c* generally shortens, perhaps to accomodate the reduction of β. These changes in the lattice parameters result in an overall expansion of the unit cell, as indicated by the increase in volume. As the material is anisotropic, overall cell volume expansion is not necessarily a direct consequence of an increase in length in all directions. Again, as in the case of imidazole, these change fluctuations could be due to the relative difference in intermolecular interactions in each direction.

5.2.2 Automated Comparison

5.2.2.1 R_{wp}

The 22 minimised predicted structures were each compared, using R_{wp}, with the experimental data collected at each temperature. The outcome of these comparisons was, as in the case of imidazole, non-discriminatory, with none of the 22 structures identified as being significantly similar to any of the experimental data sets. R_{wp} values ranging from 68.08% to 78.68% were obtained, with the lower values resulting from comparison with the data collected at 200K [Table 5.3, Figure 5.7 and 5.8]. Identification of the correct predicted structure (fc45) would have been impossible based purely on these R_{wp} values. A comparison of these predicted structure data sets with the experimental data is given in Appendix A3.2.

Table 5.3. Structures with lowest R_{wp} identified at each temperature. The difference is that between the R_{wp} for the top ranked structure [$R_{wp}(x)$] and the correct prediction [$R_{wp}(fc45)$]. Red numbers denote incorrect structures ranked as the best.

Temperature (K)	***Top ranked structure***	***R_{wp} (x) (%)***	***R_{wp} (fc45) (%)***	***Difference (%) [$R_{wp}(x)$ - $R_{wp}(fc45)$]***
100	az19	72.3	74.1	-1.8
150	bd13	68.9	69.2	-0.3
200	fc47	68.1	68.4	-0.3
250	fc48	72.5	73.0	-0.5
293	az19	73.9	76.1	-2.2
D5000	ab37	72.9	77.4	-4.5

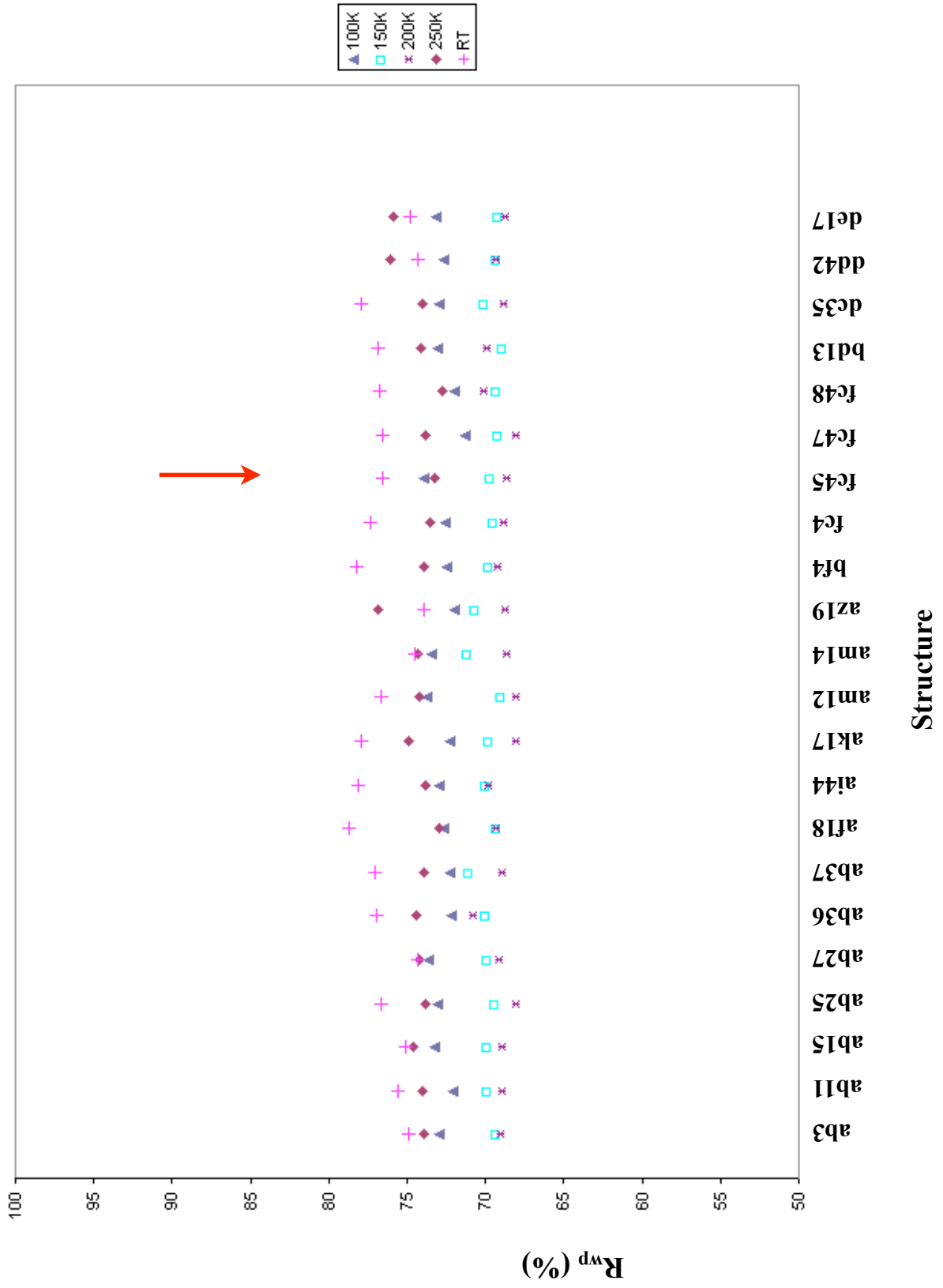

Figure 5.7 R_{wp} values for each structure at each temperature. The arrow indicates structure fc45.

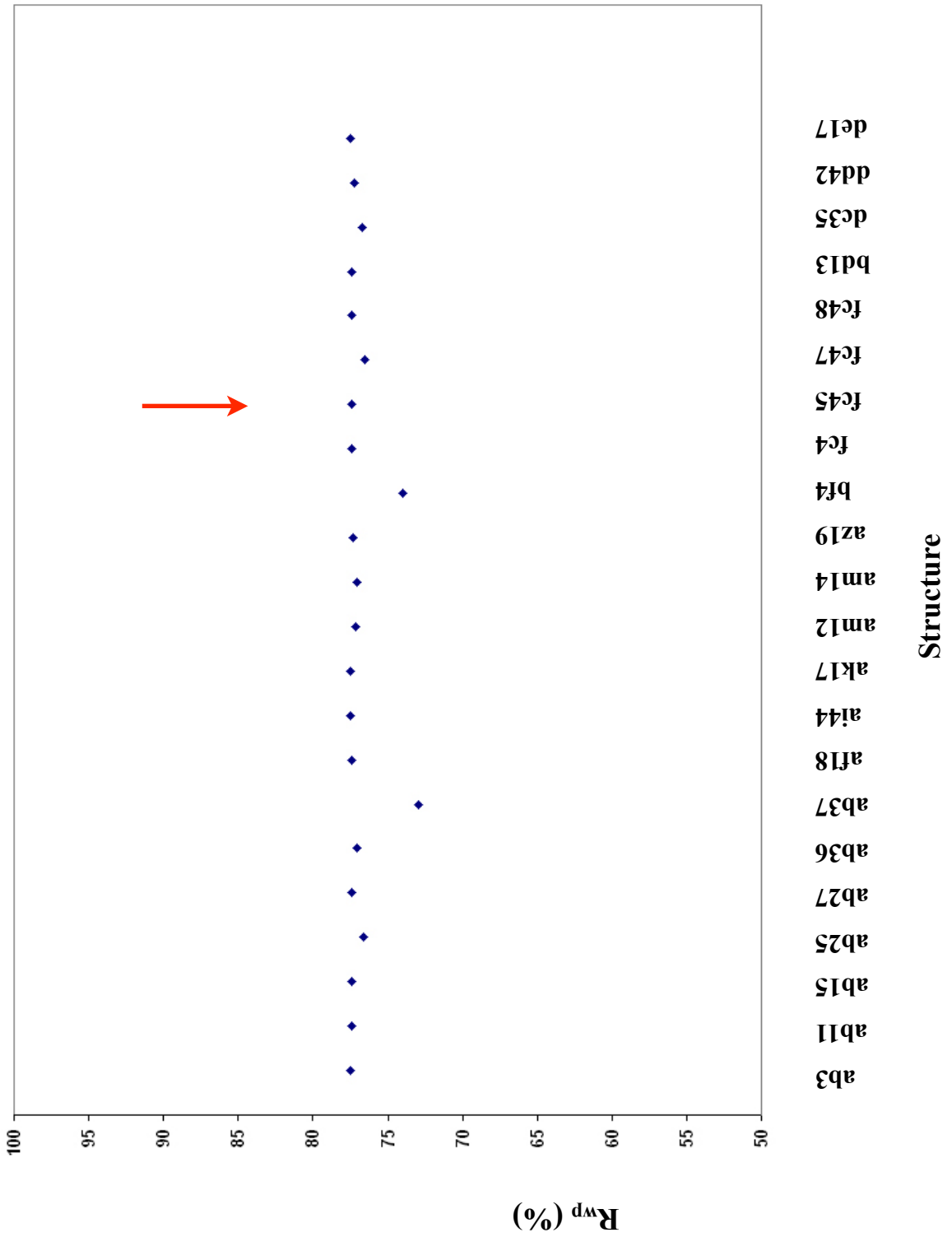

Figure 5.8 R_{wp} values for each structure against the D5000 data at room temperature. The arrow indicates structure fc45.

5.2.2.2 PolySNAP

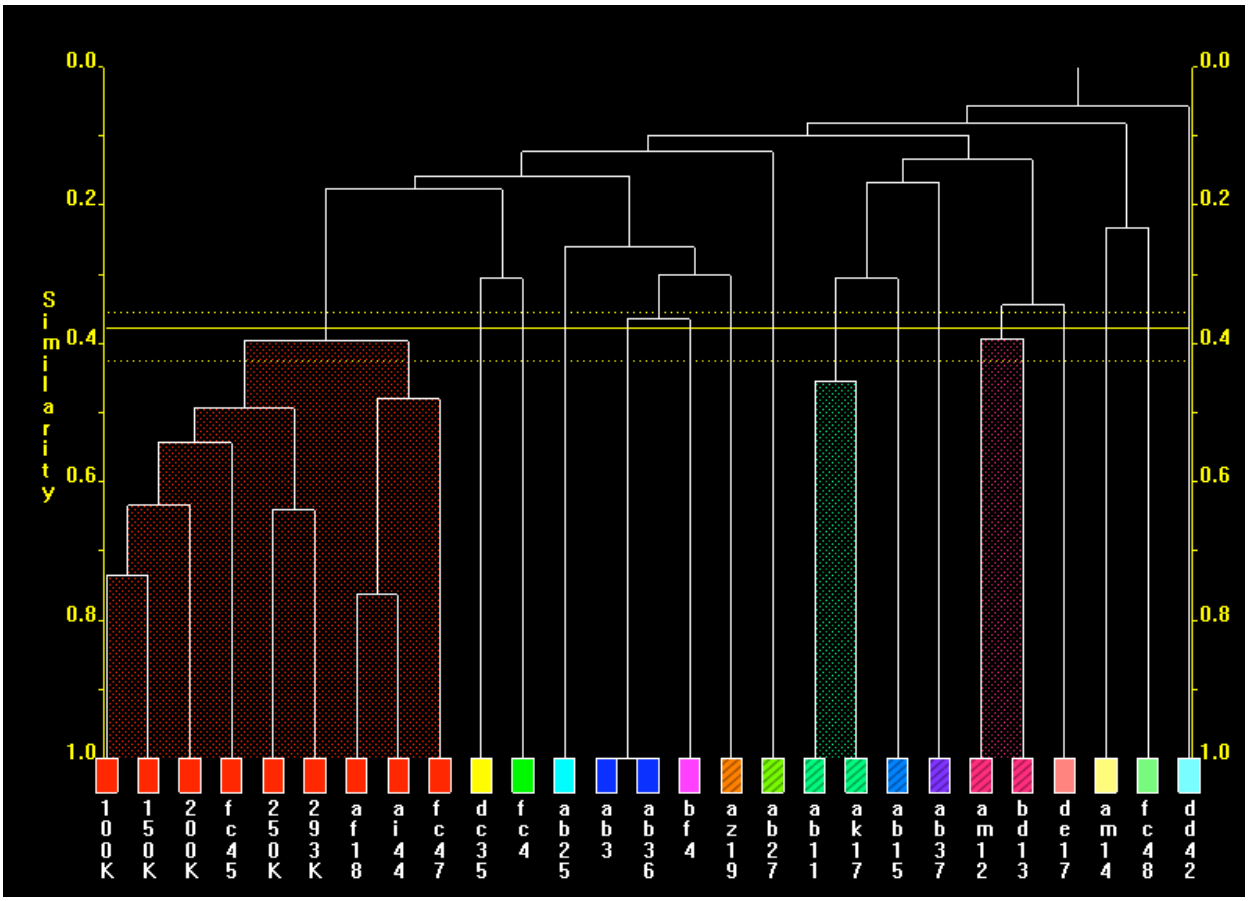

Figure 5.9. Dendrogram showing similarity clusters for chlorothalonil predicted and D5005 experimental powder patterns

For *PolySNAP* analysis, the data collected on the different diffractometers were analysed separately due to the difference in wavelength between the two setups. In the dendrogram comparing all 22 structures with the D5005 data [Figure 5.9], structure fc45, which corresponds to the published structure, was grouped with the entire set of experimental data collected at all temperatures (cluster shown in red in Figure 5.9). Also grouped in the same set, albeit at a higher tie-bar level, were structures af18, ai44 and fc47. Although these powder patterns show similarities to the experimental data, it is clear that the powder pattern from structure fc45, bears a more significant resemblance [Figure 5.10 and Appendix A3.3]. As in the case of imidazole, the experimental data are all grouped together, and within this cluster were paired subsets, with the data from lower temperatures ranked as more similar to each other than the higher temperatures. Considering each temperature separately, and

looking at the structure with the highest correlation in each case, structure fc45 was the top-ranked structure at all temperatures below 250K [Table 5.4].

Table 5.4. Structures with highest correlation coefficient [P(x)] at each temperature, and the difference to the value obtained for the correct structure [P(fc45)]. If P(fc45) = P(x), then the difference between P(fc45) and the next best structure is taken. Black numbers denote cases where the correct structure was identified, and the difference was positive. An incorrect match gave a negative difference, as shown by the values in red.

Temperature (K)	***Top ranked structure***	***Correlation coefficient of top ranked structure***	***Correlation coefficient***	***Difference [P(fc45) - P(x)]***
100	fc45	0.4639	0.4534 (fc4)	0.0105
150	fc45	0.5697	0.4292 (ai44)	0.1405
200	fc45	0.6167	0.3966 (ai44)	0.2201
250	ai44	0.4347	0.4046 (fc45)	-0.0301
293	ai44	0.5583	0.2377 (fc45)	-0.3206
293 (D5000)	af18	0.0675	-0.0564 (fc45)	-0.1239

Although at higher temperatures an incorrect structure was ranked first, taking the values obtained for the lower temperatures up to 200K the general trend observed with imidazole was retained. The correlation plot [Figures 5.11 and 5.12 and Table 5.4] clearly illustrates that up to 200K, the degree of similarity between the predicted structure fc45 and the experimental data increases with a rise in temperature; the higher temperatures (up to 200K) also show better discriminating ability denoted by a greater difference [P(fc45) - P(x)] between the correlation value obtained for the correct structure (fc45) and the next best ranking structure. Visually, correlation plots at each temperature show a clear trend which is retained as temperature varies. At higher temperatures an incorrect structure was identified as being most similar. This mismatch could be attributed to the fact that predictions were carried out at 0K, and therefore lower temperature powder data would naturally bear higher correlation with the simulated powder pattern than higher temperature data would.

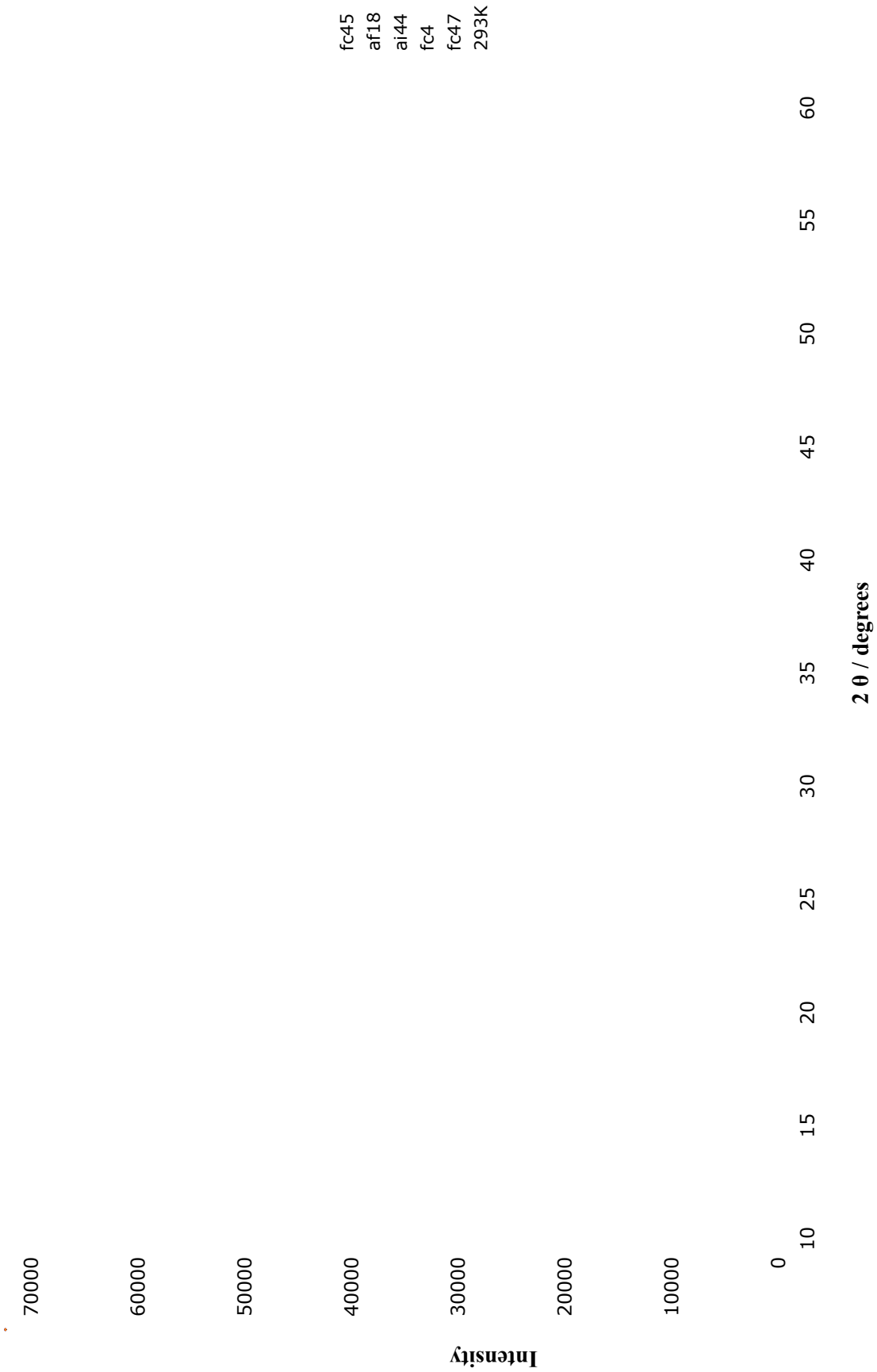

Figure 5.10 Powder diffraction patterns for five selected predicted structures and the experimental structure at room temperature (D5005).

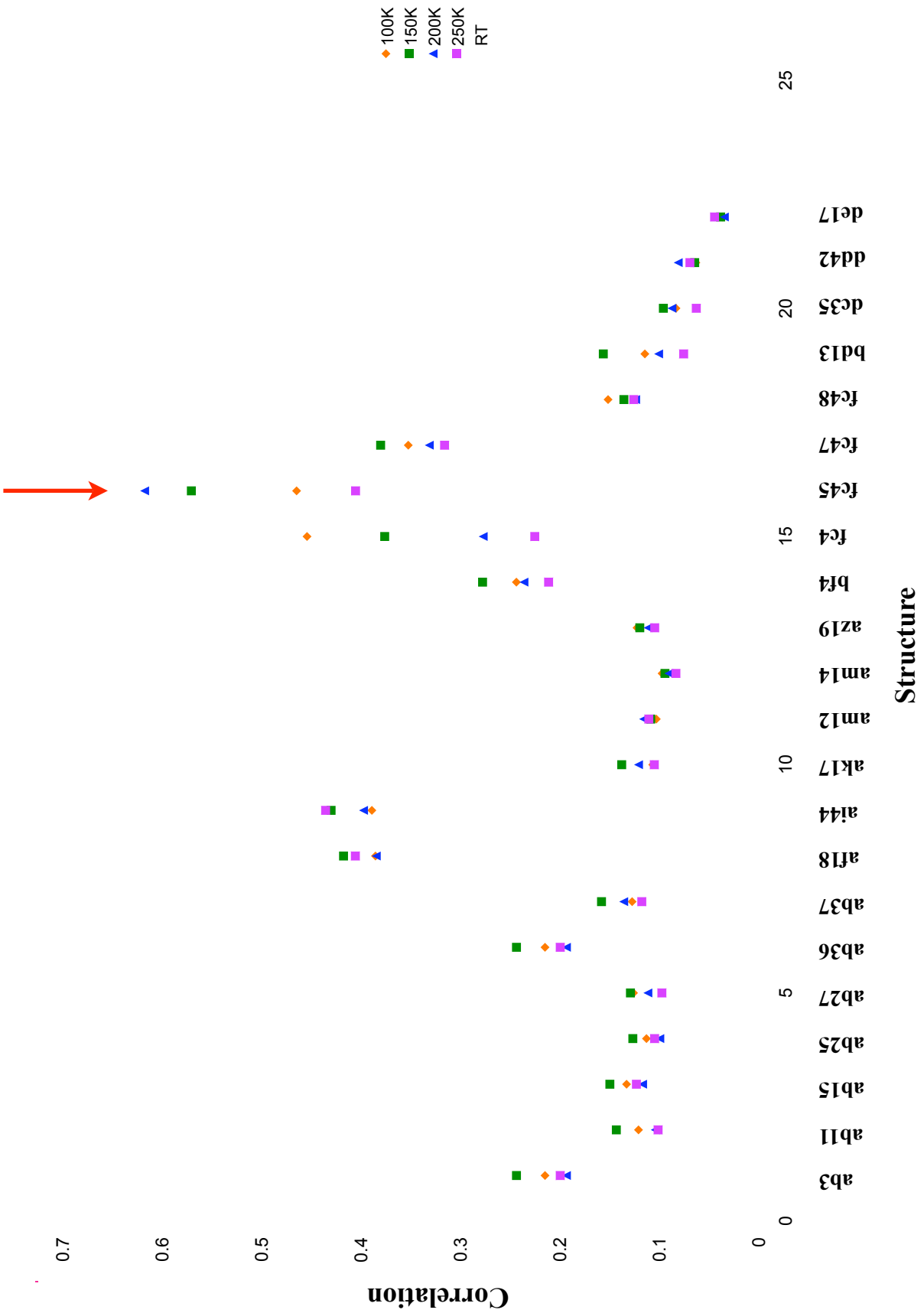

Figure 5.11 Correlation coefficients of all 22 structures at each temperature (D5005). The arrow indicates structure fc45.

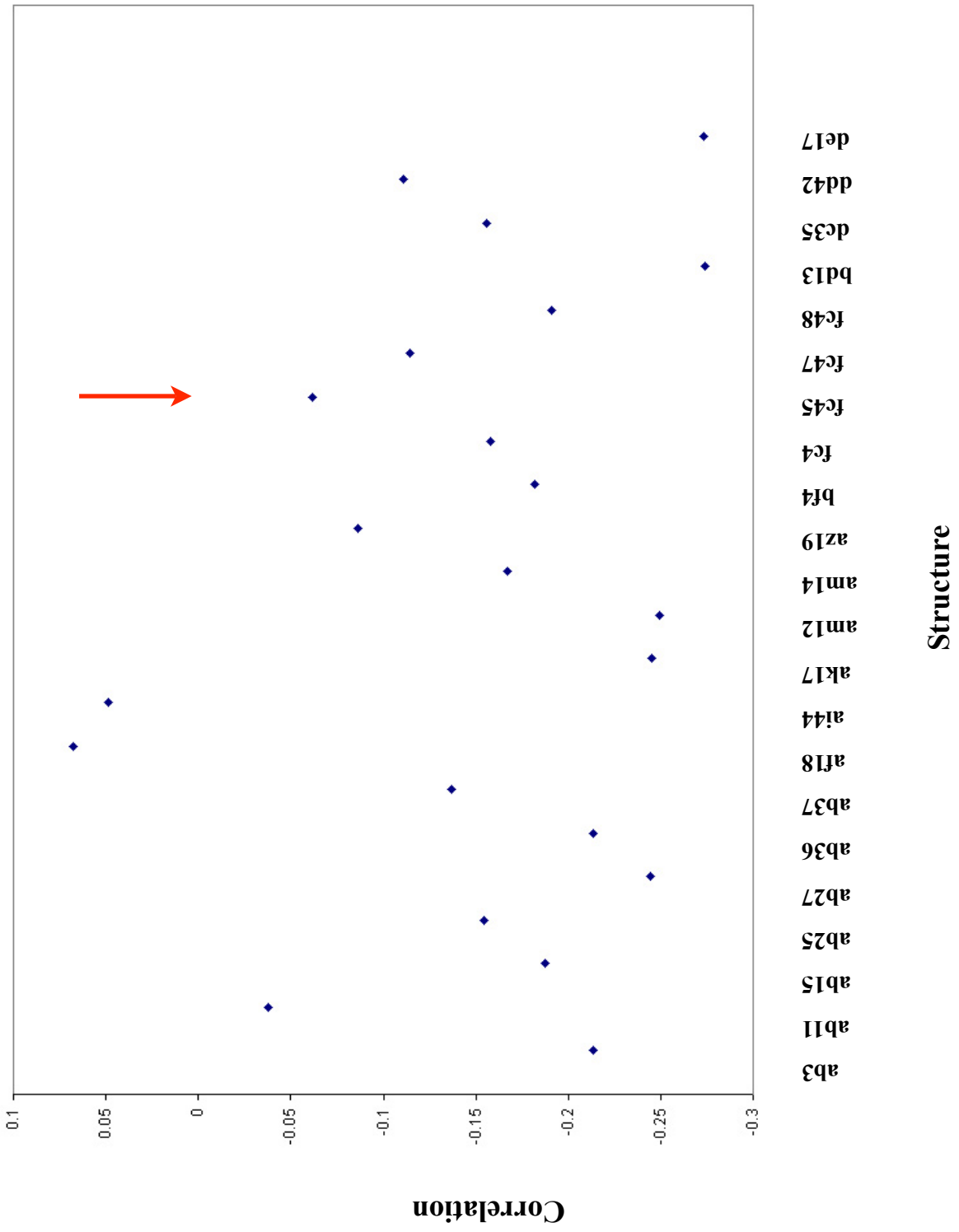

Figure 5.12 Correlation coefficients of all 22 structures against the D5000 data at room temperature. The arrow indicates structure fc45.

5.2.2.3 Compare.x

Using the default triangle window value of 2, *Compare.x* identified the correct structure fc45 at the three intermediate temperatures 150K, 200K and 250K (in a similar way to the results obtained for imidazole) [Table 5.5, Figures 5.13 and 5.14]. In contrast to the *PolySNAP* analysis, the structures ranked first at the lowest and highest temperatures were fc4 and fc47. The respective powder patterns from both these structures exhibit similarities with the experimental data, but neither are as close a match as structure fc45 [Figure 5.10 and Appendix A3.4]. In addition, fc4 and fc47 were not identified by *PolySNAP* as potential "first" matches at any temperature.

Table 5.5. Structures with highest correlation coefficient [C(x)] at each temperature, and the difference to the value obtained for the correct structure [C(fc45)]. Black numbers denote cases where the correct structure was identified, the difference was positive. An incorrect match gave a negative difference, as shown by the values in blue. In all cases where an incorrect match was made, the correct structure fc45 was ranked second.

Temperature (K)	***Top ranked structure***	***Correlation coefficient of top ranked structure***	***Correlation coefficient***	***Difference [C(fc45) - C(x)]***
100	fc4	0.9409	0.9300 (fc45)	-0.0109
150	fc45	0.9279	0.9240 (fc4)	+0.0039
200	fc45	0.9319	0.9216 (fc4)	+0.0103
250	fc45	0.9200	0.9173 (fc47)	+0.0027
293	fc47	0.9195	0.9068 (fc45)	-0.0127
293 (D5000)	fc47	0.7471	0.6436 (fc45)	-0.1035

Although the default triangle window value of 2 was selected for this work, a range of triangle windows ranging from 0.5 to 4.0 in increments of 0.5 were also tested [Appendix A3.4-tables A3.4.1-A3.4.8]. As in the case of imidazole, the narrower the window, the closer to a pointwise comparison the method became. Large triangle windows, conversely, produced false high correlations due to too much flexibility. This resulted in incorrect identification of structures at either end of the window spectrum.

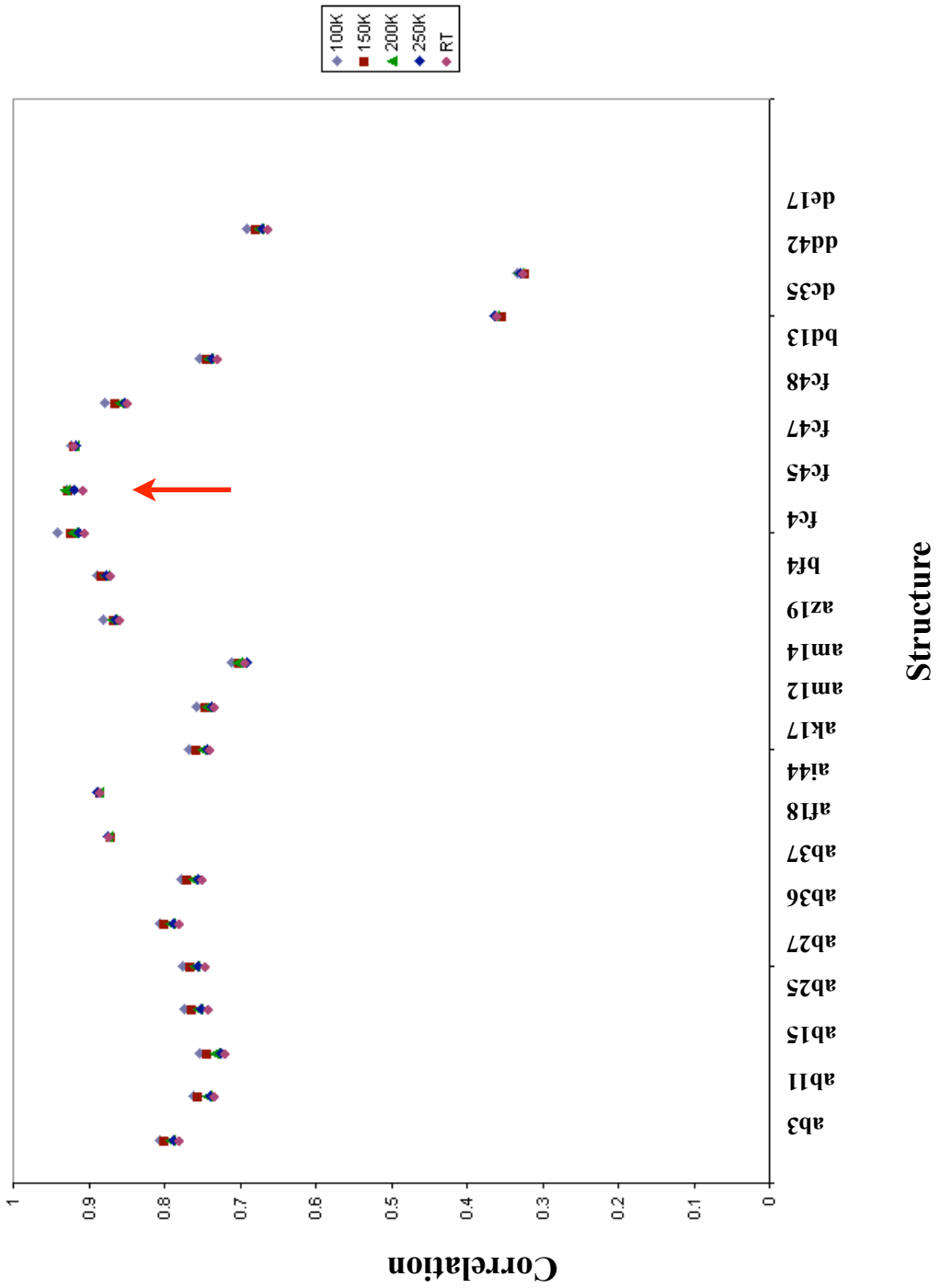

Figure 5.13 Correlation coefficients of all 22 structures at each temperature. The arrow indicates structure fc45.

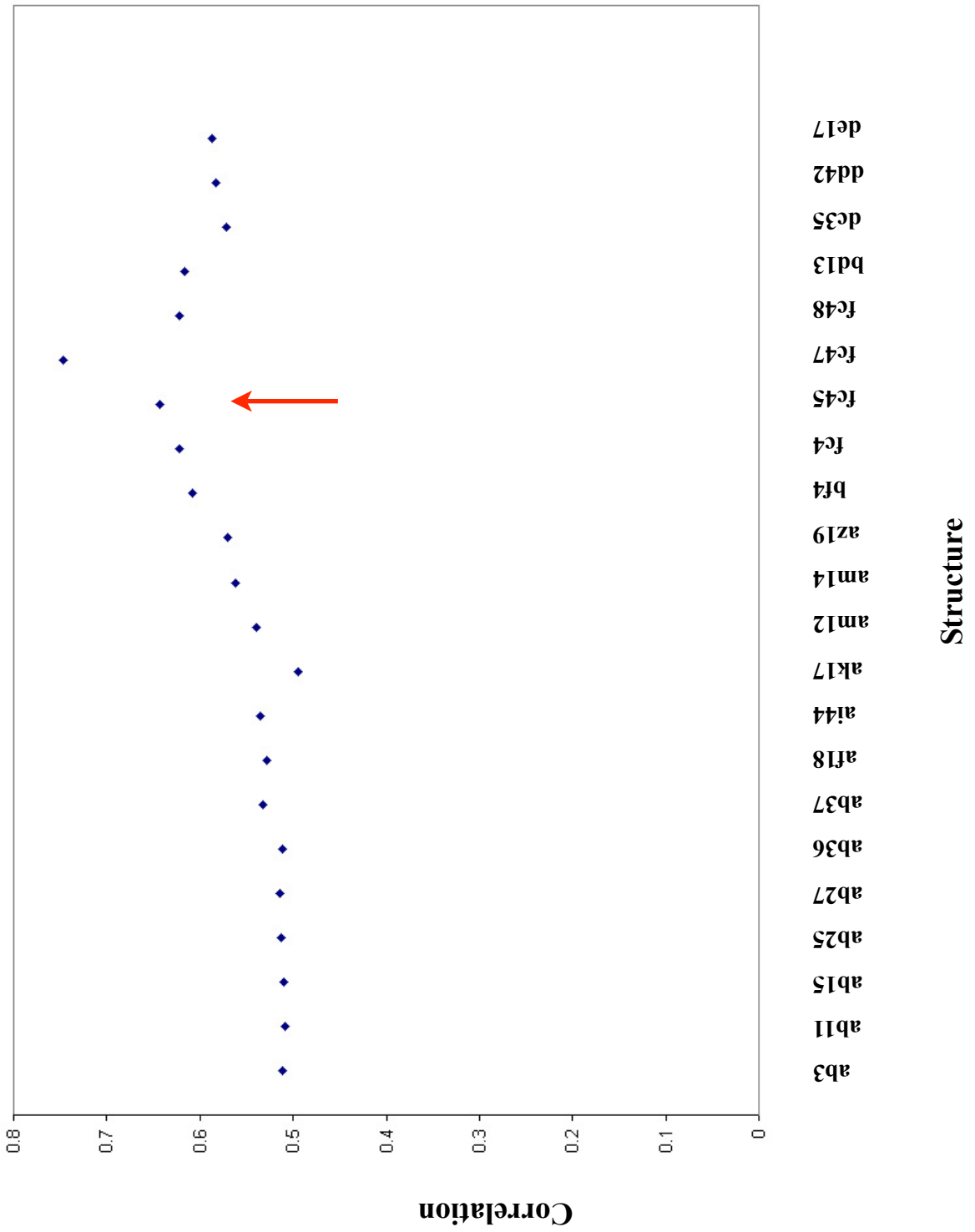

Figure 5.14. Correlation coefficients of all 22 structures against the D5000 data at room temperature. The arrow indicates structure fc45.

5.3 Discussion

Table 5.6. Comparison of the ability of the three methods in automated identification of the correct predicted structure. Values in red denote the difference (modulus of the difference for R_{wp}) between the correct structure and the structure ranked first. If the correct structure ranked first, then the values denote the difference between the correct structure and the next best one (shown in black).

Temperature (K)	***R_{wp}***	***PolySNAP***	***Compare.x***
100	1.8	0.0105	0.0109
150	0.3	0.1405	0.0039
200	0.3	0.2201	0.0103
250	0.5	0.0301	0.0027
293	2.2	0.3206	0.0127
293 (D5000)	4.5	0.1239	0.1035

R_{wp} again failed to identify the correct structure and instead selected top-ranked structures with powder diffraction data bearing little resemblance to that from the correct structure [Appendix A3.2].

With the more temperature-sensitive methods, only lower temperatures were found to correlate well with the predicted structure [Table 5.6]. The reason behind this could possibly be zero point error, and this would also explain why the room temperature data collected from the two different diffractometers gave differing correlation values. As in the case of imidazole, *Compare.x* matched the correct theoretical structure with the three intermediate temperatures.

In comparison with *PolySNAP*, *Compare* again gave higher overall correlation coefficients, and although the discrimination between the highest ranking structure and the structure with the second highest correlation coefficient increased with temperature there was less discrimination between the data when compared with the values obtained from the *PolySNAP* analysis [Figure 5.15]. Notwithstanding the fact that the incorrect structures were identified at higher temperatures, *PolySNAP* correlation values increased with temperature. This further confirms the notion that *PolySNAP* comparative studies are more sensitive to changes in temperature (and the resulting shifts in 2θ) as opposed to *Compare.x*.

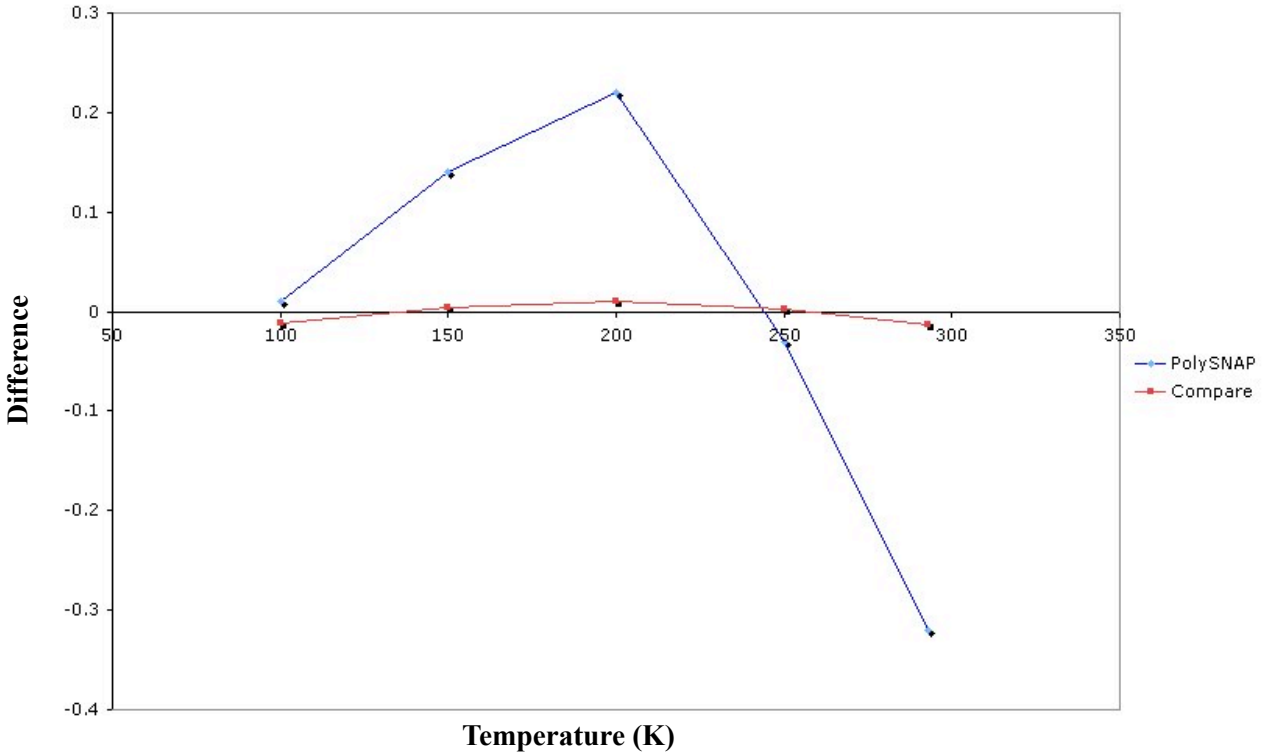

Figure 5.15 Difference in correlation coefficients between fc45 and the structure with the next highest correlation. In cases where fc45 was not ranked first, the difference between fc45 and the structure with the highest correlation is shown.

While *Compare.x* maintained a fairly consistent degree of discrimination over the range of temperatures, *PolySNAP'*s discriminating ability showed a marked sensitivity to temperature up to 200K.

Despite the fact that predictions were carried out at low temperatures, both *PolySNAP* and *Compare.x* analysis resulted in the highest correlation between the correct predicted structure and the experimental data being found at 200K. As in the case of imidazole, this could imply that a zero point error, resulting in a considerable shift in 2θ, may be distorting the results away from the better matches at the expected temperatures. Again, predefining a reliably measurable zero point error before a *PolySNAP* comparison is run would minimise this discrepancy. This can only be done with a reasonably consistent zero point error.

5.4 References

1. Farm Chemical Handbook 2002: Global Guide to Crop Protection, Meister Publishing, Willoughby, OH, 2002.
2. M. Tremayne, L. Grice, C. Pyatt, C. C. Seaton, B. M. Kariuki, H. H. Y. Tsui, S. L. Price and J. C. Cherryman, *J. Am. Chem. Soc.*, 2004, **126**, 7071
3. D. Britton, *Cryst. Struct. Commun.,* 1981, **10**, 1501
4. J. P. Lommerse, A. J. Stone, R. Taylor and F. H. Allen, *J. Am. Chem. Soc.*, 1996, **118**, 3108
5. G. R. Desiraju and R. L. Harlow, *J. Am. Chem. Soc.*, 1989, **111 (17)**, 6757
6. G. M. Day, S. L. Price and M. Leslie, *Cryst. Growth Des*., 2001, **1**, 3
7. D. Britton, *Acta Cryst. B,* 2002, **58**, 553

6. 5-AZAURACIL

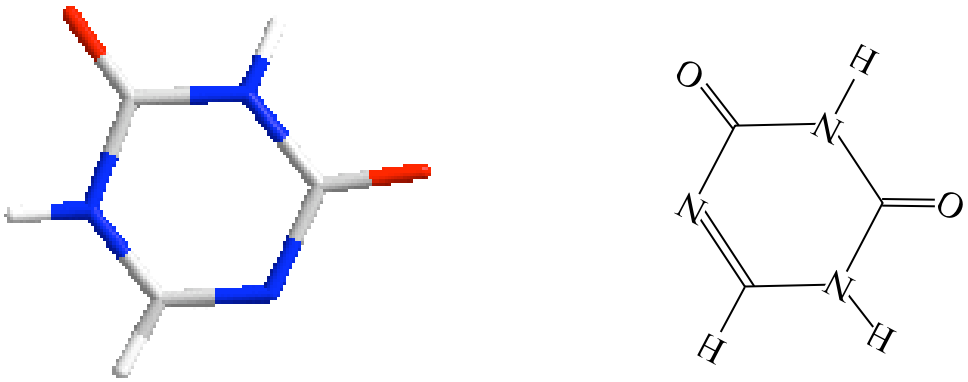

Figure 6.1. 5-Azauracil (1,3,5-triazine-2,4(1H,3H)-dione)

6.1 Background

5-Azauracil, a white crystalline colourless solid, is the aza analogue of the pyrimidine uracil, one of the bases found in ribonucleic acid (RNA). Azapyrimidines (for example 5-azauracil and its isomer 6-azauracil) differ from the nucleic acid bases in that they have a nitrogen instead of a carbon atom at some position on the heterocyclic ring. When introduced at a strategic location on the ring, this apparently minor change causes major electronic perturbation in the vicinity of the substitution thus changing the structural, physico-chemical, and subsequently biological properties of the base.

Purine and pyrimidine analogues (especially aza analogues of uracil[1,2]) are of particular interest due to their potential uses as antineoplastic agents[3,4] and enzyme inhibitors[5]. They also exhibit bacteriostatic and fungicidal[6,7] properties, and can be used in molecular biology protocols[8] and as reagents for mutagenicity testing in microbial systems[9].

5-Azauracil is of significant biological importance as it is a specific inhibitor of orotate phosphoribosyl transferase, an enzyme involved in nucleic acid synthesis *in vivo*. Its biological effects differ significantly from those of other closely-related azapyrimidines, such as 6-azauracil[10].

6.1.1 Crystal Structure

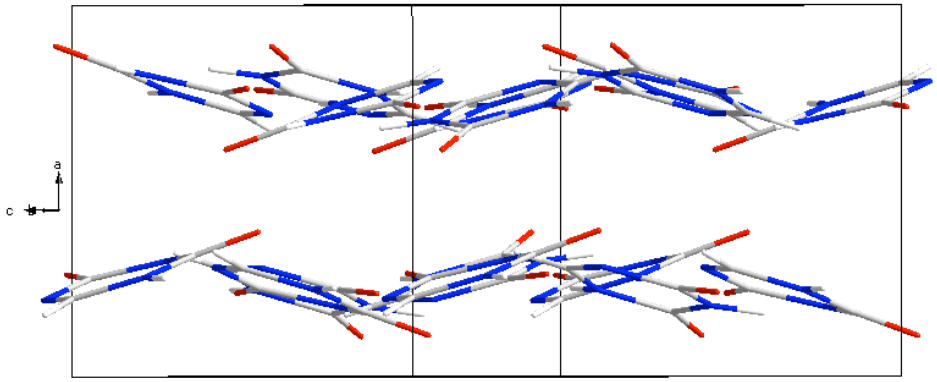

Figure 6.2. 5-Azauracil molecules forming chains along the b axis.

The crystal structure of 5-azauracil was determined from X-ray diffraction data at room temperature[10]. It has the orthorhombic spacegroup *Pbca*, with 8 molecules in the unit cell. Both the heterocyclic nitrogen and its neighbouring carbonyl group can accept hydrogen bonds giving the material a propensity to form sheets. The crystal structure [Figure 6.2] consists of crinkled layers held together by strong NH----O and NH----N hydrogen bonds and several weaker intermolecular interactions. These sheets are approximately perpendicular to the *a* axis and are stacked so that there is very minimal overlap of the molecules between the layers [Figure 6.3]. Unit cell parameters for 5-azauracil are given in Table 6.2.

6.1.2 Crystal Structure Prediction

If a crystal structure is predictable to a useful extent[11], then any structurally-related molecule should, in theory, also be "predictable". 5-Azauracil is an isomer of 6-azauracil, a molecule that had already been investigated computationally[12]. This situation prompted a blind test to assess the methodology employed in finding probable packings of rigid molecules with a choice of hydrogen donors and acceptors.

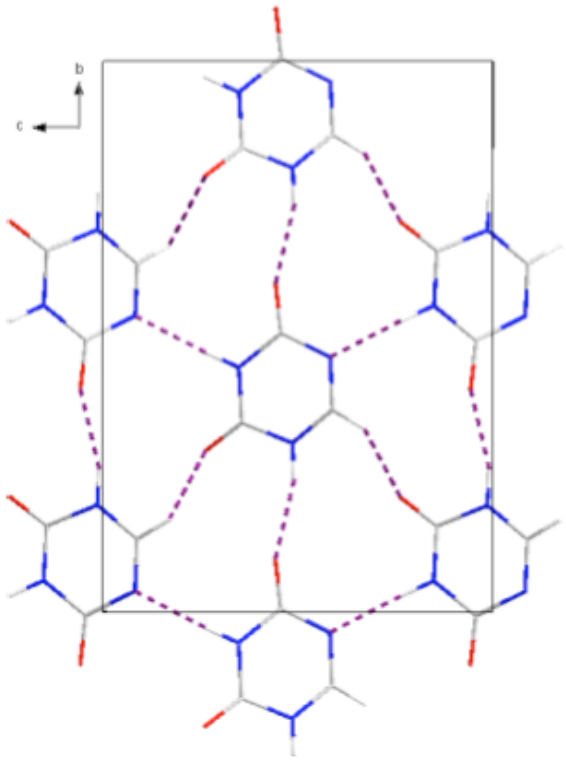

Figure 6.3. A view of 5-azauracil down the a axis.
(Hydrogen bonds NH...N are shown by the dotted lines in violet.)

The prediction of the structure of 5-azauracil was carried out given that the computational search for 6-azauracil resulted in numerous distinct structures[12], including some with different atoms involved in the hydrogen bonding, and lying within 1 kJmol^{-1} of the global minimum. The search for 5-azauracil was therefore expected to result in a lattice energy plot with the known structure among a group of thermodynamically plausible structures.

The first search carried out in 1999 yielded 42 structures[10], and a more recent and extensive search (carried out by Price et al in 2004)[13] resulted in 49 theoretical structures, with the lower energy structures corresponding to those obtained in the earlier search [Figure 6.4 and Table 6.1].

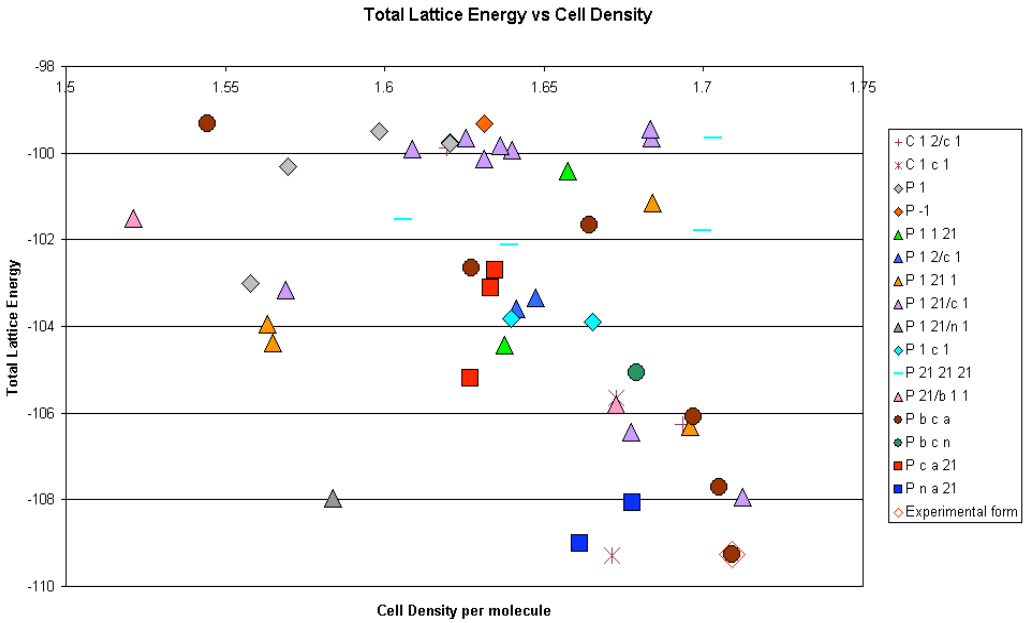

Figure 6.4 The distribution of the lowest energy structures found in a search for minima in the lattice energy of 5-azauracil. The minimum corresponding to the known crystal structure is denoted by the red open rhombus. Reproduced from the CPOSS database.

Table 6.1. Unit cell parameters of the seven lowest energy predicted structures for 5-Azauracil.

	Space Group	E_{latt} (kJ mol $^{-1}$)	*a* (Å)	*b* (Å)	*c* (Å)	*β* (°)
da92	*Cc*	-109.28	3.731	13.405	9.730	112.55
cb2	*Pbca*	-109.25	6.824	13.897	9.269	90.00
au87	$Pna2_1$	-109.00	13.964	3.602	8.988	90.00
au58	$Pna2_1$	-108.06	12.400	3.791	9.523	90.00
am8	$P2_1/n$	-107.97	5.031	9.638	9.893	98.66
ai37	$P2_1/c$	-107.93	9.565	7.351	9.790	39.58
cb7	*Pbca*	-107.71	7.333	9.812	12.246	90.00

All seven low energy structures of 5-azauracil are variations on the same hydrogen bonded sheet, with some appearing flatter than others and exhibiting different stacking. The presence of the same hydrogen bonding motif implies that the structures could have many macroscopic properties in common. Once thermal motion was included in the prediction calculation it would be probable that some of the low-energy structures would transform into others. Consequently,

this predicts that it is unlikely that polymorphs of 5-azauracil having very different physical properties would be readily found. Predicted structure da92, which has almost the same energy as the experimentally known form, is polar. The crystal dipole correction term is likely to destabilise this structure, leaving the known structure as the most stable. Cb2 is the correct predicted structure, and it corresponds with the experimentally known form.

6.2 Results

6.2.1 Low Temperature Data

On visual comparison, the powder pattern collected at room temperature is similar to the simulated patterns from both the published structure and the correct predicted structure cb2 [Figure 6.5 and Table 6.2]. Initially, a LeBail fit was carried out on the room temperature data using the unit cell parameters from the published structure as a starting point. Subsequent LeBail fits were carried out on the remainder of the data obtained using the same methodology. Although the unit cell volume decreased with temperature, there was a marked difference between the volume of the published structure which was collected at room temperature, and the volume of the structure obtained experimentally at the same temperature. For this reason, all the data obtained over the range of temperatures were indexed, and LeBail fits were subsequently carried out on the indexed data. The volume of the unit cell obtained from the data at room temperature after indexing was very close to the volume of the published structure. Consequently the indexed data were used for the rest of this study.

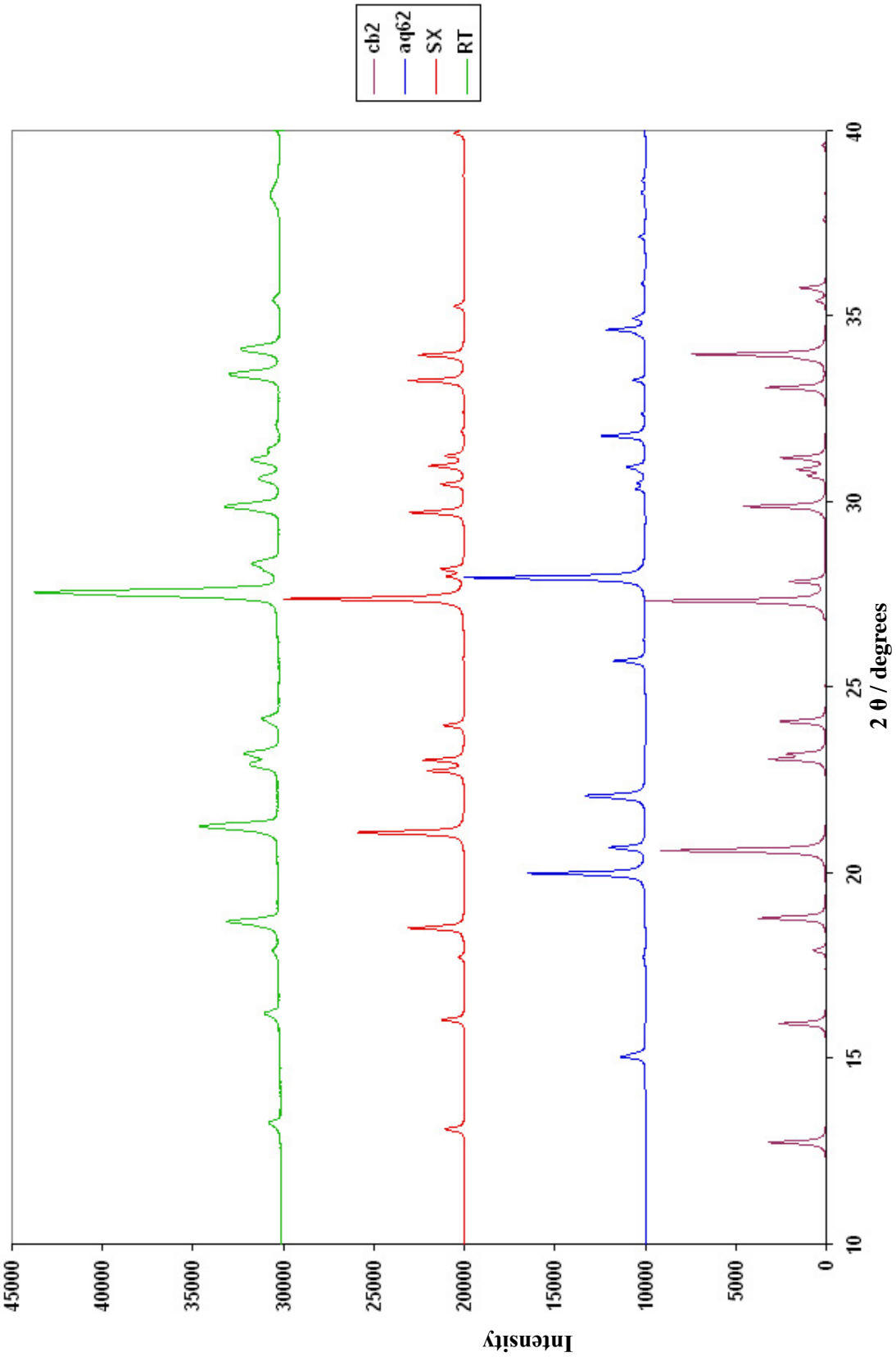

Figure 6.5 Simulated powder patterns for the published single crystal (SX) structure, the correct predicted structure cb2, predicted structure aq62, and the D5000 experimental data recorded at room temperature (RT).

Table 6.2 Unit cell parameters of the published crystal structure, correct predicted structure and those extracted from the experimental data over a range of temperatures. The numbers in brackets denote the percentage change with respect to those values obtained from the 10K data.

Temperature (K)	***a (Å)***	***b (Å)***	***c (Å)***	***Volume (Å^3)***
Published values (298K)[10]	6.514 (3)	13.522 (4)	9.582 (4)	843.96 (6)
Predicted values (0K)	6.824	13.897	9.269	879.01
10	6.385 (1) *(0.00)*	13.513 (3) *(0.00)*	9.547 (1) *(0.00)*	823.78 (1) *(0.00)*
100 ***(% change)***	6.398 (1) *(+0.21)*	13.523 (2) *(+0.07)*	9.560 (1) *(+0.13)*	827.12 (4) *(+0.40)*
150 ***(% change)***	6.425 (1) *(+0.63)*	13.487 (1) (-0.20)	9.549 (3) *(+0.02)*	827.48 (1) *(+0.45)*
200 ***(% change)***	6.433 (1) *(+0.75)*	13.491 (3) *(-0.16)*	9.575 (1) *(+0.02)*	828.76 (2) *(+0.60)*
250 ***(% change)***	6.490 (1) *(+1.65)*	13.526 (1) *(+0.09)*	9.579 (2) *(+0.29)*	840.57 (1) *(+2.04)*
293 ***(% change)***	6.514 (3) *(+2.02)*	13.513 (1) *(-0.01)*	9.646 (1) *(+0.33)*	843.09 (2) *(+2.34)*
293 (D5000)	6.513 (3) (+2.00)	13.512 (2) (-0.01)	9.575 (2) (+0.29)	842.65 (3) (+2.29)

The powder diffraction patterns indicate a clear contraction in the unit cell with decreasing temperature, as shown by the clear shift in peak position (200) towards the right [Figure 6.6]. This change can be observed over the range of 5 to 45 degrees along 2θ for the full set of experimental data in Appendix A4.1. The percentage differences in *a*, *b*, *c* and volume with varying temperature were calculated and as expected, the volume decreased with lower temperatures. Values for *a* also decreased uniformly while *b* and *c* fluctuated to accomodate this contraction. Over the temperature range studied, the unit cell volume would be expected to increase as a result of thermal expansion. Although *b* and *c* exhibited atypical fluctuations, these changes in the lattice parameters still resulted in an overall expansion of the unit cell with temperature, as indicated by the increase in volume [Figure 6.7].

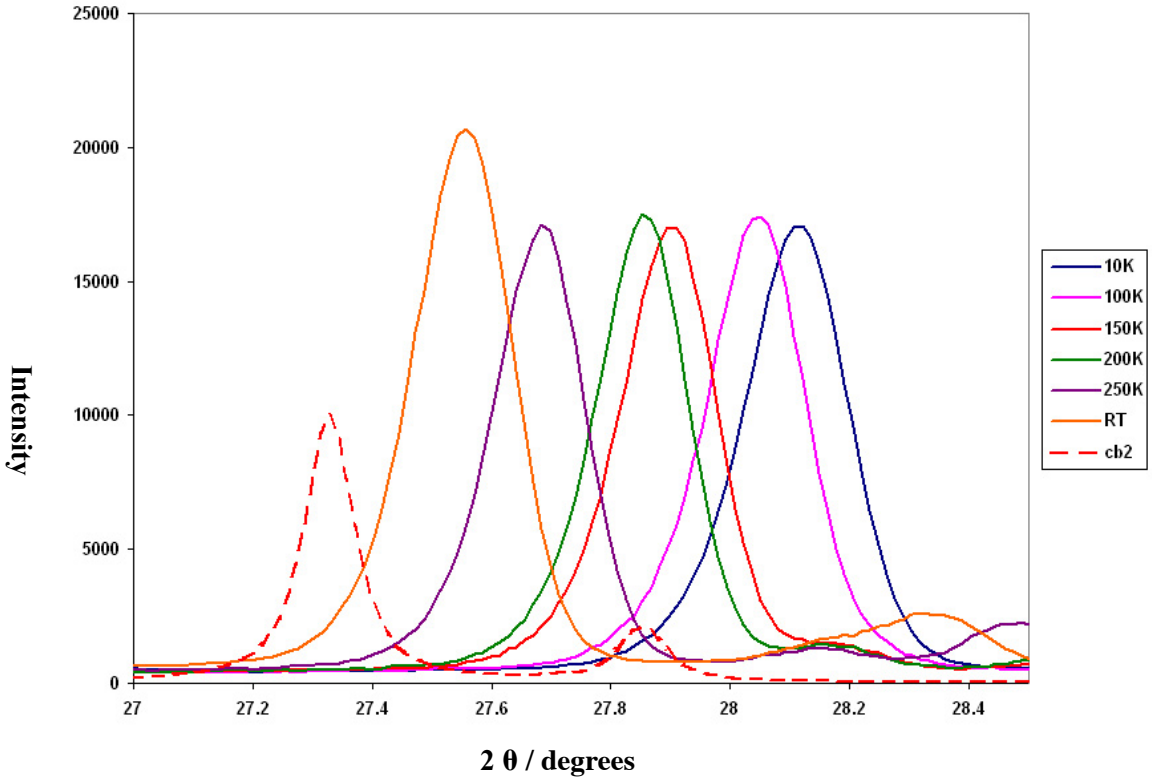

Figure 6.6 Section of superimposed powder diffraction data at all temperatures showing peak (200) shifting towards the right with decreasing temperature. The predicted structure (cb2) is indicated by the red dotted line.

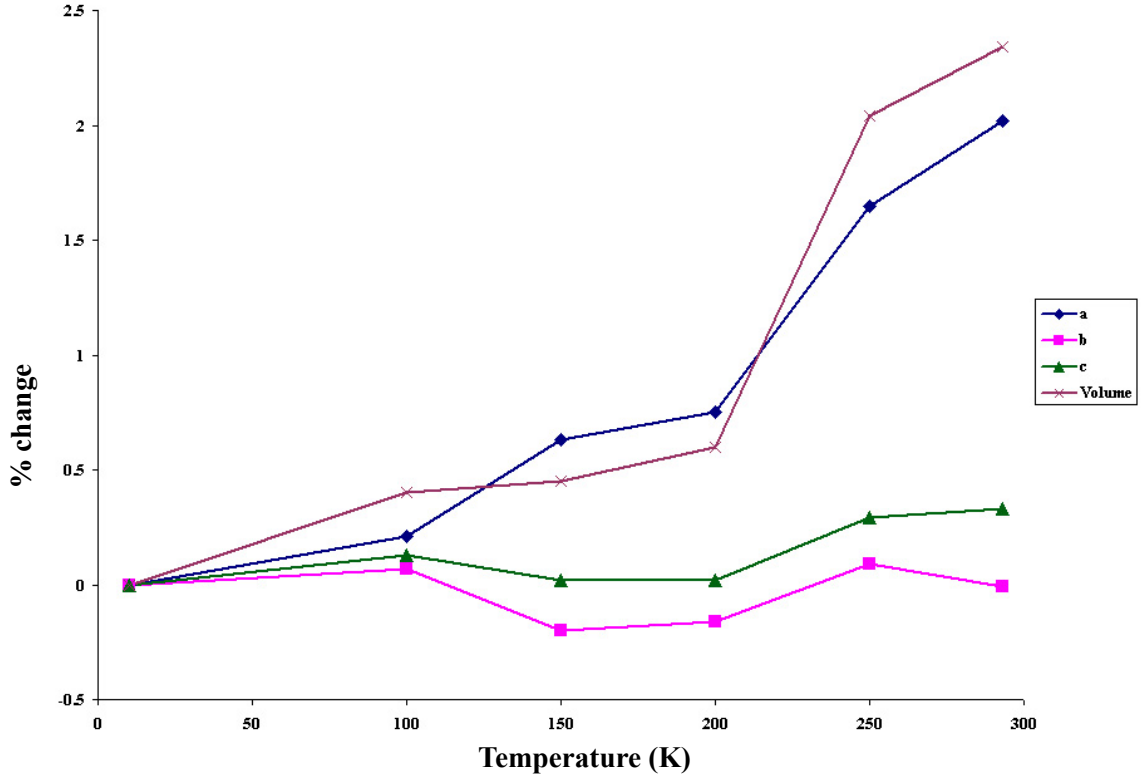

Figure 6.7 Graph showing the percentage change in unit cell dimensions with temperature.

6.2.2 Automated Comparison

6.2.2.1 R_{wp}

The 49 predicted structures were each compared, using R_{wp}, with the experimental data collected at each temperature. The outcome of these comparisons was again non-discriminatory, with none of the structures singled out as being significantly similar to any of the experimental data. R_{wp} values ranging from 59.5% to 78.6% were obtained, although in most cases, no significant discrimination was found [Table 6.3, Figure 6.8]. None of the predictions were ranked as the best fit to data recorded at two different temperatures. The correct predicted structure (cb2) was not identified by R_{wp} as having a similar powder pattern to the data collected at any of the temperatures. The simulated pattern for structure aq62, which ranked first at room temperature, does not match the corresponding experimental powder pattern [Figure 6.5]. The simulated patterns for all predicted structures shown in the table and the corresponding experimental patterns are found in Appendix A4.2.

Table 6.3. The structure with lowest R_{wp} identified at each temperature. The difference is that between the R_{wp} for the top ranked structure [$R_{wp}(x)$] and the correct prediction [$R_{wp}(cb2)$]. Red numbers denote incorrect structures ranked as the best.

Temperature (K)	*Top ranked structure*	*R_{wp} (x) (%)*	*R_{wp} (cb2) (%)*	*Difference (%) [$R_{wp}(x)$ - $R_{wp}(cb2)$]*
10	ad62	75.1	77.1	-2
100	au87	72.1	73.2	-1.1
150	ak85	70.6	71.7	-1.1
200	ay98	66.7	69.4	-2.7
250	bh51	66.1	67.7	-1.6
293	aq62	59.5	61.8	-2.3
D5000 (293K)	cb117	57.3	59.2	-1.9

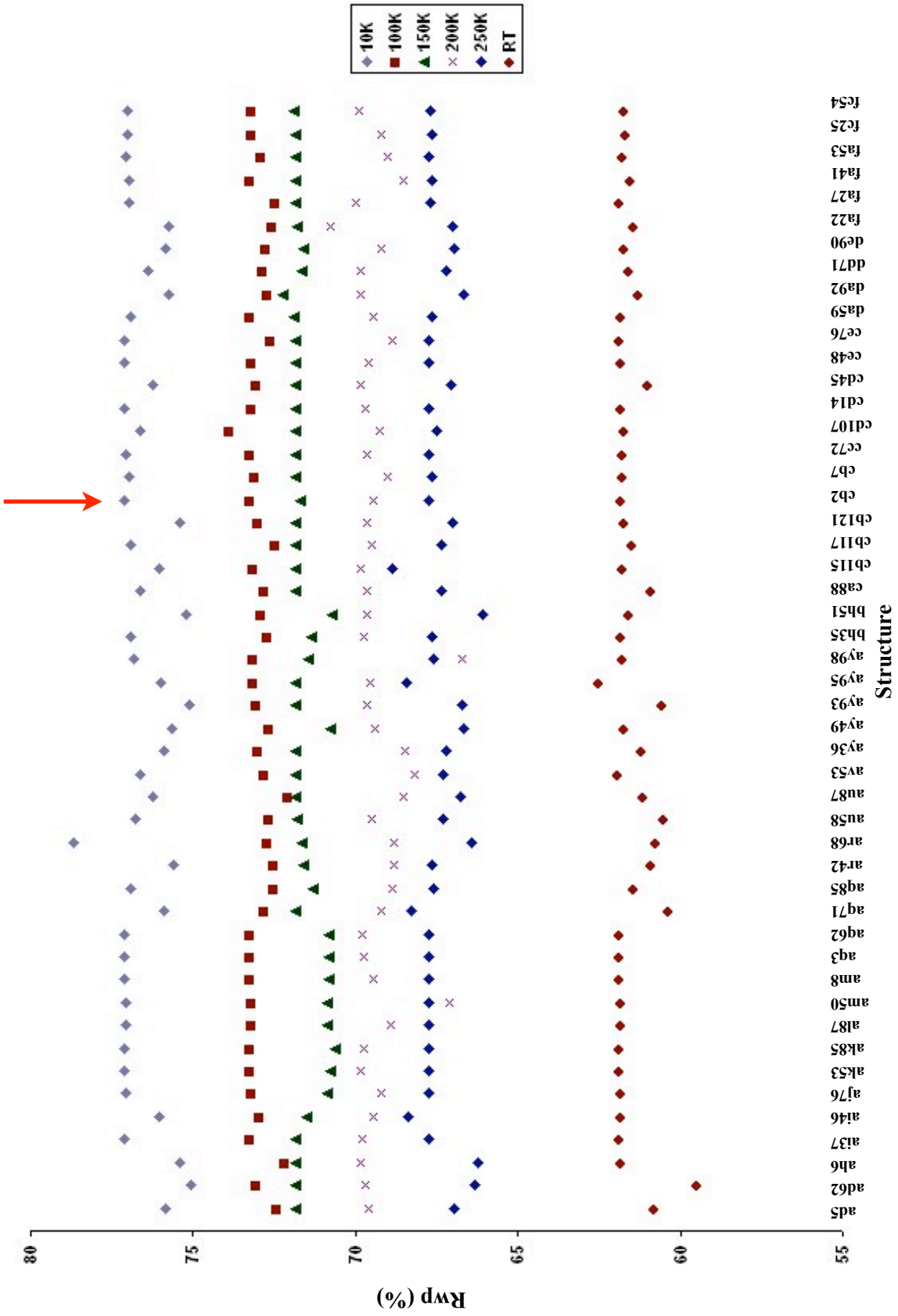

Figure 6.8 R_{wp} values for each predicted structure at each temperature (D5005). The arrow indicates structure cb2.

6.2.2.2 PolySNAP

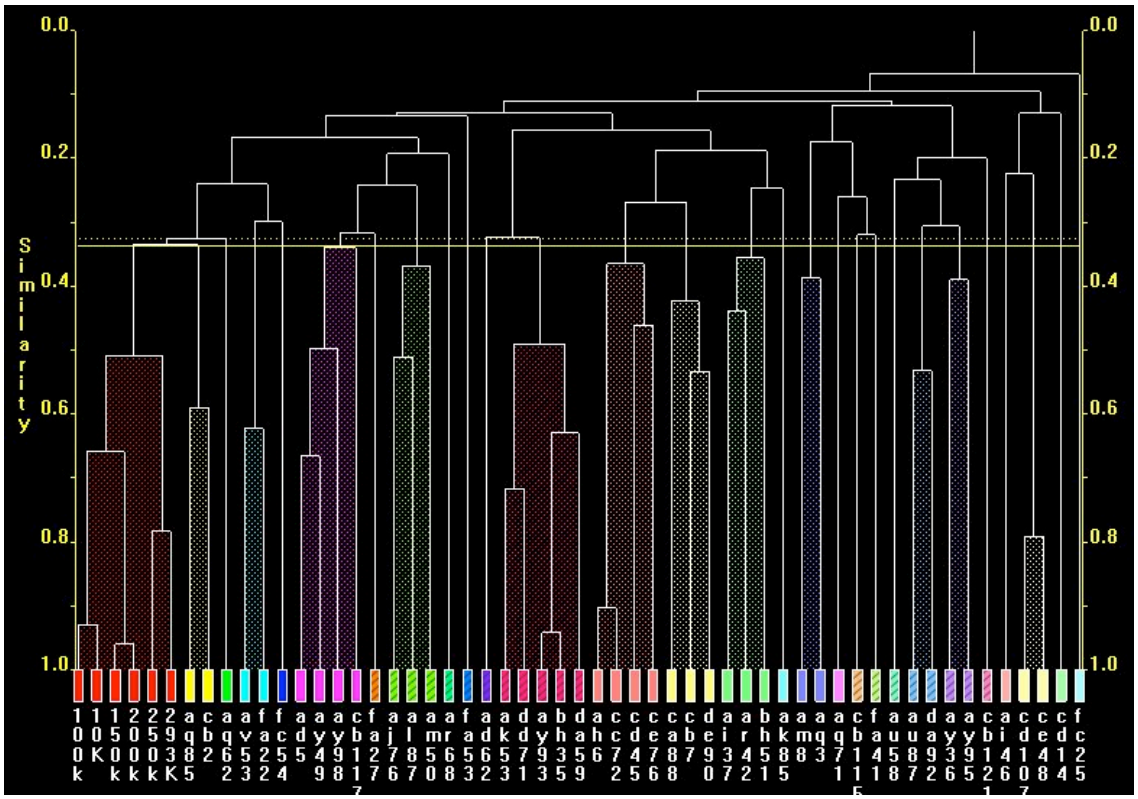

Figure 6.9. Dendrogram showing similarity clusters for 5-azauracil predicted and experimental powder patterns

For PolySNAP analysis, the data collected on the different diffractometers were analysed separately due to the difference in wavelength between the two machines. In the dendrogram above, all 49 predicted structures are compared with the D5005 data [Figure 6.9]. Structures cb2 and aq85 were grouped as most similar to the experimental data collected at all temperatures, and slightly lower on the similarity scale is structure aq62. Once again, although all experimental data sets were grouped together, there is clear clustering into paired subsets with the lower temperature data pair (10K and 100K) being ranked as more similar to each other than the next highest. On analysis of each temperature separately and consideration of the structure with the highest correlation in each case, structure aq85 was ranked as the most similar to the experimental data at 10K and 100K, while structure cb2 was identified as a match at temperatures of 150K and above [Table 6.4].

Table 6.4. Structures with highest correlation coefficient [P(x)] at each temperature, and the difference to the value obtained for the correct structure [P(cb2)]. If P(cb2) = P(x), then the difference between P(cb2) and the next best structure is taken. An incorrect match gave a negative difference, as shown by the values in red.

Temperature (K)	***Top ranked structure***	***Correlation coefficient of top ranked structure***	***Correlation coefficient***	***Difference [P(cb2) - P(x)]***
10	aq85	0.616	0.220 (cb2)	-0.396
100	aq85	0.576	0.222 (cb2)	-0.354
150	cb2	0.509	0.367 (fa22)	+0.142
200	cb2	0.477	0.336 (aq85)	+0.141
250	cb2	0.389	0.367 (fa22)	+0.022
293	cb2	0.377	0.372 (fc54)	+0.005
D5000 (293K)	cb117	0.279	0.146 (cb2)	-0.133

On analysis of the corresponding correlation coefficients at the higher temperatures, two other structures (fc54, with a correlation value of 0.372 at 293K, and fa22 with a correlation value of 0.367 at 250K) could be considered to be placed significantly higher than the rest, with fc54 only differing by a correlation value of 0.005 from structure cb2 [Figure 6.10]. However, on visual comparison of the respective powder diffraction patterns it was clear that neither of these two patterns bear a great similarity to the experimental data or cb2 [Figure 6.12]. The powder pattern of the structure having the highest correlation coefficients when compared with the experimental data at the lower temperatures 10K and 100K was found to differ significantly from these data, on visual comparison [Appendix A4.3].

The degree of similarity between the predicted structure cb2 and the experimental data decreased with increasing temperature, as did the difference between the correlation value of the correct structure (ranked first) and the next best structure [Figures 6.10 and 6.11 and Table 6.4]. Hence discriminatory ability in this case decreased with increasing temperature. This was not the case in any of the other examples, where the best fit was obtained at low temperatures. One possible reason is that the predictions were carried out taking thermal expansion into consideration. Possible over-compensation would then justify the larger volume of the predicted structure when compared with the experimental volume at room temperature.

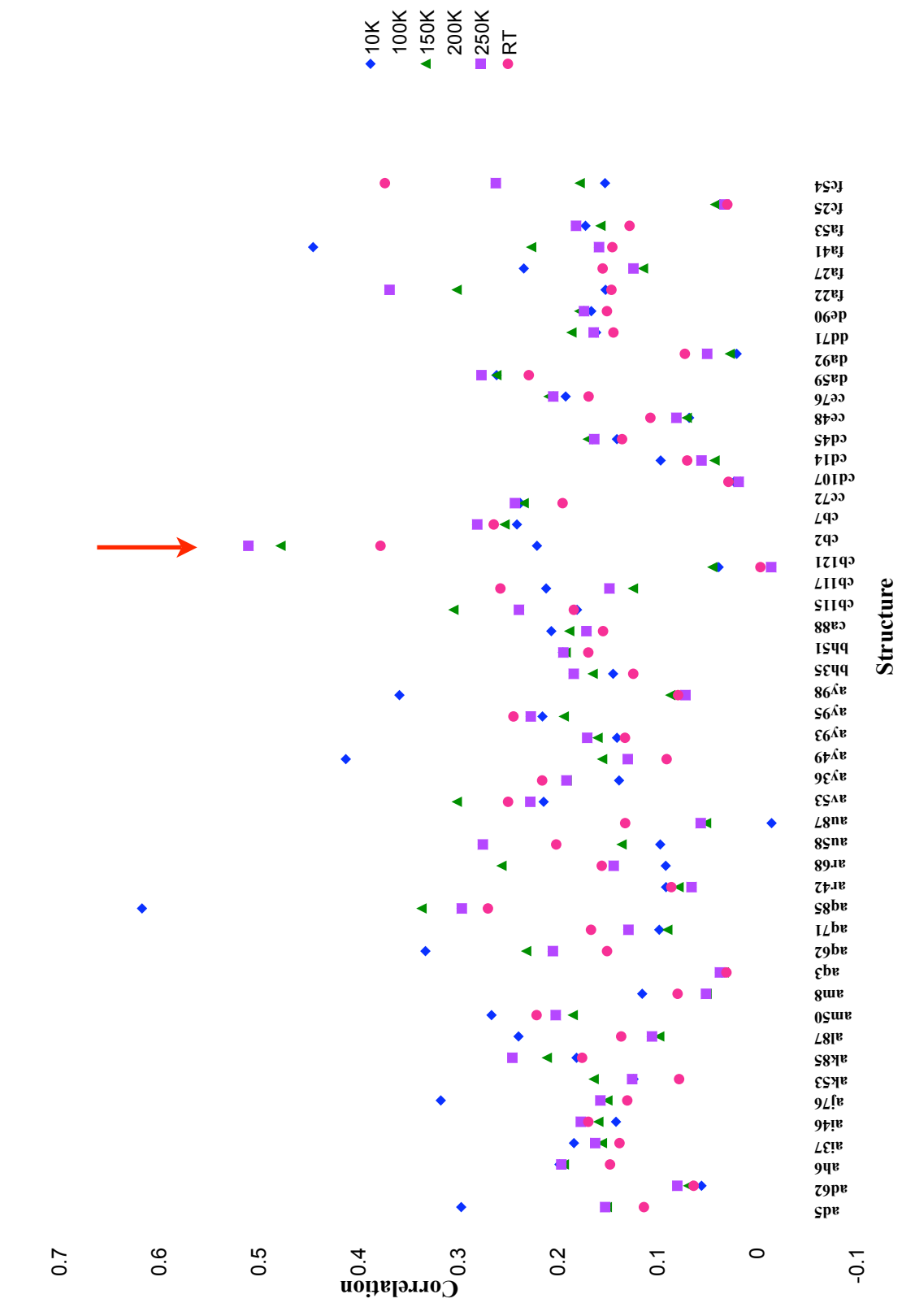

Figure 6.10 Correlation coefficients of all 49 structures at each temperature (D5005). The arrow indicates structure cb2.

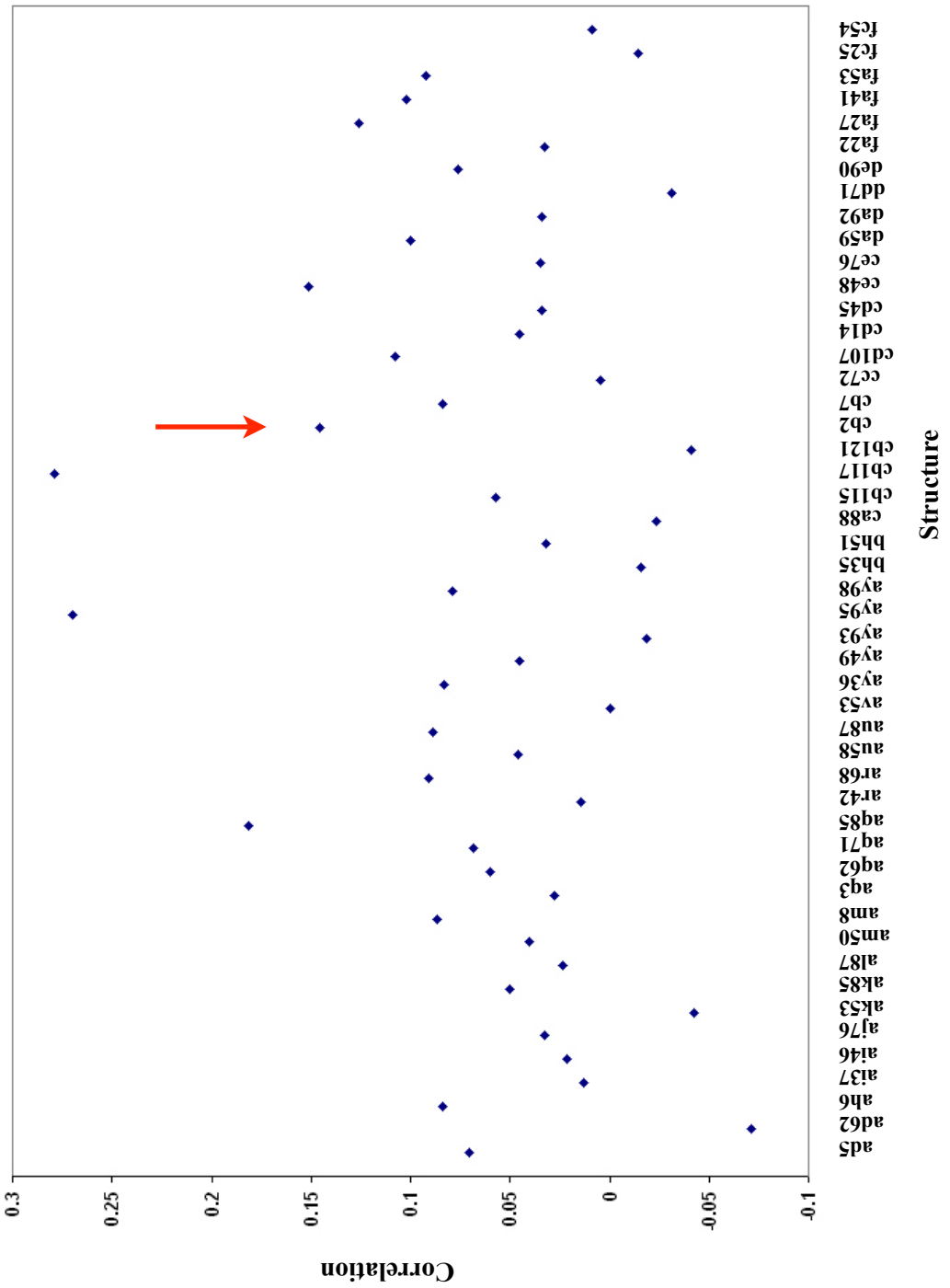

Figure 6.11 Correlation coefficients of all 49 structures against the D5000 data. The arrow indicates structure cb2.

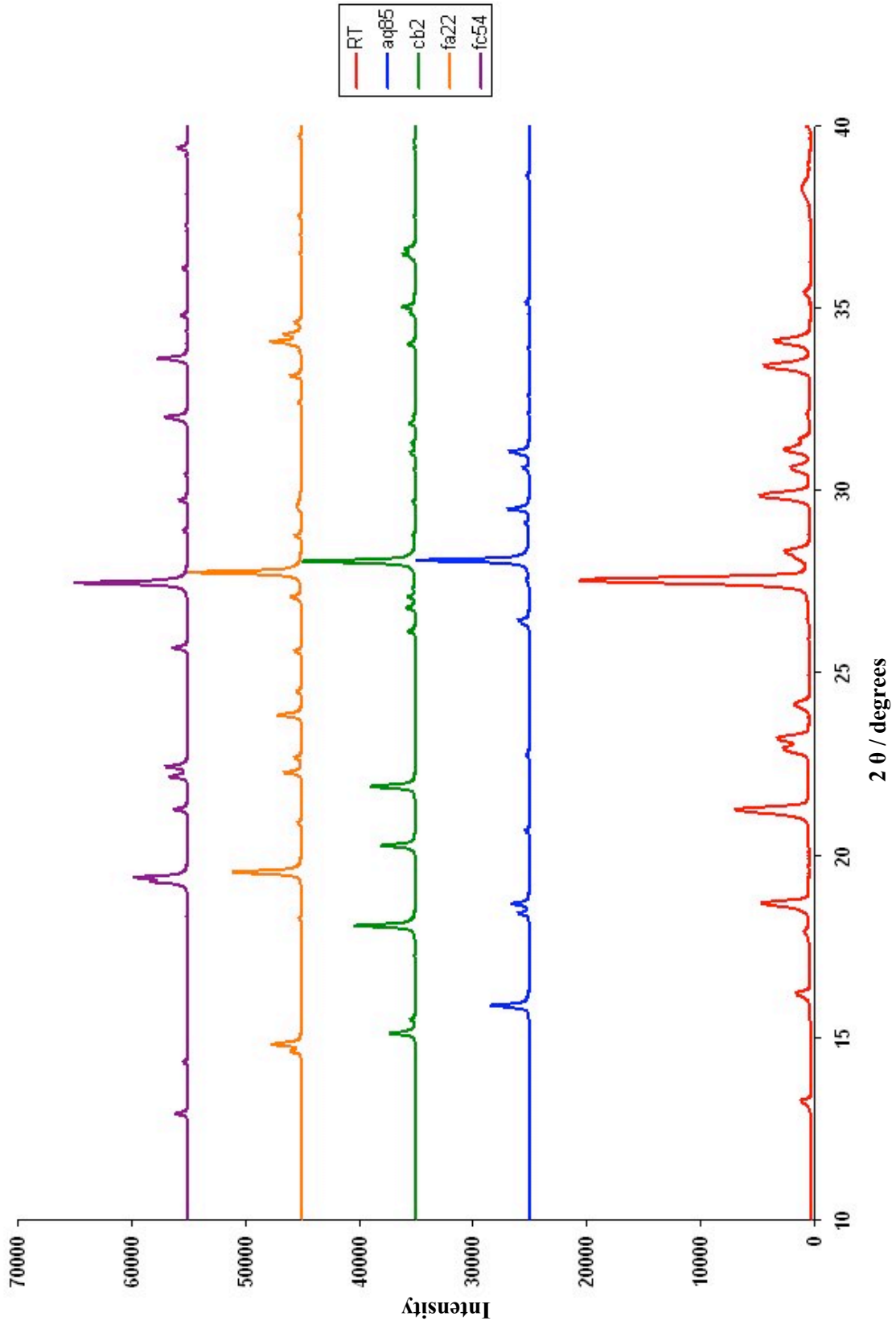

Figure 6.12 Powder diffraction patterns for four selected predicted structures and the experimental structure at room temperature (D5005).

6.2.2.3 Compare.x

Using a default triangle window value of 2, *Compare* identified the correct structure cb2 at intermediate temperatures of 150K, 200K and 250K. While at lower temperatures structure fa41 ranked highest, the room temperature data collected on the D5005 had the greater correlation with structure cb117, while that obtained with the D5000 was matched with structure fa53. The correct structure cb2 did not rank second in any of the cases. On visual comparison with the respective experimental data, there are some areas of similarity with the structures selected at either end of the temperature spectrum, however they are clearly not the same structure [Table 6.5, Figures 6.13 - 6.17, Appendix A4.4].

Table 6.5. Structures with highest correlation coefficient [C(x)] at each temperature, and the difference to the value obtained for the correct structure [C(cb2)]. Black numbers denote cases when the correct structure was identified, and the difference was positive. An incorrect match gave a negative difference, as shown by the values in red.

Temperature (K)	*Top ranked structure*	*Correlation coefficient of top ranked structure*	*Correlation coefficient*	*Difference [C(cb2) - C(x)]*
10	fa41	0.855	0.827 (cb2)	-0.028
100	fa41	0.856	0.838 (cb2)	-0.018
150	cb2	0.861	0.857 (ar68)	0.004
200	cb2	0.866	0.857 (au58)	0.009
250	cb2	0.875	0.860 (au58)	0.015
293	cb117	0.889	0.872 (cb2)	-0.017
D5000	fa53	0.748	0.687 (cb2)	-0.061

Although the default triangle window value of 2 was selected for this work, a variety of triangle windows ranging from 0.5 to 4.0 in increments of 0.5 were tested using this data [Appendix A4.4, Tables A4.4.1 - A4.4.8]. As expected, the narrower the window, the more dissimilar the structures were considered to be, whereas when wider windows were used, higher correlation values resulted from too much flexibility within the comparison parameters.

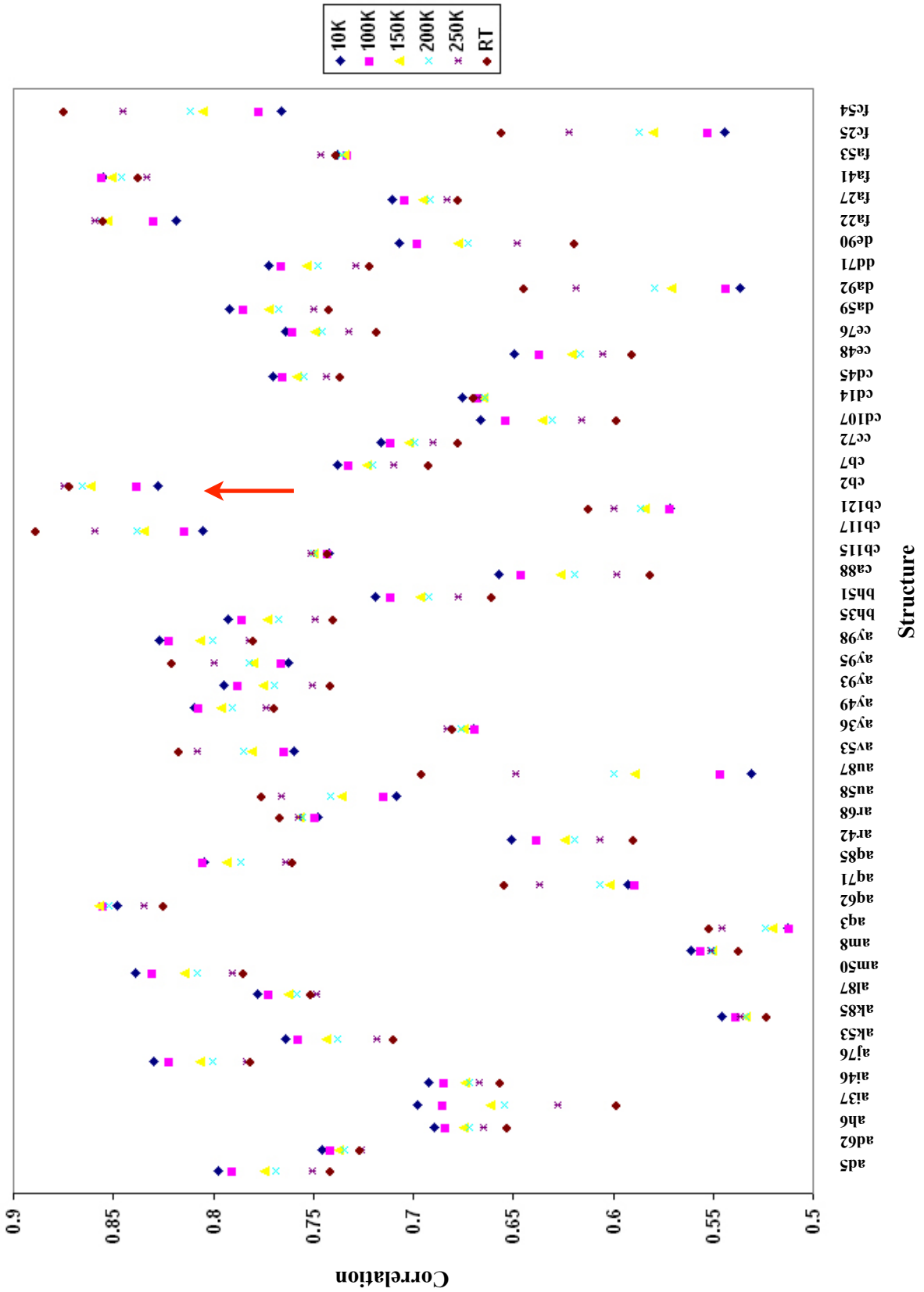

Figure 6.13 Correlation coefficients of all 49 structures at each temperature. The arrow indicates structure cb2.

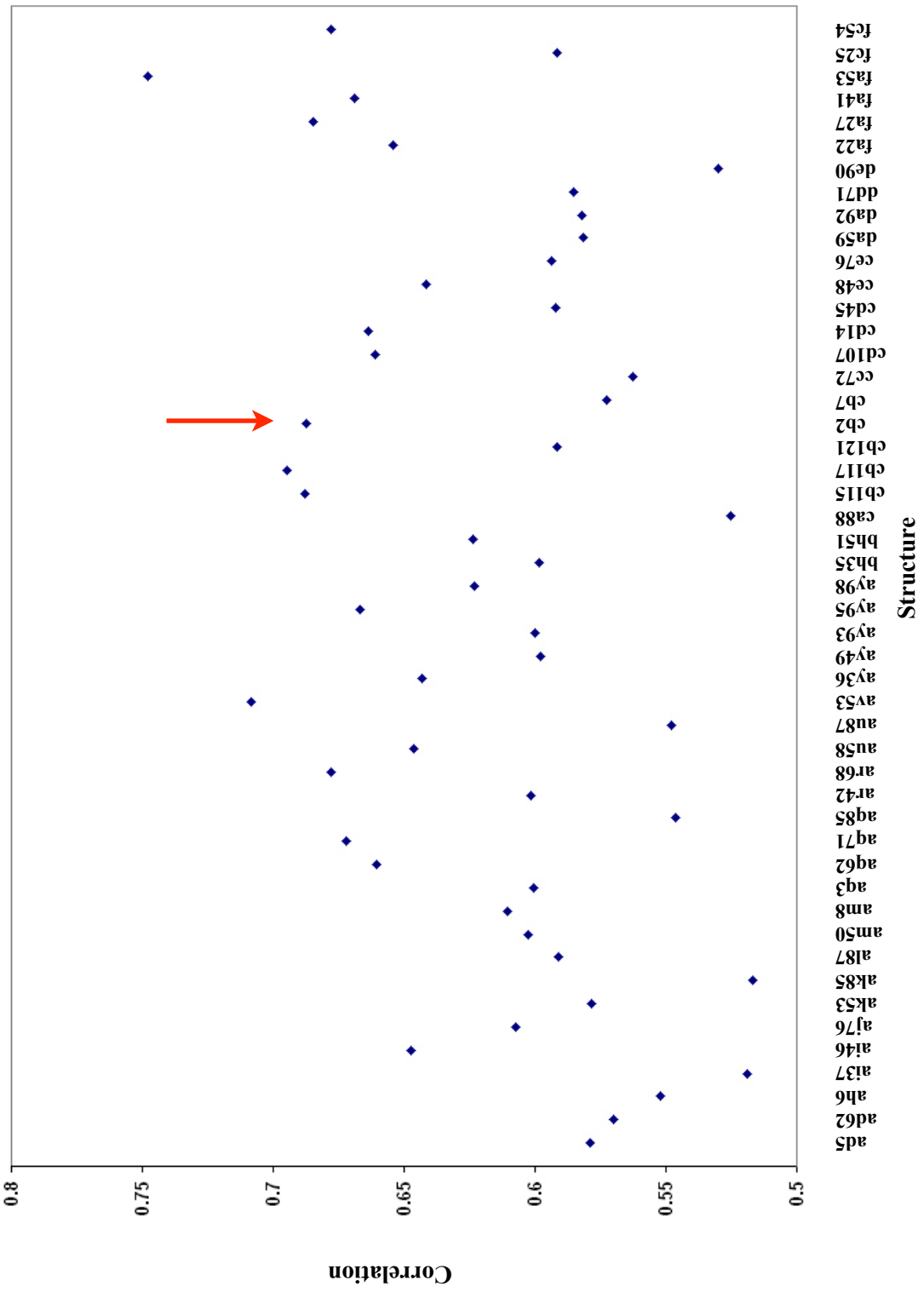

Figure 6.14 Correlation coefficients of all 49 structures against the D5000 data. The arrow indicates structure cb2.

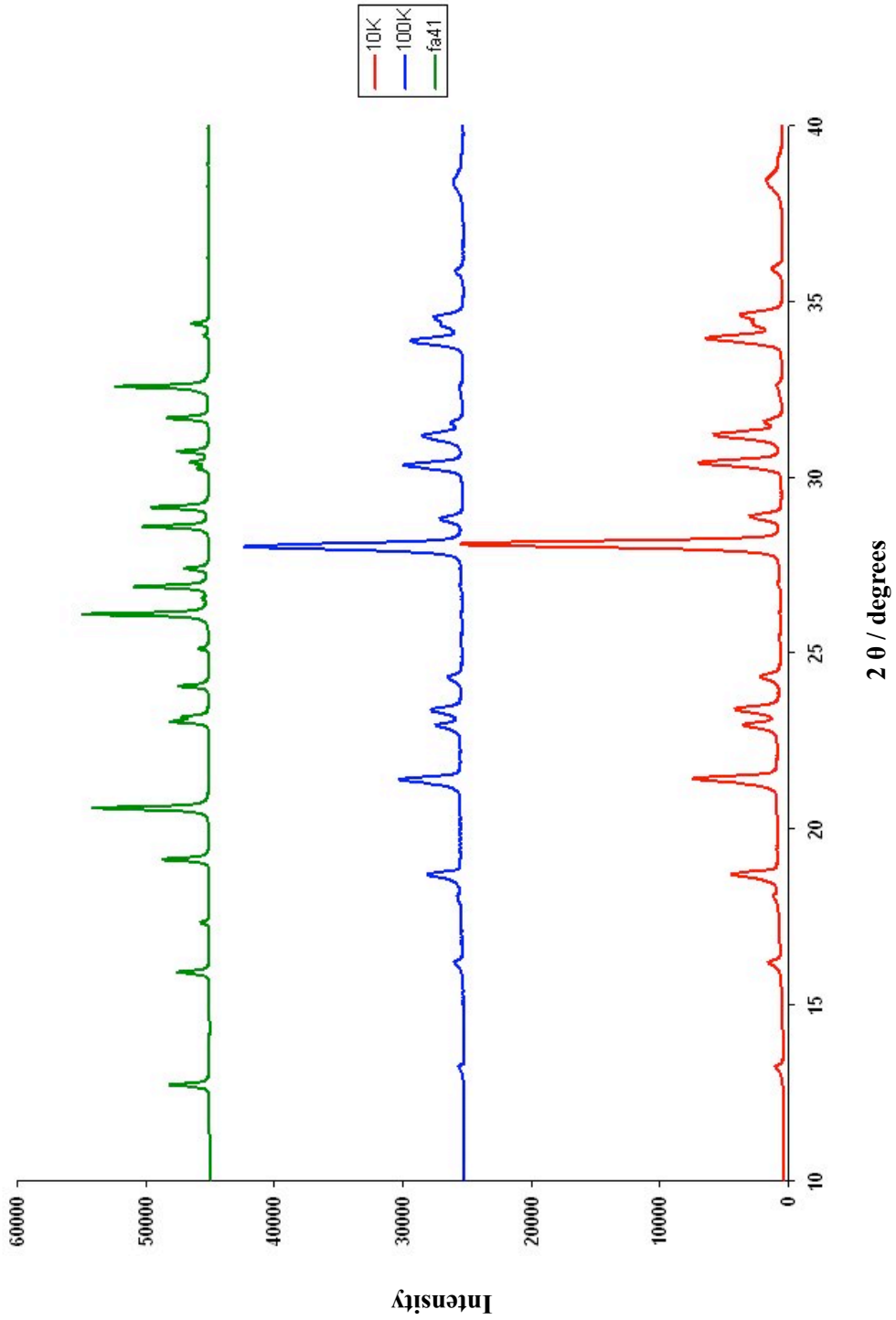

Figure 6.15 Powder diffraction patterns for fa41 and the experimental structure at 10K and 100K.

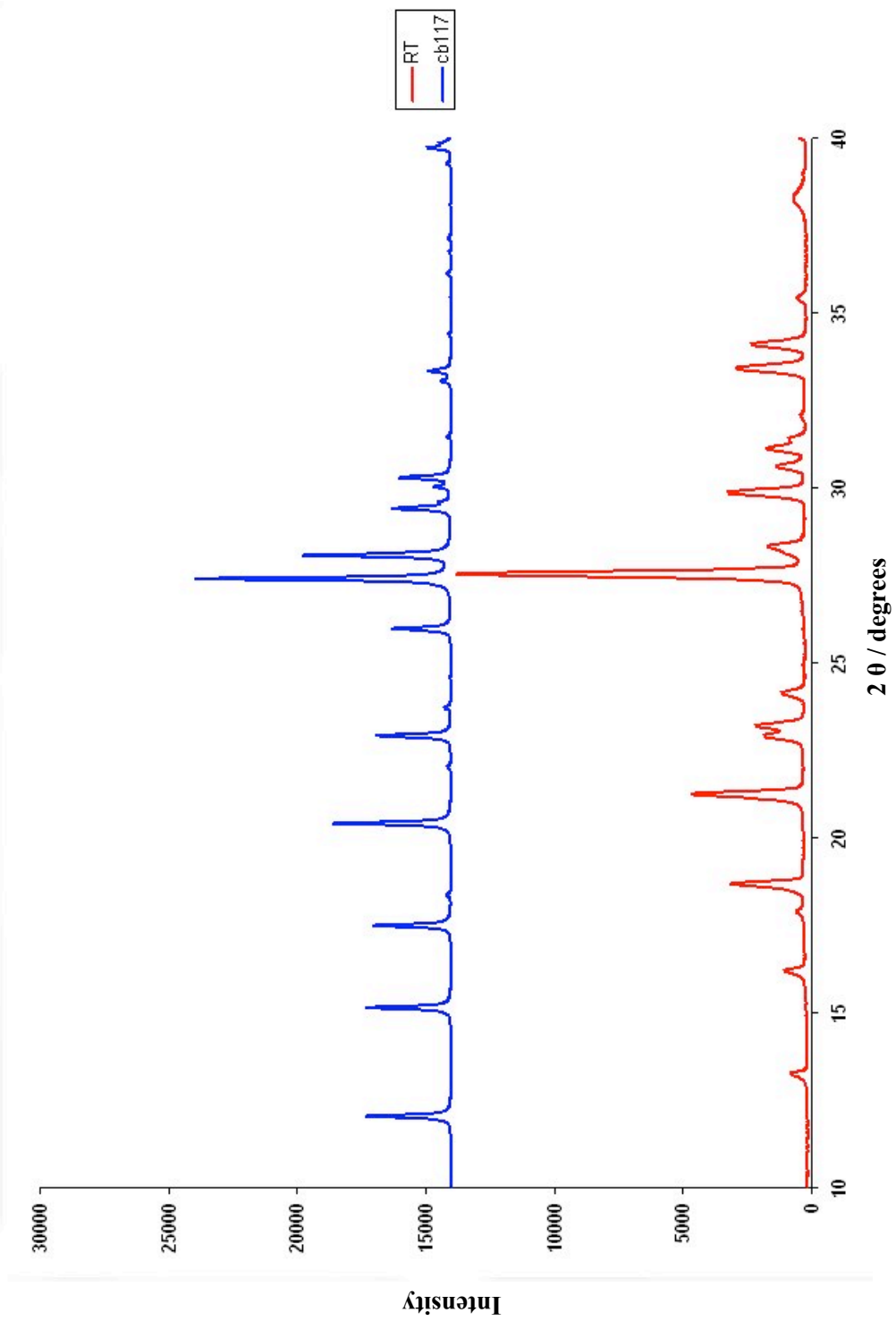

Figure 6.16 Powder diffraction patterns for cb117 and the experimental structure at room temperature.

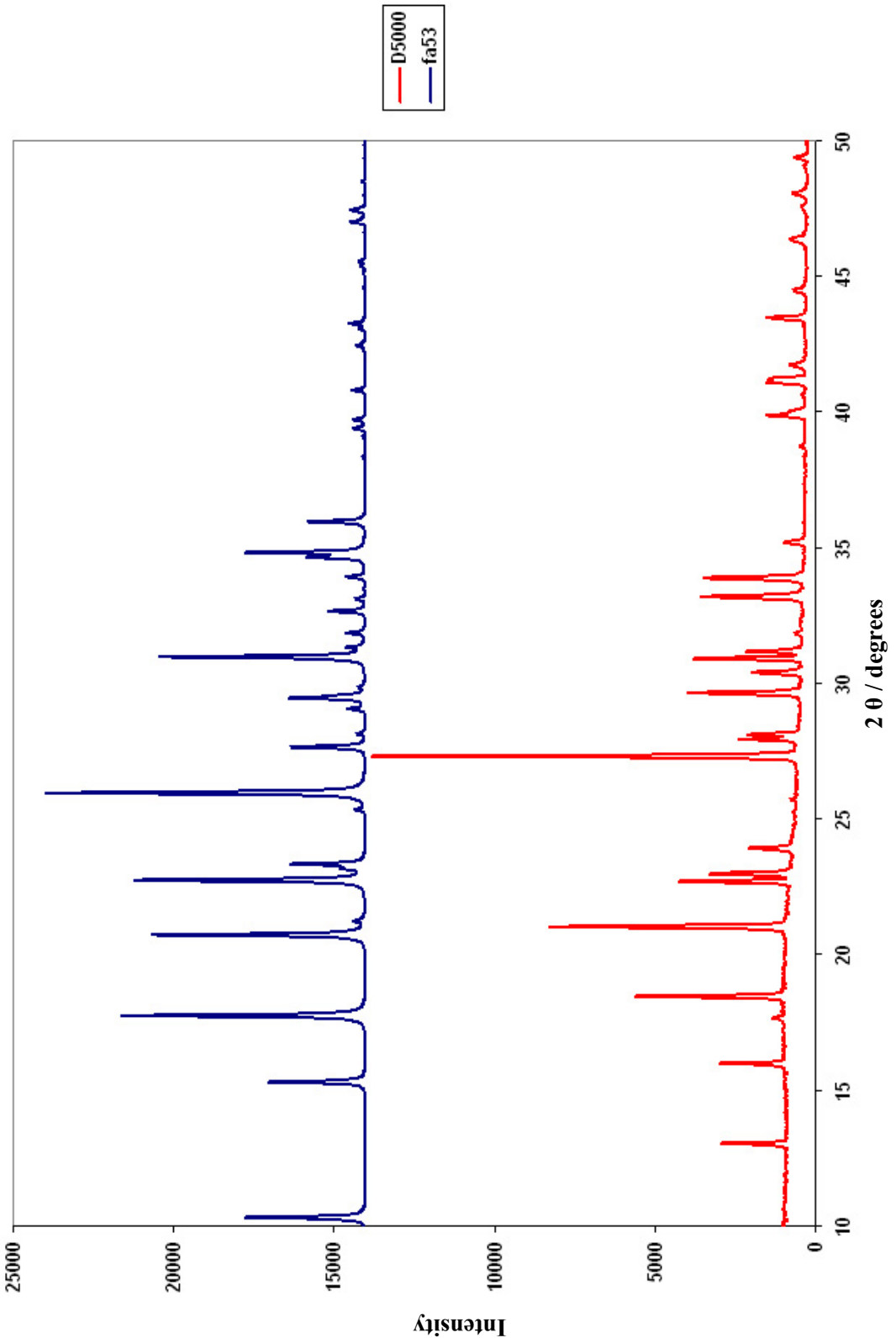

Figure 6.17 Powder diffraction patterns for fa53 and the D5000 experimental structure.

6.3 Discussion

Table 6.6. Comparison of the ability of the three methods in automated identification of the correct predicted structure. Values in red denote the difference (modulus of the difference for R_{wp}) between the correct structure and the structure ranked first. If the correct structure ranked first, the values denote the difference between the correct structure and the next best one (shown in black).

Temperature (K)	***R_{wp}***	***PolySNAP***	***Compare***
10	2	0.396	0.028
100	1.1	0.354	0.018
150	1.1	0.142	0.004
200	2.7	0.141	0.009
250	1.6	0.022	0.015
293	2.3	0.005	0.017
D5000 (293K)	1.9	0.133	0.061

The R_{wp} method once again yielded negative results, further proving its unreliability in selecting correct predictions in relation to experimental powder data. Although *Compare.x* did not identify cb2 as the correct structure at room temperature, the difference in correlation value between cb2 and the next-ranking structure up to that temperature increased overall. Past 250K, a different structure was selected, possibly implying a shift in 2θ that was large enough to enable different peaks to fall within the confines of the triangle window.

In the cases where *PolySNAP* identified the correct structure, both correlation values and discriminatory ability decreased markedly with temperature, the highest correlation between experimental data and cb2 being observed at 150K. This corresponds with the temperature at which there was the greatest discrimination between the correct structure (ranked first) and the structure with the next best correlation.

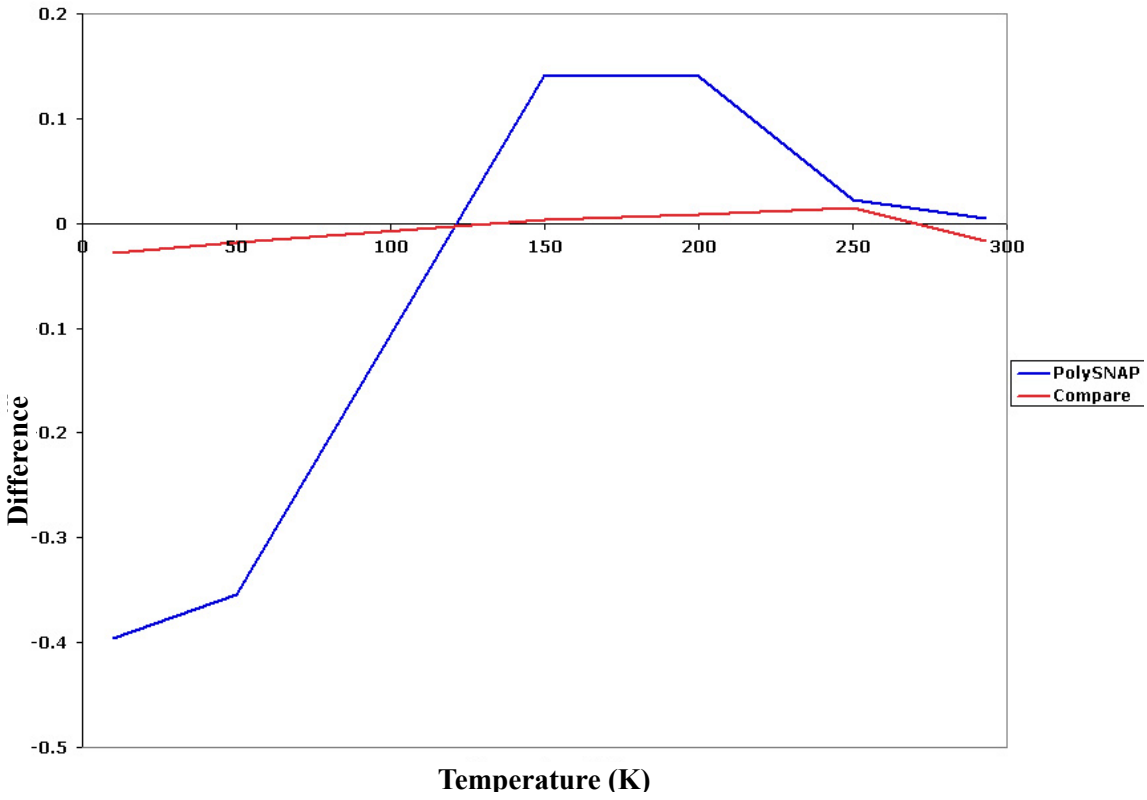

Figure 6.18 Difference in correlation coefficients between cb2 and the structure with the next highest correlation. In cases where cb2 was not ranked first, the difference between cb2 and the structure with the highest correlation was plotted.

In comparison with *PolySNAP*, *Compare.x* once again gave higher overall correlation coefficients and a greater discrimination with increasing temperature. Although the *PolySNAP* comparison gave positive results at intermediate and higher temperatures suggesting an overall sensitivity to the peak shift arising from expansion of the unit cell, the discrimination between the correct structure and the structure with the second highest correlation coefficient did not show any particular sensitivity to temperature [Figure 6.18].

6.4 References

1. J. Skoda, in D. Shugar (Ed.), *Biochemical Aspects of Antimetabolites and Drug Hydroxylation*, Academic Press, New York, 1969 **16**, 29

2. J. K. Lindquist, in A. Katriztky, C. W. Rees (Eds.), *Comprehensive Heterocyclic Chemistry*, Permagon Press, Oxford, 1984, 159

3. J. Beranek and E. M. Acton, *Collect. Czech Chem. Commun.*, 1984, **49**, 2551

4. L. H. Li, G. C. Neil, T. E. Morley and E. J. Olin, *Cancer Chemotherapy Rep.*, 1974, **Part 1 56**, 345

5. J. Skoda, *Prog. Nucl. Acid. Res.,* 1963, **2**, 197

6. A. M. Gero, W. J. O'Sullivan and D. Brown, *Biochem. Med.,* 1985, **34**, 60

7. W. H. Prussoff and A. D. Welch, *J. Biol. Chem.,* 1956, **218**, 929

8. C. H. Schalbe and W. Saenger, *J. Mol. Biol.*, 1973, **75**, 129

9. A. El-Tarrass, R. Braun, E. Stenz and G. Schuster, *Zentralblatt fur Mikrobiologie*, 1989, **144**, 197

10. B. S. Potter, R. A. Palmer, R. Withnall, B. Z. Chowdry and S. L. Price, *J. Mol. Struct.*, 1999, **349**, 485

11. A. Gavezzotti, *Acc. Chem. Res.*, 1994, **27**, 309

12. S. L. Price and K. S. Wibley, *J. Phys. Chem. A,* 1997, **101**, 2198

13. A. E. Gray, G. M. Day, M Leslie and S L Price, *Molecular Physics,* 2004, **102 (9)**, 1067

7. DNA BASES

Adenine and guanine are two of the nitrogen bases found in nucleic acids, along with the pyrimidines cytosine (found in both DNA and RNA), uracil (found only in RNA) and thymine (normally found in DNA, although sometimes tRNA will contain some thymine as well a uracil). The hydrogen bonding interactions between purines and pyrimidines are among the core factors determining the structure (and consequently also the function) of DNA. These hydrogen bonds formed by the base pairs of adenine and thymine, and guanine and cytosine, constitute the "rungs" that are responsible for the double helical nature of DNA. In this chapter, the structure solution and structure prediction calculations of the two DNA purines will be discussed.

7.1 Adenine

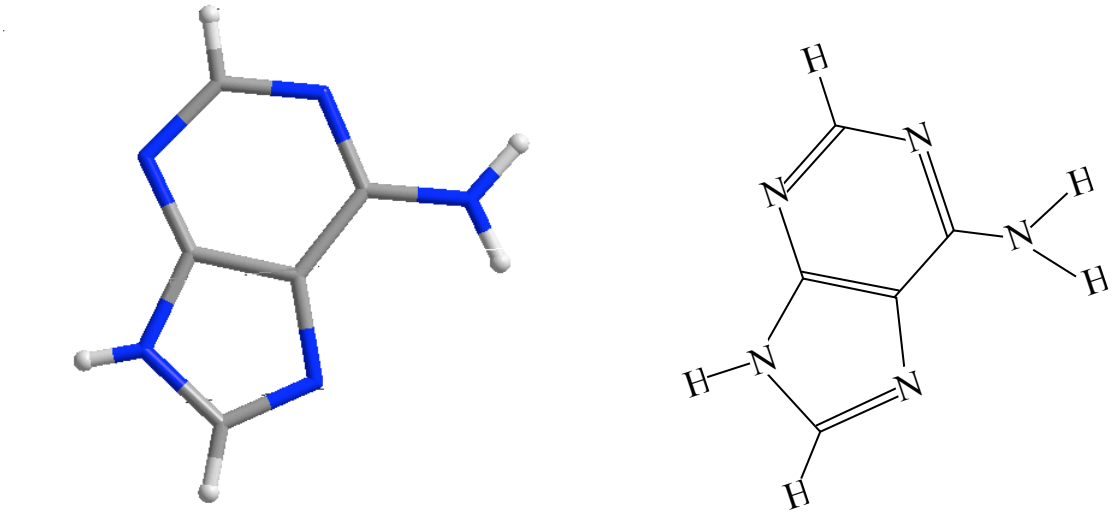

Figure 7.1.1 Adenine (6-aminopurine)

7.1.1 Background

Besides DNA and RNA, adenine is also an important constituent of adenosine triphosphate (ATP). It is essential due to its ability to phosphorylize, or add a phosphate group to other molecules. The transfer of a phosphate group allows energy to be released, and it is this energy that is used by cells in living organisms.

Although it is quite a high-profile molecule, the structure of adenine had not been previously determined, and no evidence of polymorphism has been reported. However, structures with adenine existing as a complex with riboflavin[1], phthalic acid[2], hydrogen peroxide[3], and N-methyl-2-pyrrolidone[4] can be found on the CSD. Other published structures include adenine in trihydrate form[5] and in adeninium tetrafluoroborate dihydrate[6].

7.1.1.1 Experimental Polymorph Search[7]

An extensive polymorph search was carried out using 42 solvents[7], and crystallisations were mainly carried out by slow evaporation. The majority of solvents gave either no solid for analysis, or small particles of solid that were unsuitable for characterisation purposes. Crystallisation from 2,2,2-trifluoroethanol, acetic acid, dimethylamine in water and 2-methoxyethylamine yielded adenine as a polycrystalline solid with a powder diffraction pattern that matched the stock sample. Adeninium chloride hemihydrate and adeninium dichloride structures were also found in the search [Appendix A5.1 Table A5.1.1].

7.1.1.2 Computational Polymorph Searches[7]

In the computational polymorph search based on the *ab initio* molecular structure, 2900 structures were generated, with 11 unique structures lying within 7 kJ mol^{-1} of the global lattice energy minimum. A further search using the planar molecular structure resulted in 14 unique structures in the same energy range[7] [Table 7.1.1 and Figure 7.1.2], and 8 of which had Z'=2. The *ab initio* search found the structure

am62 at the global lattice energy minimum, ~2 kJ mol^{-1} more stable than the next structure and with about the same estimated energy difference at room temperature. Three hypothetical structures were found within 4.5 kJ mol^{-1} of the global lattice energy minimum (this difference decreases to 2.5 kJ mol^{-1} at room temperature).

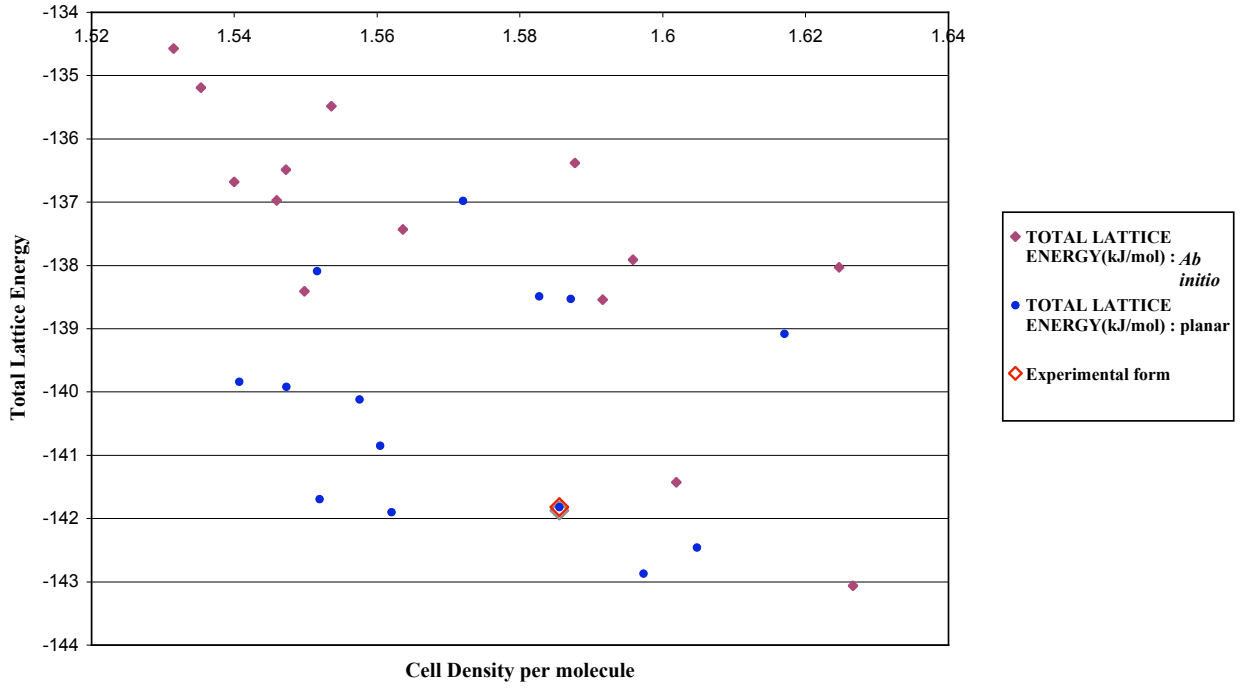

Figure 7.1.2 The results of both computational searches (ab initio and planar) showing the predicted structure corresponding to the experimental form denoted by the red open diamond. [Figure reproduced with permission from the CPOSS database]

The computational search based on the planar molecular structure gave five unique hypothetical structures with a range of densities, and lying within 1.2 kJ mol^{-1} of the global lattice energy minimum. In both computational searches, all but one of the low energy structures consisted of hydrogen bonded sheets. Three main types of sheet structure were identified, exhibiting only minor rearrangement of the molecules in the sheets, attributed to the use of various combinations of donors and acceptors [Figure 7.1.3]. There were also slight changes in the orientation of the sheets relative to each other.

Table 7.1.1. The low energy crystal structures found within 7 kJ mol^{-1} of the global lattice energy minimum for adenine, using the ab initio and planar molecular structures. All the structures consist of molecules that use N1, N2, and N3 as hydrogen bond acceptors, and all contain hydrogen bonded sheets, except for de56 which contains a three-dimensional hydrogen bonding network.

STRUCTURE	SPACE GROUP	LATTICE ENERGY (kJ/mol)	FREE ENERGY (kJ/mol)	DENSITY (g/cm3)	REDUCED CELL					
					a(Å)	*b*(Å)	*c*(Å)	*α*(°)	*β*(°)	*γ*(°)
***Ab initio* molecular structures**										
am62	*P* 2$_1$ /*c*	-143.06	-152.26	1.6266	6.637	12.181	9.530	90.00	45.74	90.00
fc84	*P* 2$_1$ /*c*	-141.43	-150.42	1.6019	4.696	8.167	14.846	90.00	79.73	90.00
cb24	*P b c a*	-138.54	-149.74	1.5916	14.371	12.186	6.440	90.00	90.00	90.00
fc4	*P* 2$_1$ /*c*	-138.41	-148.39	1.5498	4.718	8.164	21.824	90.00	43.55	90.00
ab102	*P* -1	-138.03	-147.06	1.6247	8.514	5.315	7.970	106.25	70.32	125.06
dc46	*C* 2/*c*	-137.91	-146.97	1.5958	10.028	8.352	13.750	90.00	77.63	90.00
ab16	*P* -1	-137.43	-147.02	1.5636	8.541	4.596	8.136	98.65	114.38	89.73
dd101	*C* 2/*c*	-136.97	-145.48	1.5459	6.884	12.223	23.829	90.00	35.39	90.00
am21	*P* 2$_1$ /*c*	-136.68	-147.11	1.54	5.234	14.969	7.480	90.00	96.04	90.00
cd110	*Pna*2$_1$	-136.49	-148.03	1.5472	6.398	14.913	12.161	90.00	90.00	90.00
cb89	*P* -1	-136.38	-147.14	1.5877	7.027	13.230	12.161	90.00	90.00	90.25
Planar molecular structures										
fc33	*P* 2$_1$ /*c*	-142.87	-151.5	1.5973	4.851	8.092	14.600	90.00	101.36	90.00
am9	*P* 2$_1$ /*c*	-142.46	-151.95	1.6048	6.458	12.170	7.121	90.00	88.14	90.00
ak71	*P* 2$_1$ /*c*	-141.9	-150.93	1.562	6.650	7.862	12.390	90.00	62.49	90.00
cc71	*P* 2$_1$ /*c*	-141.82	-152.81	1.5855	8.330	7.496	21.831	90.00	90.00	56.16
fc1	*P* 2$_1$ /*c*	-141.69	-150.91	1.5519	4.879	7.871	21.999	90.00	43.21	90.00
aj80	*P* -1	-140.85	-150.03	1.5604	8.089	4.725	22.654	47.76	74.76	94.92
ce73	*Pca*2$_1$	-140.12	-150.42	1.5575	21.958	8.007	6.555	90.00	90.00	90.00
am43	*P* 2$_1$ /*c*	-139.92	-150.47	1.5473	5.301	14.952	8.576	90.00	58.58	90.00
cb108	*P* 2$_1$ /*c*	-139.84	-151.13	1.5407	12.221	14.943	6.736	90.00	71.28	90.00
ab72	*P* -1	-139.08	-148.09	1.617	8.492	4.926	8.426	103.83	73.81	124.48
bf37	*P* -1	-138.53	-148.59	1.5871	8.356	21.789	5.429	125.88	55.08	89.87
ai116	*P* 2$_1$ /*c*	-138.49	-147.8	1.5827	8.832	8.112	8.382	90.00	70.79	90.00
ca73	*P* -1	-138.09	-147.51	1.5516	9.810	4.770	7.994	100.13	116.62	60.05
de56	*C* 2/*c*	-136.98	-147.91	1.572	19.452	3.779	23.120	90.00	137.78	90.00

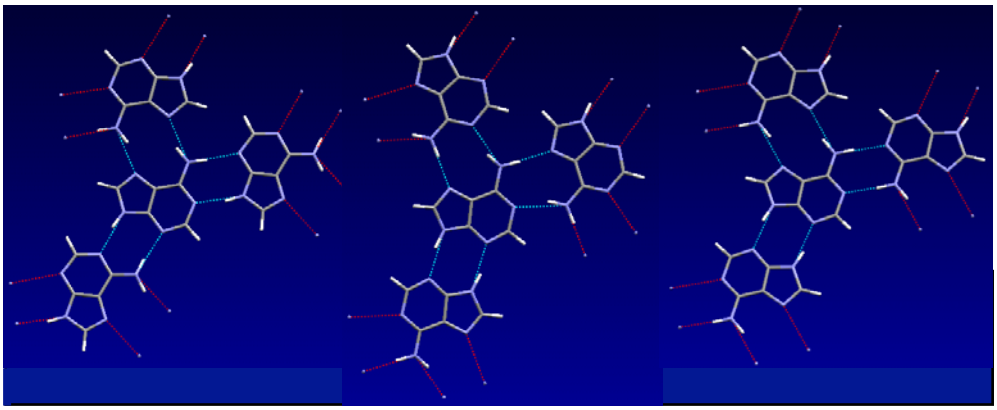

I **II** **III**

Figure 7.1.3 The three different hydrogen bonded sheet structures present in the low energy structures in both computational polymorph searches on adenine

The majority of the elastic constants of the low energy structures were relatively low (<1 GPa), possibly indicating a tendency for the hydrogen bonded sheets to slip over each other[7]. This would decrease the mechanical stability, suggesting that the energetically favourable crystal packings of adenine give relatively soft crystals, and could hence indicate problematic crystal growth.

7.1.2 Results

As an unknown crystal structure, attempts were made to index the experimental data and proceed with a traditional structure solution. However, the data could not be indexed reliably, i.e. a suitable cell could not be identified amongst the others in the indexing results. Therefore, the structure prediction results were examined to establish whether these could be used to aid determination of this elusive crystal structure.

7.1.2.1 *PolySNAP*

PolySNAP was used to identify any similarities between the experimental powder data and that simulated for all the predicted structures. As low temperature data had not yet been recorded at this early stage of the adenine study, the room temperature transmission data (D5000) was used for comparison. The computational crystal structure cc71 (Z' = 2) from the planar molecular structure

search (1 kJ mol^{-1} above the global lattice energy minimum), was selected as having the highest correlation with the experimental data [Figures 7.1.4 and 7.1.5]. This identified the similarity between the two powder data sets, as subsequently confirmed by visual inspection [Figure 7.1.6].

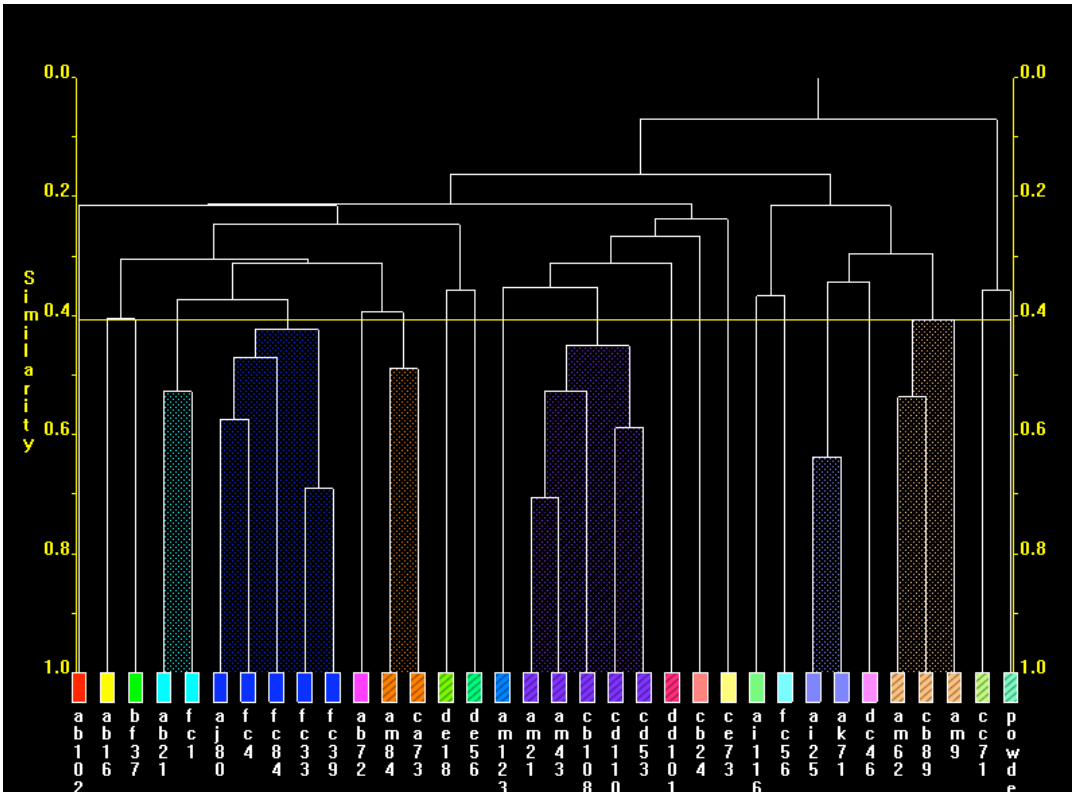

Figure 7.1.4. Dendrogram showing similarity correlation clusters for predicted adenine and experimental adenine powder diffraction patterns. Experimental data is denoted as ***powder****.*

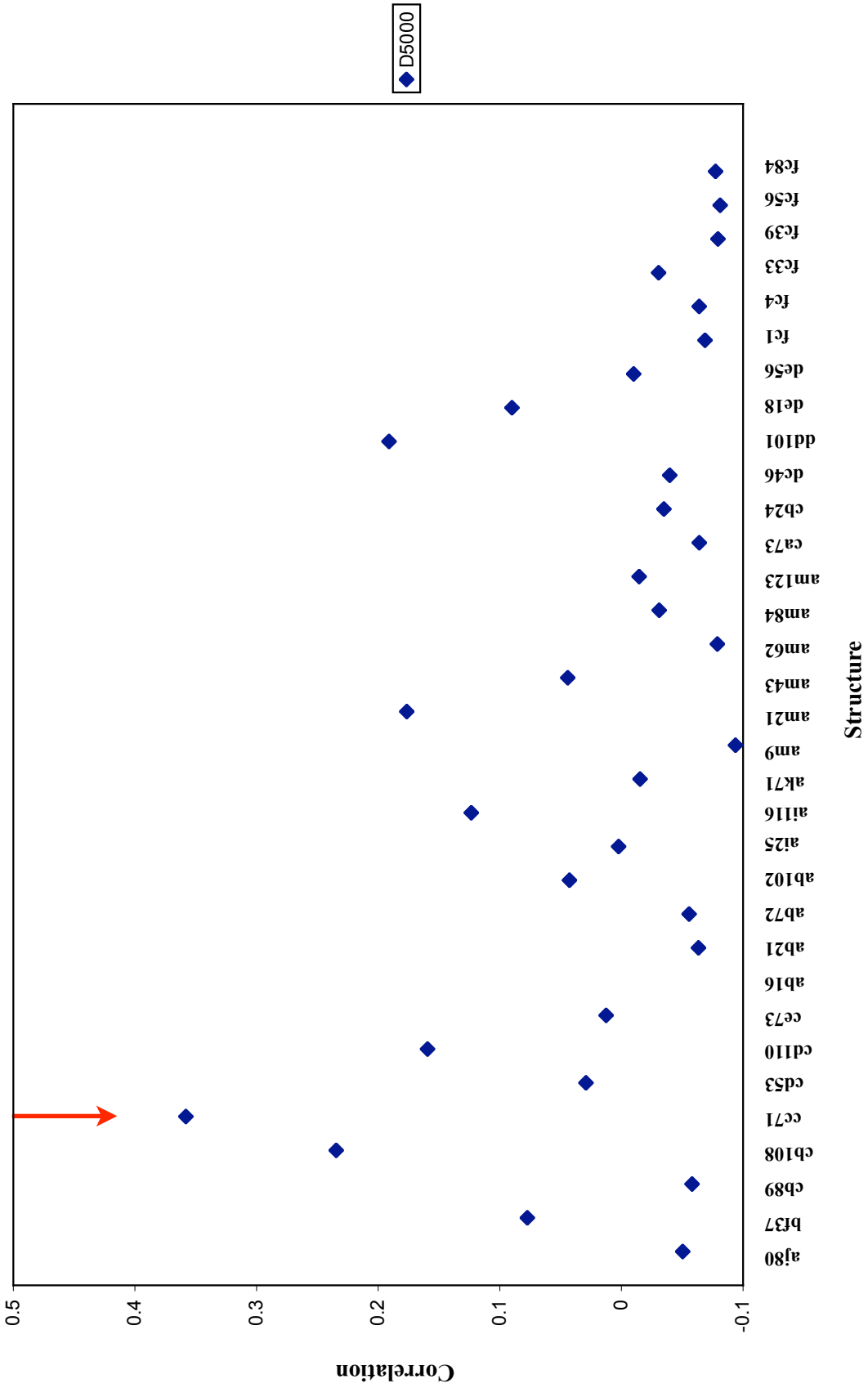

Figure 7.1.5 Correlation coefficients of all 33 predicted structures with room temperature (D5000) data. The arrow indicates structure cc71.

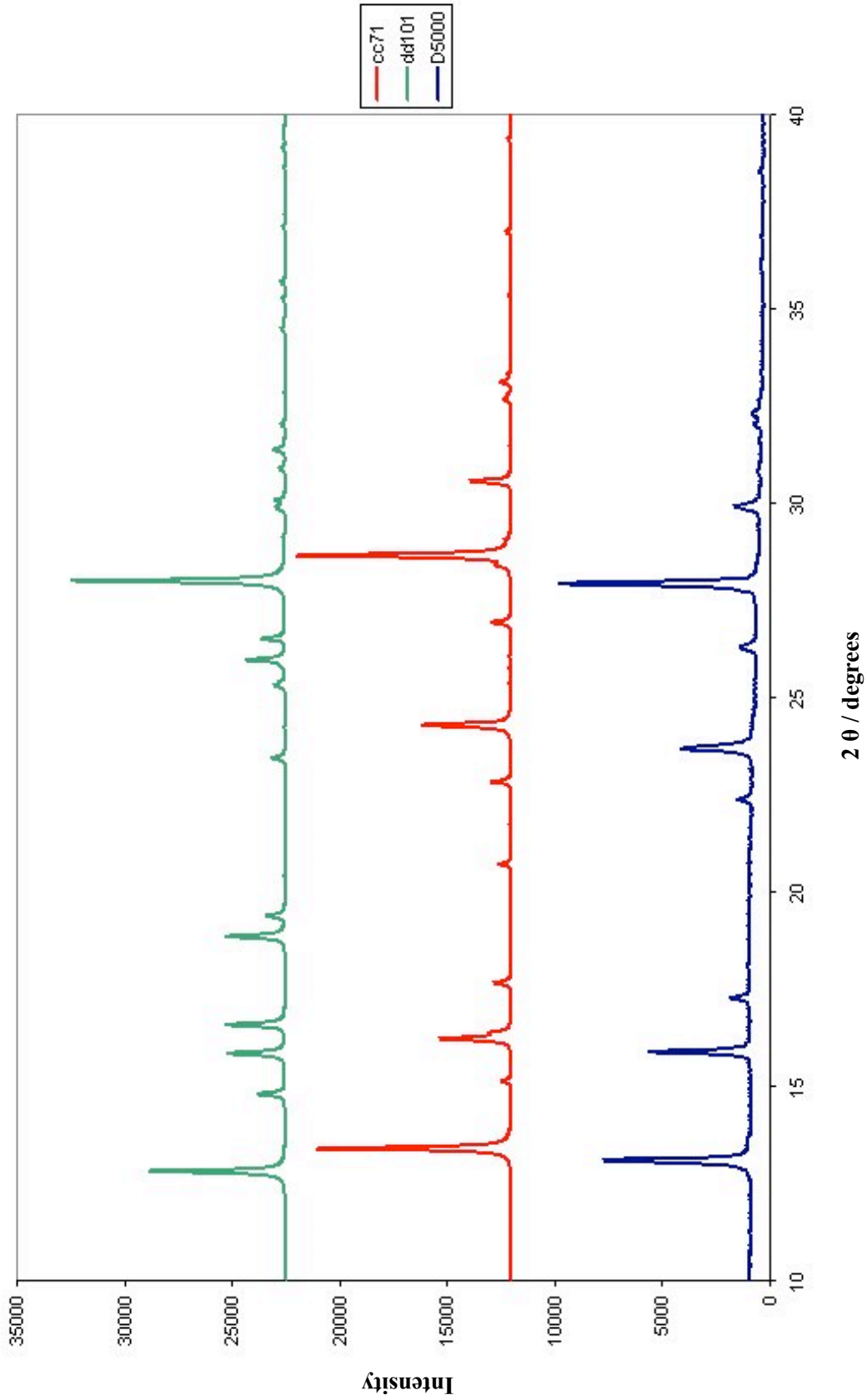

Figure 7.1.6 Powder diffraction patterns for two selected predicted structures and the experimental data (D5000) at room temperature.

In order to complete the study of this structure and complete investigation of the effectiveness of automated structure prediction comparison, the *PolySNAP* analysis was repeated using low temperature data when this became available. Structure cc71 was identified as having the highest correlation to the experimental data at each temperature [Table 7.1.2, Figure 7.1.8].

As observed in our other studies, the predicted structure (cc71) was found to have higher correlation coefficients with experimental data collected at low temperatures than with data collected at higher temperatures. The discrimination between structures ranked best and second did not vary widely at the lower temperatures, though a slightly greater discrimination was observed with the 150K data. At higher temperatures however, there was a reduction in discriminating ability, with the best two structures exhibiting only marginal differences in correlation coefficients. Figure 7.1.7 shows the simulated patterns of the best two structures and the experimental data at all temperatures.

Table 7.1.2. Correlation coefficient of the correct structure [P(cc71)] at each temperature, and the difference to the value obtained for the structure ranked second [P(x)]. In all cases, the correct structure (cc71) was identified.

Temperature (K)	***Top ranked structure***	***Correlation coefficient of top ranked structure***	***Correlation coefficient***	***Difference [P(cc71) - P(x)]***
10	cc71	0.5072	0.3622 (bf37)	0.1450
50	cc71	0.5356	0.4149 (bf37)	0.1207
100	cc71	0.5211	0.3817 (bf37)	0.1394
150	cc71	0.4875	0.3185 (bf37)	0.1690
200	cc71	0.3973	0.2448 (bf37)	0.1525
250	cc71	0.2997	0.2013 (fc84)	0.0984
293	cc71	0.2292	0.2240 (dd101)	0.0052
293 (D5000)	cc71	0.3581	0.2345 (cb108)	0.1236

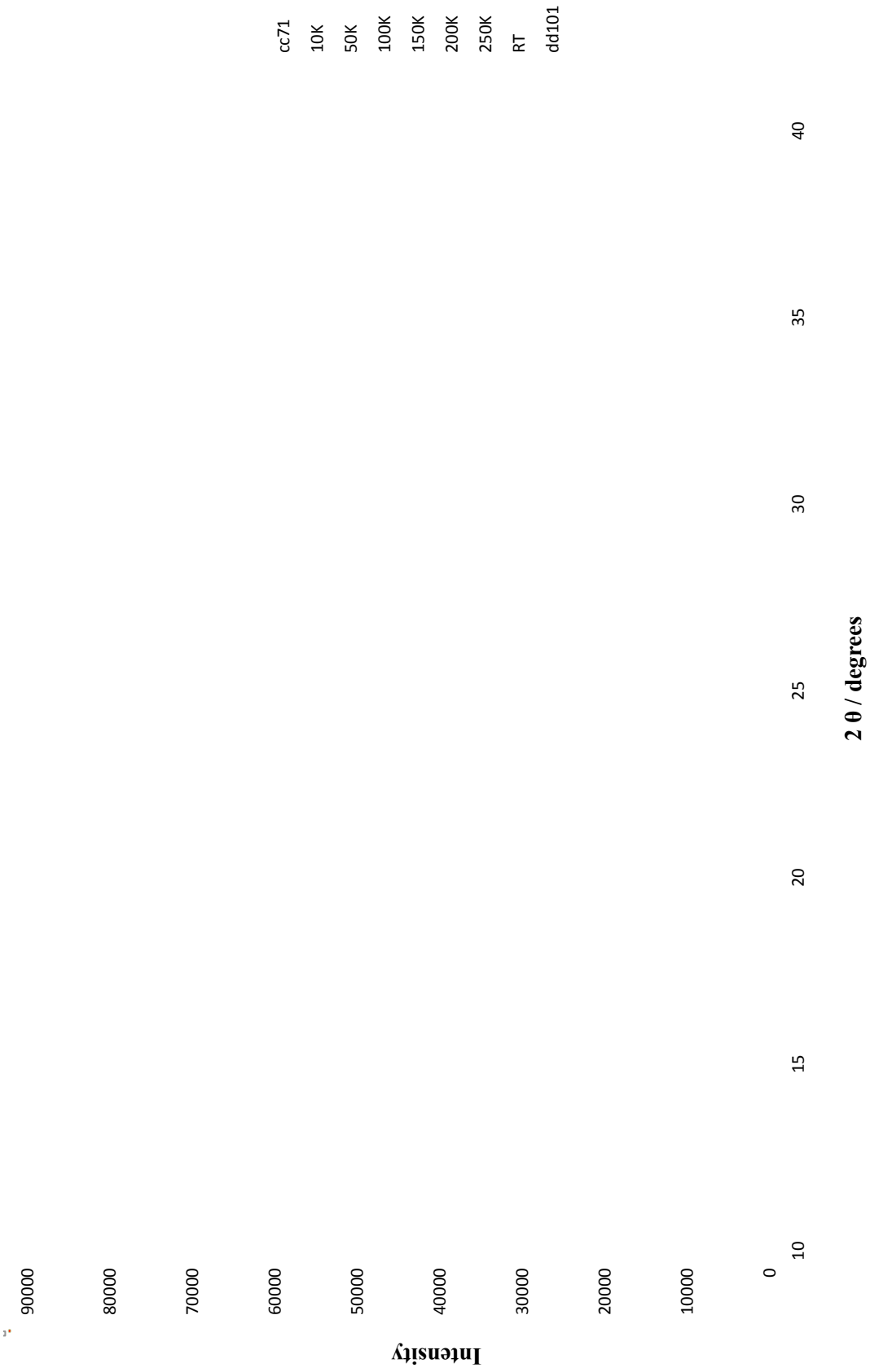

Figure 7.1.7 Powder diffraction patterns for two selected predicted structures and the experimental data (D5005) at all temperatures.

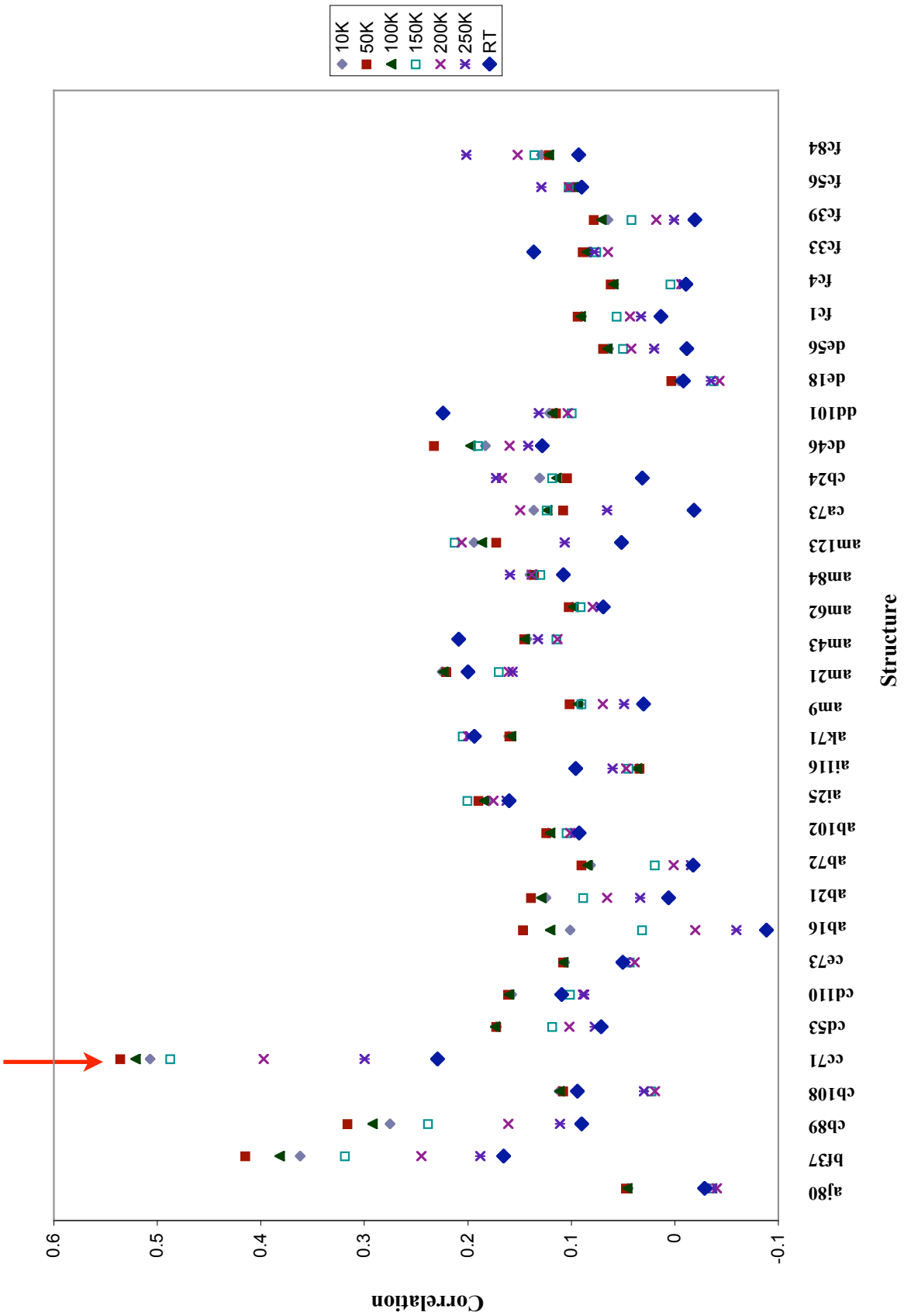

Figure 7.1.8 Correlation coefficients of all 33 predicted structures at each temperature. The arrow indicates structure cc71.

7.1.2.2 *Compare.x*

Using the default triangle window value of 2, *Compare.x* also identified the correct structure, cc71, as having the highest correlation with the experimental data at all temperatures but 293K. The room temperature data showed highest correlation with structure dd101, while cc71 was ranked second with a difference of 0.02411 with the D5005 data, but even lower down the list when compared to the D5000 data [Table 7.1.3 and Figures 7.1.9 and 7.1.10].

Table 7.1.3. Structures with highest correlation coefficient [C(x)] at each temperature, and the difference to the value obtained for the correct structure [C(cc71)]. Black numbers denote cases where the correct structure was identified, and the difference was positive. An incorrect match gave a negative difference, as shown by the values in red and blue. Blue denotes cc71 being ranked second, while values in red correspond to cc71 being ranked third or lower.

Temperature (K)	***Top ranked structure***	***Correlation coefficient of top ranked structure***	***Correlation coefficient***	***Difference [C(cc71) - C(x)]***
10	cc71	0.87413	0.81431 (ab21)	0.05982
50	cc71	0.87812	0.81961 (ab21)	0.05851
100	cc71	0.87276	0.81489 (ab21)	0.05787
150	cc71	0.86874	0.81522 (dd101)	0.05352
200	cc71	0.85485	0.81826 (dd101)	0.03659
250	cc71	0.83472	0.82841 (dd101)	0.00631
293	dd101	0.83534	0.81123 (cc71)	-0.02411
293 (D5000)	dd101	0.72463	0.70376 (cc71)	-0.02087

As the temperature increases, the unit cell expands and this translates as a shift in peak position along 2θ. As the cc71 structure is predicted at 0K and *Compare.x* uses a triangular window approach to define the correlation range, comparison with data recorded at 293K results in some of the peaks in the simulated cc71 powder pattern to fall outside the defined range. The powder diffraction pattern of structure dd101 has more peaks than cc71 [Figure 7.1.6] and was identified as having the best correlation with the experimental data purely on the basis of more peaks falling within the pre-defined triangle window. This "apparent" similarity can be discounted upon visual comparison of the respective powder diffraction patterns.

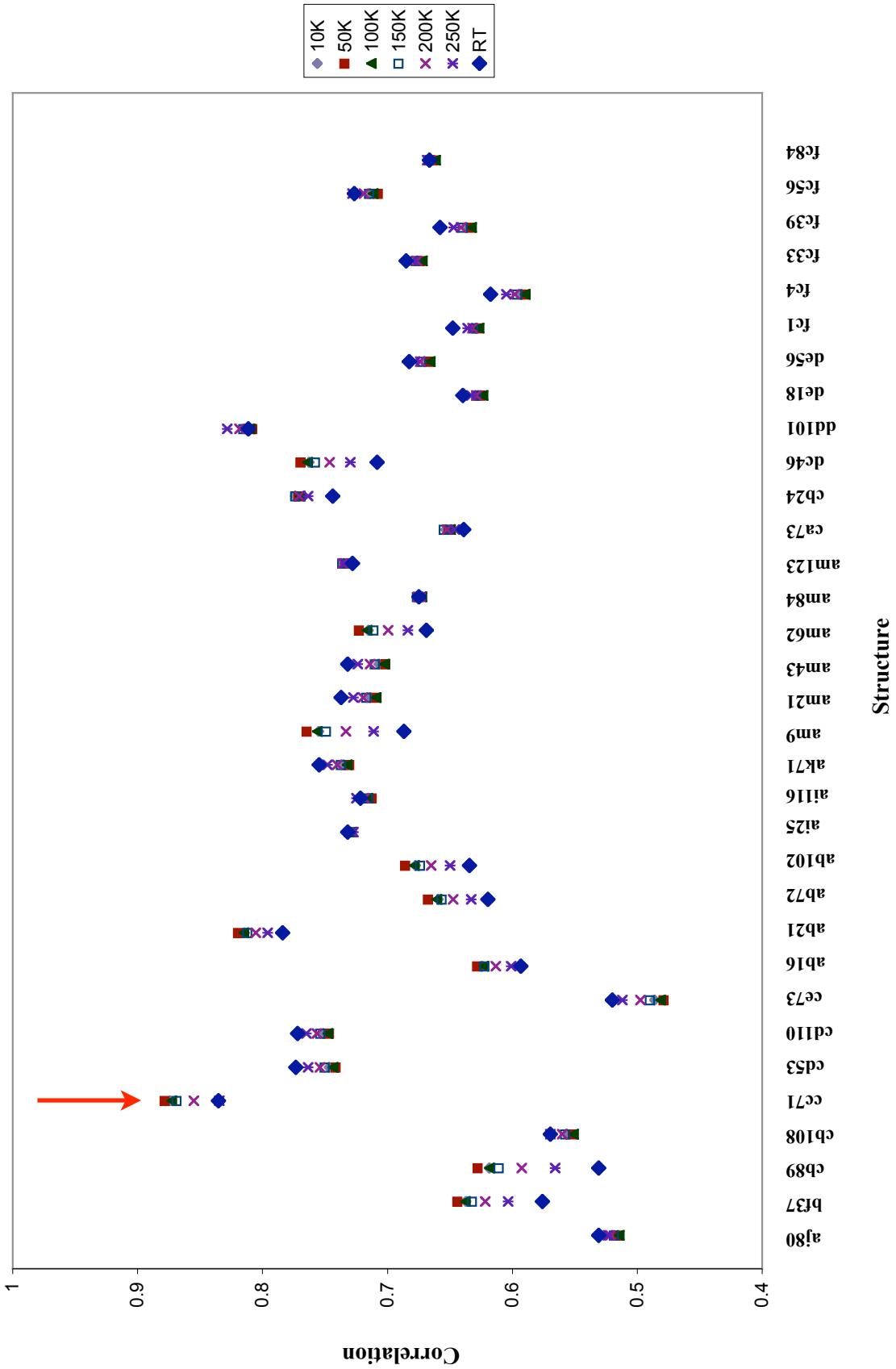

Figure 7.1.9 Correlation coefficients of all 33 structures at each temperature. The arrow indicates structure cc71.

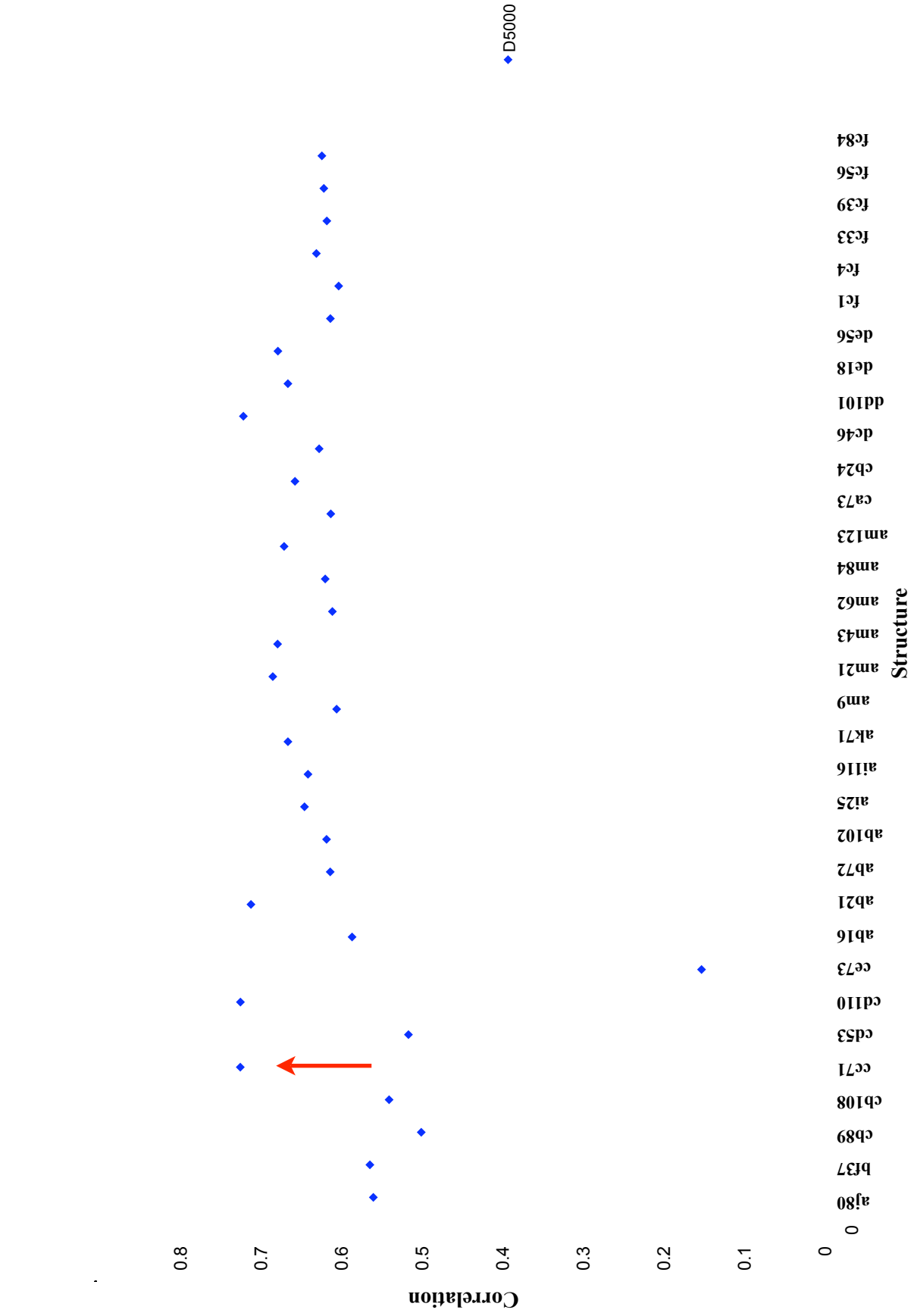

Figure 7.1.10 Correlation coefficients of all 33 predicted structures with room temperature (D5000) data. The arrow indicates structure cc71.

As in other chapters, although the default triangle window value of 2 was selected for this work, a range of triangle windows from 0.5 to 4.0 in increments of 0.5 was also tested using this data [Appendix A5.1.4 - Tables A5.1.4.1-A5.1.4.8]. The narrower the window, the more dissimilar the structures were considered to be, while wider windows resulted in higher correlation values, as explained in Chapter 4, Section 4.2.2.3.

7.1.2.3 R_{wp}

The 33 predicted structures were each compared, using R_{wp}, with the experimental data collected at each temperature. As in previous chapters, the outcome of these comparisons was non-discriminatory, and none of the 33 structures were singled out as being significantly similar to any of the experimental data. R_{wp} values ranging from 44.93% to 60.57% were obtained, although in most cases, no significant discrimination was found [Table 7.1.4, and Figures 7.1.11 and 7.1.12]. In addition, only one of the predictions (cb89) was ranked as the best fit to data recorded at two different temperatures. The correct predicted structure (cc71) was not identified by R_{wp} as having a similar powder pattern to the data collected at any of the temperatures. The simulated patterns for all predicted structures shown in the table and the corresponding experimental patterns are found in Appendix A5.1.3.

Table 7.1.4. Structures with lowest R_{wp} identified at each temperature. The difference is that between the R_{wp} for the top ranked structure [$R_{wp}(x)$] and the correct prediction [$R_{wp}(cc71)$].

Temperature (K)	***Top ranked structure***	***R_{wp} (x) (%)***	***R_{wp} (cc71) (%)***	***Difference (%) [$R_{wp}(x)$ - $R_{wp}(cc71)$]***
10	fc33	57.41	58.46	-1.05
50	fc56	54.98	57.23	-2.25
100	cb89	51.29	53.25	-1.96
150	ai116	50.58	51.61	-1.03
200	cb89	48.01	50.95	-2.94
250	fc33	48.05	49.99	-1.94
293	dd101	45.26	47.39	-2.13
293 (D5000)	ab16	44.93	45.98	-1.05

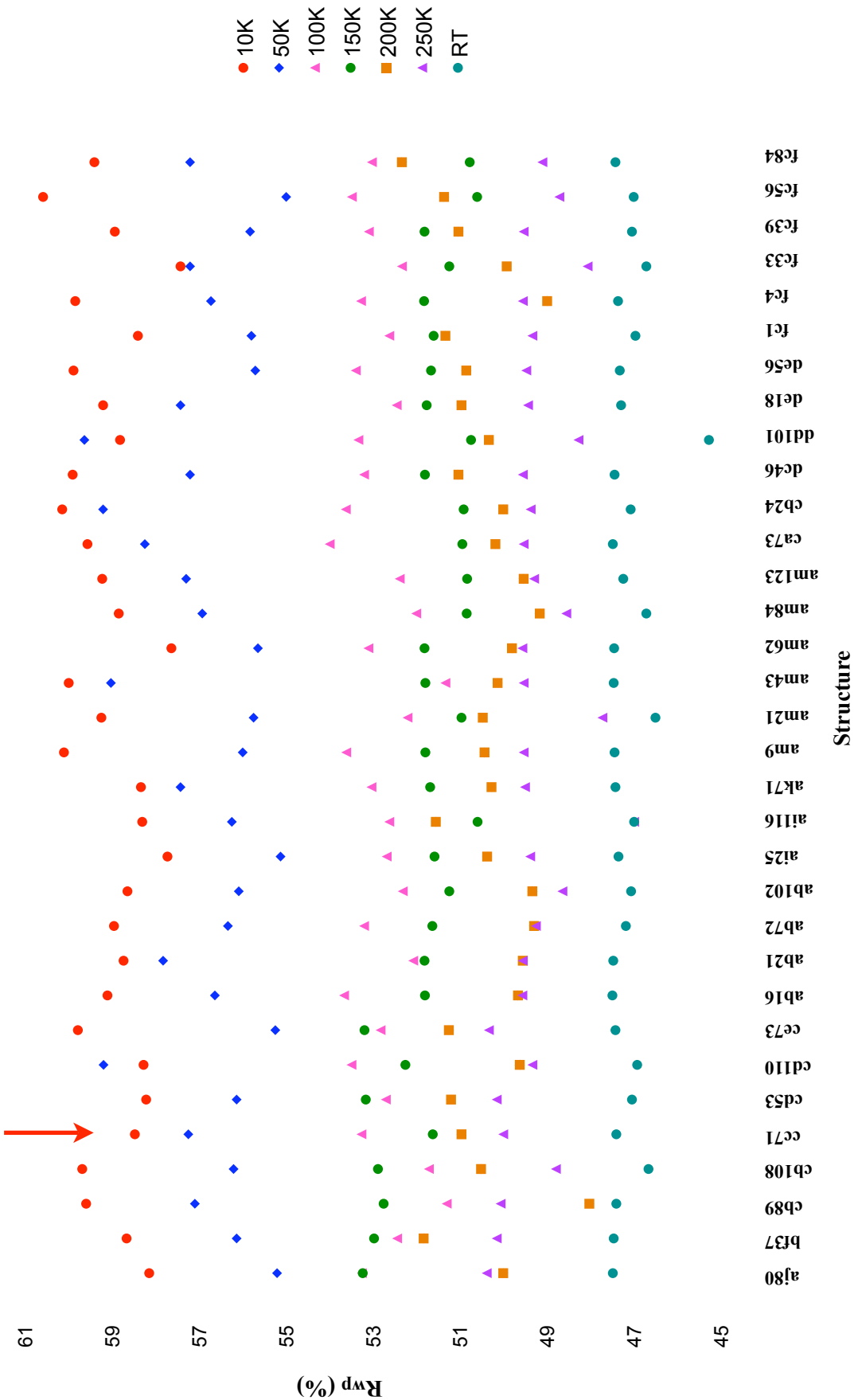

Figure 7.1.11 R_{wp} values for each predicted structure at each temperature with the D5005 data. The arrow indicates structure cc71.

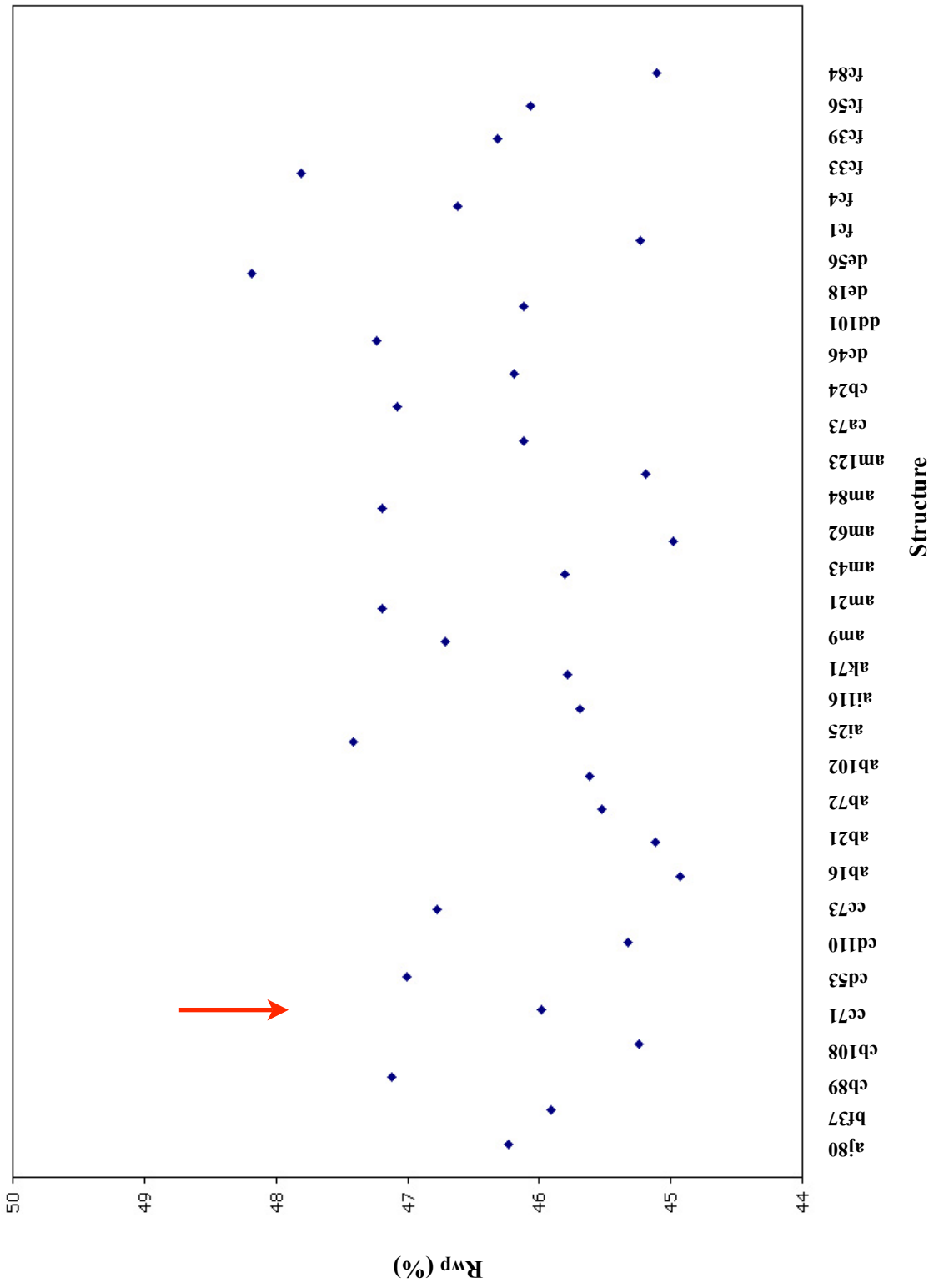

Figure 7.1.12 R_{wp} values for each predicted structure with the D5000 data. The arrow indicates structure cc71.

7.1.3 Structure Determination

Once a theoretical predicted structure with a high correlation to the experimental data was identified, this structure was used as the basis for crystal structure determination. Initial LeBail profile analysis was carried out using the unit cell parameters from cc71 as a starting point. This gave a good profile fit against the transmission geometry data (over the range $10^{o} \leqslant 2\theta \leqslant 60^{o}$) with an R_{wp} equal to 8.2%. Subsequent Rietveld refinement using cc71 as the initial structure was successful, giving an R_{wp} of 12.3% [Tables 7.1.5 - 7.1.9 and Figures 7.1.13 - 7.1.14].

Refinements were carried out using the GSAS program package[8]. The positions of all atoms were refined subject to soft constraints (weighting factor of 0.001 for bond distances and 0.005 for geminal non-bonded distances) on standard geometry. The amine hydrogen atoms were placed in positions calculated from the coordinates of hydrogen bond donors and acceptors. Refinement also required variation of a preferred orientation parameter in the [121] direction using the March-Dollase correction[9].

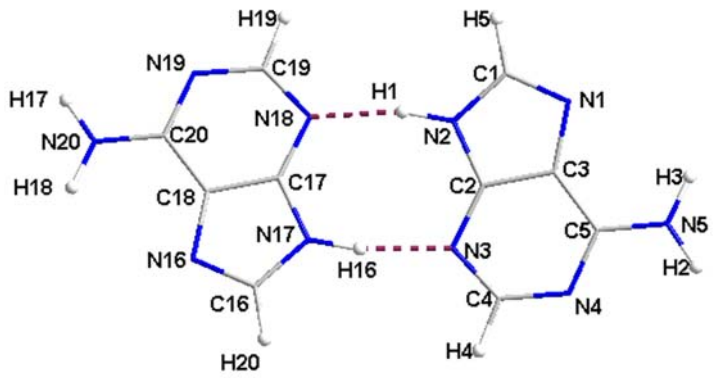

Figure 7.1.13 Atomic positions of the 2 molecules in the asymmetric unit relative to each other

Table 7.1.5 Final refined atomic positions for adenine.

Atom	x	y	z	Atom	x	y	z
N1	0.518 (2)	0.275 (1)	0.274 (2)	N16	0.034 (1)	0.039 (2)	0.266 (2)
N2	0.594 (1)	0.178 (1)	0.347 (1)	N17	0.088 (2)	-0.060 (1)	0.323 (1)
H1	0.579 (1)	0.143 (1)	0.352 (2)	H16	0.075 (1)	-0.100 (1)	0.305 (1)
N3	0.899 (1)	0.191 (2)	0.623 (2)	N18	0.359 (3)	-0.053 (2)	0.597 (2)
N4	0.969 (3)	0.297 (2)	0.692 (1)	N19	0.452 (2)	0.048 (1)	0.729 (1)
N5	0.782 (2)	0.375 (2)	0.513 (1)	N20	0.282 (1)	0.131 (2)	0.552 (2)
H2	0.862 (2)	0.406 (1)	0.585 (1)	H17	0.364 (1)	0.157 (1)	0.640 (1)
H3	0.673 (2)	0.389 (2)	0.425 (1)	H18	0.181 (1)	0.149 (2)	0.445 (1)
C1	0.471 (1)	0.218 (1)	0.22 (1)	C16	-0.018 (1)	-0.017 (2)	0.200 (1)
H5	0.363 (1)	0.207 (2)	0.128 (1)	H20	-0.119 (1)	-0.026 (2)	0.094 (2)
C2	0.742 (1)	0.211 (3)	0.476 (1)	C17	0.234 (1)	-0.032 (2)	0.467 (1)
C3	0.692 (1)	0.271 (2)	0.424 (2)	C18	0.195 (1)	0.029 (3)	0.428 (2)
C4	1.005 (1)	0.237 (1)	0.717 (2)	C19	0.477 (2)	-0.013 (2)	0.739 (2)
H4	1.113 (1)	0.236 (2)	0.814 (2)	H19	0.576 (1)	-0.026 (2)	0.841 (1)
C5	0.812 (2)	0.315 (3)	0.543 (1)	C20	0.309 (2)	0.070 (1)	0.569 (2)

Table 7.1.6 Intramolecular bond lengths (Å).

Bond	Length	Bond	Length
N1-C1	1.3255	N2-C1	1.3724
N1-C3	1.3789	N17-C16	1.3715
N16-C18	1.3808	N2-C2	1.3853
N16-C16	1.3269	N5-C5	1.3511
C2-C3	1.3977	N20-C20	1.3661
C3-C5	1.4092	C1-H5	0.8998
C17-C18	1.3969	C4-H4	0.8704
C18-C20	1.4093	C16-H20	0.8996
N3-C2	1.3601	C19-H19	0.9001
N3-C4	1.3395	N2-H1	0.7827
N4-C4	1.3469	N5-H2	0.9505
N5-C5	1.3575	N5-H3	0.8991
N18-C17	1.1783	N17-H16	0.9010
N18-C19	1.4225	N20-H17	0.9276
N19-C19	1.3620	N20-H18	0.9595
N19-C20	1.3749	N17-C17	1.3834

Table 7.1.7 Hydrogen bond lengths (Å).

D—H···*A*	Symmetry code of *A*	H···*A* / Å	*D*···*A* / Å	*D*—H···*A* / °
N2H1---N18	1-*x*, -*y*, 1-*z*	2.07(1)	2.56 (1)	160 (1)
N5H2---N16	1+*x*, 0.5-*y*, 0.5+*z*	1.93(1)	2.87 (1)	171 (3)
N5H3---N19	*x*, 0.5-*y*, 0.5+*z*	2.26(1)	3.12 (2)	161 (2)
N17H16---N3	1-*x*, -*y*, 1-*z*	2.07(1)	2.92 (1)	157 (1)
N20H17---N1	*x*, 0.5-*y*, 0.5+*z*	1.94(1)	2.85 (1)	166 (1)
N20H18---N4	1+*x*, 0.5-*y*, 0.5+*z*	2.32(1)	3.28 (1)	171 (2)

Table 7.1.8 Bond angles (°).

Atoms	Angle	Atoms	Angle
C3-N1-C1	104.09 (2)	N1-C3-C2	111.87 (1)
C1-N2-H1	126.66 (1)	N1-C3-C5	131.59 (1)
C2-N2-H1	125.40 (1)	C5-C3-C2	115.99 (1)
C1-N2-C2	107.65 (1)	N3-C4-H4	127.03 (2)
C2-N3-C4	109.87 (1)	N3-C4-N4	103.39 (2)
C4-N5-C5	118.33 (1)	N5-C4-H4	129.53 (1)
H2-N5-H3	112.43 (2)	N5-C5-N5	118.17 (2)
C5-N5-H3	120.85 (3)	N5-C5-C3	118.51 (1)
C5-N5-H2	126.42 (2)	C3-C5-N5	123.25 (2)
C16-N16-C18	103.85 (1)	N16-C16-H20	125.03 (1)
C16-N17-H16	126.24 (2)	H20-C16-N17	122.27 (2)
C17-N17-H16	125.66 (1)	N16-C16-N17	112.42 (2)
C16-N17-C17	107.49 (3)	N18-C17-C18	127.40 (1)
C17-N18-C19	116.98 (2)	N17-C17-C18	103.75 (1)
C19-N19-C20	116.23 (2)	N17-C17-N18	128.79 (1)
H17-N20-H18	117.18 (2)	C17-C18-C20	111.94 (2)
C20-N20-H18	121.87 (1)	N16-C18-C20	131.56 (2)
C20-N20-H17	120.91 (2)	N16-C18-C17	115.93 (2)
H5-C1-N1	124.56 (1)	N19-C19-H19	121.95 (1)
H5-C1-N2	122.72 (2)	N18-C19-N19	114.72 (1)
N1-C1-N2	112.21 (2)	N18-C19-H19	123.31 (2)
N3-C2-C3	127.47 (2)	N20-C20-C18	118.08 (1)
N2-C2-C3	103.64 (1)	N20-C20-N19	119.89 (2)
N2-C2-N3	128.88 (2)	N19-C20-C18	122.03 (2)

Table 7.1.9 Crystal data, lattice parameters for theoretical structure, LeBail and Rietveld agreement factors and final refined unit cell parameters for adenine.

Crystal data	
Chemical formula	$C_5H_5N_5$
Space group	$P2_1/c$
Theoretical Structure (cc71)	
a (Å)	7.4956
b (Å)	21.8311
c (Å)	7.4854
β (°)	112.43
Volume (Å^3)	1132.2
Z'	2
LeBail	
R_{wp} (%)	8.17
R_p (%)	6.12
χ^2	1.05
Refinement	
R_{wp} (%)	12.29
R_p (%)	10.03
χ^2	1.77
R_F^2 (%)	27.41
Preferred orientation ratio [direction]	1.1356 [121]
No. of observations	2992
No. of parameters	100
No. of restraints	80
No. of reflections	358
Final *a* (Å)	7.6685 (9)
Final *b* (Å)	22.2006 (3)
Final *c* (Å)	7.6240 (9)
Final β (°)	112.892 (6)
Final volume (Å^3)	1195.7 (4)

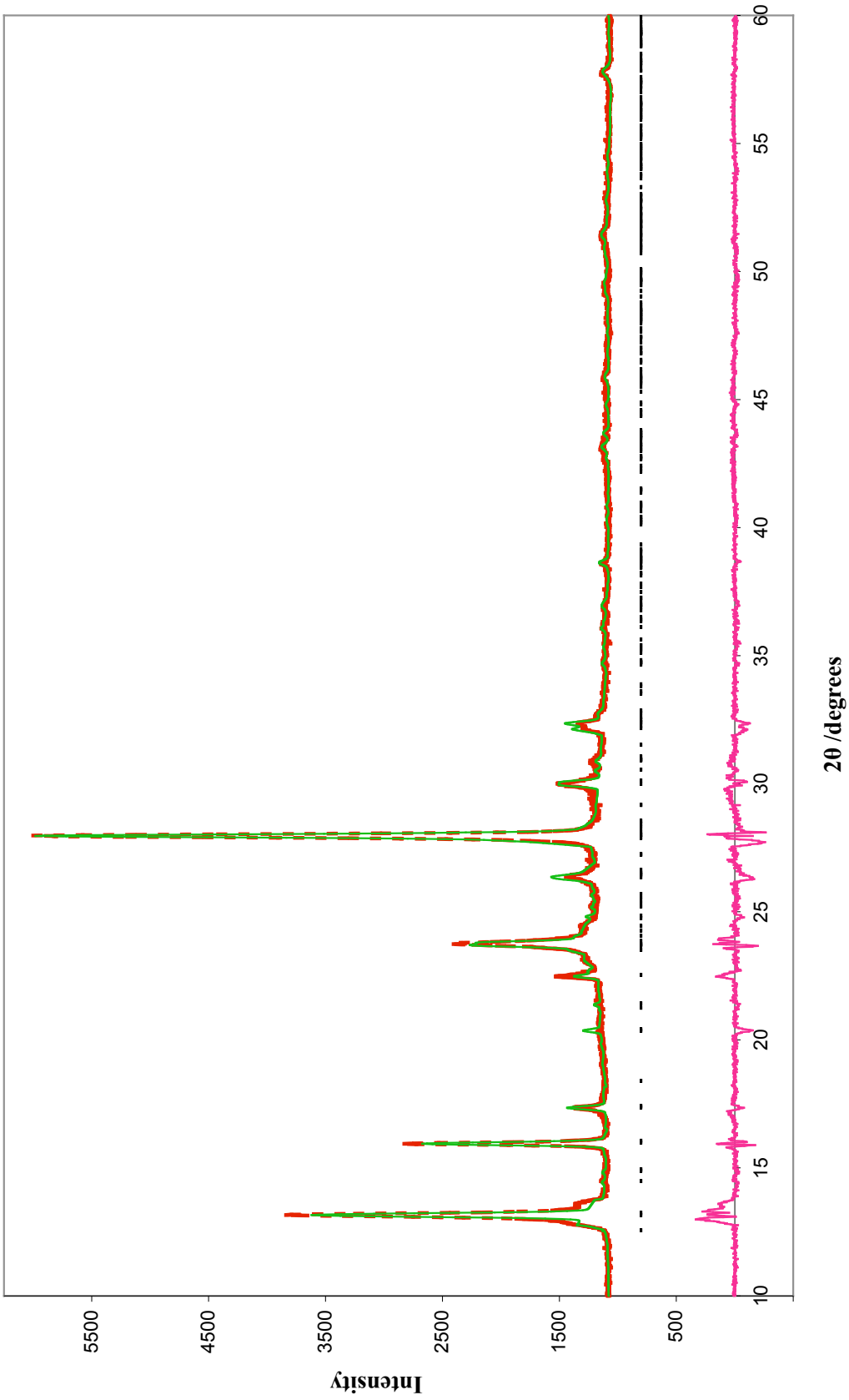

Figure 7.1.14 Rietveld refinement of adenine against the D5000 room temperature data. The green line denotes the calculated powder pattern, the red dots the experimental data, and the pink line the difference between them. Reflection positions are shown by the black dots

7.1.4 Crystal Structure

The crystal structure of adenine contains hydrogen bonded sheets with an interlayer spacing of 3.75 Å. It contains the sheet motif (II) shown in Figure 7.1.3, in which each molecule is linked via NH---N hydrogen bonds to three others using all strong donors and acceptors. Each molecule is bonded through 6 hydrogen bonds, donating 3 and accepting 3, and forming $R_2^2(8)$ and $R_2^2(9)$ motifs. Each ring of six molecules is surrounded by six other rings, forming a honeycomb pattern [Figure 7.1.15].

(a)

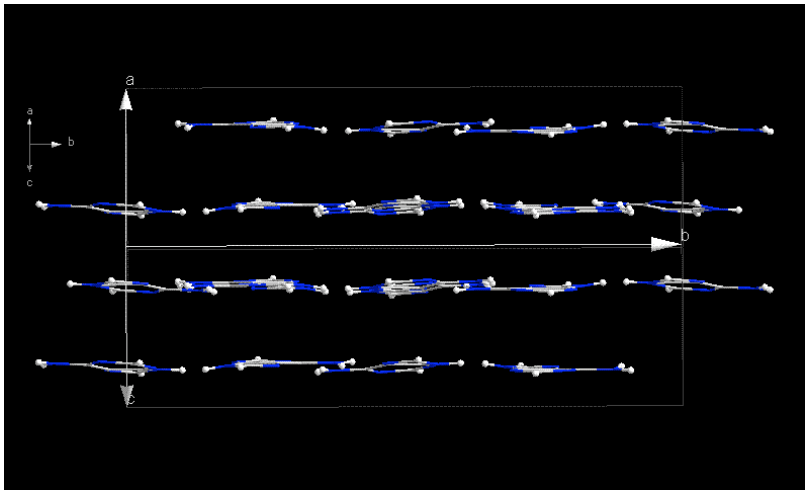

(b)

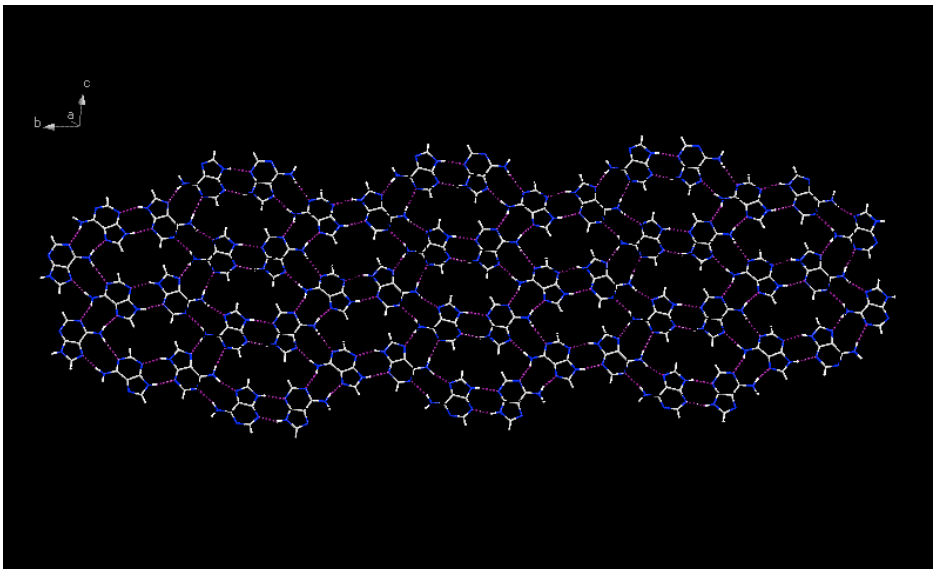

(c)

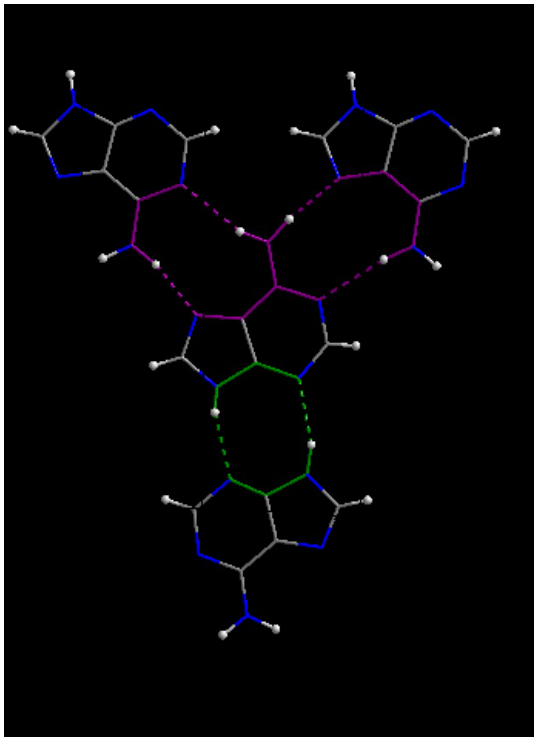

Figure 7.1.15 (a) Crystal packing of adenine, (b) sheet made of hydrogen-bonded rings forming a honeycomb pattern and (c) $R_2^2(8)$ and $R_2^2(9)$ motifs shown in green and violet respectively.

7.1.4.1 Single-Crystal Structure Determination

Following our work on the crystal structure determination of adenine by structure prediction and Rietveld refinement, we were alerted by personal communication of the concurrent work being done by Dr Andrew Bond from the University of Southern Denmark, on the single crystal structure determination of adenine.

His studies[10] using recrystallisation by slow cooling of a saturated solution in *N,N*-dimethylformamide, identified adenine as having a disordered *Fddd* structure (a = 8.470Å, b = 12.536Å, c = 22.297Å). The two components of disorder are related by a 2-fold rotation axis that passes through N2 and the midpoint of C4 [Figure 7.1.16].

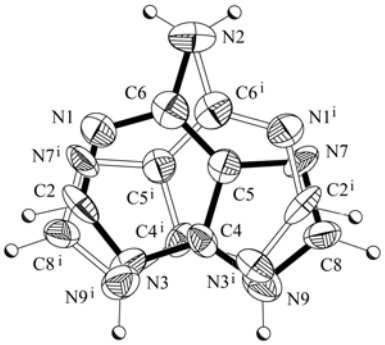

Figure 7.1.16 Two components of the adenine molecule disordered about a 2-fold rotation axis passing through N1 and the midpoint of C4 and C4^{i}. Displacement ellipsoids are shown at 50% probability for non-H atoms.

The resulting crystal packing is a two-dimensional hydrogen-bonded layer in which the same honeycomb pattern is formed within the layer if the disorder components are removed [Figure 7.1.17]. Close analysis of this disordered structure and our predicted/powder structure show that the ordered structure presented earlier in this chapter can be considered as an ordered approximation of the disordered structure, in which the structure within each layer is illustrated by our strong hydrogen-bonded honeycomb pattern, but that there is disorder between these layers. This is demonstrated by projection down multiple layers of the structure in which a 4-layer repeat of the ordered $P2_1/c$ model gives the same electron density as a 2-layer repeat of the disordered *Fddd* model.

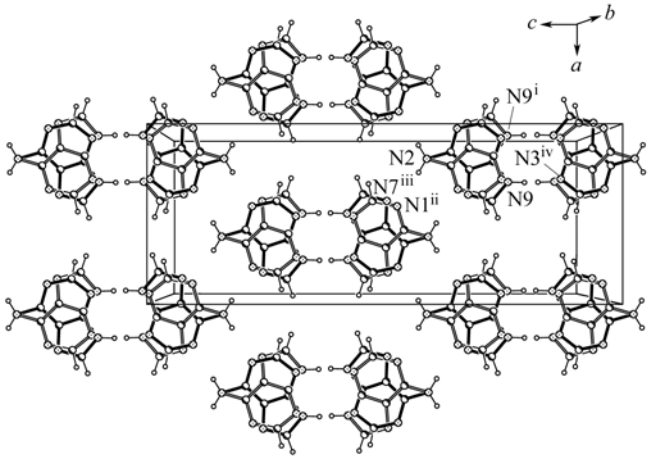

Figure 7.1.17 A single two-dimensional hydrogen-bonded layer in the ac plane, showing all disorder components.

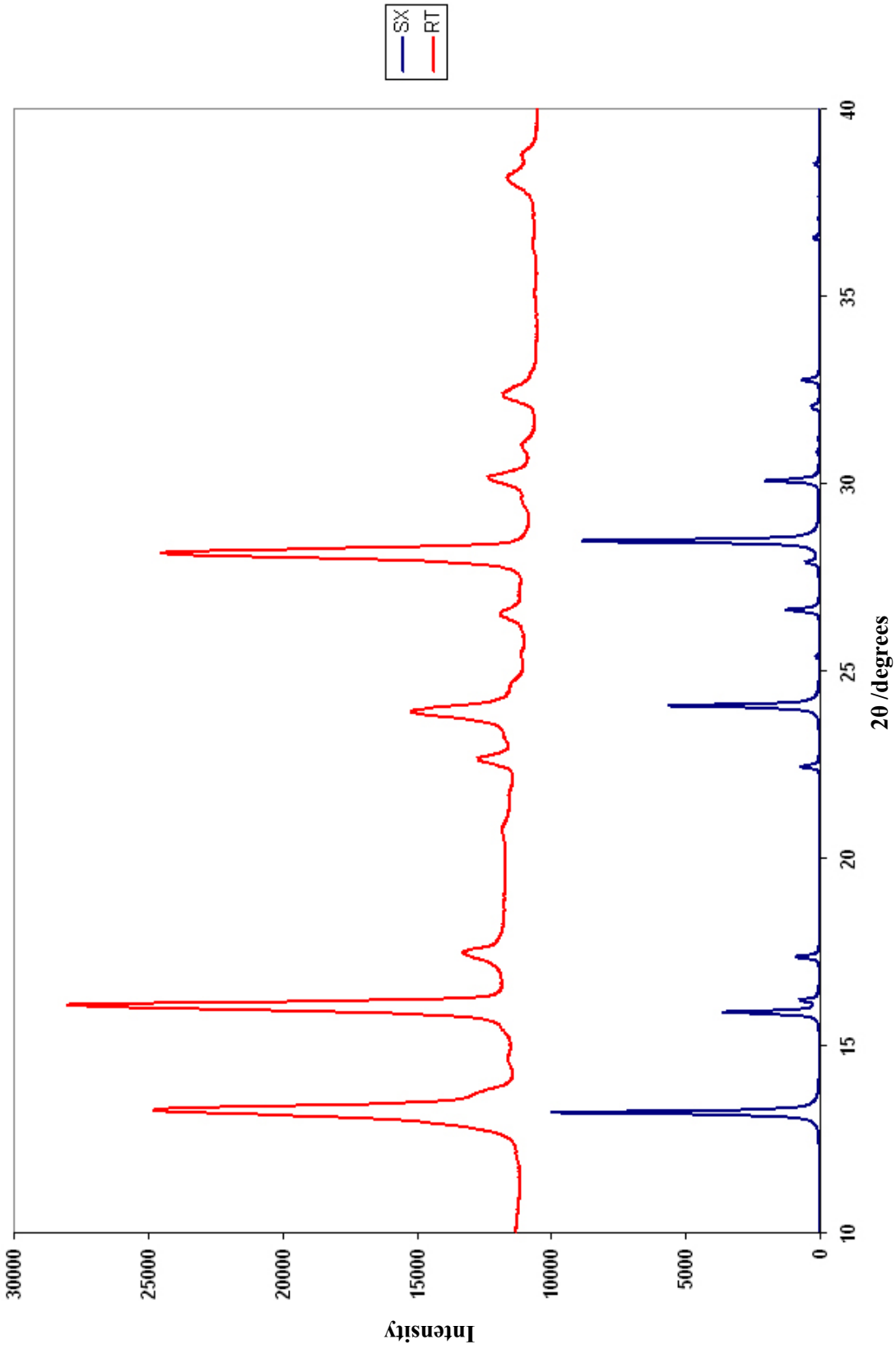

Figure 7.1.18 Powder diffraction patterns simulated from the single-crystal structure (SX) and the D5000 experimental data at room temperature (RT).

The close relationship between these two structural models is shown by the similarity between the experimental powder diffraction pattern used in Rietveld refinement and that simulated from the single-crystal structure [Figure 7.1.18]. As crystal structure prediction calculations cannot generate disordered structures, the difference between these structures is not unprecedented [Chapter 5], and is seen as a valuable insight into the possible nature of the disorder that is observed, although further work is needed on this aspect.

7.1.5 Low Temperature Data

Table 7.1.10 Unit cell parameters of predicted structure cc71 and from experimental data. The numbers in brackets denote the percentage change with respect to those values obtained from the 10K data.

Temperature (K)	***a (Å)***	***b (Å)***	***c (Å)***	***β(°)***	***Volume (Å³)***
Predicted values (0K)	7.495 (1)	21.831 (1)	7.485 (2)	112.43	1132.20
10 ***(% change)***	7.539 (1) (0.00)	22.166 (2) (0.00)	7.456 (3) (0.00)	112.23 (0.00)	1153.35 (0.00)
50 ***(% change)***	7.533 (2) (-0.08)	22.175 (1) (+0.04)	7.537 (1) (+1.09)	111.98 (-0.22)	1167.48 (+1.23)
100 ***(% change)***	7.525 (1) (-0.19)	22.183 (2) (+0.08)	7.589 (2) (+1.79)	111.94 (-0.26)	1175.09 (+1.88)
150 ***(% change)***	7.513 (1) (-0.34)	22.235 (1) (+0.31)	0.599 (1) (+1.91)	112.14 (-0.08)	1175.80 (+1.95)
200 ***(% change)***	7.621 (2) (+1.09)	22.252 (2) (+0.39)	7.675 (1) (+2.94)	113.19 (+0.86)	1196.27 (+3.72)
250 ***(% change)***	7.628 (1) (+1.17)	22.322 (1) (+0.70)	7.714 (1) (+3.47)	113.16 (+0.83)	1207.63 (+4.71)
293 ***(% change)***	7.703 (1) (+2.17)	22.477 (1) (+1.40)	7.790 (2) (+4.48)	113.17 (+0.84)	1239.99 (+7.51)

Since the theoretical predictions for adenine were carried out at 0K, the unit cell parameters of the lowest energy predicted structure were used as a starting point for a LeBail fit on the 10K data. The unit cell parameters obtained from this fit were used as a starting point for a LeBail fit on the 50K data. Subsequent LeBail fits on the remaining temperature data sets followed the same "stepwise" methodology [Table 7.1.10]. The powder diffraction pattern indicates a clear contraction in the unit cell with decreasing temperature, as indicated by the shift in position of peak ($\bar{1}12$) to an increase in 2θ [Figure 7.1.19]. The effect of changing temperature over the entire diffraction pattern from 10 to 40 degrees along 2θ is shown in Appendix A5.1.2.

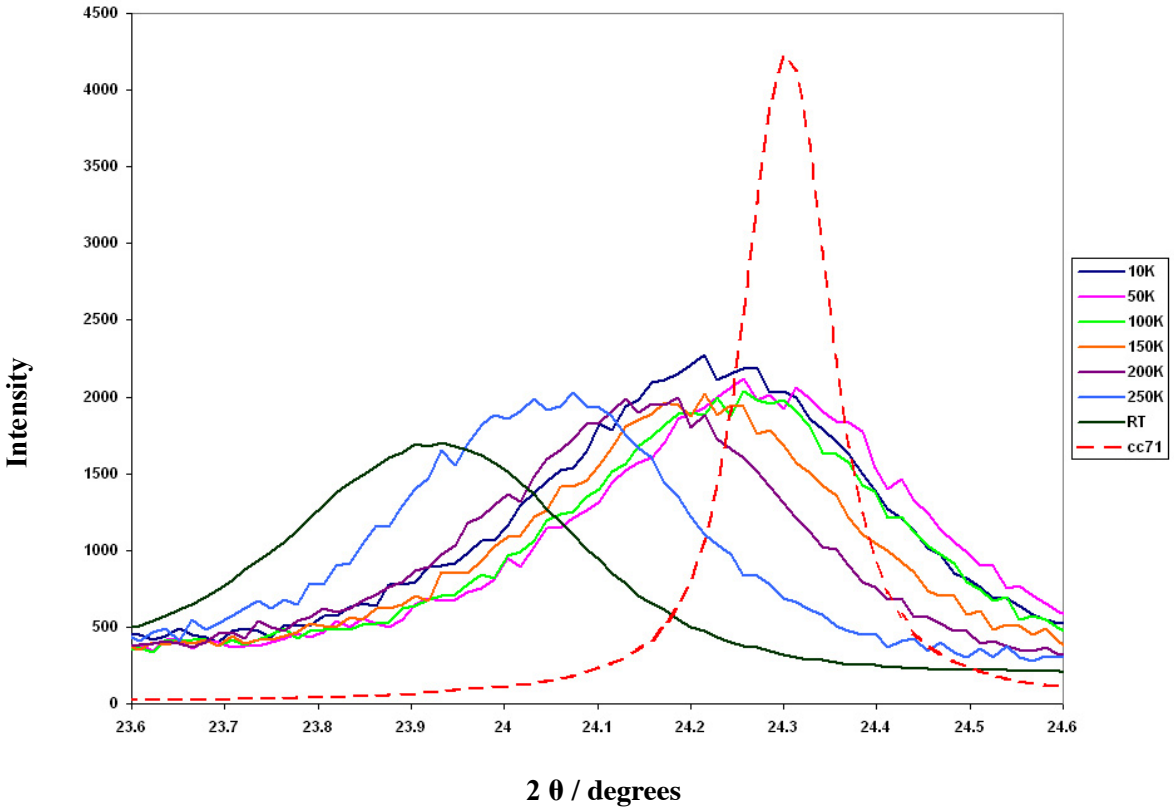

Figure 7.1.19 Section of superimposed powder diffraction data at all temperatures showing selected peak ($\bar{1}12$) shifting towards the right with decreasing temperature. The predicted structure (cc71) is indicated by the red dotted line.

The relatively poor crystallinity of this material (compared to other compounds studied in this thesis) is illustrated by the broader peaks in the experimental data shown in figure 7.1.19. This can often also be an indication of disordered components in the structure.

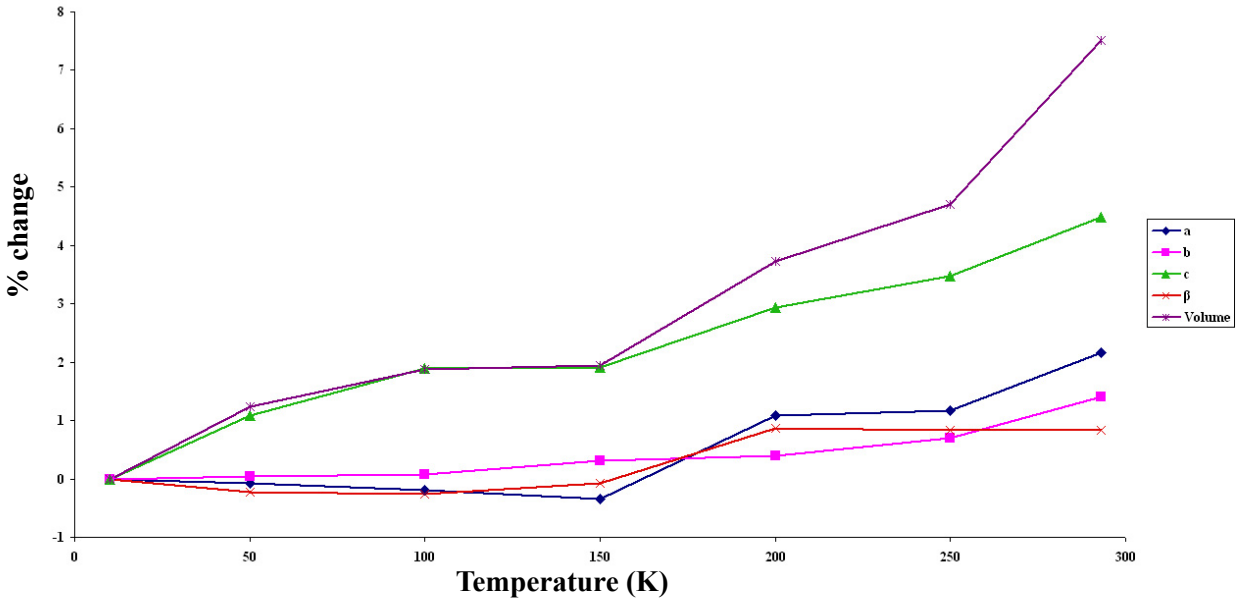

Figure 7.1.20 Graph showing the percentage change in unit cell dimensions with temperature.

The percentage differences in *a, b, c, β* and volume with varying temperature were calculated and show an overall increase in volume with temperature [Table 7.1.10]. Although generally, *a, b, c* and *β* also increased, there were minor fluctuations over the temperature range studied [Figure 7.1.20].

7.1.6 Discussion

The crystal structure of adenine was successfully solved using a combination of experimental data and computational predictions. R_{wp} was yet again too sensitive to the inherent shift in 2θ that arises due to the very nature of the comparison, and was therefore unsuccessful in identifying the correct structure. This was verified by visual comparison of the powder patterns obtained experimentally against the respective simulated patterns of the structures ranked first for each temperature [Appendix A5.1.3].

Although *PolySNAP* selected structure cc71 at all temperatures, the simulated powder pattern was visually compared to the experimental patterns to verify the similarity. Simulated patterns of the

structures ranked second at each temperature were also visually compared with the respective experimental patterns to substantiate the initial results. Successful refinement confirmed this further. Although *Compare.x* selected the wrong structure at room temperature, the correct structure was identified at all other temperatures, providing sufficient evidence in support of structure cc71. Analysis of the correlation results obtained with *Compare.x* over the range of triangle windows [Appendix A5.1.4] shows a predominance of structure cc71 for temperatures between 10K and 250K.

Following the visual and numerical verification of the correct structure, subsequent refinement, and discussions with Dr. Bond, adenine was found to be disordered. This is a feature that cannot be factored into computational predictions, and it remains to be deduced experimentally. It is also what possibly contributed to the broadening of peaks in the experimental powder patterns - and what made initial indexing impossible. Therefore in such cases, the combination of computational predictions with experimentally obtained powder data provides a means to overcoming these problems.

7.2 Guanine

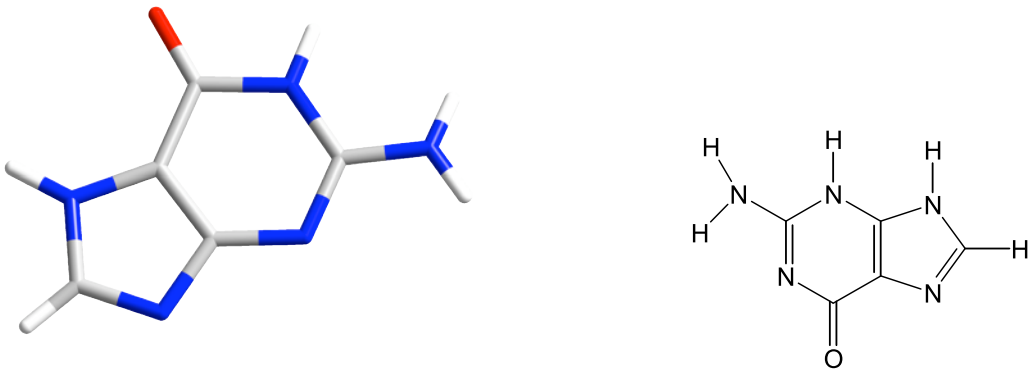

Figure 7.2.1 Guanine (2-amino-1,7-dihydro-6H-purin-6-one); 2-amino-6-oxypurine

7.2.1 Background

Guanine is another organic base belonging to the purine family, and it is one of the major constituents of nucleic acids. When combined with the sugar ribose in a glycosidic linkage, guanine forms a derivative called guanosine (a nucleoside) which in turn can be phosphorylated with from one to three phosphoric acid groups, yielding the three nucleotides GMP (guanosine monophosphate), GDP (guanosine diphosphate), and GTP (guanosine triphosphate). Analogous nucleosides and nucleotides are formed from guanine and the sugar deoxyribose.

The nucleotide derivatives of guanine perform important functions in cellular metabolism. GTP acts as a coenzyme in carbohydrate metabolism and in the biosynthesis of proteins; it can readily donate one of its phosphate groups to adenosine diphosphate (ADP) to form adenosine triphosphate (ATP), an extremely important derivative of adenine that acts as an intermediate in the transfer of chemical energy in living systems. GTP is the source of guanosine found in RNA and deoxyguanosine triphosphate (dGTP) is the source of deoxyguanosine in DNA. Thus guanine is intimately involved in the preservation and transfer of genetic information

Prior to the commencement of this study, the crystal structure of guanine had not yet been characterised, but related structures such as the monohydrate[11] have been published.

7.2.1.1 Experimental Polymorph Search[7]

An extensive polymorph search was carried out using a range of solvents, and crystallisations were mainly carried out by slow evaporation. The majority of solvents gave either guanine derivatives, or small particles of solid that were unsuitable for characterisation purposes.

7.2.1.2 Computational Polymorph Searches

Guanine contains both a six and a five-membered ring, along with an amine and a carbonyl group. At the time that the initial computational predictions were carried out, there was no crystal structure published for guanine. The most closely-related structure available was guanine monohydrate[11], in which the amino group is approximately coplanar with the ring (H-N-C-N 171.27°). For this reason, the initial searches were carried out using a planar molecular model. These calculations resulted in 22 unique structures lying within 7 kJ mol^{-1} of the global lattice energy minimum. The lowest energy hypothetical structures all consisted of three-dimensional hydrogen bond networks in which the carbonyl oxygen acts as a hydrogen bond acceptor.

The publication of the low temperature single crystal structure of guanine (120K) by Guille and Clegg[12] in 2006 led to the decision to carry out additional computational searches, in which three possible tautomers were considered. The original tautomer that was used in the initial search was derived from the monohydrate structure and corresponds to tautomer 39. The published single crystal structure was found to contain tautomer 17, while a search on another possible tautomer (tautomer 19) was also carried out for completion. [Figure 7.2.2]

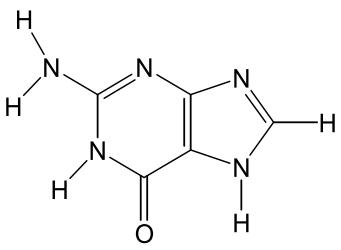

TAUTOMER 39
(initial search)

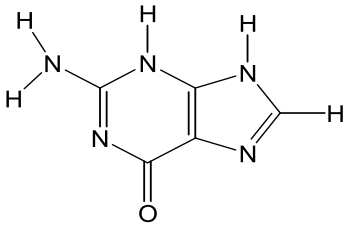

TAUTOMER 17
(published single crystal)

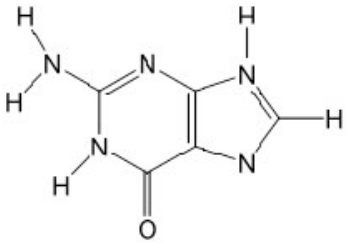

TAUTOMER 19
(hypothetical)

Figure 7.2.2 The three tautomers for guanine.

The searches resulted in 45 low-energy structures for tautomer 17 (with 9 structures within 7 kJ mol^{-1} of the lattice energy minimum), 40 structures for tautomer 19, and 23 structures for tautomer 39 [Figures 7.2.3 - 7.2.5 and Table 7.2.1]. In each of the latter two searches four structures were clearly lower in lattice energy when compared to the rest. These were found within 4-5 kJ mol^{-1} of the global minimum. The lattice energy minimum in the search for tautomer 17 was structure am8; this structure corresponded to the published experimental structure[12] [Table 7.2.2]. In the search for tautomer 19, the lattice energy minimum was structure ai48; this structure was later chosen as the starting point for LeBail fitting. In terms of the lowest energy minimum overall, this was identified as structure de43 in the tautomer 39 search. Structure am18 was ranked lowest overall (also in the tautomer 39 search) according to free energy.

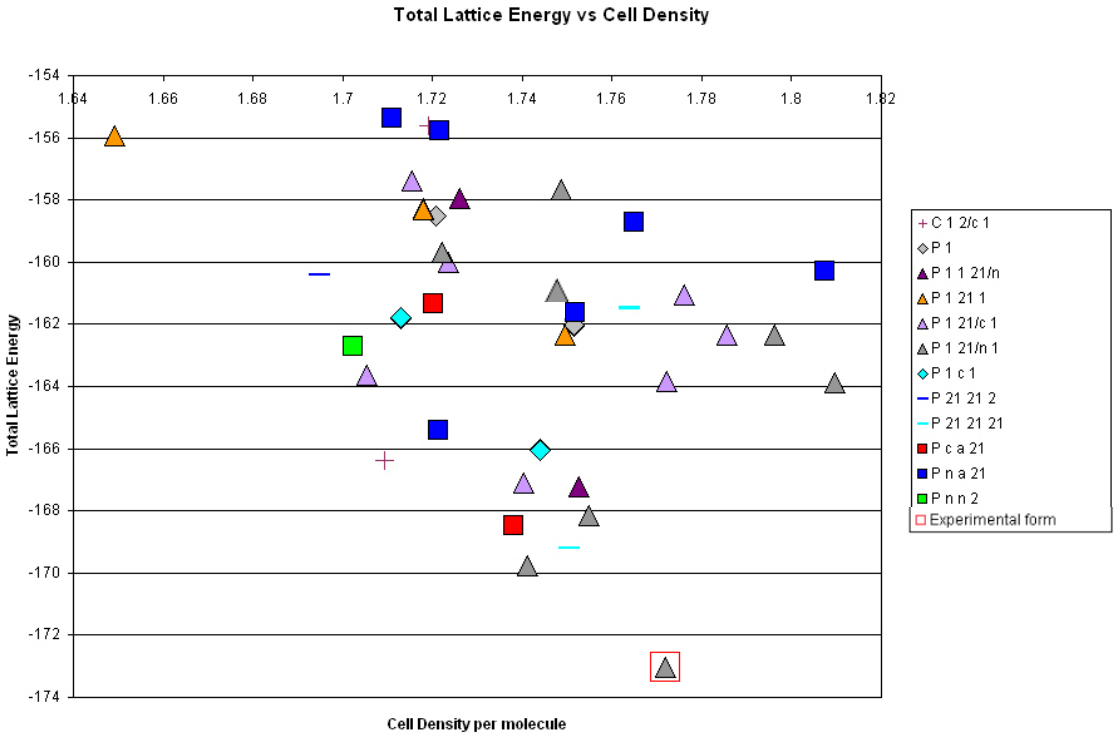

Figure 7.2.3 The results of the computational search for tautomer 17. The predicted structure corresponding to the published structure is shown by the red square. [This graph was reproduced from the CPOSS database with permission.]

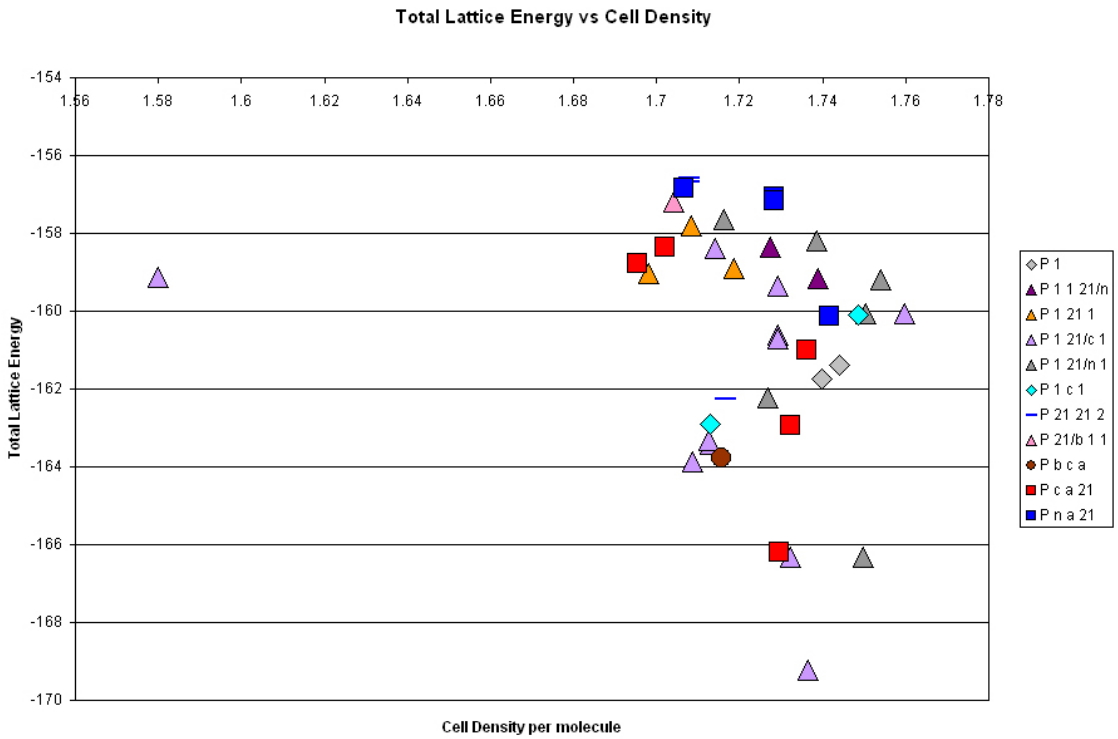

Figure 7.2.4 The results of the computational search for tautomer 19. [This graph was reproduced from the CPOSS database with permission.]

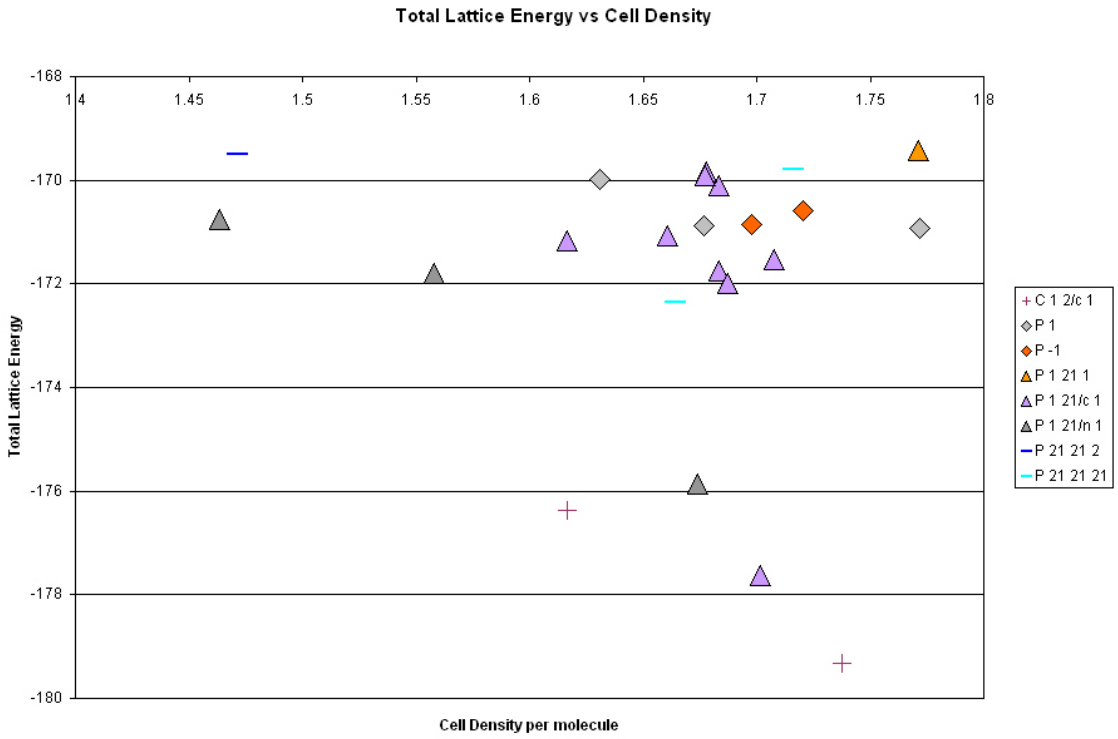

Figure 7.2.5 The results of the computational search for tautomer 39. [This graph was reproduced from the CPOSS database with permission.]

*Table 7.2.1 The low energy crystal structures (found within a maximum of 7 kJ mol^{-1}) of the global lattice energy minimum in the computational searches for the three tautomers. Structures marked * have Z=8 (Z'=2), while all the rest have Z=4 (Z'=1).*

STRUCTURE	SPACE GROUP	LATTICE ENERGY (kJ/mol)	FREE ENERGY (kJ/mol)	DENSITY (g/cm3)	REDUCED CELL					
					a(Å)	*b*(Å)	*c*(Å)	*α*(°)	*β*(°)	*γ*(°)
Tautomer 17										
am8	$P\,2_1/n$	-173.03	-184.5	1.7719	3.541	9.808	16.431	90	83.166	90
am72	$P\,2_1/n$	-169.75	-180.16	1.7411	8.787	9.798	10.796	90	38.336	90
aq10	$P\,2_12_12_1$	-169.19	-169.19	1.7504	17.23	9.865	3.3734	90	90	90
cd44*	$P\,c\,a\,2_1$	-168.48	-180.123	1.738	9.788	6.502	18.151	90	90	90
am1	$P\,2_1/n$	-168.14	-180.655	1.7549	3.767	18.25	8.4544	90	79.84	90
cd25*	$P\,2_1/n$	-167.22	-179.3	1.7527	18.58	6.261	9.8485	90	90	89.99
am12	$P\,2_1/c$	-167.11	-179.4	1.7404	3.474	9.639	19.101	90	115.599	90
dd94	$C\,2/c$	-166.37	-176.22	1.7094	9.77	9.839	12.97	90	70.388	90
cd49*	$P\,c$	-166.07	-166.07	1.7441	18.58	9.845	6.4459	90	77.559	90
Tautomer 19										
ai48	$P\,2_1/c$	-169.22	-181.566	1.7366	3.466	9.63	17.332	90	92.269	90
am101	$P\,2_1/n$	-166.33	-176.809	1.7498	4.292	16.18	8.4036	90	79.362	90
ai83	$P\,2_1/c$	-166.31	-166.31	1.7324	3.565	16.59	10.112	90	75.709	90
cb24*	$P\,c\,a\,2_1$	-166.2	-176.787	1.7296	16.18	10.07	7.1285	90	90	90
am63	$P\,2_1/c$	-163.86	-176.044	1.7087	3.586	9.542	17.245	90	84.519	90
Tautomer 39										
de43	$C\,2/c$	-179.32	-188.424	1.7375	12.43	7.465	19.408	90	39.922	90
ai79	$P\,2_1/c$	-177.64	-188.241	1.7015	7.061	7.391	12.7	90	117.105	90
de87	$C\,2/c$	-176.36	-186.641	1.6168	13.3	6.786	14.162	90	76.31	90
am18	$P\,2_1/n$	-175.86	-189.538	1.674	3.693	11.27	15.949	90	64.602	90
aq91	$P\,2_12_12_1$	-172.35	-185.481	1.6639	13.92	11.46	3.7833	90	90	90

Table 7.2.2 Unit cell parameters of the published single crystal structure and the corresponding predicted structure for tautomer 17.

Structure	***a (Å)***	***b (Å)***	***c (Å)***	***β (°)***	***Volume (Å³)***	***Space Group***
Published Values[12] (120K)	3.553(16)	9.693(4)	16.345(7)	95.148(6)	560.1(4)	$P2_1/c$
am8 (0K)	3.541	9.808	16.431	83.17	566.6	$P2_1/n$

7.2.2 Results

When powder data were collected for guanine, the single crystal structure had not been published yet. As it was an unknown crystal structure, the room temperature data were indexed by the DICVOL[13] program on the basis of the first nineteen lines [Appendix A5.2.2]. A monoclinic cell resulted, and this was found to be closely-related to structure ai48, the lowest energy structure from the search for tautomer 19. The powder pattern of ai48 was simulated for visual comparison with the experimental powder pattern [Figure 7.2.6], and a LeBail fit was done on the indexed data. [Figure 7.2.7, Table 7.2.3]

Table 7.2.3 Unit cell parameters of the predicted structure ai48, those obtained from the Le Bail fit and the index results.

Structure	***a (Å)***	***b (Å)***	***c (Å)***	***β (°)***	***Volume (Å³)***	***Space Group***
ai48 (0K)	3.466	9.630	17.332	92.27	578.03	$P\,2_1/c$
LeBail	3.449	8.652	18.644	99.67	548.37	$P\,2_1/c$
Index Results	3.442	8.660	18.687	99.59	549.31	$P\,2_1/c$

Additional powder data were obtained from Toni Llinas (Department of Chemistry, University of Cambridge) and these were included in subsequent comparisons, both visual and automated. Subtle differences were observed between these data, the single crystal simulated pattern, and the experimental pattern [Figure 7.2.8]. In the experimental pattern, the range of peaks at positions 20-22° and the peak at 29.5° along 2θ appear in Llinas' data, but do not have single crystal counterparts. In addition, the peak at 43.5° on the experimental pattern does not appear in either of the other two patterns. This suggests that although the three structures are clearly related, Llinas' data appears to be a mixture of the other two.

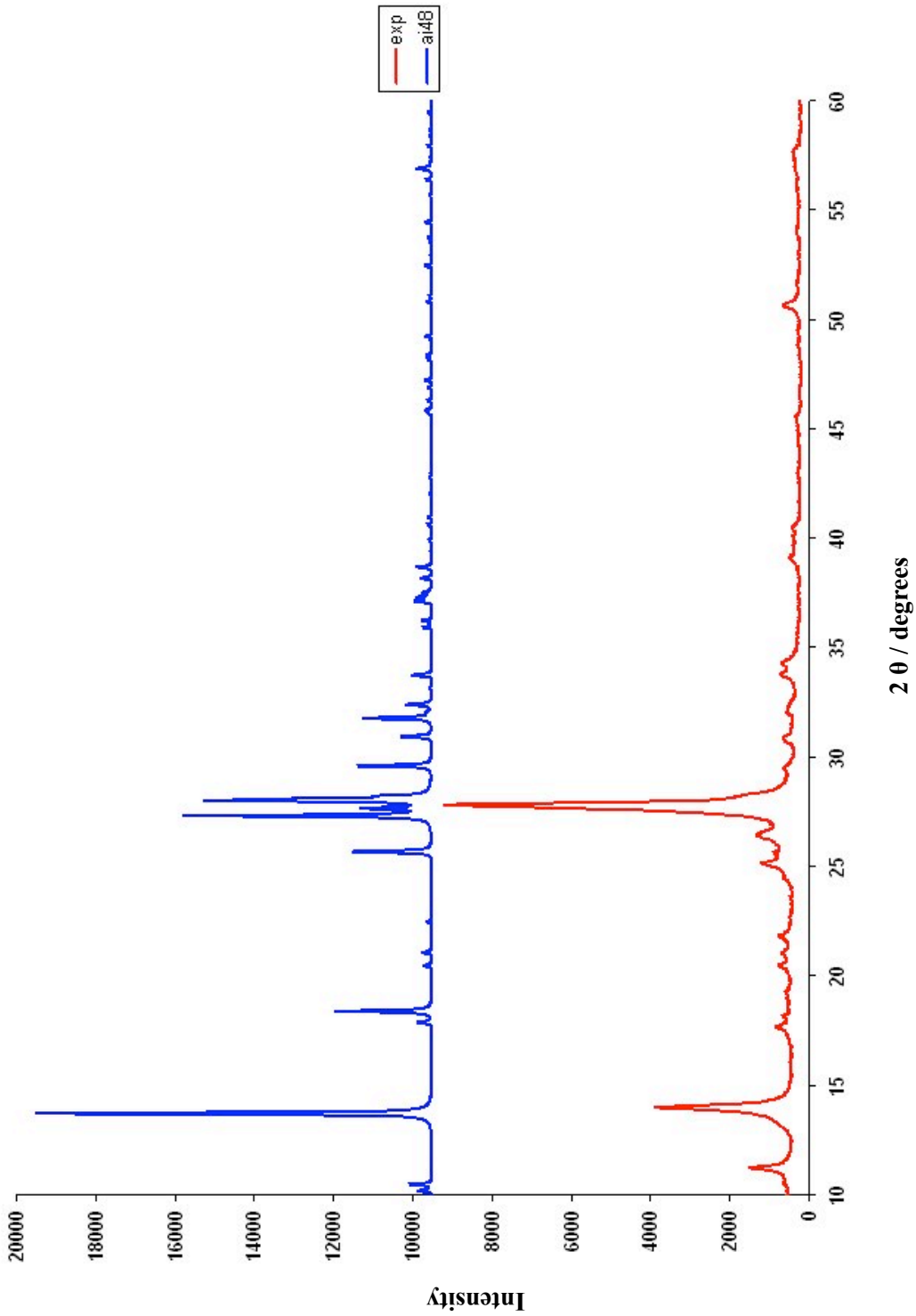

Figure 7.2.6 Powder diffraction pattern of predicted structure ai48 and the experimental data at room temperature (D5000).

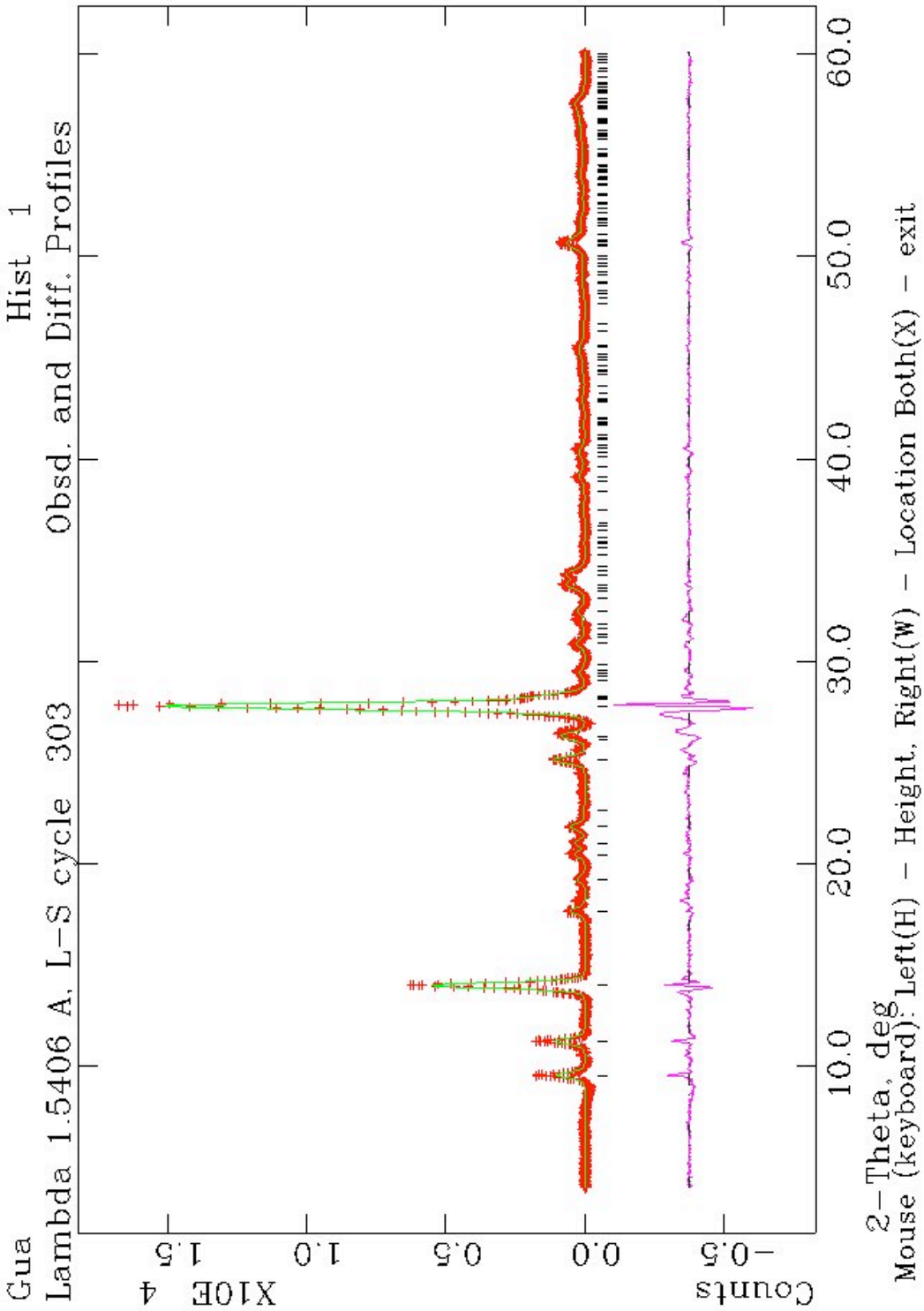

Figure 7.2.7 Le Bail fit of the experimental data at room temperature (D5000) using parameters from structure ai48 as a starting point.

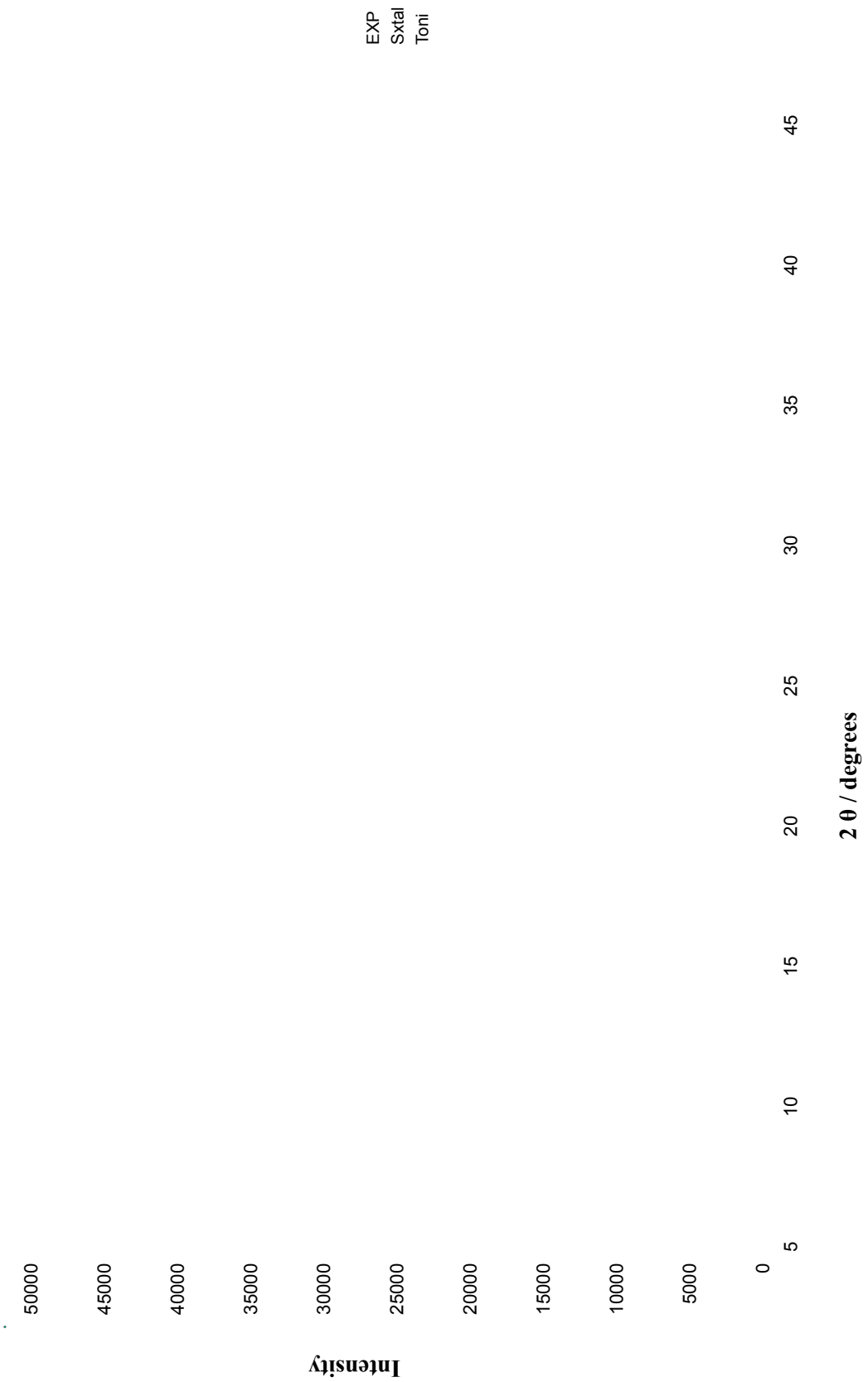

Figure 7.2.8 (a) Powder diffraction patterns of the single crystal structure, Toni Llinas' structure and the experimental data at room temperature (full range in 2θ).

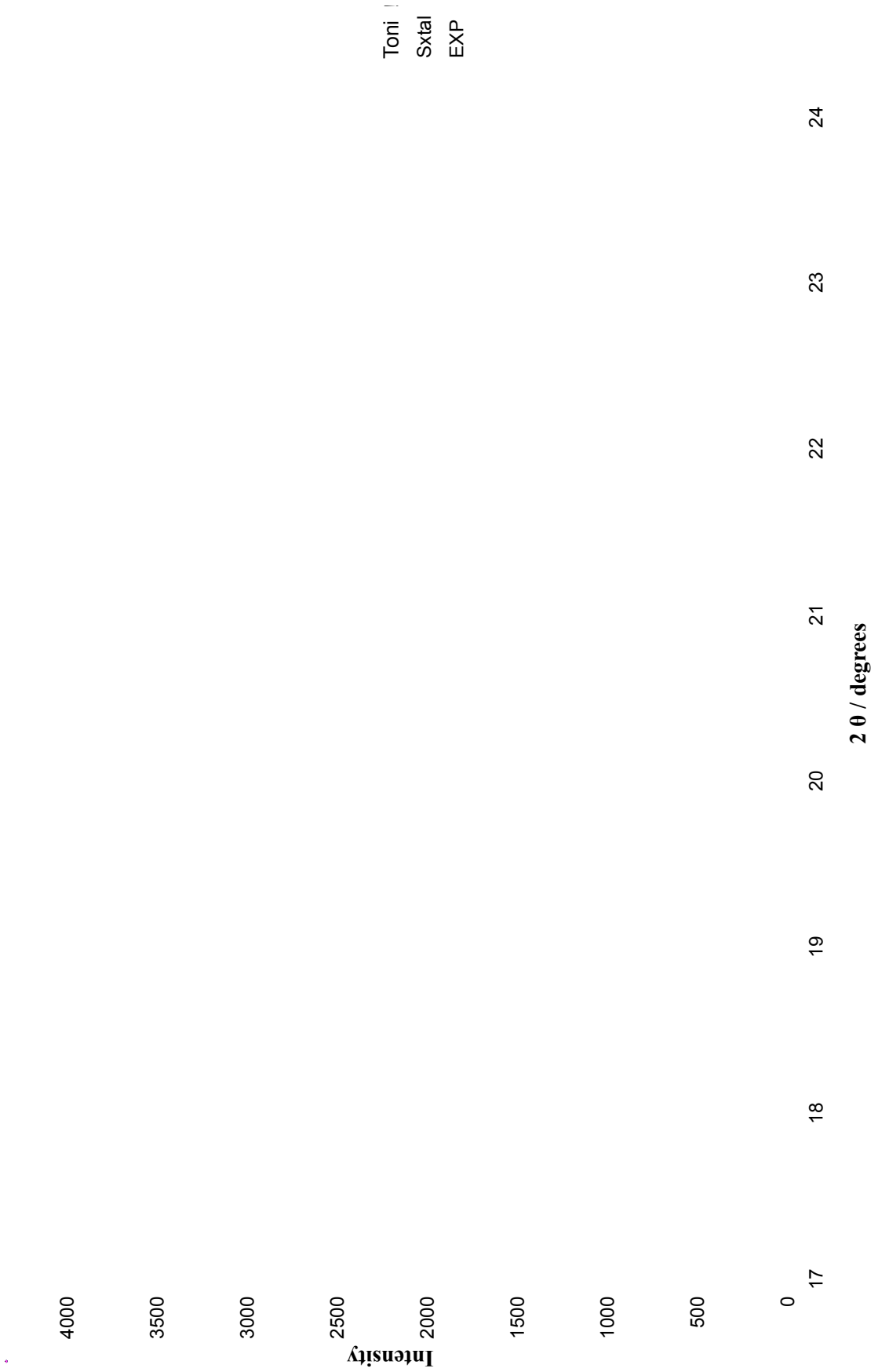

Figure 7.2.8 (b) Powder diffraction patterns of the single crystal structure, Toni Llinas' structure and the experimental data at room temperature (section in 2θ).

7.2.2.1 PolySNAP

PolySNAP analysis was carried out using all seven experimental data sets (from 10K to 293K), Toni Llinas' data and that simulated from the single crystal structure, against all the structures predicted for the three tautomers [Figures 7.2.9-7.2.14]. The powder diffraction pattern simulated from the single crystal structure gave the highest correlation with that simulated from structure am8; the lowest energy structure in the computational search for tautomer 17. Toni Llinas' structure was ranked as being most similar to aq10 (tautomer 17), while our experimental data was grouped with structures dd94 and am92, from the searches for tautomers 17 and 19 respectively. Upon visual comparison of the simulated patterns for these structures and structure ai48 with the D5005 room temperature powder pattern, some similarities were found between the experimental data and both dd94 and ai48 [Figure 7.2.15].

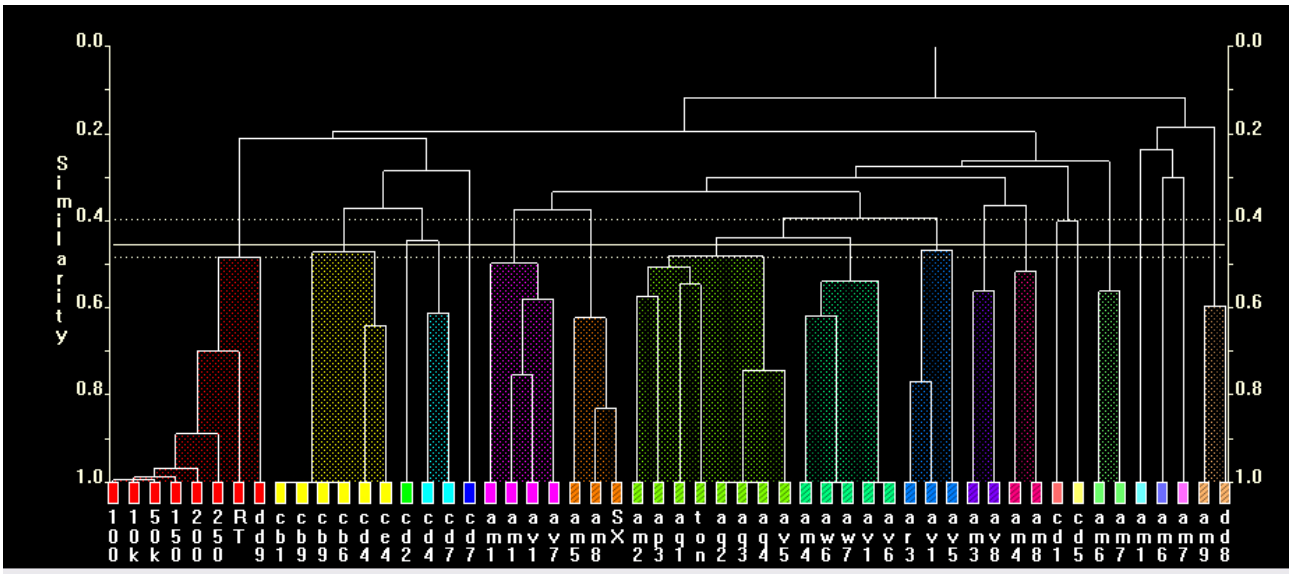

Figure 7.2.9. Dendrogram showing similarity correlation clusters for predicted tautomer 17 structures, the published structure (shown as SX), Toni Llinas' data (shown as Toni) and experimental guanine powder diffraction patterns over a range of temperatures.

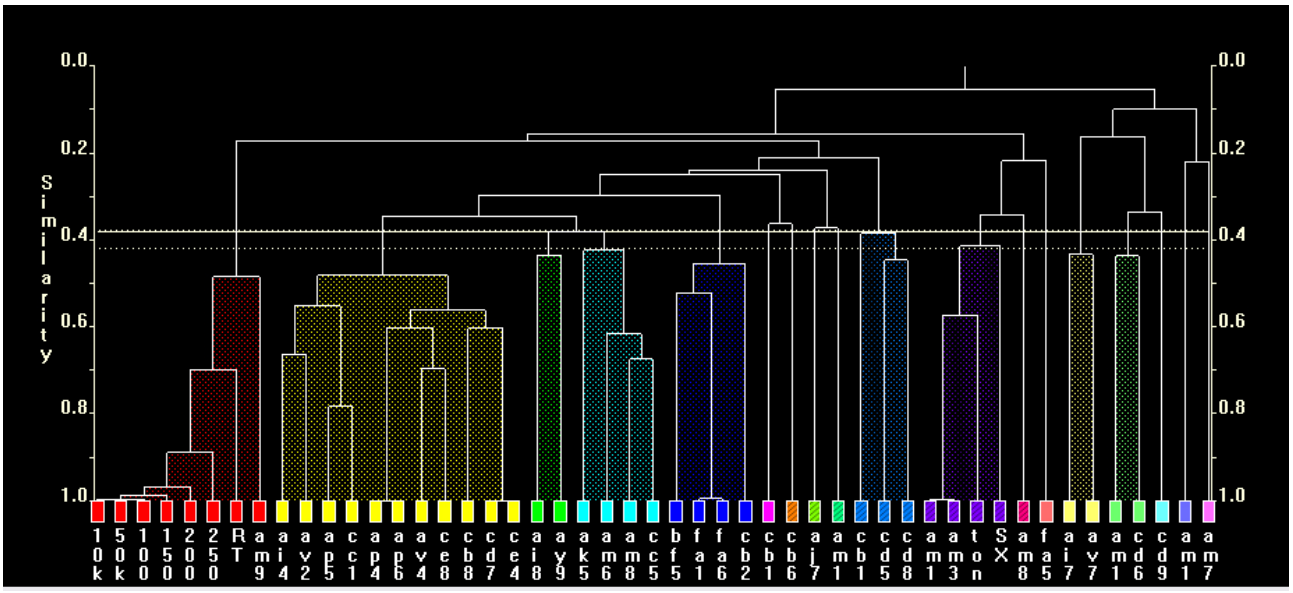

Figure 7.2.10. Dendrogram showing similarity correlation clusters for predicted tautomer 19 structures, the published structure (shown as SX), Toni Llinas' data (shown as Toni) and experimental guanine powder diffraction patterns over a range of temperatures.

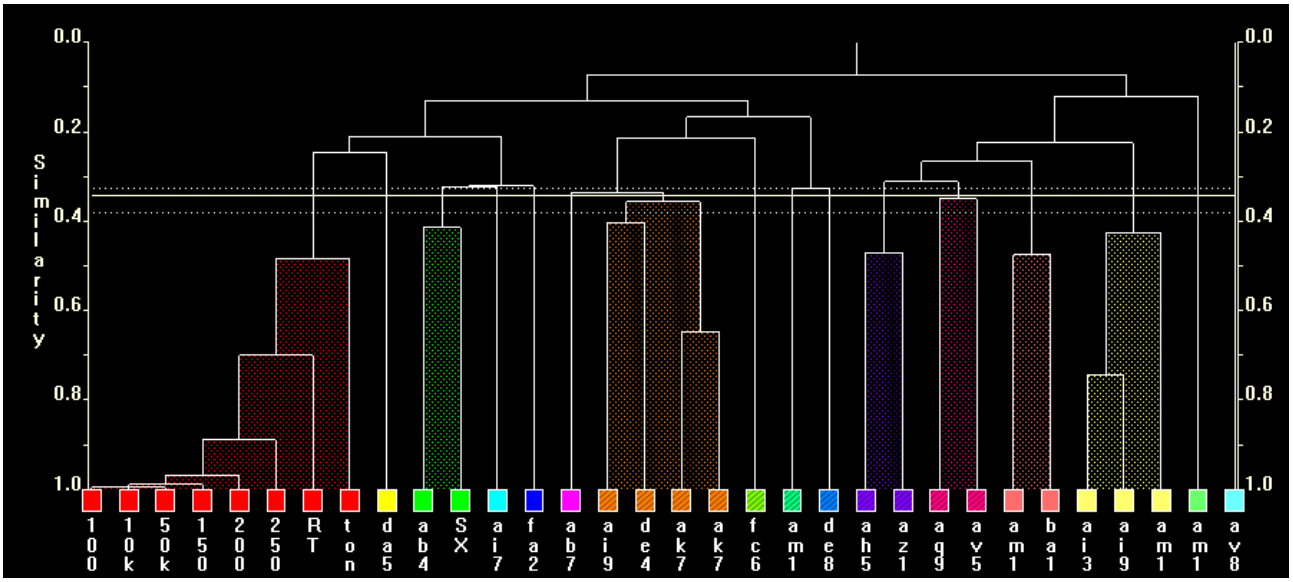

Figure 7.2.11. Dendrogram showing similarity correlation clusters for predicted tautomer 39 structures, the published structure (shown as SX), Toni Llinas' data (shown as Toni) and experimental guanine powder diffraction patterns over a range of temperatures.

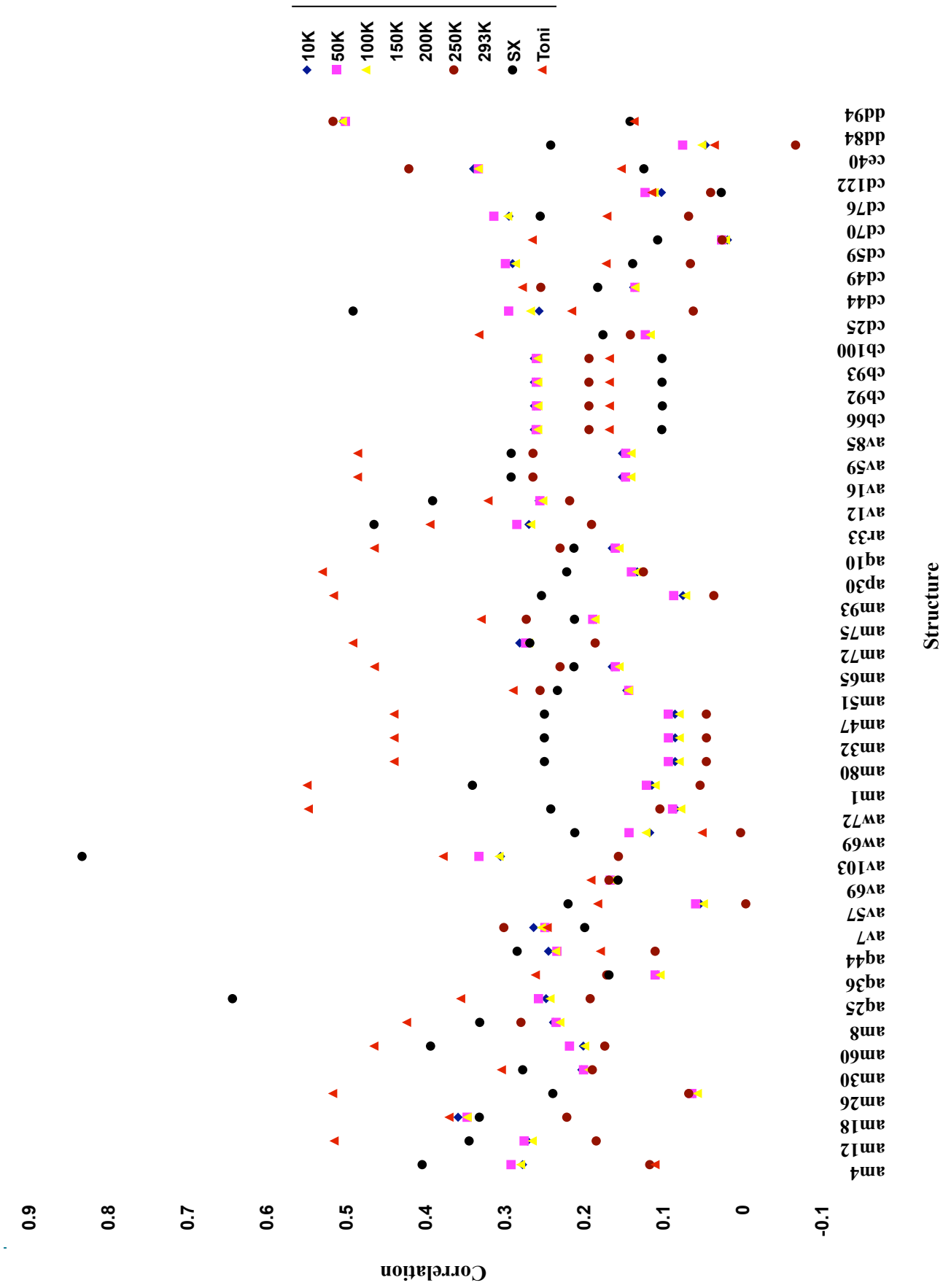

Figure 7.2.12 Correlation coefficients of all predicted structures for tautomer 17 at each experimental temperature and against the published structure (SX) and Toni Llinas' data (Toni)

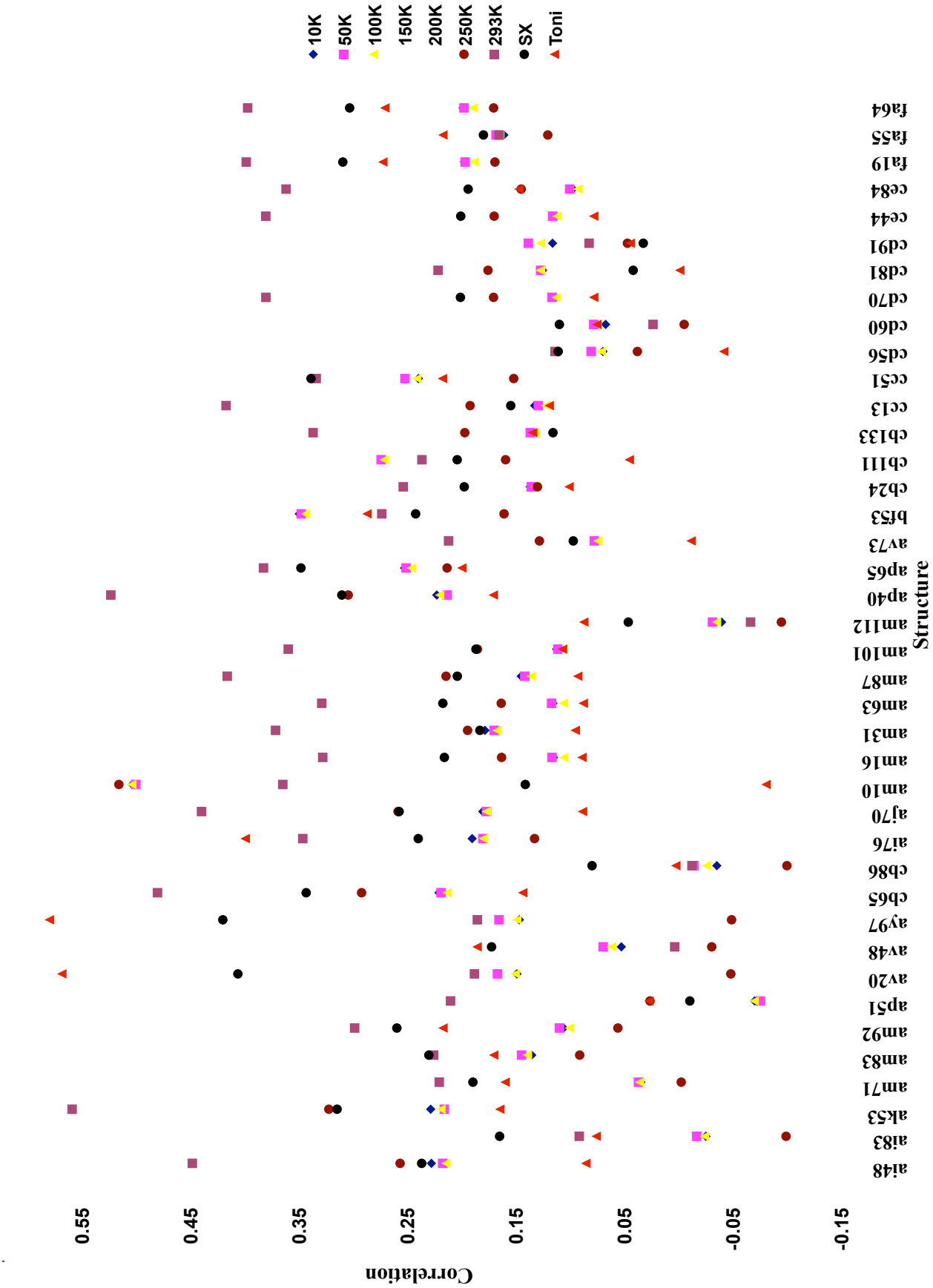

Figure 7.2.13 Correlation coefficients of all predicted structures for tautomer 19 at each experimental temperature and against the published structure (SX) and Toni Llinas' data (Toni)

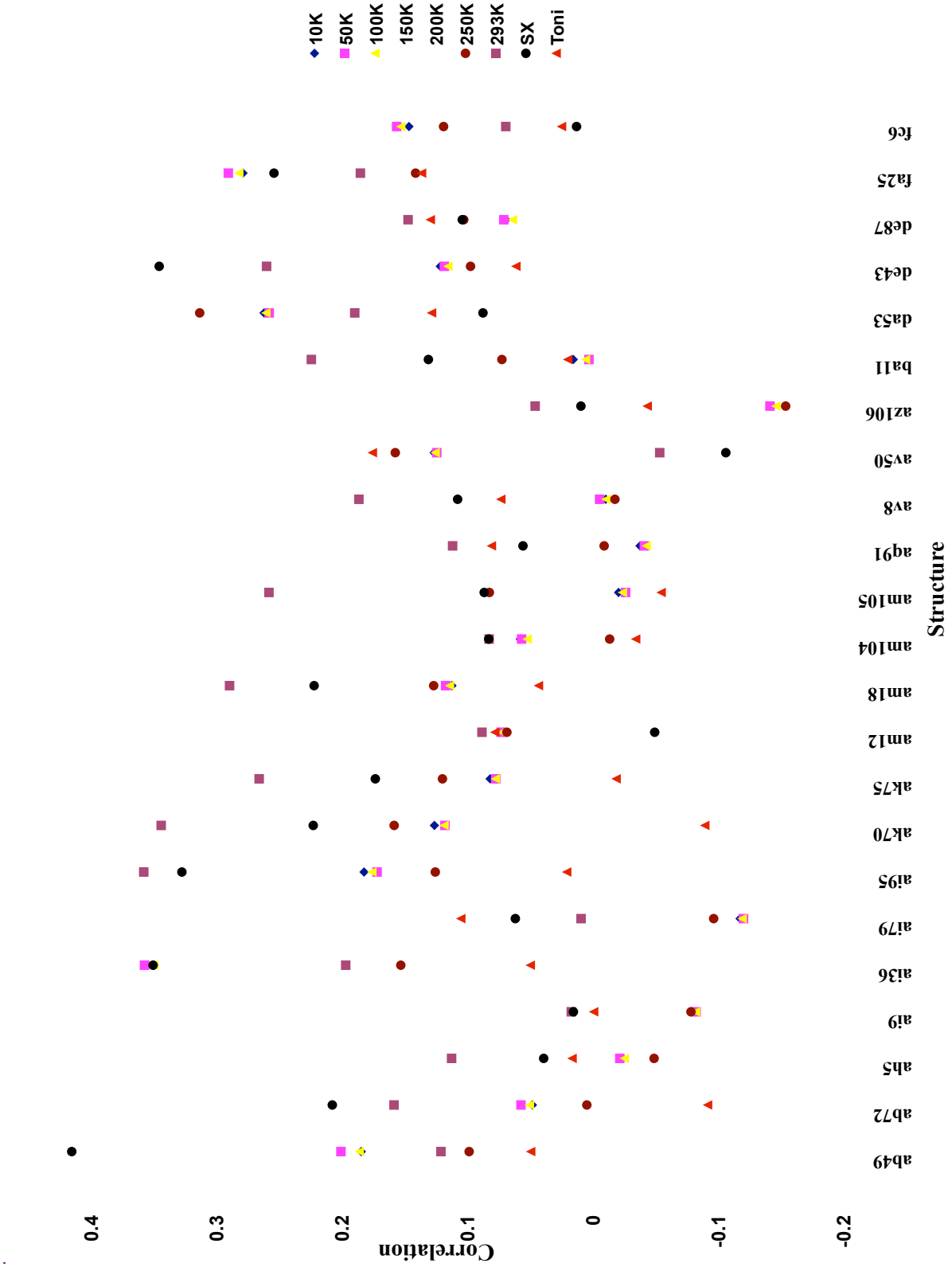

Figure 7.2.14 Correlation coefficients of all predicted structures for tautomer 39 at each experimental temperature and against the published structure (SX) and Toni Llinas' structure (Toni)

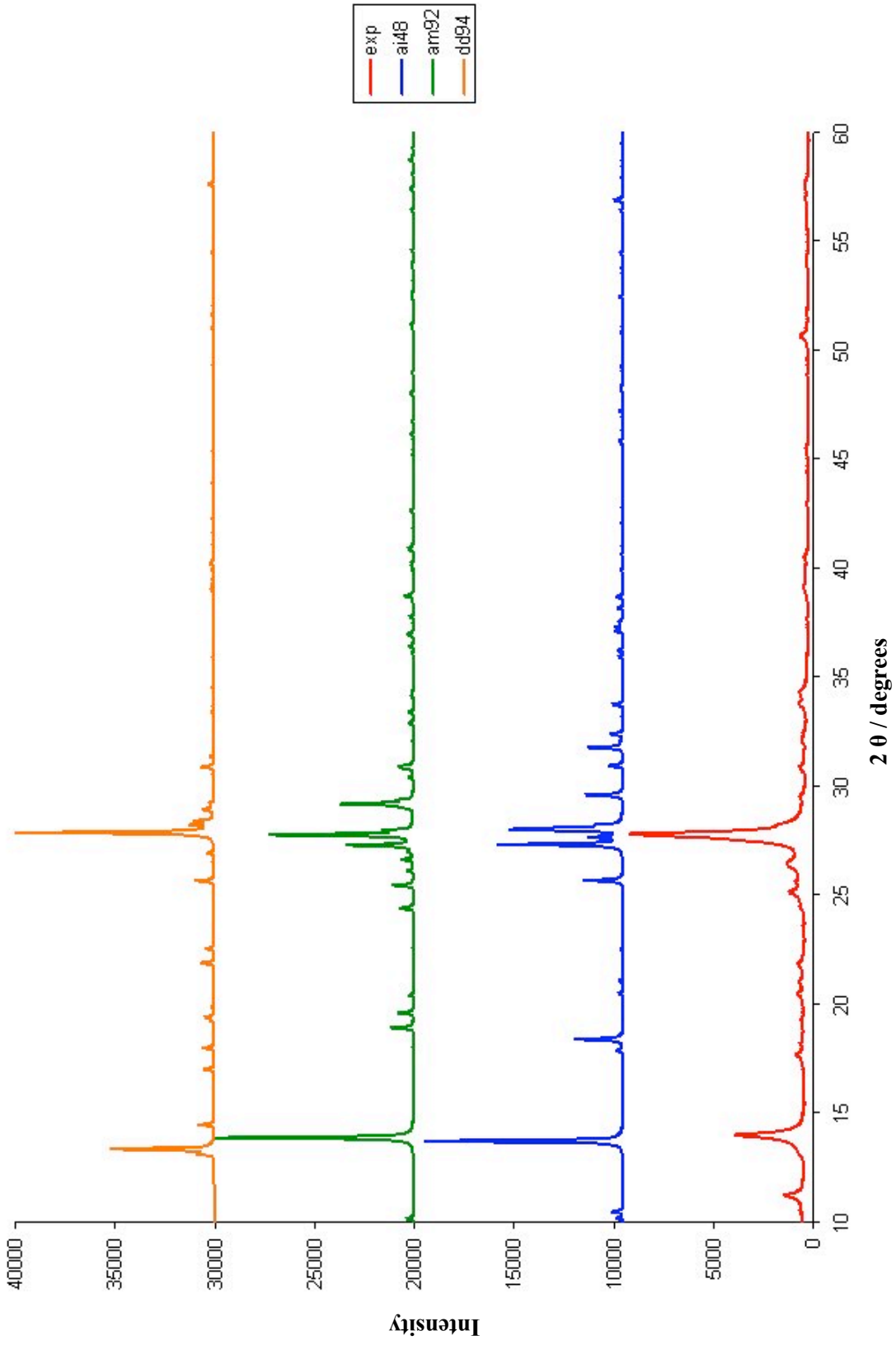

Figure 7.2.15 Powder diffraction patterns of predicted structures dd94, am92 and ai48 and the D5000 experimental structure at room temperature.

In all cases, low temperature data were once again classed together (denoted in red in the dendrograms). Within this cluster, the three lower temperature data sets (10K, 50K and 100K) bore the highest correlation to one another. In the comparison for tautomer 17 [Figure 7.2.9], the three experimental data sets were placed in separate clusters (ours in red, the published data in orange and Llinas' in green), though raising the cut-off point from its arbitrary position of 0.47 would see Llinas' data being grouped with the published structure. The tautomer 19 comparison [Figure 7.2.10] grouped the published structure and Llinas' data in the same cluster (denoted in purple), while in the comparison for tautomer 39, our data was grouped with Llinas' (red), and the published data was grouped separately (in green) [Figure 7.2.11]. Raising the cut-off point for the latter would lead to all three data sets being grouped together. The fact that *PolySNAP* comparisons employ PCA for classification of structure patterns [Chapter 2.1.2] justifies the experimental structures being classified differently for each tautomer comparison. This is primarily because clustering of experimental patterns by this method depends greatly on the structure patterns with which they are being compared.

7.2.3 Low Temperature Data

Using the unit cell parameters from the Le Bail fit on the D5000 data, a Le Bail fit was done on the room temperature reflection geometry data. The unit cell parameters obtained from this fit were then used as a starting point for fitting the data obtained at 250K. Subsequent Le Bail fits were carried out on the remaining data collected over a range of temperatures, using the same methodology [Table 7.2.4].

As expected, there is a clear contraction of the unit cell with decreasing temperature. This is shown by the marked decrease in volume, and the steady decrease in a and b with temperature. In order to accomodate this change in volume, c and β fluctuate accordingly. The percentage differences in a, b, c, β and volume with varying temperature with respect to the 10K data were calculated [Figure 7.2.16]. The contraction in the unit cell with decreasing temperature can also be observed in the powder diffraction patterns, as indicated by the shift in position of peak (111) to a higher 2θ value as lower temperatures are reached [Figure 7.2.17]. The effect of changing temperature over the entire diffraction pattern from 10 to 50 degrees along 2θ is shown in Appendix A5.2.1.

Table 7.2.4 Unit cell parameters of published structure and those obtained from the LeBail fit on the D5000 and D5005 experimental data over a range of temperatures. The numbers in brackets denote the percentage change with respect to those values obtained from the 10K data.

Structure	***a (Å)***	***b (Å)***	***c (Å)***	β ***(º)***	***Volume (Å³)***
Published values (120K)	3.553	9.693	16.345	95.148	560.1
D5000 (after index)	3.469	8.652	18.644	99.67	548.37
10 ***(% change)***	3.2001 *(0.00)*	8.2581 *(0.00)*	18.2816 *(0.00)*	96.86 *(0.00)*	479.67 *(0.00)*
50 ***(% change)***	3.3500 *(+4.68)*	8.2405 *(-0.21)*	18.2365 *(-0.25)*	96.22 *(-0.66)*	500.48 *(+4.34)*
100 ***(% change)***	3.3743 *(+5.44)*	8.3385 (+0.97)	18.4346 *(+0.84)*	96.33 *(-0.55)*	515.52 *(+7.47)*
150 ***(% change)***	3.3926 *(+6.02)*	8.5169 *(+3.13)*	18.3957 *(+0.62)*	97.37 *(+0.53)*	527.14 *(+9.90)*
200 ***(% change)***	3.4097 *(+6.55)*	8.5319 *(+3.32)*	18.5333 *(+1.38)*	97.04 *(+0.19)*	535.08 *(+11.55)*
250 ***(% change)***	3.4380 *(+7.43)*	8.5546 *(+3.59)*	18.5477 *(+1.46)*	97.36 *(+0.52)*	540.99 *(+12.78)*
293 ***(% change)***	3.4531 *(+7.91)*	8.6123 *(+4.29)*	18.5236 *(+1.32)*	97.27 *(+0.42)*	546.46 *(+13.92)*
293 (D5000)	3.4486 *(+7.77)*	8.6517 *(+4.77)*	18.6439 *(+1.98)*	99.66 *(+2.89)*	548.37 *(+14.32)*

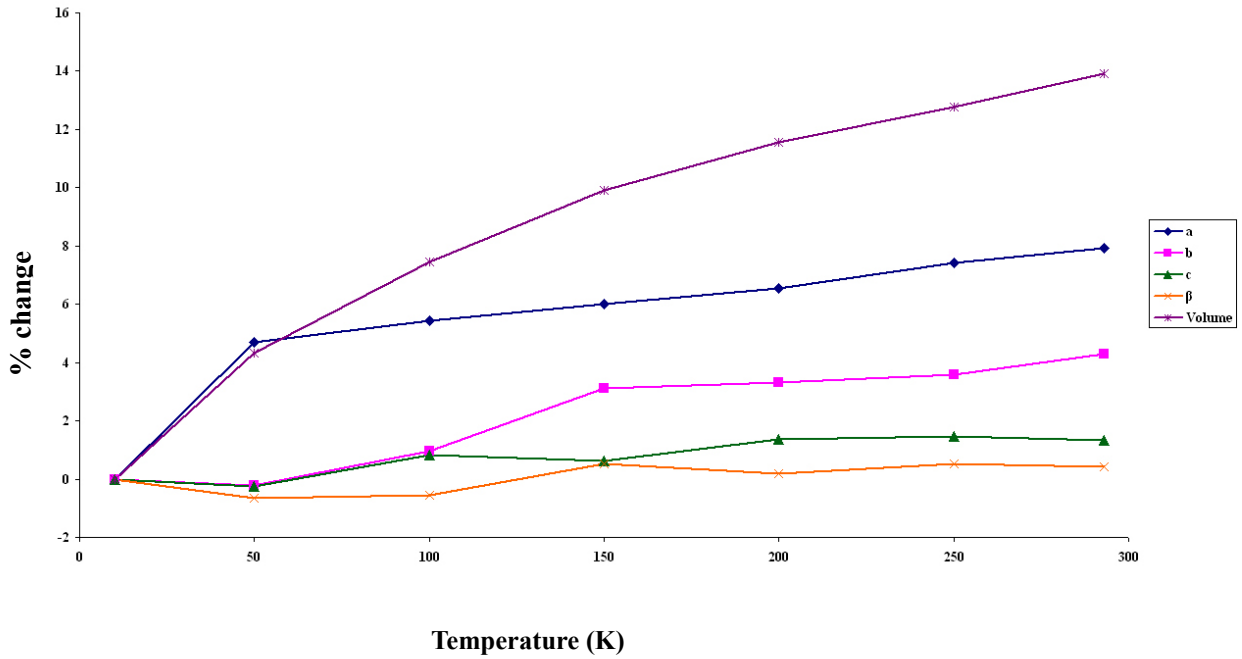

Figure 7.2.16 Graph showing the percentage change in unit cell dimensions with temperature.

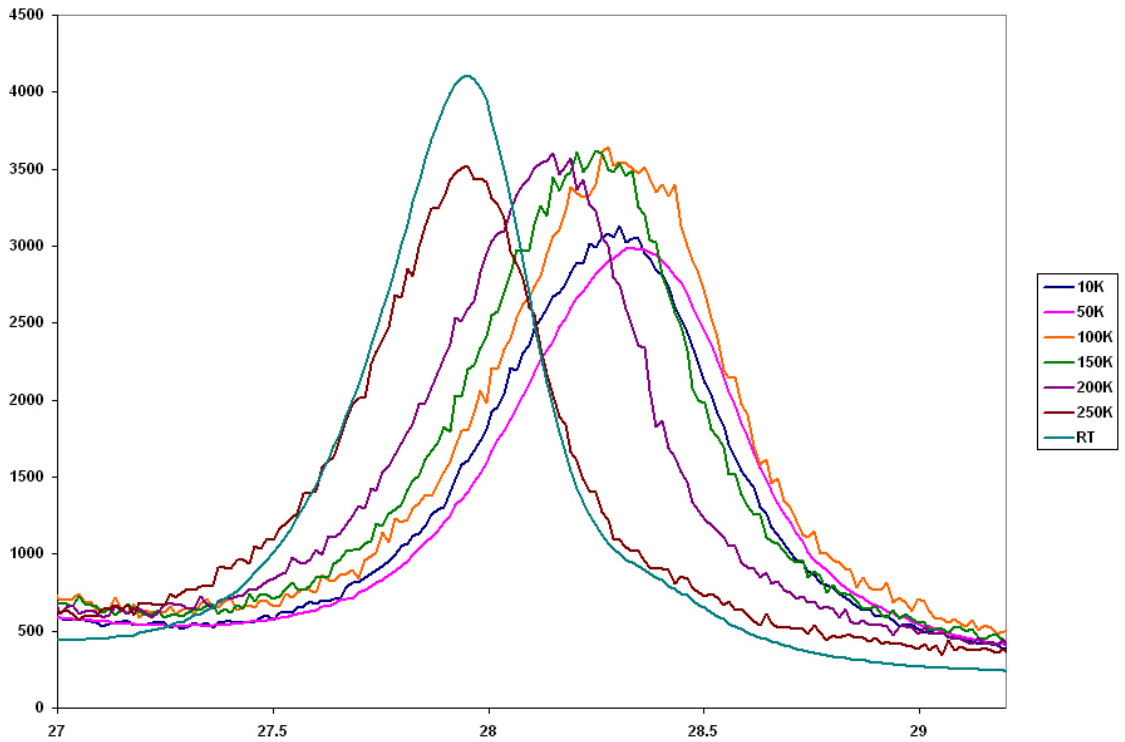

Figure 7.2.17 Section of superimposed powder diffraction data at all temperatures showing selected peak (111) shifting towards a higher 2θ with decreasing temperature.

7.2.4 Discussion

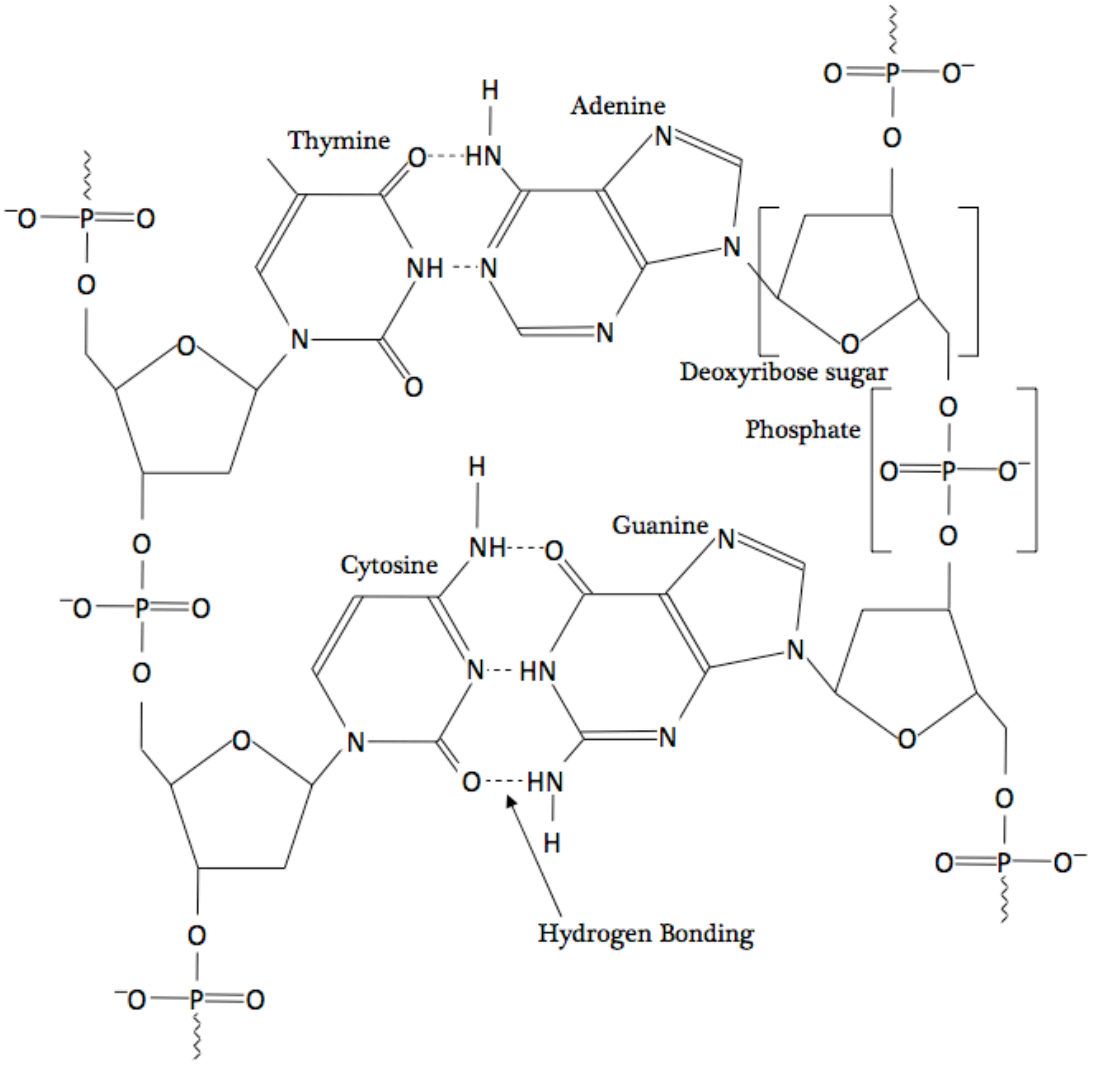

Figure 7.2.18 DNA monomer showing guanine as tautomer 19. [Figure reproduced from D. J. Taylor, N. P O. Green and G. W. Stout, "Biological Science 1 & 2", Cambridge University Press, 3rd Edition, 1997]

Although the crystal structure of tautomer 19 has not been previously documented, its existence in nature is certain. A detailed examination of the structure of DNA reveals that in order for guanine to form hydrogen bonds with cytosine, thus enabling the formation of the double-helical structure characteristic of this nucleic acid, the purine must exist as tautomer 19, with hydrogen atoms attached to N1 and N9. The possible existence of polymorphs of this structure is not to be excluded. However, the lowest energy structures resulting from the computational search for this tautomer all exhibited the same hydrogen bonding motif. This implies that, although possible, the chances of the occurrence of a thermodynamically stable structure having a different arrangement are rather remote.

7.3 Adenine vs Guanine

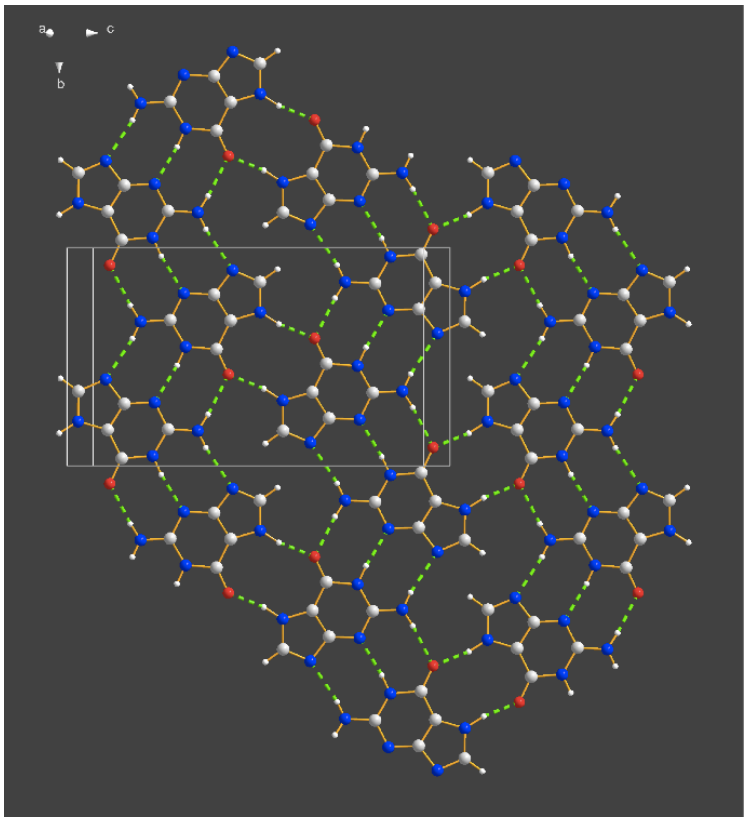

Figure 7.3.1 Crystal structure of guanine[12]. Hydrogen bonds are shown by the green dotted lines.

The crystal structure of guanine[12] contains hydrogen bonded sheets which are comparable to those found in adenine [Section 7.1]. However, the presence of a carbonyl group in guanine is responsible for differences in the hydrogen bonding networks of the two purines. As opposed to having only NH----N hydrogen bonds, each molecule in guanine is linked via four NH---N and four NH---O hydrogen bonds to three others using all strong donors and acceptors. Every molecule is bonded through 8 hydrogen bonds, donating 4 and accepting 4, and forming $R_2^2(8)$ and $R_2^2(10)$ motifs. Each ring of six molecules is again surrounded by six other rings, forming a honeycomb pattern in much the same way as adenine does [Figures 7.3.1 and 7.3.2].

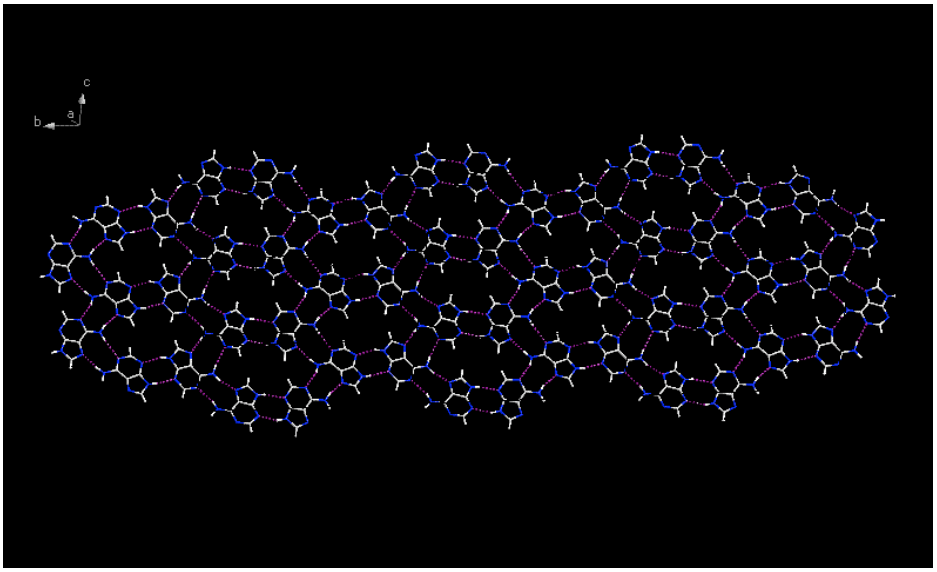

Figure 7.3.2 Crystal structure of adenine. Hydrogen bonds are shown by the purple dotted lines.

Although the crystal structures of adenine and guanine are comparable, there are some fundamental differences between them. While adenine has two molecules in the asymmetric unit, guanine has only one. Their graph sets, both made up of two rings each having a pair of donors and a pair of acceptors, follow $R_2^2(8)$ and $R_2^2(9)$ motifs in adenine, and $R_2^2(8)$ and $R_2^2(10)$ motifs in guanine. Additionally, adenine is a disordered structure, while guanine is not.

7.4 References

1. S. Fuji, K. Kawasaki, A. Sato, T. Fujiwara and K.-I. Tomita, *Archives of Biochemistry and Biophysics*, 1977, **181**, 363
2. A. Takénaka and Y. Sasada, *Bull. Chem. Soc. Jpn.*, 1982, **55**, 680-686
3. M. A. Serra, B. K. Dorner and M E Silver, *Acta Cryst. C*, 1992, **48**, 1957-1960
4. V. Langer and K. Huml, *Acta Cryst. C*, 1984, **40**, 2080-2082
5. S. M. Tretyak, V. V. Mitkevich and L. F. Sukhodub, *Kristallografiya*, *(SoV. Phys. Crystallogr.)*, 1987, **32**, 1268-1271 (748-750)
6. A. C. M. Young and J. C. Dewan, *Acta Cryst. C*, 1991, **47**, 580-584
7. Thomas C. Lewis, PhD Thesis submitted at UCL, 2007
8. A C Larson and R B Von Dreele, *GSAS. General Structure Analysis System*, Report No. LAUR-86-748, Los Alamos National Laboratory, Los Alamos, New Mexico, USA, 1987
9. W.A. Dollase, *J. Appl. Cryst.*, 1986, **19**, 267
10. Liana Vella-Zarb, Maryjane Tremayne, Andrew D Bond, Tom C Lewis, Derek A Tocher and Sarah L Price, 2008 *(in preparation)*
11. U. Thewalt, C. E. Bugg and R. E. Marsh, *Acta Cryst. C*, 1971, **27**, 2358
12. K. Guille and W. Clegg, *Acta Cryst.C*, 2006, **62**, 515
13. A. Boultif and D. Louër, *J. Appl. Cryst.*, 1991, **24**, 987

8. CONCLUSIONS AND FURTHER WORK

If various polymorphic forms of an active pharmaceutical ingredient exhibit different physico-chemical properties, characteristics such as bioavailability and toxicity may be affected. It is primarily for this reason that during the pre-formulation stage of drug development, polymorph screening is a time and resource-consuming, but essential process. Before a drug is launched on the market, pharmaceutical companies apply for patents on various aspects of the drug product to prevent others from marketing the same product. Patenting all solid forms of a drug substance does not only protect the company that has invested money on researching that drug, but it also serves as an assurance to patients that the relevant polymorph screens have been carried out. This reduces the likelihood of drug substances changing form (to a potentially lethal or ineffective form) on the shelf - a phenomenon that has proven fatal to some patients in the past. The development of a high-throughput combinatorial strategy by which new polymorphs may be predicted and confirmed experimentally may therefore eventually lead to the controlled production of desired polymorphs, thus saving time and money, and reducing the risk of *Ritonavir*® repetitions.

For combined techniques such as the one adopted in this project to be effective, an agreement factor which is more reliable than R_{wp} is necessary for the comparison of theoretical and experimental structures. From the study of the three known structures imidazole, chlorothalonil and 5-azauracil described in this report, the respective R_{wp} values showed no agreement between predicted and experimental structures, neither at 0K or the temperatures at which potentials were derived, nor at temperatures corresponding to the experimental single crystal structures used for reference. In all three cases, however, the predicted structures are correct.

The nature of the comparison made in this study imposes inevitable discrepancies between the two powder patterns being compared. Factors which result in peak shifts along 2θ, such as temperature difference and experimental error among others, make a pointwise comparison such as R_{wp} futile, even in the case of two matching structures. More contemporary comparison techniques such as those employed by *PolySNAP* and *Compare* allow more flexibility. Although in the study of the three known structures neither *PolySNAP* nor *Compare.x* identified the correct

structure at all temperatures, there was reasonable overlap in all three cases. *Compare.x* generally gave higher correlation values, possibly due to triangular windows encompassing more than one peak on the corresponding powder pattern.

The inclusion of neighbourhood weighting factors (such as those used in *Compare.x*) leads to a more discriminatory comparison between powder patterns, when compared with conventional pointwise approaches. In the case of experimentally-obtained powder data, factors such as zero point errors, preferred orientation, peak broadening, and noise may influence the outcome of the comparison. *PolySNAP* comparisons, based on a principal component analysis system, search for distinct patterns within the structures, thus overcoming some of the problems associated with comparing experimental and theoretical data. The degree of discrimination between structures ranked first and the next best ones was greater than that obtained during *Compare.x* analysis. Again, this is probably due to the presence of more than one peak in the stipulated search window. *PolySNAP* showed a greater sensitivity to temperature as opposed to *Compare.x*, which demonstrated more stability across the temperature range. This could lead to a slight difference in application of the two methods. Although there is generally an appreciable overlap of the results obtained with both approaches, *Compare.x* would be the method of choice if there is a considerable but non-definable zero-point error. If the error can be measured, then this could be defined in *PolySNAP* prior to comparison. On the other hand, the presence of experimental factors such as noise, broad peaks or preferred orientation would make *PolySNAP* the method of choice.

It is clear from this study that automated comparisons are useful in enabling both the solution of crystal structures from non-ideal powder data as well as the identification of the most likely predicted structure out of a group of low-energy structures. Human input, however, still remains crucial to the successful outcome of such comparisons, because while automated comparisons reduce analysis time drastically, no two structure solution stories are identical. Numerical criteria provided by the automated comparisons are important for the assessment of the fit in quantitative detail. These must always, however, be complemented by graphical criteria which are essential for visual comparison of the structures which, numerically, have resulted as best-fitting. This step

still remains crucial in any success story, because it is usually by looking at the global picture that early noting of errors or omissions may be made.

In future, a closer look at thermal expansion and its implications could possibly be translated into numerical form in order to be incorporated into automated comparison calculations. This would be done in view to standardise the methods, thus making them more reproducible and applicable to most small molecules.

9. APPENDICES

A1. R_{wp}

```
c  Rwp code

 program im

 implicit double precision (a-h/o-z)
 integer natom
 character*10 line1
 character*70 line2
 character*4 line3
 character*6 atom_label
 character*12 line4
 character*68 line5
 character*60 res
 character*18 resnam
 real aa,bb,cc,alpha,beta,gamma
 real atom_type,xx,yy,zz
 dimension atom_label(100),atom_type(100),xx(100),yy(100),zz(100)

 OPEN (UNIT=15,STATUS='unknown',FILE='2IMIDB.EXP')
 OPEN (UNIT=l,STATUS='unknown',FILE='MIXU.EXP')
 OPEN (UNIT=21,STATUS = 'unknown',FILE='rwpval.txt')
 OPEN (UNIT=12,STATUS = 'unknown',FILE='rwp.txt')

c  This section asks how many atoms are included in the molecule

30  WRITE (*,*) 'How many atoms are present?'
 READ (*,*) natom


c  This part askes which res file to use

40  WRITE (*,*) 'Enter res file to use'
 READ (*,*) res

41  OPEN (UNIT=16,FILE=res,FORM='formatted' ,STATUS='old')

c  This section reads in a,b,c,alpha,beta,gamma from the res file

98  READ (16,400,END=103) LINE3
 if (line3.eq. 'TITL') GOTO 99
 GOTO 98

103  continue

99  READ (16,300) AA,BB,CC,ALPHA,BETA,GAMMA
```

```
c  This section replaces the no of atoms in the exp file with natom

56  READ (15,100,END=58) LINE1,LINE2
 if (line1.eq. 'CRS1 NAT') GOTO 58
 WRITE (1,100) LINE1,LINE2
 GOTO 56

57  continue

58  WRITE (1,550) 'CRS1 NATOM',natom


c  This section copies the GSAS exp file onto another file and
c  enters the new values of a,b, and c from the res file


101  READ (15,100,END=102) LINE1,LINE2
 if (line1.eq. 'CRS1 ABC ') GOTO 90
 WRITE (1,100) LINE1,LINE2
 GO TO 101

102  continue

90  WRITE (1,500) 'CRS1 ABC ',AA,BB,CC


c  This section continues to copy the GSAS exp file and enters
c  the new values of alpha, beta, and gamma from the res file


104  READ (15,100,END=105) LINE1,LINE2
 if (line1.eq. 'CRS1 ANGL') GO TO 96
 WRITE (1,100) LINE1,LINE2
 GOTO 104

105  continue

96  WRITE (1,800) 'CRS1 ANGLES',ALPHA,BETA,GAMMA


c  This section continues to copy the GSAS exp file and enters
c  the new values of x,y, and z from the res file


109  READ (15,600,END=205) LINE4,LINE2
 if (line4.eq. 'CRS1 AT 1A') GOTO 50
 WRITE (1,600) LINE4,LINE2
 GOTO 109

205  continue

50  READ (16,440,END=55) LINE3
```

```
 if (line3.eq. 'SFAC') GO TO 60
 GO TO 50

55  continue


c This is a loop which copies the info from the res file for as
c many atoms as stated earlier in the answer to the question asked

60  DO 70 i=l,natom

 READ (16,330) atom_label(i),atom_type(i),xx(i),yy(i),zz(i)

80  WRITE (1,220) 'CRS1 AT ',(i),'A','N',xx(i),yy(i),zz(i),
    1  'l.000000',atom_label(i),'4 000'
 WRITE (1,110) 'CRS1 AT ',(i),'B','0.02500','I'

70  continue


c  This section continues to copy the GSAS exp file to the end


107  READ (15,100,END=108) LINE1,LINE2
 if (line1.eq. 'CRS1 AT') GOTO 107
 if (line1.eq. 'CRS1 CELV') GOTO 118

118  WRITE (1,100) LINE1,LINE2

108  continue

129  READ (15,100,END=119) LINE1,LINE2
 WRITE (1,100) LINE1,LINE2

40  GOTO 129

119 continue

C This section will call gsas to convert new exp file to correct
c format then it will call gsas, run genles and generate a LST file

18  call system('/home/gsas/exe/cnvfile MIXU.EXP')

31  continue

32  call system('/home/gsas/exe/powpref MIXU')
 call system('/home/gsas/exe/genles MIXU >gsas.out')
 call system('rm MIXU.LST')
 call system('grep totals gsas.out > rwp.txt')

 continue
```

```
c  This will read the rwp values and write them and res name to
c  rwpval.out


33  READ (12,880,end=35)rwp
 GOTO 33

35  rwp=rwp*100

39  continue

36  WRITE (21,900)res,rwp
 close (12)
 return
 continue




100  format (A10,A70)
200  format (A10,3f9.6)
300  format (8x,6f10.4)
400  format (A4,A4,A60)
500  format (A12,3f10.6)
600  format (A12,A68)
700  format (A12,A5)
800  format (A12,3f10.5)
900  format (A18,f7.4)
110 format (A10,I1,A1,2x,A7,A54)
220  format (A10,I1,A1,A3,7x,3f10.6,A10,A6,A10)
330  format (A6,A2,3f13.8)
440  format (A4,A4,A60)
550  format (A12,3x,I2,A63)
880  format (36x,f6.4)

510  stop

 end
```

A2. IMIDAZOLE

A2.1 Low Temperature Data

Figure A2.1 Powder diffraction data at all temperatures (D5005)

A2.2 R_{wp}

Figure A2.2.1 Powder pattern of top ranked predicted structure at 10K (D5005) and experimental pattern at that temperature

Figure A2.2.2 Powder pattern of top ranked predicted structure at 50K (D5005) and experimental pattern at that temperature

Figure A2.2.3 Powder pattern of top ranked predicted structure at 150K and 250K (D5005) and experimental patterns at these temperatures

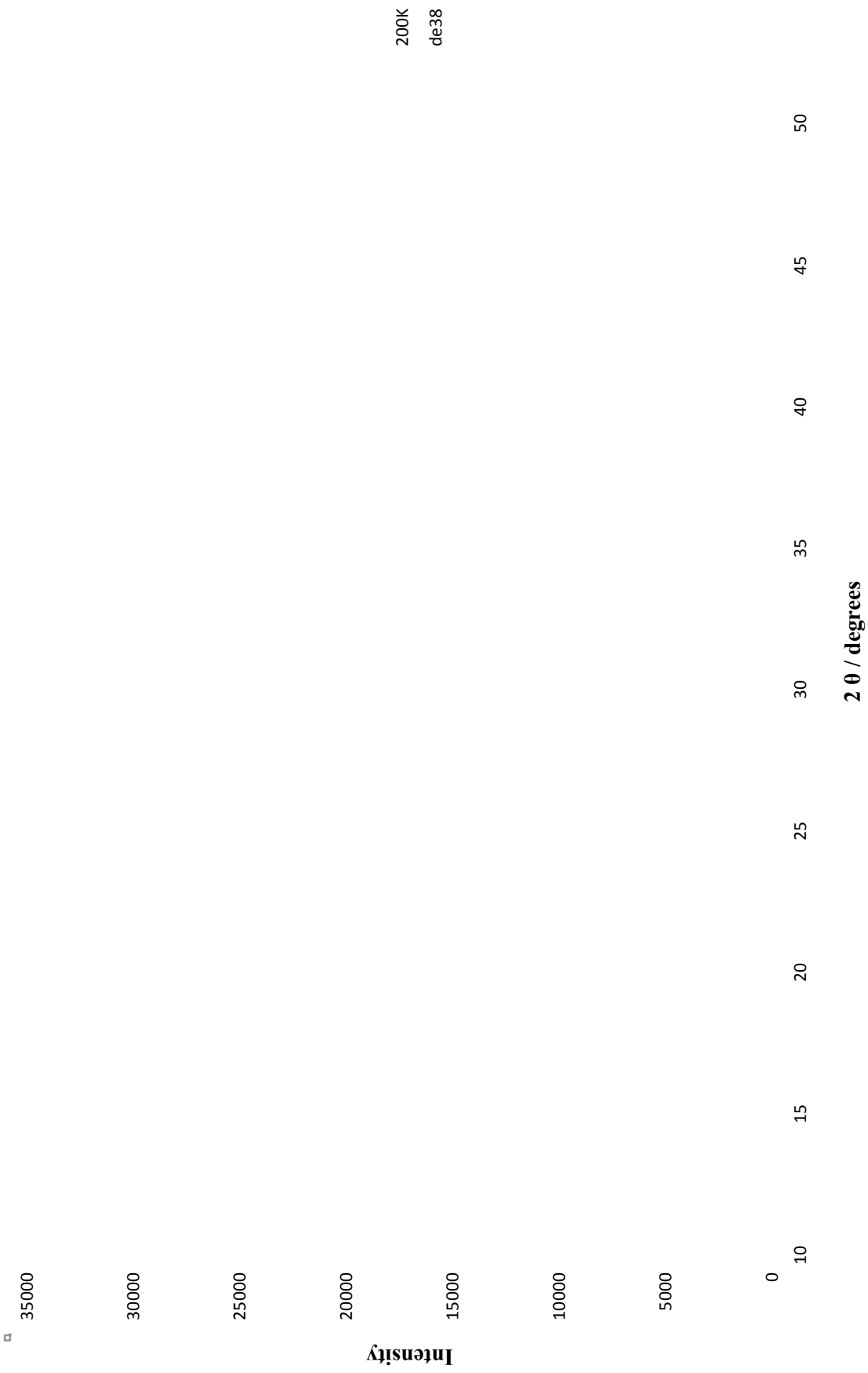

Figure A2.2.4 Powder pattern of top ranked predicted structure at 200K (D5005) and experimental pattern at that temperature

Figure A2.2.5 Powder pattern of top ranked predicted structure at room temperature (D5005) and experimental pattern at that temperature

Figure A2.2.6 Powder pattern of top ranked predicted structure at room temperature (D5000) and experimental pattern at that temperature

A2.3 PolySNAP

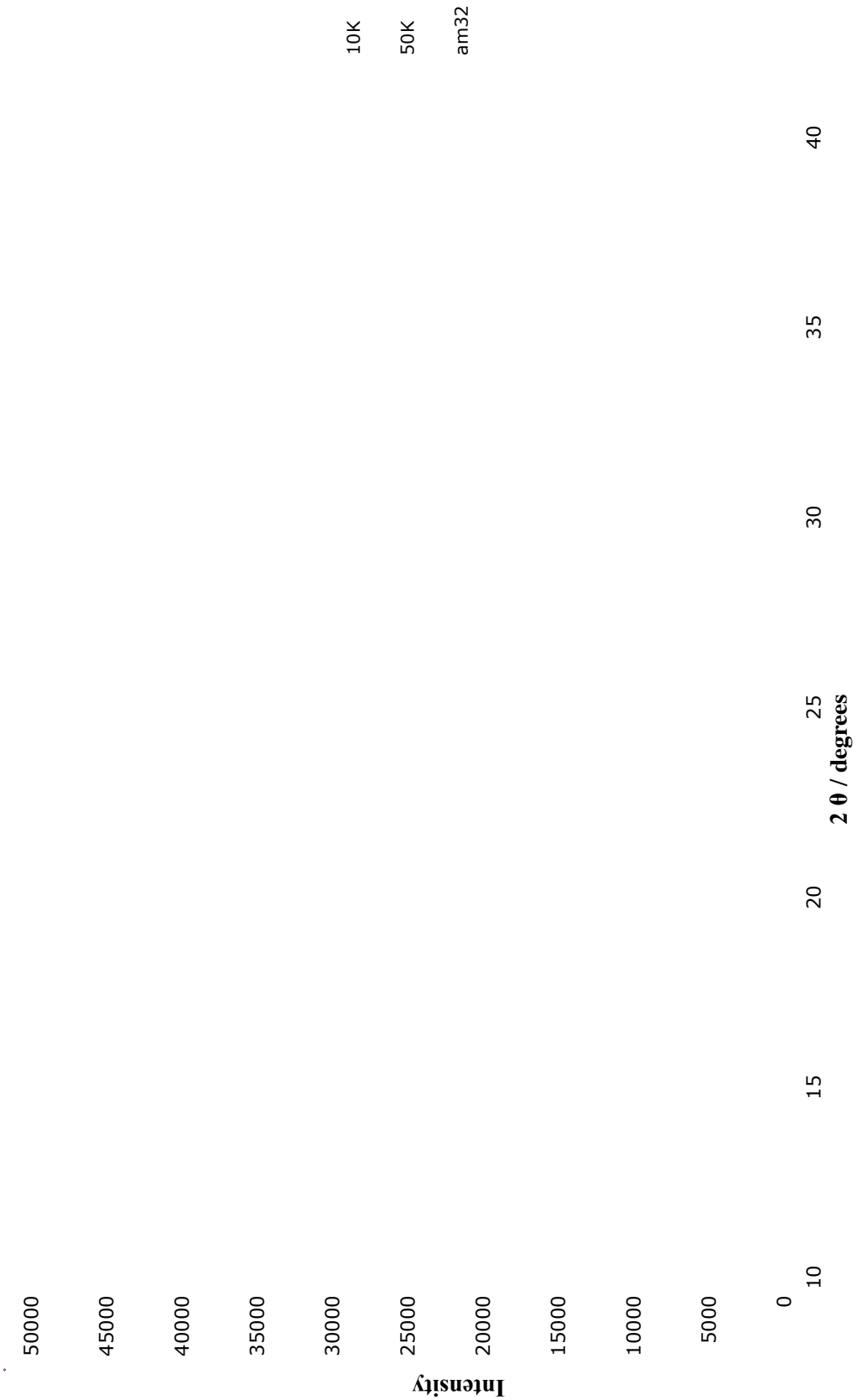

Figure A2.3.1 Powder pattern of top ranked predicted structure at 10K and 50K (D5005), and experimental patterns at those temperatures

Figure A2.3.2 Powder patterns of top ranked predicted structure at 150K, 200K, 250K and room temperature (D5005) and experimental patterns at those temperatures

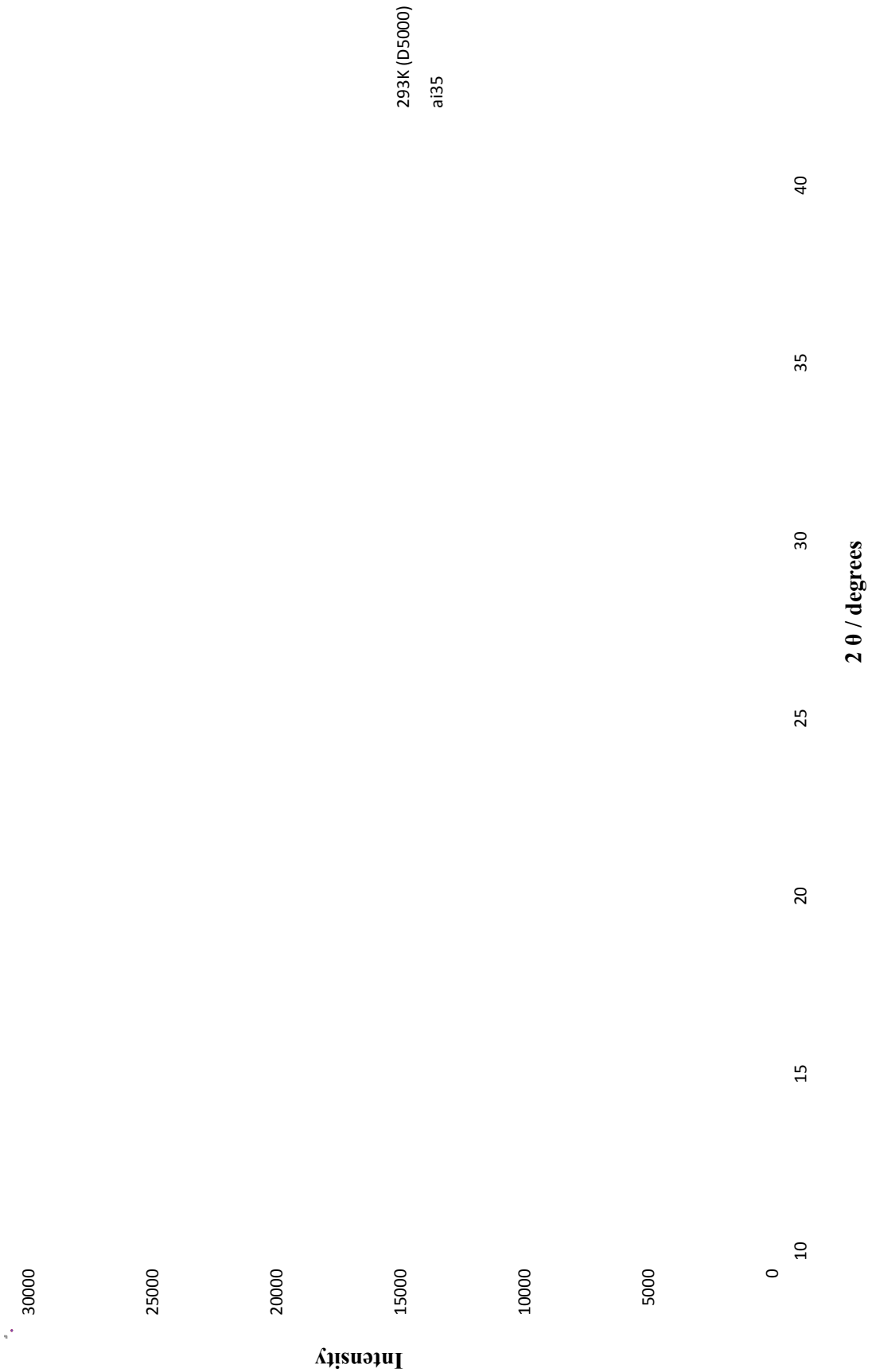

Figure A2.3.3 Powder patterns of top ranked predicted structure at room temperature (D5000) and experimental patterns at those temperatures

A2.4 Compare.x

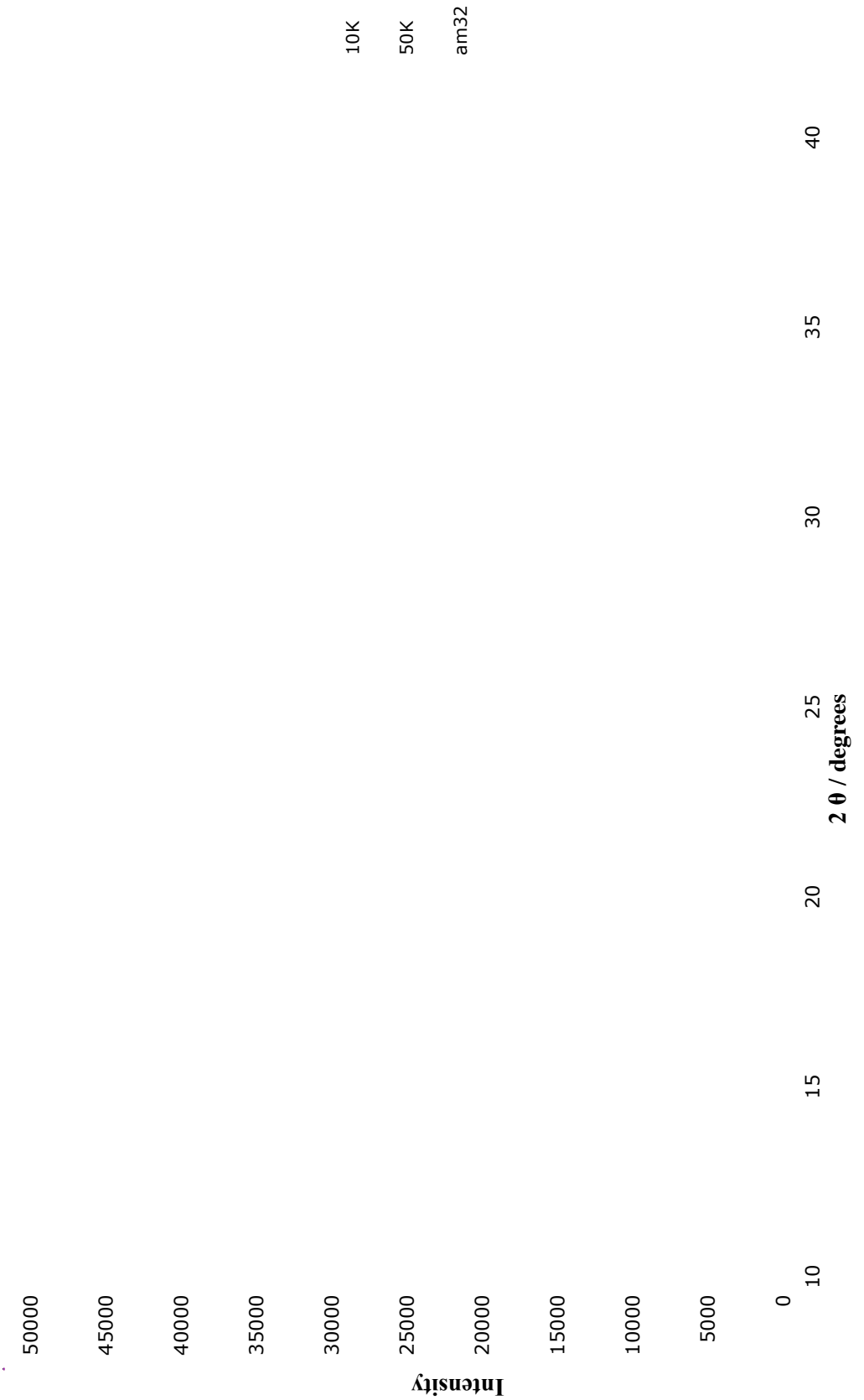

Figure A2.4.1 Powder pattern of top ranked predicted structure at 10K and 50K (D5005) and experimental patterns at those temperatures

Figure A2.4.2 Powder pattern of top ranked predicted structure at 150K, 200K and 250K (D5005) and experimental patterns at those temperatures

Figure A2.4.3 Powder pattern of top ranked predicted structure at room temperature (D5000 and D5005) and experimental patterns at those temperatures

Results obtained using *Compare.x* with various values of triangle windows. In each case, the tables show the structure with the highest correlation coefficient [C(x)] at each temperature, and the difference to the value obtained for the correct structure [C(ak34)]. In cases where the correct structure was identified, the difference was positive. An incorrect match gave a negative difference, as shown by the values in red and blue. Blue denotes ak34 being ranked second, while values in red correspond to ak34 being ranked third or lower.

Table A2.4.1. Triangle window 0.5.

Temperature (K)	***Structure***	***Correlation Coefficient***	***Difference [C(ak34) - C(x)]***
10	am32	0.66294	-0.19810
50	am32	0.67067	-0.17771
150	ak66	0.73371	-0.07523
200	ak66	0.76105	-0.06888
250	ak34	0.76115	0.01505
293	ai35	0.71675	-0.12950
293 (D5000)	ai35	0.65683	-0.19758

Table A2.4.2. Triangle window 1.0.

Temperature (K)	***Structure***	***Correlation Coefficient***	***Difference [C(ak34) - C(x)]***
10	am32	0.76926	-0.12467
50	am32	0.78164	-0.11389
150	ak66	0.83363	-0.02332
200	ak66	0.83856	-0.00668
250	ak34	0.87510	0.03544
293	ai35	0.81807	-0.06026
293 (D5000)	ai35	0.77485	-0.10092

Table A2.4.3. Triangle window 1.5.

Temperature (K)	***Structure***	***Correlation Coefficient***	***Difference [C(ak34) - C(x)]***
10	am32	0.83533	-0.08420
50	am32	0.84838	-0.07779
150	ak66	0.86600	-0.00920
200	ak66	0.86577	-0.00446
250	ak34	0.88965	0.00686
293	ai35	0.86348	-0.03613
293 (D5000)	ai35	0.85226	-0.07900

Table A2.4.4. Triangle window 2.0.

Temperature (K)	***Structure***	***Correlation Coefficient***	***Difference [C(ak34) - C(x)]***
10	am32	0.86910	-0.05156
50	am32	0.87991	-0.04717
150	ak34	0.89473	0.00721
200	ak34	0.89512	0.01275
250	ak34	0.90977	0.01048
293	ai35	0.89375	-0.03221
293 (D5000)	ai35	0.89247	-0.03365

Table A2.4.5. Triangle window 2.5.

Temperature (K)	***Structure***	***Correlation Coefficient***	***Difference [C(ak34) - C(x)]***
10	am32	0.89112	-0.03553
50	am32	0.89888	-0.03205
150	ak34	0.91226	0.01338
200	ak34	0.91038	0.01386
250	ak34	0.92212	0.00551
293	ai35	0.90818	-0.01885
293 (D5000)	ak66	0.91188	-0.03377

Table A2.4.6. Triangle window 3.0.

Temperature (K)	***Structure***	***Correlation Coefficient***	***Difference [C(ak34) - C(x)]***
10	am32	0.90808	-0.02822
50	am32	0.91413	-0.02636
150	ak34	0.92523	0.01318
200	ak34	0.92322	0.01238
250	ak34	0.93366	0.00190
293	ak66	0.92260	-0.01650
293 (D5000)	ak66	0.92525	-0.02571

Table A2.4.7. Triangle window 3.5.

Temperature (K)	***Structure***	***Correlation Coefficient***	***Difference [C(ak34) - C(x)]***
10	am32	0.92110	-0.02490
50	am32	0.92577	-0.02319
150	ak34	0.93457	0.00755
200	ak34	0.93216	0.00494
250	ak66	0.94071	-0.00933
293	fc72	0.93305	-0.01911
293 (D5000)	ai35	0.92540	-0.01989

Table A2.4.8. Triangle window 4.0.

Temperature (K)	***Structure***	***Correlation Coefficient***	***Difference [C(ak34) - C(x)]***
10	am32	0.93231	-0.02221
50	am32	0.93623	-0.02051
150	ak34	0.94255	0.00220
200	ak34	0.93948	0.00132
250	ak66	0.94588	-0.00222
293	fc72	0.94320	-0.02327
293 (D5000)	ai35	0.92926	-0.01748

A3. CHLOROTHALONIL

A3.1 Low Temperature Data

Figure A3.1 Powder diffraction data at all temperatures (D5005)

A3.2 R_{wp}

Figure A3.2.1 Powder pattern of top ranked predicted structure at 100K and room temperature (D5005) and experimental patterns at these temperatures

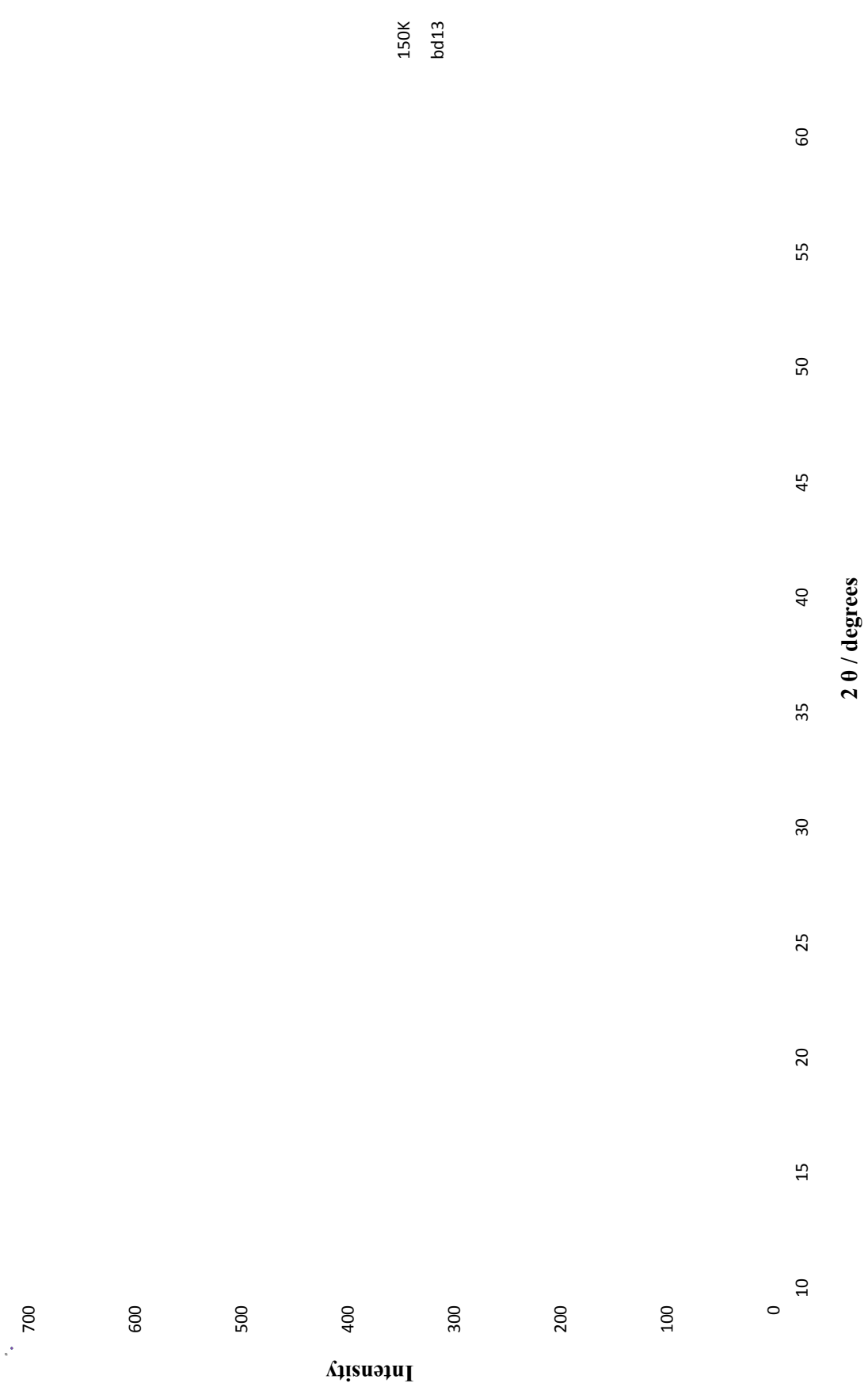

Figure A3.2.2 Powder pattern of top ranked predicted structure at 150K (D5005) and experimental pattern at that temperature

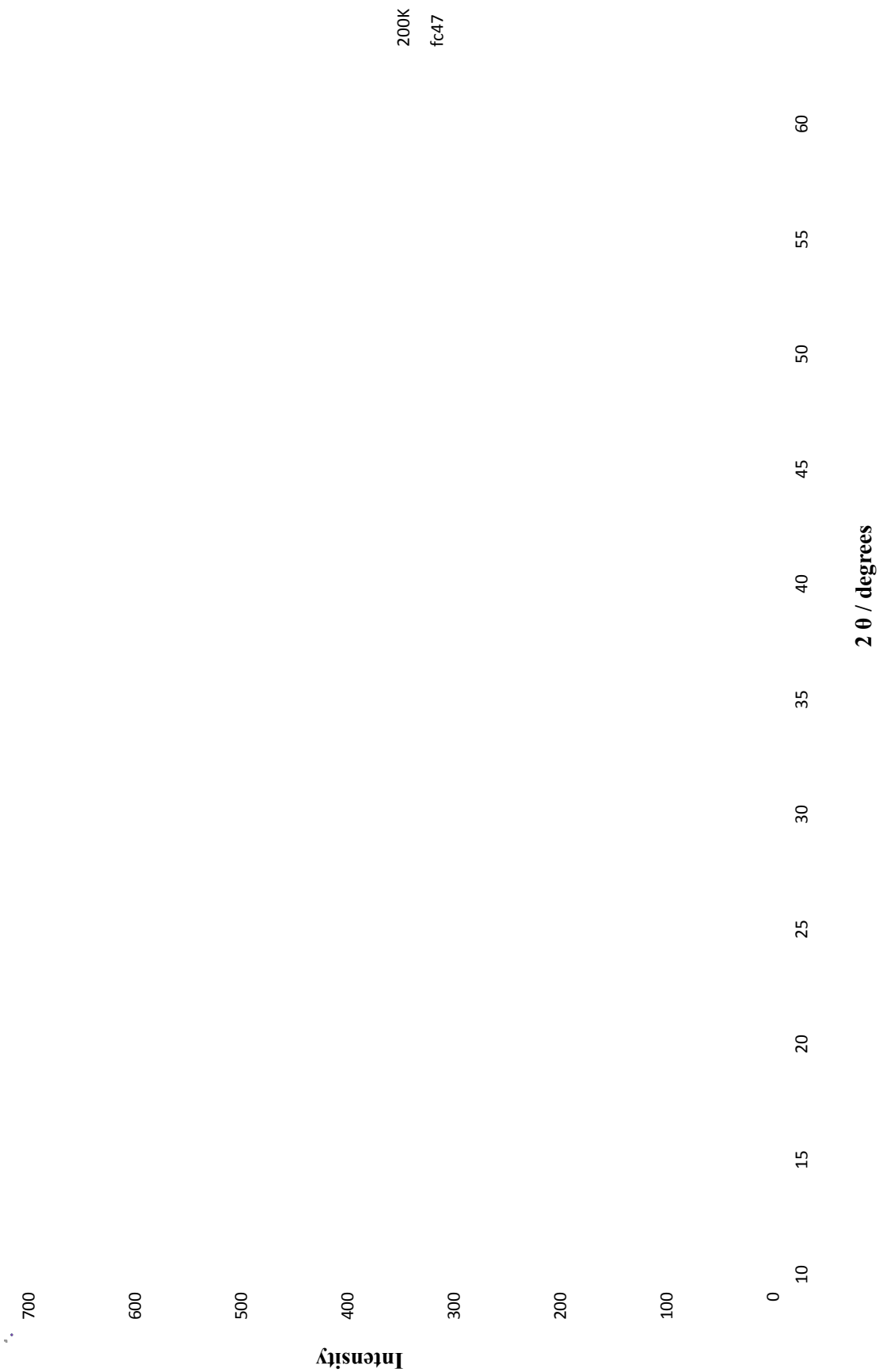

Figure A3.2.3 Powder pattern of top ranked predicted structure at 200K (D5005) and experimental pattern at that temperature

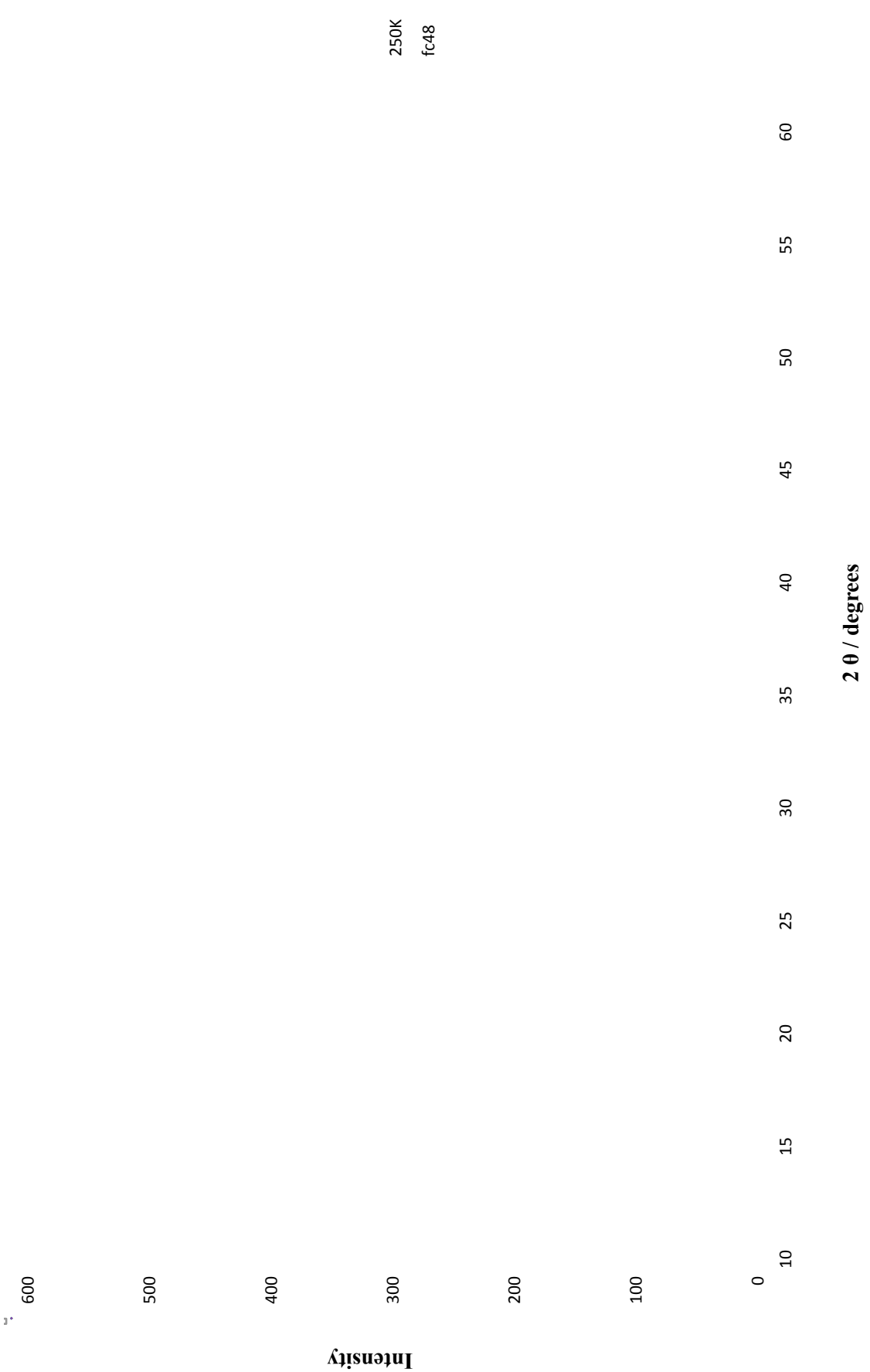

Figure A3.2.4 Powder pattern of top ranked predicted structure at 250K (D5005) and experimental pattern at that temperature

Figure A3.2.5 Powder pattern of top ranked predicted structure at room temperature (D5000) and experimental pattern at that temperature

A3.3 PolySNAP

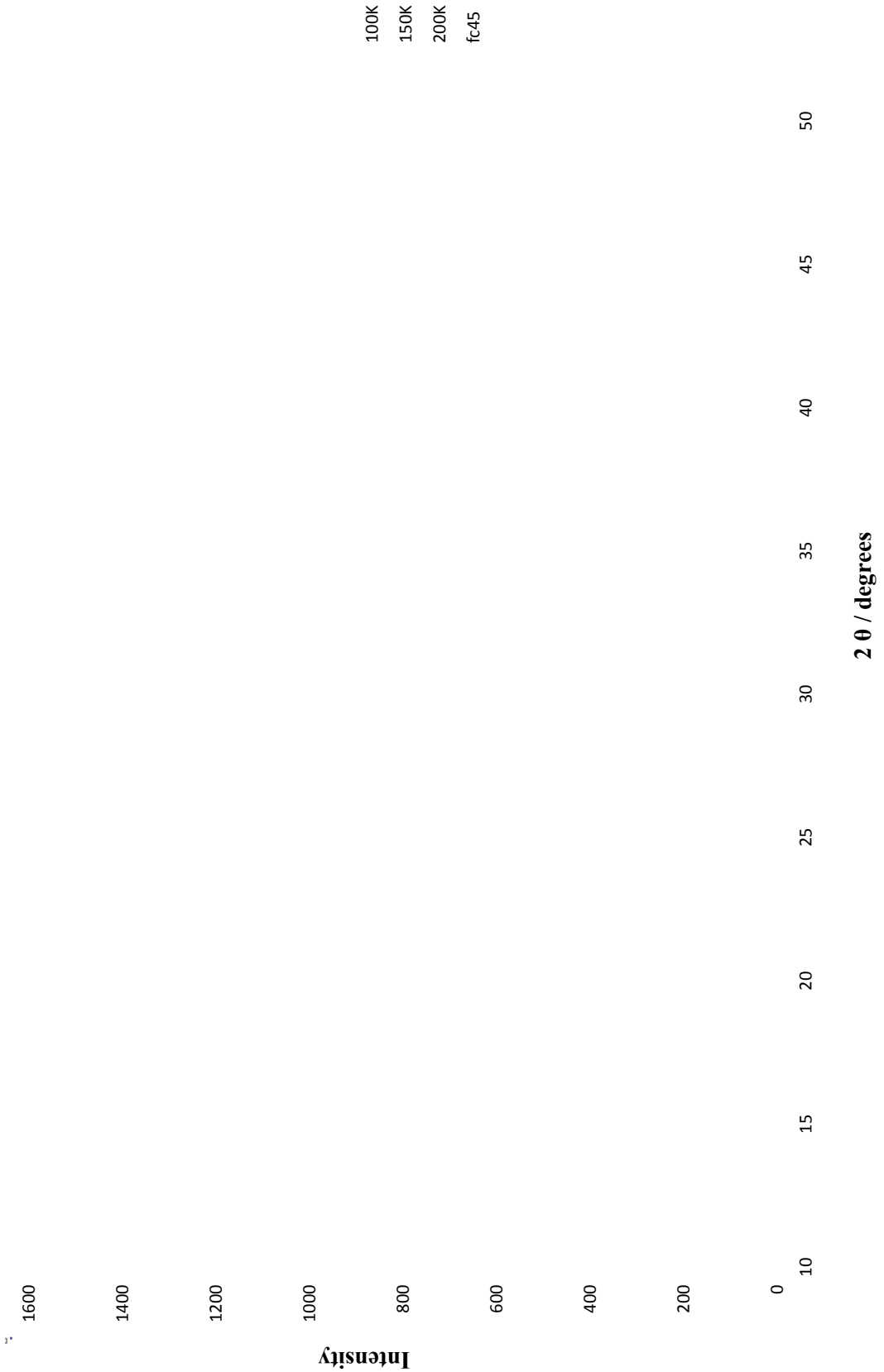

Figure A3.3.1 Powder pattern of top ranked predicted structure at 100K, 150K and 200K (D5005) and experimental patterns at these temperatures

Figure A3.3.2 Powder pattern of top ranked predicted structure at 250K and room temperature (D5005) and experimental patterns at these temperatures

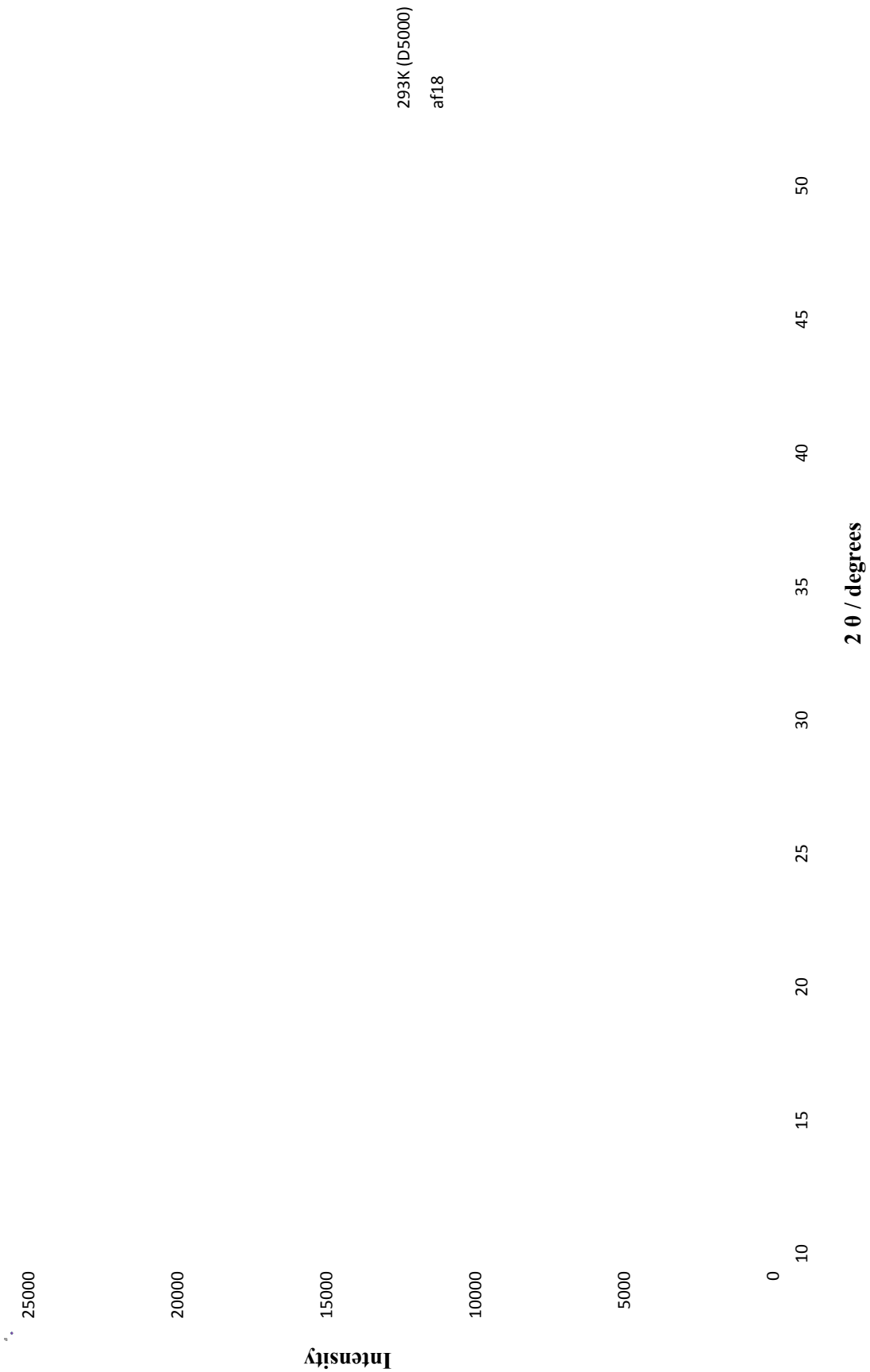

Figure A3.3.3 Powder pattern of top ranked predicted structure at room temperature (D5000) and experimental pattern at that temperature

A3.4 Compare.x

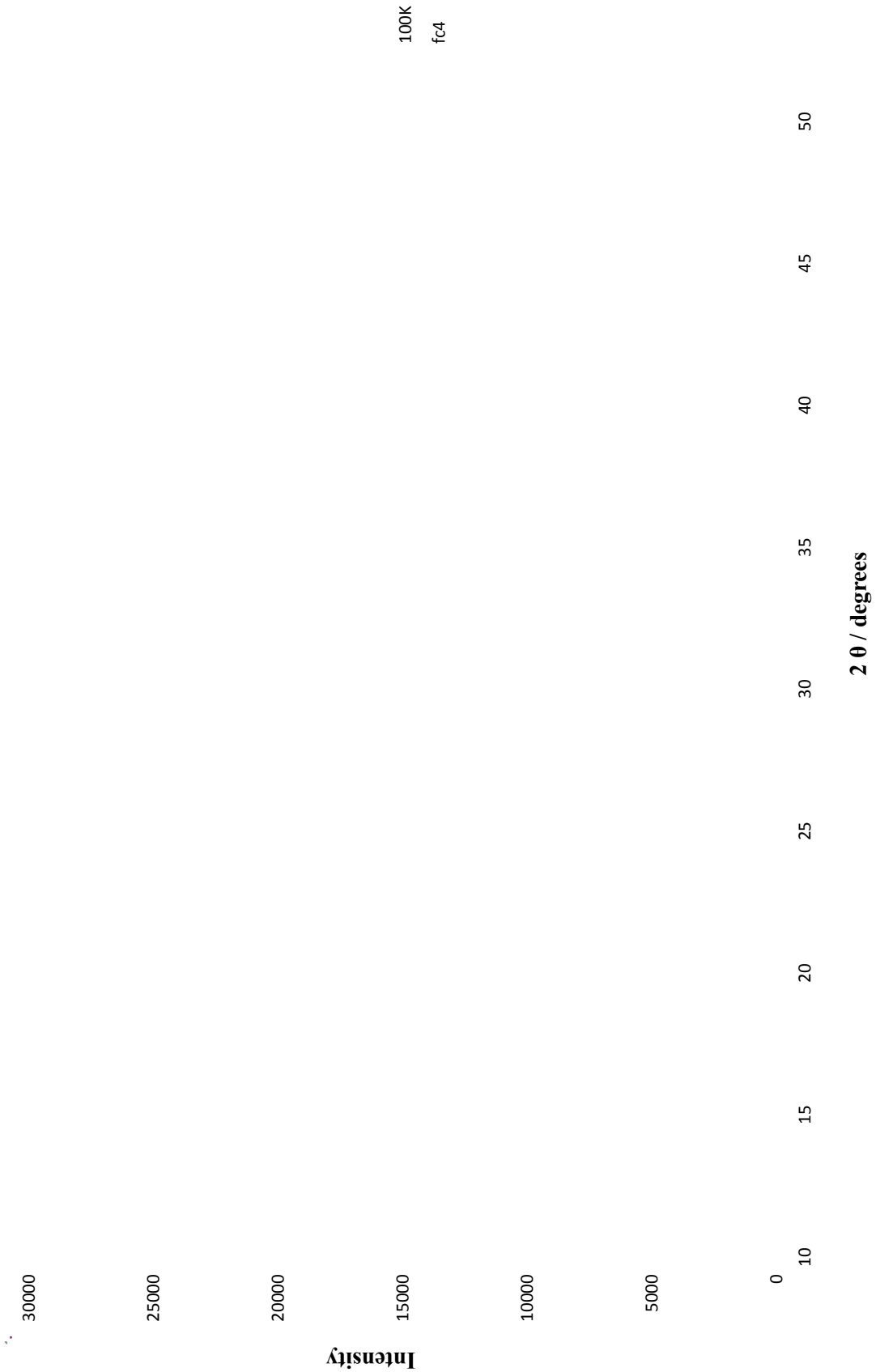

Figure A3.4.1 Powder pattern of top ranked predicted structure at 100K (D5005) and experimental pattern at that temperature

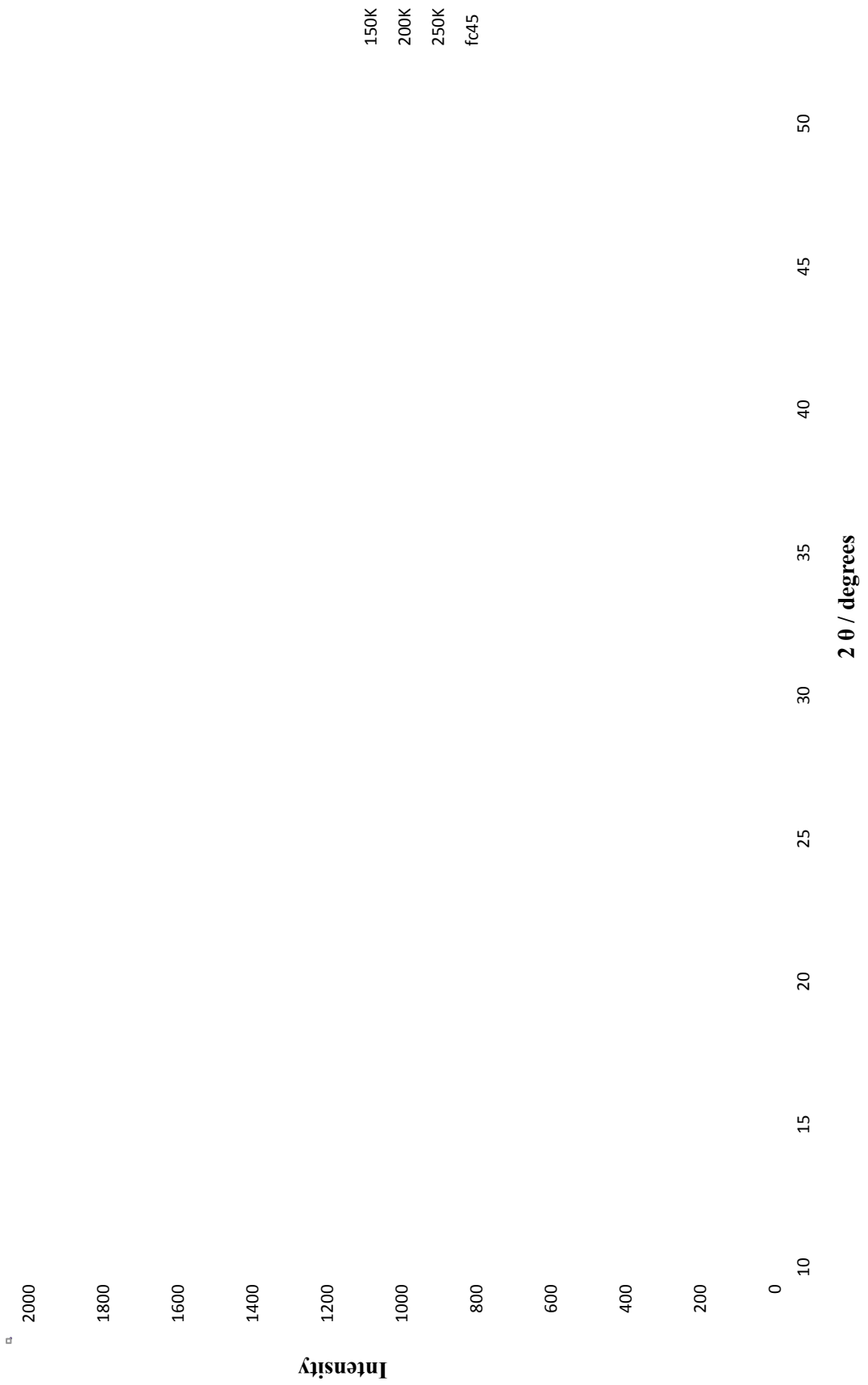

Figure A3.4.2 Powder pattern of top ranked predicted structure at 150K, 200K and 250K (D5005) and experimental patterns at these temperatures

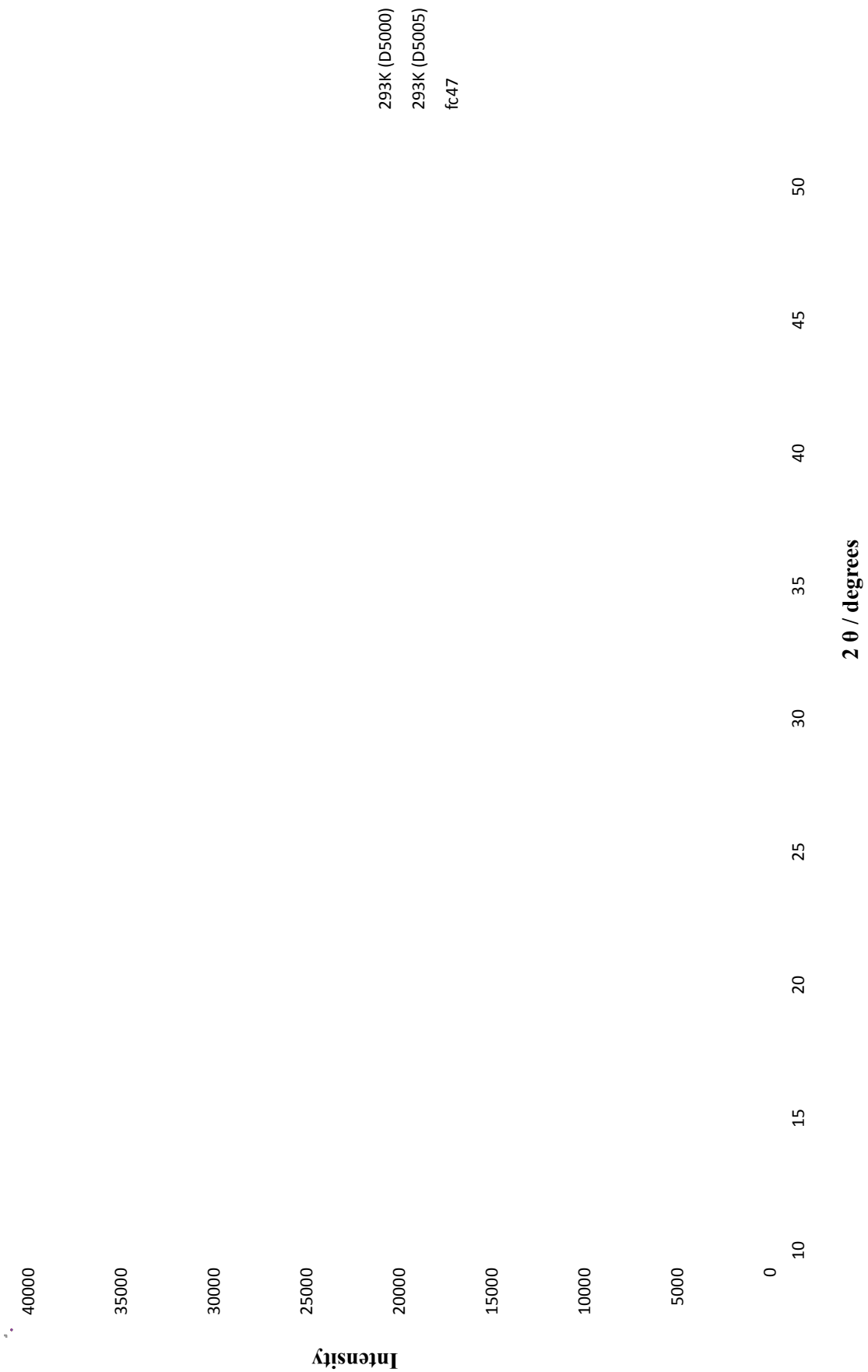

Figure A3.4.3 Powder pattern of top ranked predicted structure at room temperature (D5000 and D5005) and experimental pattern at that temperature

Results obtained using *Compare.x* with various values of triangle windows. In each case, the tables show the structure with the highest correlation coefficient [C(x)] at each temperature, and the difference to the value obtained for the correct structure [C(fc45)]. In cases where the correct structure was identified, the difference was positive. An incorrect match gave a negative difference, as shown by the values in red and blue. Blue denotes fc45 being ranked second, while values in red correspond to fc45 being ranked third or lower.

Table A3.4.1. Triangle window 0.5.

Temperature (K)	***Structure***	***Correlation Coefficient***	***Difference [C(fc45) - C(x)]***
100	fc45	0.82539	0.03170
150	fc45	0.85025	0.08551
200	fc45	0.85246	0.09692
250	fc45	0.81109	0.01029
293	ai44	0.83041	-0.07613
293 (D5000)	fc47	0.50190	-0.05690

Table A3.4.2. Triangle window 1.0.

Temperature (K)	***Structure***	***Correlation Coefficient***	***Difference [C(fc45) - C(x)]***
100	fc4	0.88291	-0.00194
150	fc45	0.88761	0.01623
200	fc45	0.88579	0.03166
250	fc45	0.87166	0.00510
293	fc47	0.87741	-0.02883
293 (D5000)	fc47	0.61438	-0.07702

Table A3.4.3. Triangle window 1.5.

Temperature (K)	***Structure***	***Correlation Coefficient***	***Difference [C(fc45) - C(x)]***
100	fc4	0.92652	-0.01652
150	fc45	0.91086	0.00351
200	fc45	0.91717	0.01243
250	fc45	0.90225	0.00372
293	fc47	0.90523	-0.02114
293 (D5000)	fc47	0.69772	-0.09278

Table A3.4.4. Triangle window 2.0.

Temperature (K)	***Structure***	***Correlation Coefficient***	***Difference [C(fc45) - C(x)]***
100	fc4	0.94087	-0.01095
150	fc45	0.92792	0.00393
200	fc45	0.93188	0.01031
250	fc45	0.92003	0.00273
293	fc47	0.91949	-0.01272
293 (D5000)	fc47	0.74710	-0.10348

Table A3.4.5. Triangle window 2.5.

Temperature (K)	***Structure***	***Correlation Coefficient***	***Difference [C(fc45) - C(x)]***
100	fc4	0.94672	-0.00218
150	fc45	0.94020	0.00057
200	fc45	0.93726	0.00164
250	fc47	0.93504	-0.00414
293	fc47	0.93098	-0.00783
293 (D5000)	fc47	0.76497	-0.10461

Table A3.4.6. Triangle window 3.0.

Temperature (K)	***Structure***	***Correlation Coefficient***	***Difference [C(fc45) - C(x)]***
100	fc4	0.95481	-0.00317
150	fc45	0.94662	0.00024
200	fc45	0.94161	0.00242
250	fc47	0.93676	-0.00025
293	fc47	0.93356	-0.00475
293 (D5000)	fc47	0.77165	-0.08863

Table A3.4.7. Triangle window 3.5.

Temperature (K)	***Structure***	***Correlation Coefficient***	***Difference [C(fc45) - C(x)]***
100	fc4	0.96368	-0.00686
150	fc4	0.95494	-0.00385
200	fc4	0.94846	-0.00232
250	fc47	0.94264	-0.00045
293	fc47	0.93894	-0.00442
293 (D5000)	fc47	0.78153	-0.10575

Table A3.4.8. Triangle window 4.0.

Temperature (K)	***Structure***	***Correlation Coefficient***	***Difference [C(fc45) - C(x)]***
100	fc4	0.96980	-0.00759
150	fc4	0.96079	-0.00474
200	fc4	0.95493	-0.00387
250	fc4	0.94900	-0.00282
293	fc4	0.94372	-0.00349
293 (D5000)	fc4	0.79224	-0.11128

A4. 5-AZAURACIL

A4.1 Low Temperature Data

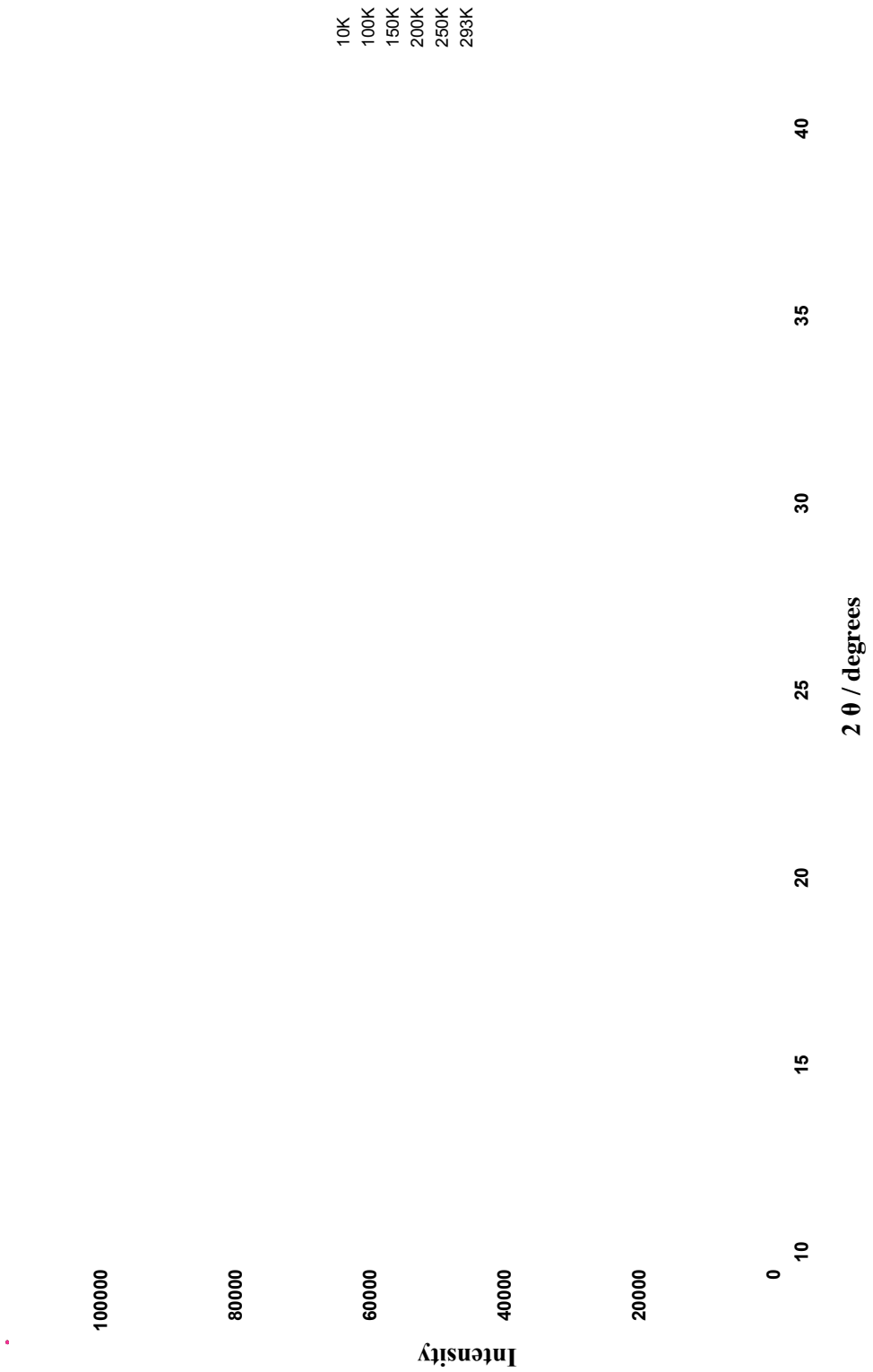

Figure A4.1 Powder diffraction data at all temperatures (D5005)

A4.2 R_{wp}

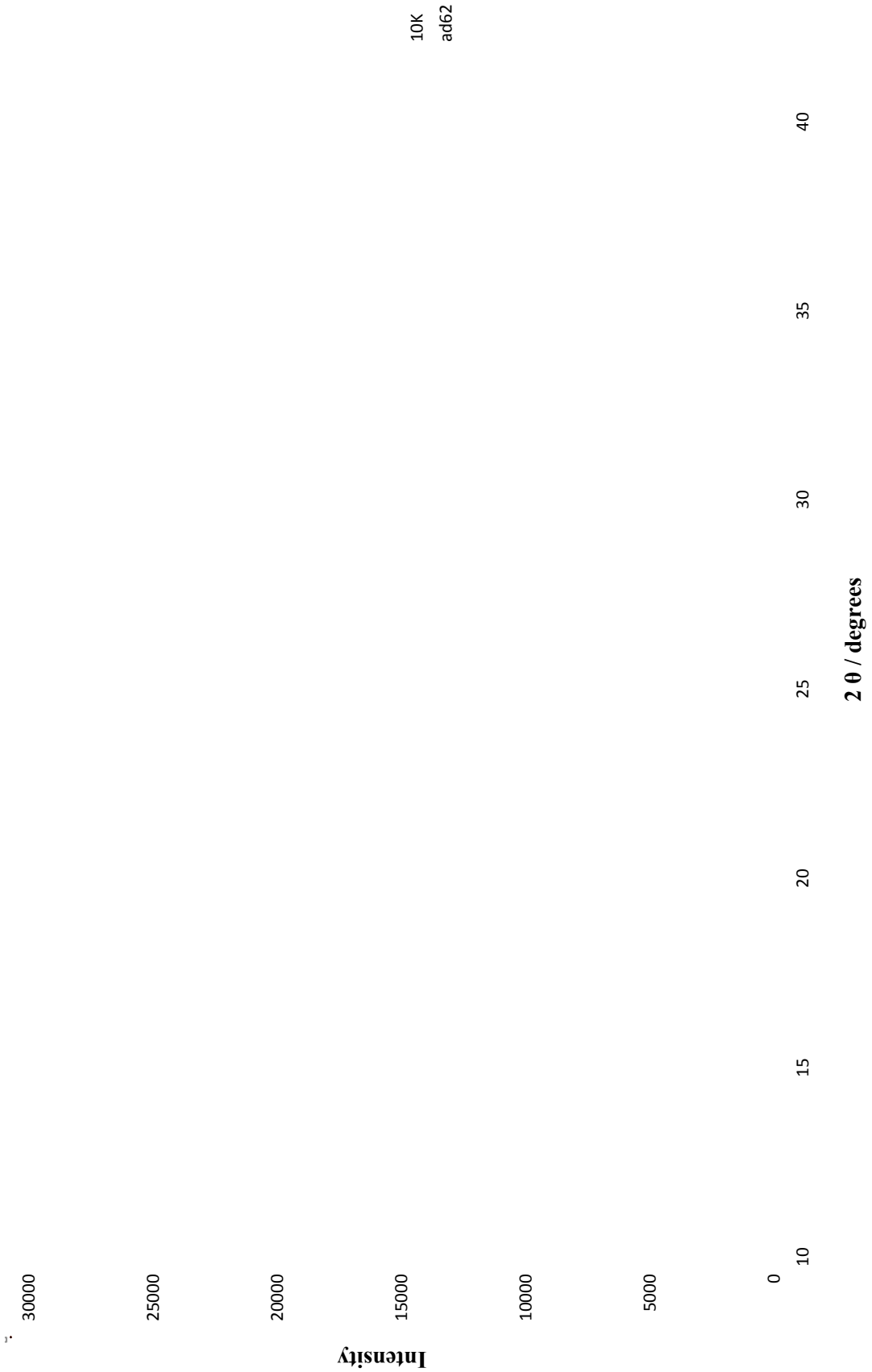

Figure A4.2.1 Powder pattern of top ranked predicted structure at 10K (D5005) and experimental pattern at that temperature

Figure A4.2.2 Powder pattern of top ranked predicted structure at 100K (D5005) and experimental pattern at that temperature

Figure A4.2.3 Powder pattern of top ranked predicted structure at 150K (D5005) and experimental pattern at that temperature

Figure A4.2.4 Powder pattern of top ranked predicted structure at 200K (D5005) and experimental pattern at that temperature

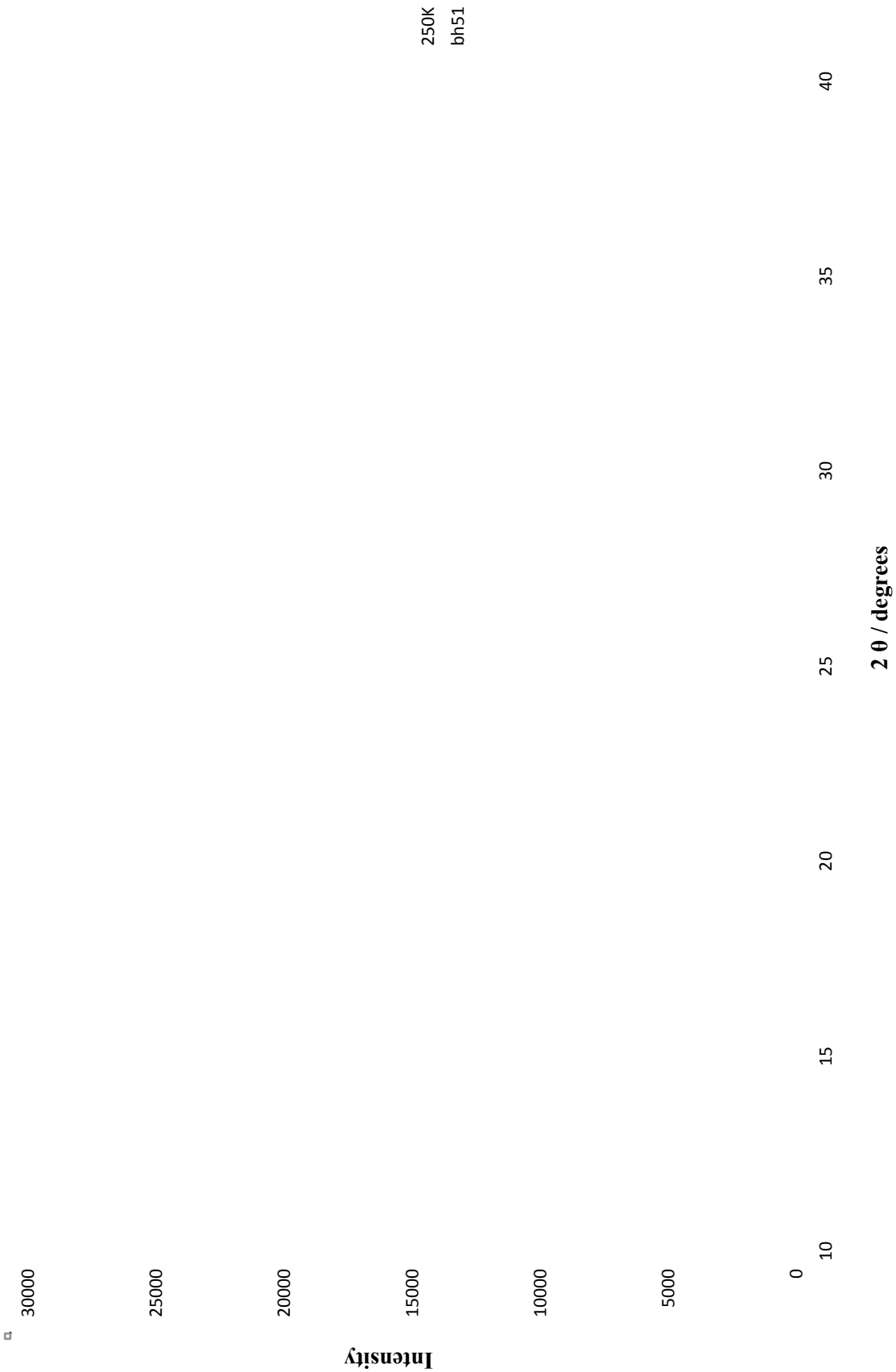

Figure A4.2.5 Powder pattern of top ranked predicted structure at 250K (D5005) and experimental pattern at that temperature

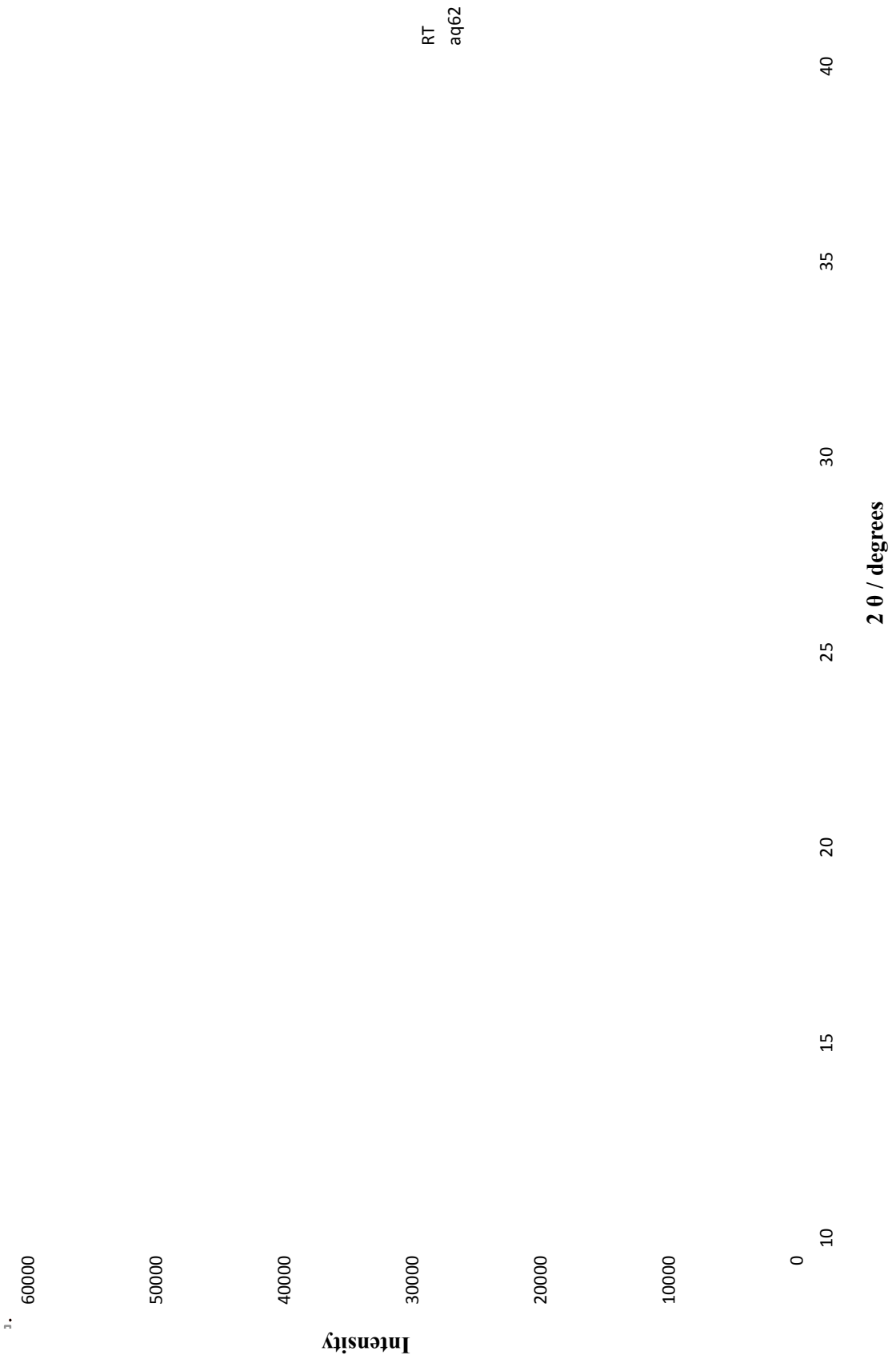

Figure A4.2.6 Powder pattern of top ranked predicted structure at room temperature (D5005) and experimental pattern at that temperature

Figure A4.2.7 Powder pattern of top ranked predicted structure at room temperature (D5000) and experimental pattern at that temperature

A4.3 PolySNAP

Figure A4.3.1 Powder pattern of top ranked predicted structure at 10K and 100K (D5005) and experimental patterns at these temperatures

Figure A4.3.2 Powder pattern of top ranked predicted structure at 150K, 200K, 250K and room temperature (D5005) and experimental patterns at these temperatures

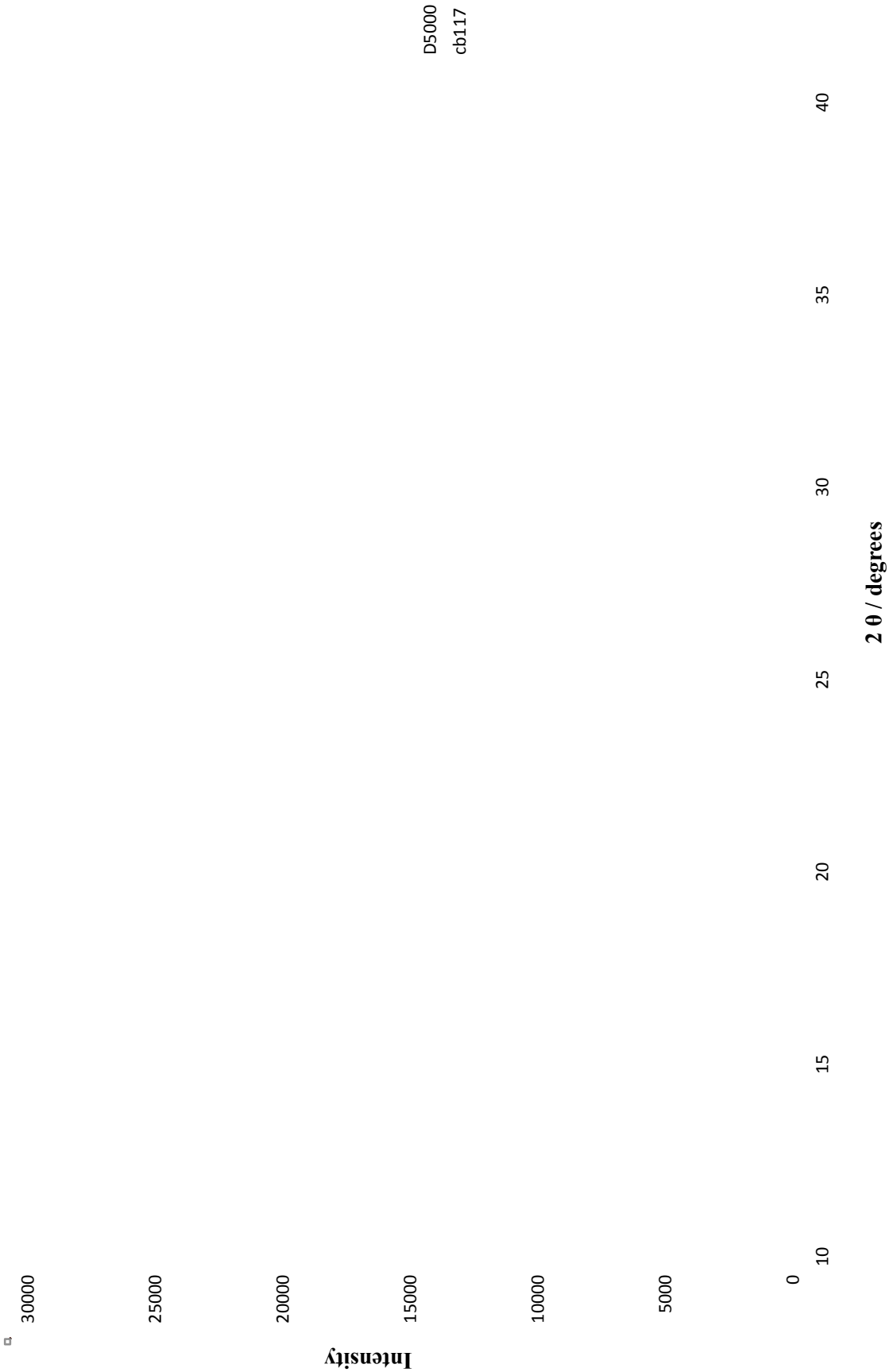

Figure A4.3.3 Powder pattern of top ranked predicted structure at room temperature (D5000) and experimental pattern at that temperature

A4.4 Compare.x

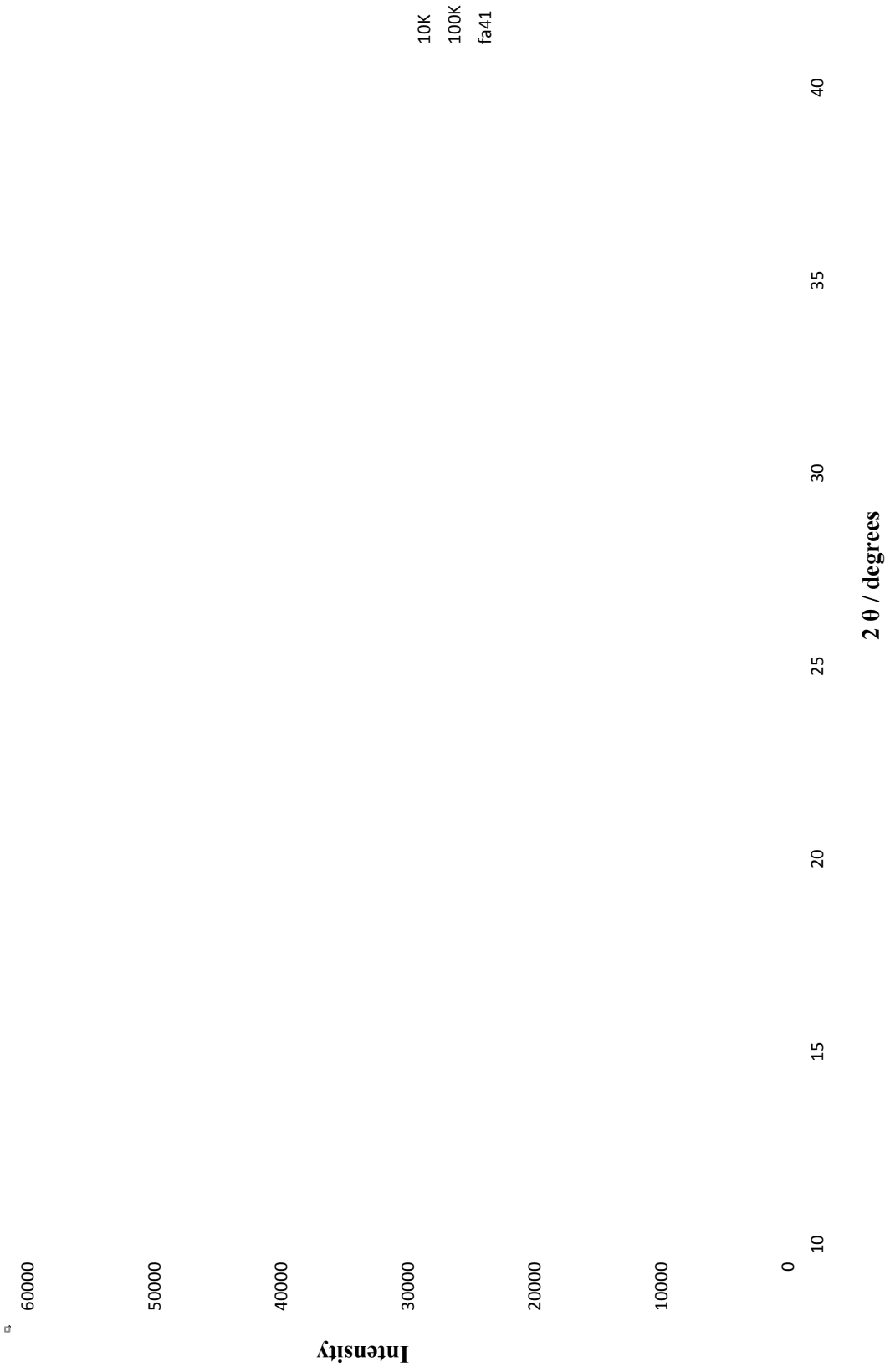

Figure A4.4.1 Powder pattern of top ranked predicted structure at 10K and 100K (D5005) and experimental patterns at these temperatures

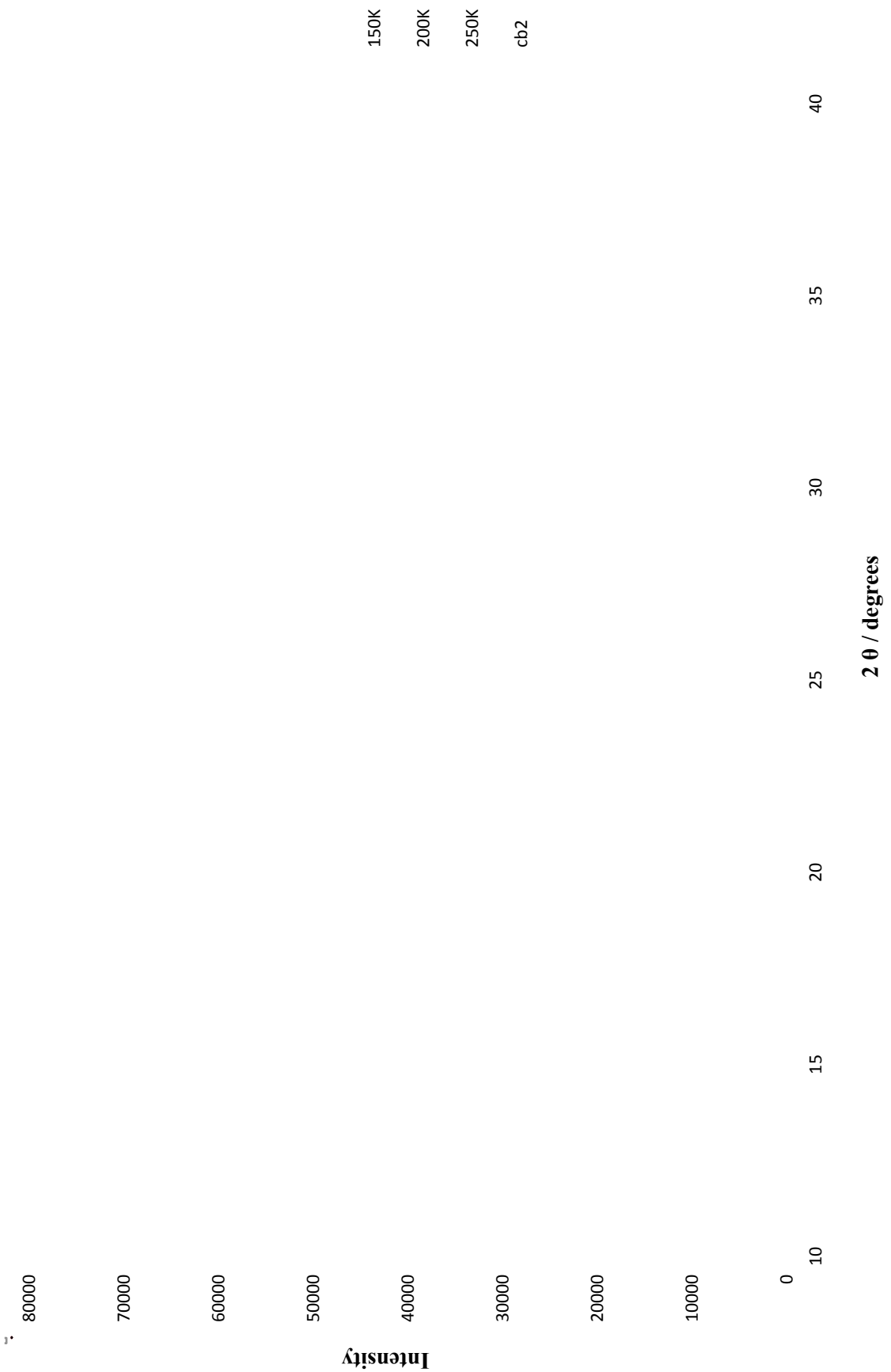

Figure A4.4.2 Powder pattern of top ranked predicted structure at 150K, 200K and 250K (D5005) and experimental patterns at these temperatures

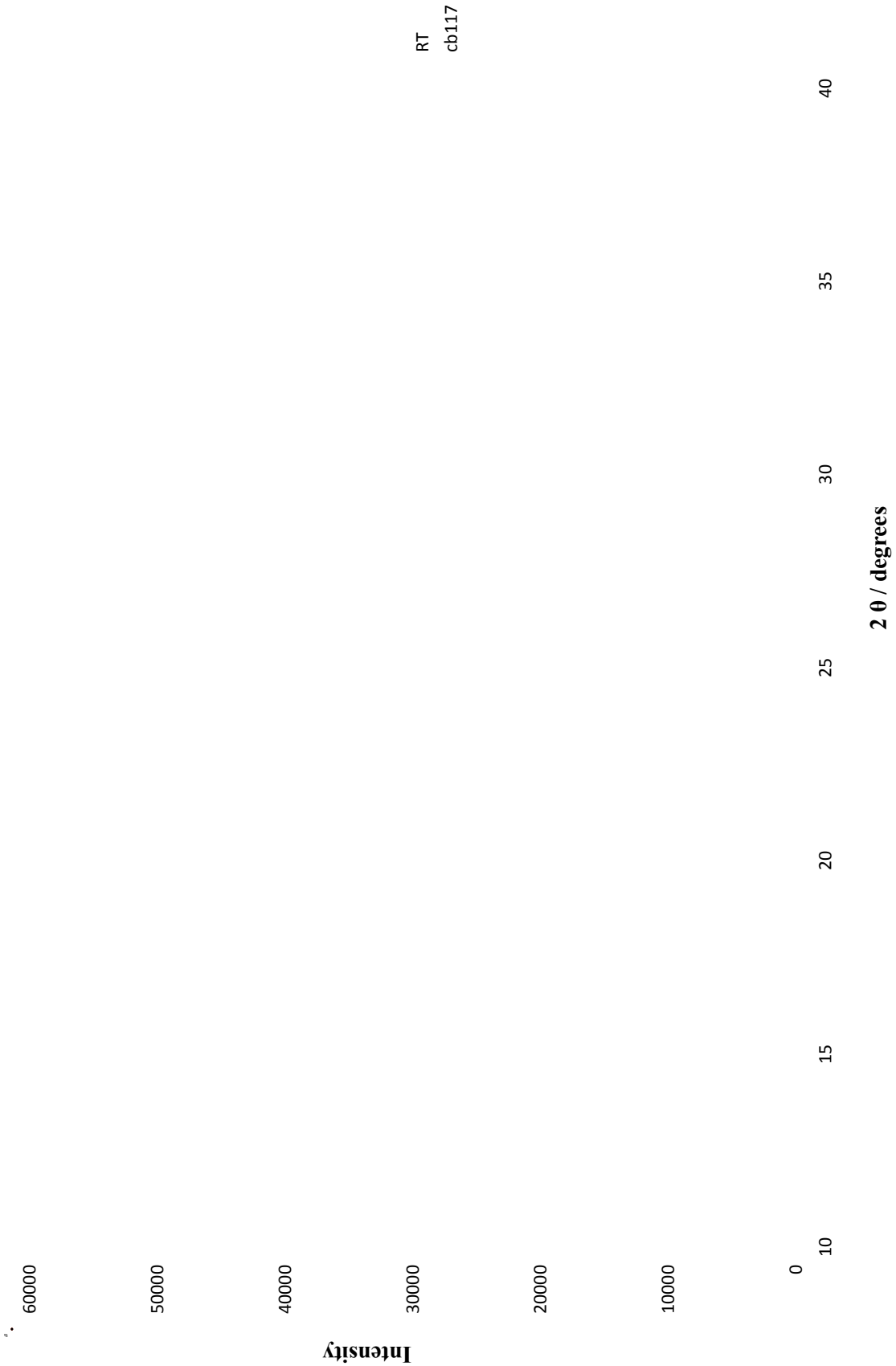

Figure A4.4.3 Powder pattern of top ranked predicted structure at room temperature (D5005) and experimental pattern at that temperature

Figure A4.4.4 Powder pattern of top ranked predicted structure at room temperature (D5000) and experimental pattern at that temperature

Results obtained using *Compare.x* with various values of triangle windows. In each case, the tables show the structure with the highest correlation coefficient [C(x)] at each temperature, and the difference to the value obtained for the correct structure [C(cb2)]. In cases where the correct structure was identified, the difference was positive. An incorrect match gave a negative difference, as shown by the values in red and blue. Blue denotes cb2 being ranked second, while values in red correspond to cb2 being ranked third or lower.

Table A4.4.1. Triangle window 0.5.

Temperature (K)	***Structure***	***Correlation Coefficient***	***Difference [C(cb2) - C(x)]***
10	aq85	0.78135	-0.34852
100	aq85	0.76313	-0.27214
150	aq62	0.68007	-0.05562
200	fa22	0.70322	-0.04605
250	cb2	0.69752	0.00385
293	fc54	0.70654	-0.10698
293 (D5000)	cb117	0.57229	-0.17499

Table A4.4.2. Triangle window 1.0.

Temperature (K)	***Structure***	***Correlation Coefficient***	***Difference [C(cb2) - C(x)]***
10	aq85	0.79499	-0.11708
100	aq85	0.79274	-0.08851
150	fa22	0.76337	-0.00333
200	fa22	0.77458	-0.00205
250	cb2	0.78864	0.00949
293	cb117	0.80960	-0.05846
293 (D5000)	cb117	0.63186	-0.08100

Table A4.4.3. Triangle window 1.5.

Temperature (K)	***Structure***	***Correlation Coefficient***	***Difference [C(cb2) - C(x)]***
10	fa41	0.82743	-0.05424
100	fa41	0.82878	-0.03887
150	cb2	0.82461	0.00694
200	cb2	0.83168	0.00784
250	cb2	0.84306	0.01560
293	cb117	0.85475	-0.02721
293 (D5000)	fa53	0.67861	-0.04626

Table A4.4.4. Triangle window 2.0.

Temperature (K)	***Structure***	***Correlation Coefficient***	***Difference [C(cb2) - C(x)]***
10	aq62	0.85495	-0.02748
100	fa41	0.85603	-0.01776
150	cb2	0.86128	0.00390
200	cb2	0.86557	0.00882
250	cb2	0.87492	0.01531
293	cb117	0.88866	-0.01638
293 (D5000)	fa53	0.74789	-0.06058

Table A4.4.5. Triangle window 2.5.

Temperature (K)	***Structure***	***Correlation Coefficient***	***Difference [C(cb2) - C(x)]***
10	fa41	0.87017	-0.01149
100	aq62	0.87444	-0.00779
150	cb2	0.88649	0.00438
200	cb2	0.89075	0.00958
250	cb2	0.90463	0.01662
293	cb2	0.91051	0.00481
293 (D5000)	fa53	0.79366	-0.06947

Table A4.4.6. Triangle window 3.0.

Temperature (K)	***Structure***	***Correlation Coefficient***	***Difference [C(cb2) - C(x)]***
10	aq62	0.88611	-0.00688
100	aq62	0.89214	-0.00606
150	cb2	0.90135	0.00310
200	cb2	0.90400	0.00332
250	cb2	0.91328	0.00682
293	fc54	0.92535	-0.00629
293 (D5000)	fa53	0.81837	-0.07854

Table A4.4.7. Triangle window 3.5.

Temperature (K)	***Structure***	***Correlation Coefficient***	***Difference [C(cb2) - C(x)]***
10	aq62	0.90390	-0.00850
100	aq62	0.90938	-0.00872
150	aq62	0.91456	-0.00124
200	fa22	0.91631	-0.00087
250	cb2	0.92382	0.00008
293	fc54	0.93173	-0.00252
293 (D5000)	fa53	0.82780	-0.07212

Table A4.4.8. Triangle window 4.0.

Temperature (K)	***Structure***	***Correlation Coefficient***	***Difference [C(cb2) - C(x)]***
10	aq62	0.92447	-0.00966
100	aq62	0.92817	-0.0095
150	fa22	0.93216	-0.00408
200	fa22	0.93389	-0.00456
250	fa22	0.94056	-0.00483
293	fa22	0.94664	-0.00548
293 (D5000)	fa53	0.83455	-0.06168

A5. DNA BASES

A5.1 Adenine

A5.1.1 Background

Method	**Solvents**	**Results**
Slow evaporation	Methanol, propan-2-ol, tertbutylmethylether, THF, butan-1-ol, propan-1-ol	Small particles of solid - not enough for characterisation analysis
Slow evaporation	2,2,2-trifluoroethanol, acetic acid, dimethylamine in H_2O, 2-methoxyetylamine	Microcrystalline solid - powder pattern matched stock sample
Slow evaporation	2-chloroethanol	Adeninium chloride hemihydrate
Slow evaporation	Equimolar amounts of thymine/adenine and cytosine/adenine in dilute hydrochloric acid, dilute hydrochloric acid, concentrated hydrochloric acid	Adeninium dichloride
Slow evaporation	H_2O	Microcrystalline solid - poor powder pattern which could not be indexed, did not match stock sample or known trihydrate structure
Sublimation	-	Microcrystalline solid - powder pattern matched stock sample

Table A5.1.1 The results of the crystallisation experiments on adenine. Other crystallisation experiments did not give any products for analysis[7] [Referenced on page 116].

A5.1.1 Low Temperature Data

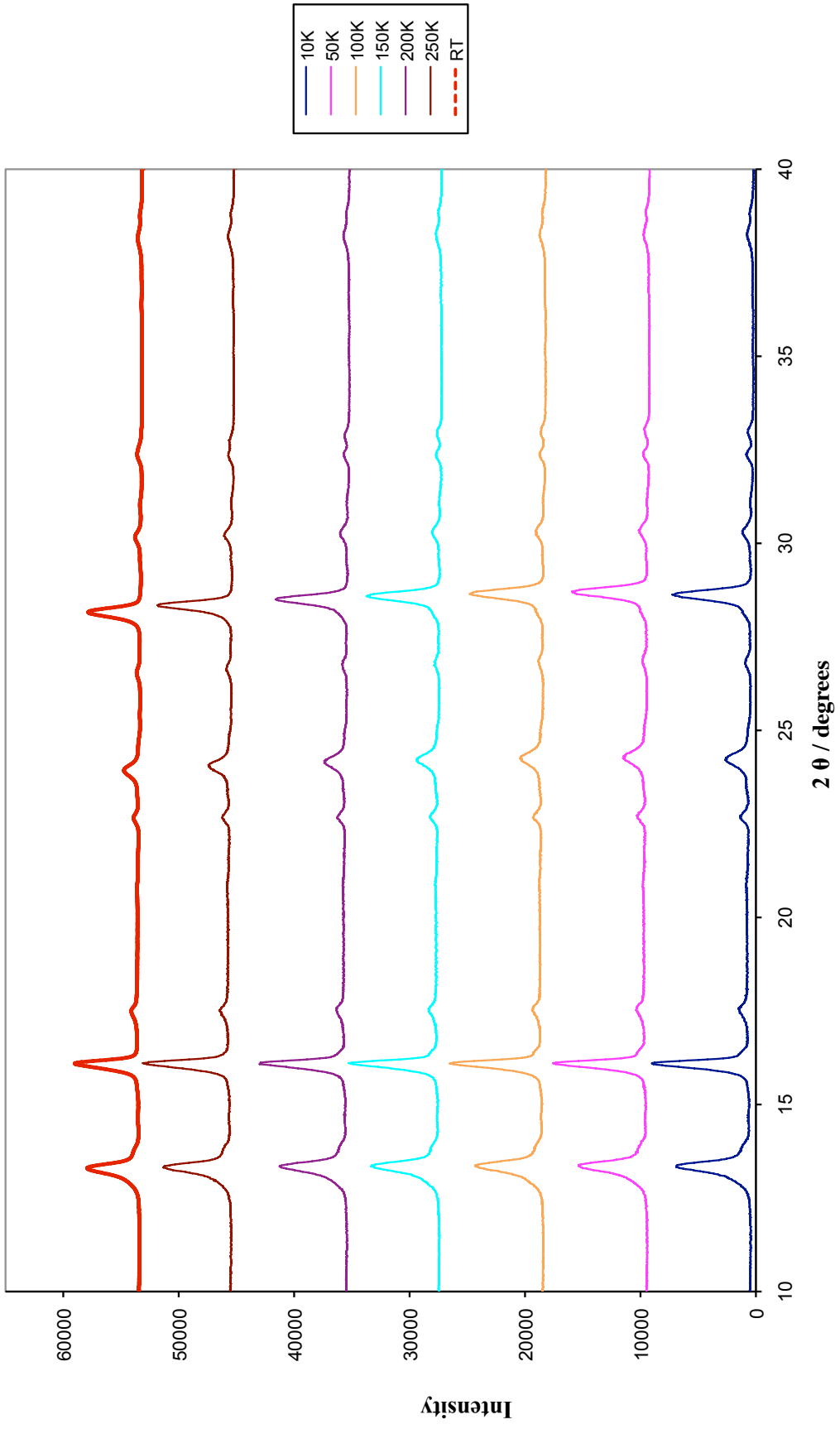

Figure A5.1.1 Powder diffraction data at all temperatures (D5005)

A5.1.3 R_{wp}

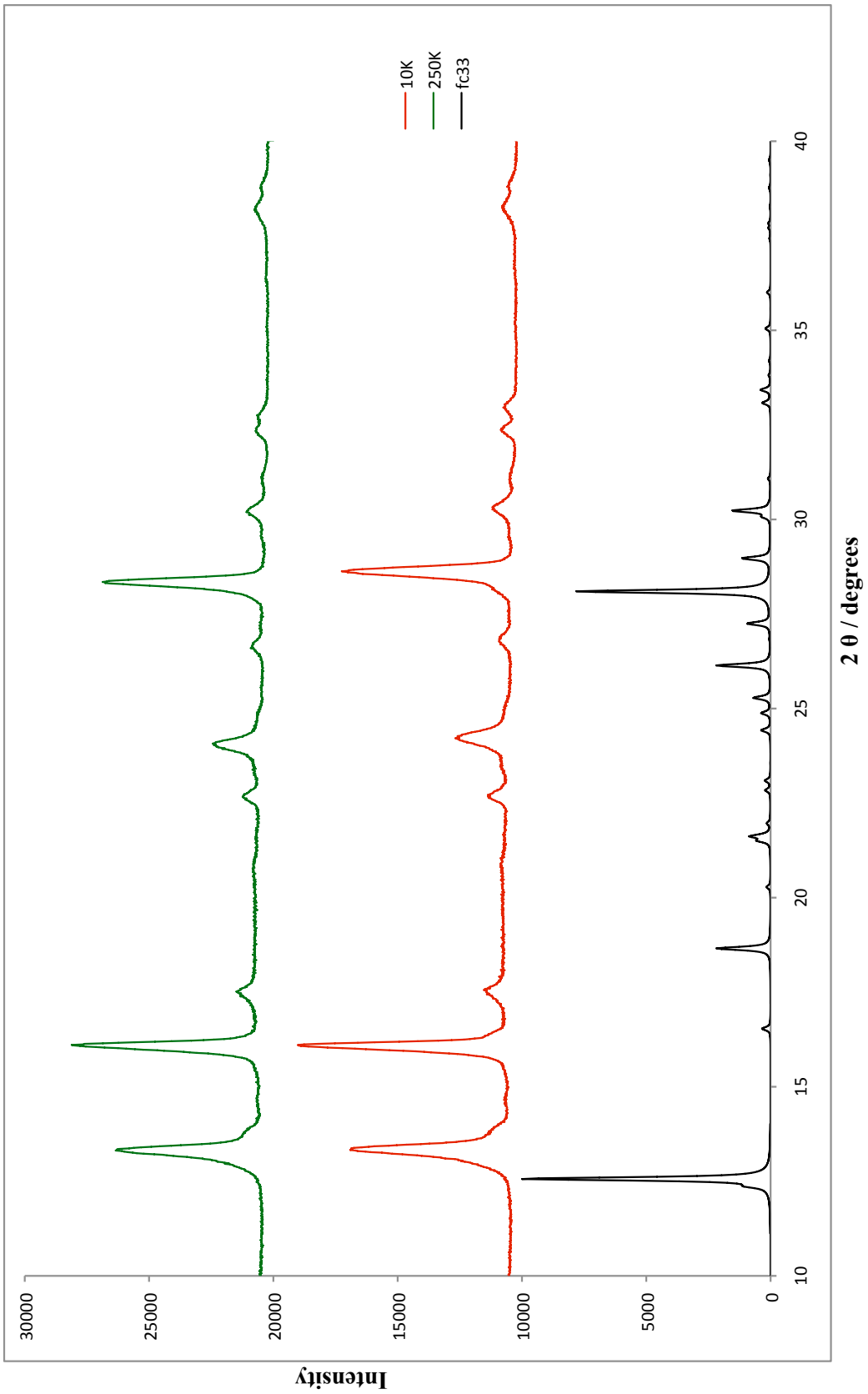

Figure A5.1.1 Powder pattern of top ranked predicted structure at 10K and 250K (D5005) and experimental patterns at these temperatures

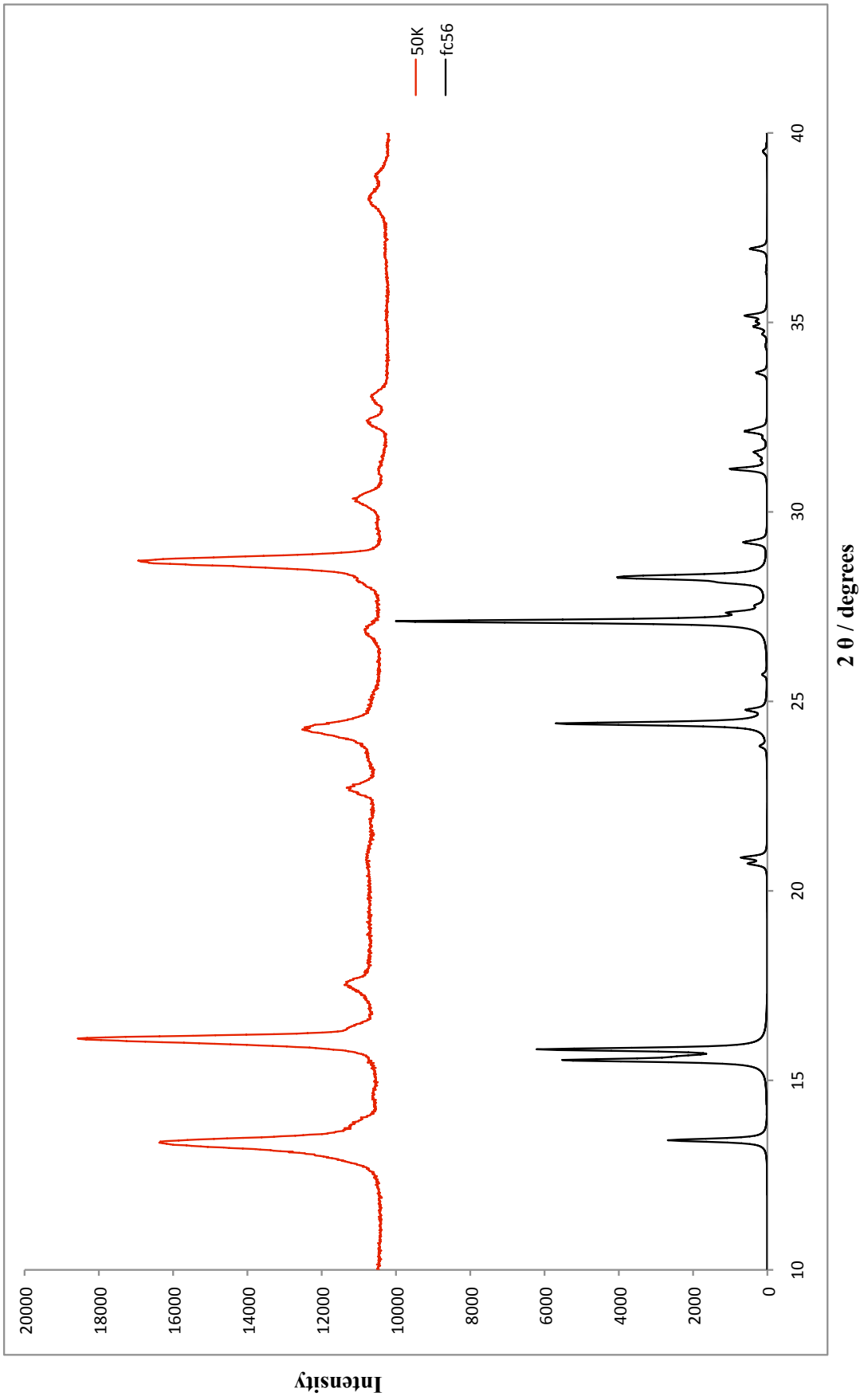

Figure A5.1.2 Powder pattern of top ranked predicted structure at 50K (D5005) and experimental pattern at this temperature

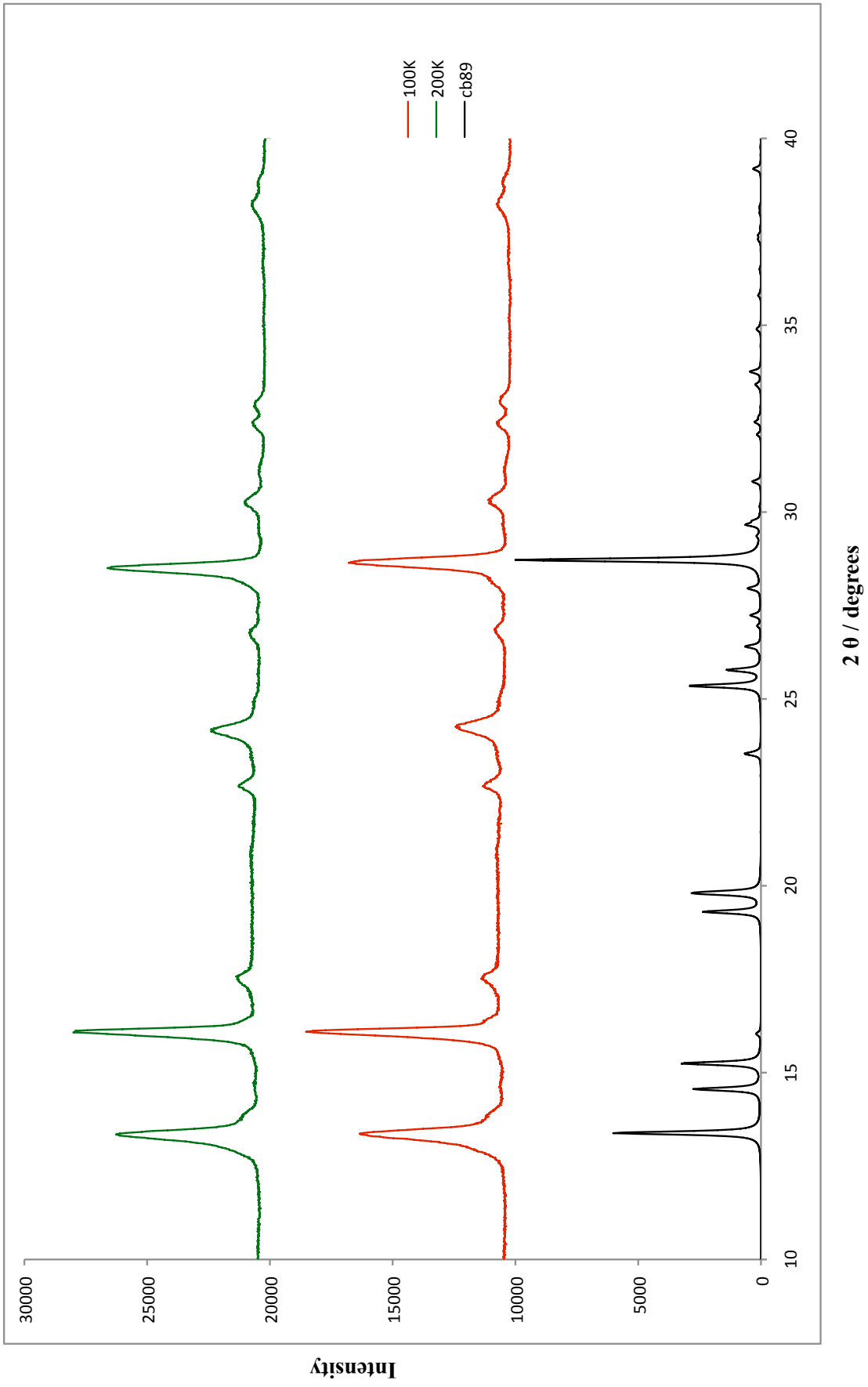

Figure A5.1.3 Powder pattern of top ranked predicted structure at 100K and 200K (D5005) and experimental patterns at these temperatures

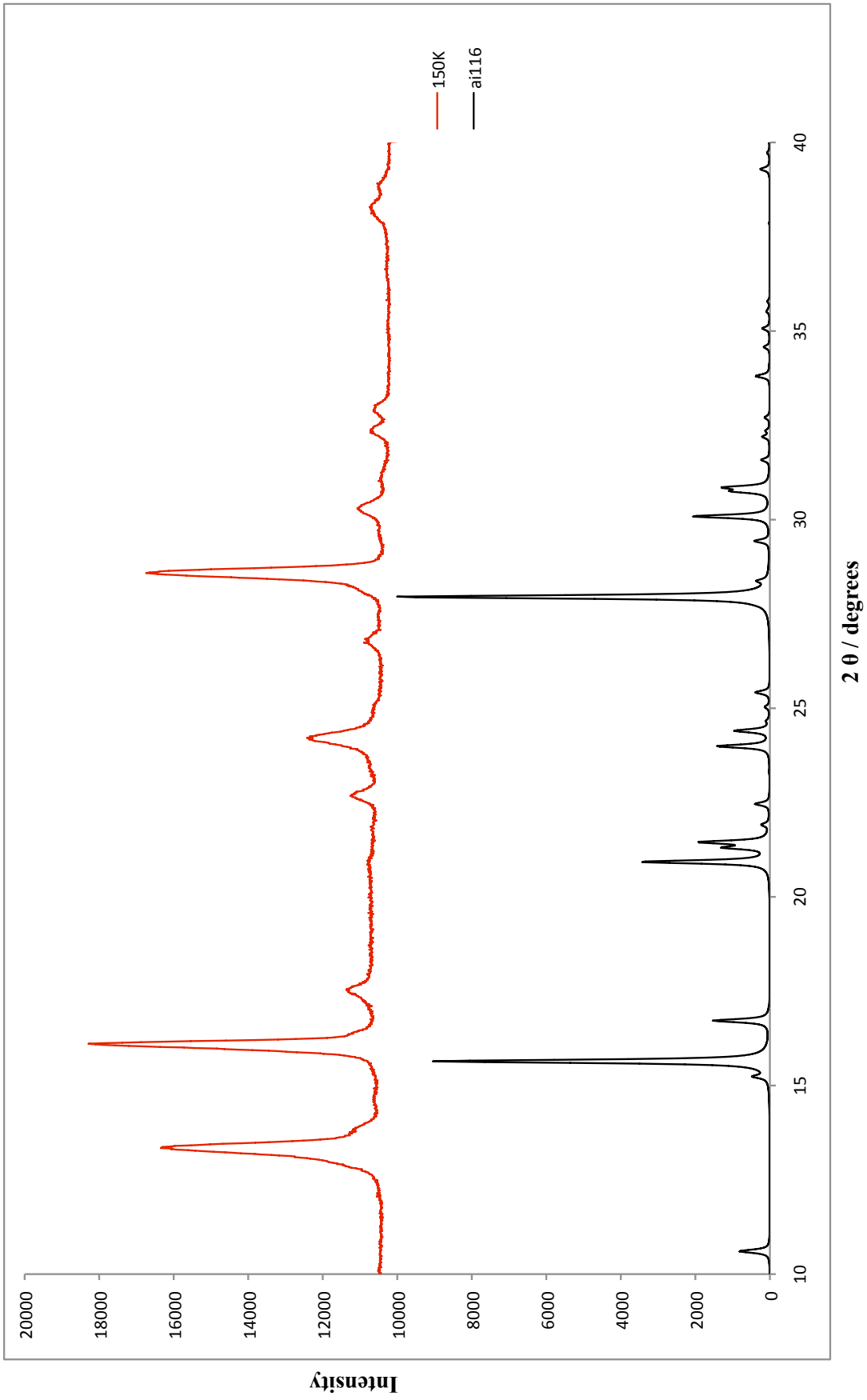

Figure A5.1.4 Powder pattern of top ranked predicted structure at 150K (D5005) and experimental pattern at this temperature

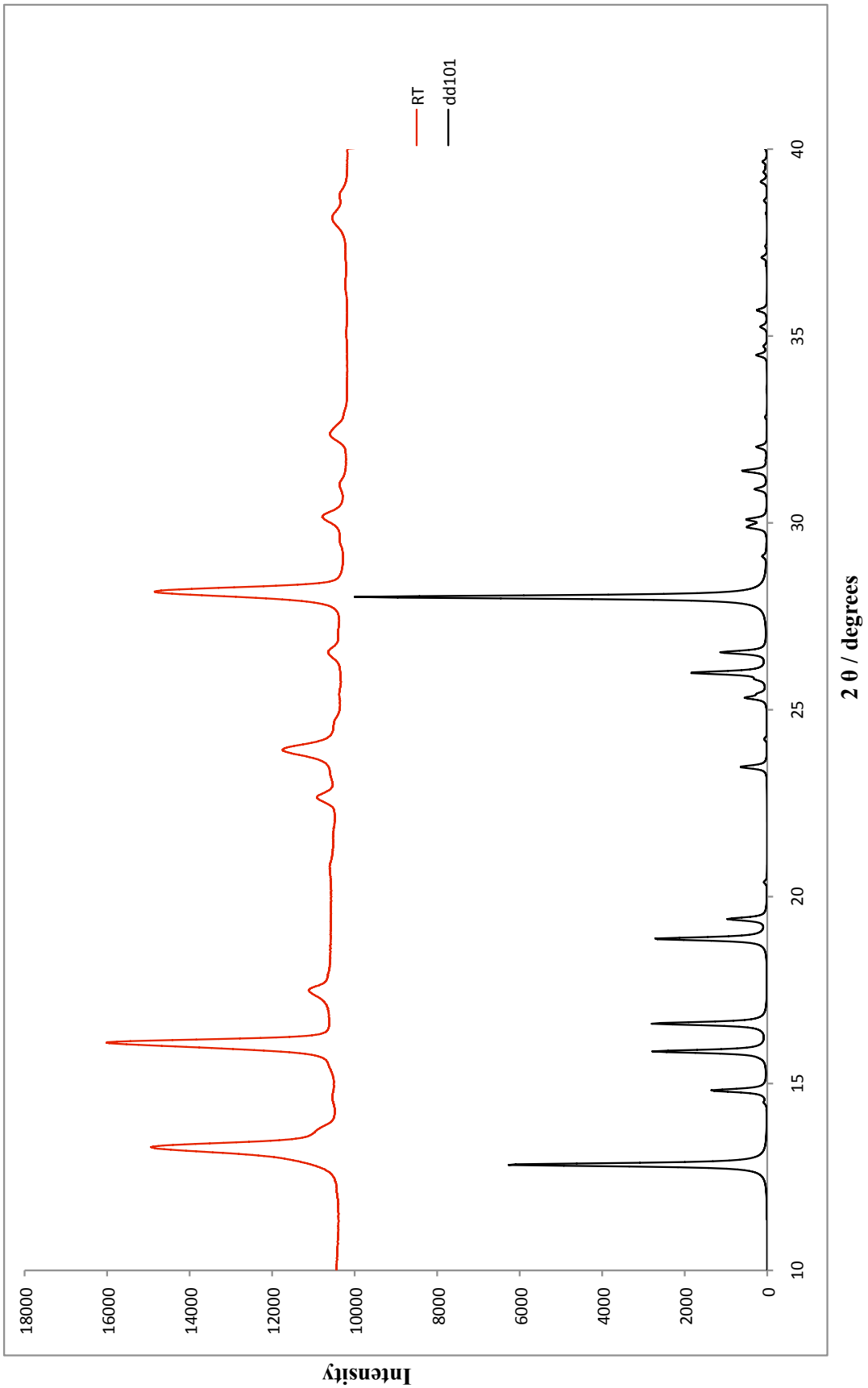

Figure A5.1.5 Powder pattern of top ranked predicted structure at room temperature (D5005) and experimental pattern at this temperature

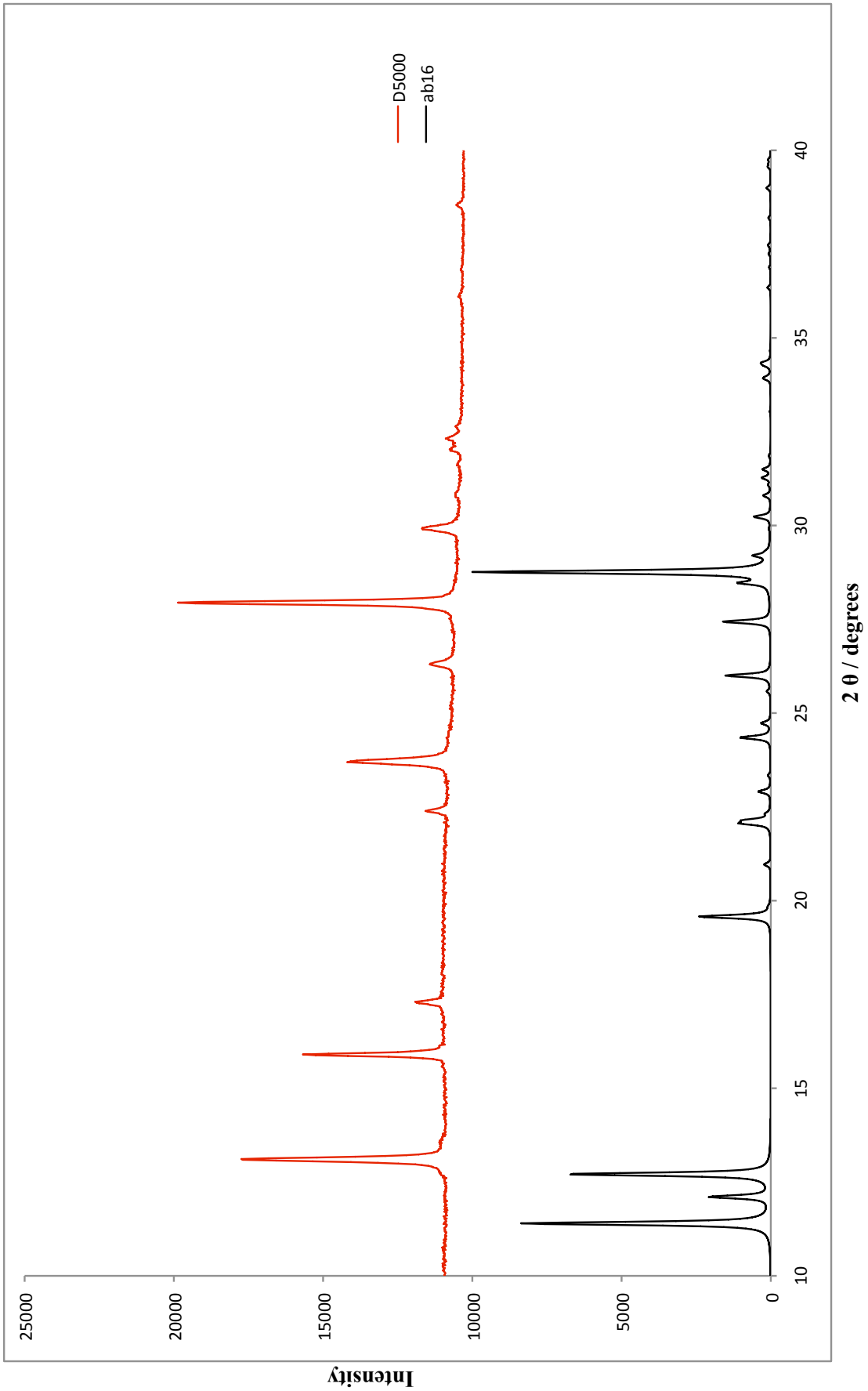

Figure A5.1.6 Powder pattern of top ranked predicted structure at room temperature (D5000) and experimental pattern at this temperature

A5.1.4 Compare.x

Results obtained using *Compare.x* with various values of triangle windows. In each case, the tables show the structure with the highest correlation coefficient [C(x)] at each temperature, and the difference to the value obtained for the correct structure [C(cc71)]. In cases where the correct structure was identified, the difference was positive. An incorrect match gave a negative difference, as shown by the values in red and blue. Blue denotes cc71 being ranked second, while values in red correspond to cc71 being ranked third or lower.

Table A5.1.4.1. Triangle window 0.5.

Temperature (K)	***Structure***	***Correlation Coefficient***	***Difference [C(cc71) - C(x)]***
10	fc4	0.79532	-0.32973
50	fc4	0.80933	-0.33646
100	fc4	0.7996	-0.32923
150	fc4	0.78255	-0.32015
200	fc4	0.73332	-0.2863
250	fc4	0.6329	-0.21183
293	am43	0.61454	-0.2076
293 (D5000)	am43	0.60252	-0.27965

Table A5.1.4.2. Triangle window 1.0.

Temperature (K)	***Structure***	***Correlation Coefficient***	***Difference [C(cc71) - C(x)]***
10	fc4	0.84304	-0.22984
50	fc4	0.85032	-0.23712
100	fc4	0.84302	-0.22966
150	fc4	0.83462	-0.22113
200	fc4	0.80994	-0.20158
250	fc4	0.76287	-0.16559
293	am43	0.74622	-0.16182
293 (D5000)	am43	0.6563	-0.22563

Table A5.1.4.3. Triangle window 1.5.

Temperature (K)	***Structure***	***Correlation Coefficient***	***Difference [C(cc71) - C(x)]***
10	cc71	0.86323	0.10665
50	cc71	0.86793	0.1147
100	cc71	0.86202	0.11012
150	cc71	0.85685	0.09648
200	cc71	0.83976	0.07151
250	cc71	0.81179	0.02576
293	cc71	0.80019	0.02112
293 (D5000)	cc71	0.69074	0.02096

Table A5.1.4.4. Triangle window 2.0.

Temperature (K)	***Structure***	***Correlation Coefficient***	***Difference [C(cc71) - C(x)]***
10	cc71	0.87413	0.05952
50	cc71	0.87812	0.05851
100	cc71	0.87276	0.05787
150	cc71	0.86874	0.05352
200	cc71	0.85485	0.03659
250	cc71	0.83472	0.00631
293	dd101	0.83534	0.02411
293 (D5000)	dd101	0.72463	0.00017

Table A5.1.4.5. Triangle window 2.5.

Temperature (K)	***Structure***	***Correlation Coefficient***	***Difference [C(cc71) - C(x)]***
10	cc71	0.88077	0.04065
50	cc71	0.88442	0.04004
100	cc71	0.87948	0.03955
150	cc71	0.87594	0.03829
200	cc71	0.86347	0.02815
250	cc71	0.84648	0.00374
293	dd101	0.84769	0.02057
293 (D5000)	cd53	0.75726	0.00124

Table A5.1.4.6. Triangle window 3.0.

Temperature (K)	***Structure***	***Correlation Coefficient***	***Difference [C(cc71) - C(x)]***
10	cc71	0.89341	0.03835
50	cc71	0.89651	0.03771
100	cc71	0.89221	0.03773
150	cc71	0.88901	0.03611
200	cc71	0.87819	0.02628
250	cc71	0.86445	0.00767
293	dd101	0.85934	-0.01084
293 (D5000)	cd53	0.77648	-0.00118

Table A5.1.4.7. Triangle window 3.5.

Temperature (K)	***Structure***	***Correlation Coefficient***	***Difference [C(cc71) - C(x)]***
10	cc71	0.90172	0.02793
50	cc71	0.90453	0.02682
100	cc71	0.90068	0.02676
150	cc71	0.89778	0.02777
200	cc71	0.88817	0.021
250	cc71	0.87658	0.00667
293	dd101	0.87026	-0.00722
293 (D5000)	cd53	0.79197	-0.00298

Table A5.1.4.8. Triangle window 4.0.

Temperature (K)	***Structure***	***Correlation Coefficient***	***Difference [C(cc71) - C(x)]***
10	cc71	0.90983	0.01494
50	cc71	0.91243	0.01424
100	cc71	0.90887	0.01445
150	cc71	0.90626	0.01462
200	cc71	0.89769	0.01341
250	cc71	0.88819	0.00376
293	dd101	0.88282	-0.00495
293 (D5000)	cd53	0.81021	-0.00463

A5.2 Guanine

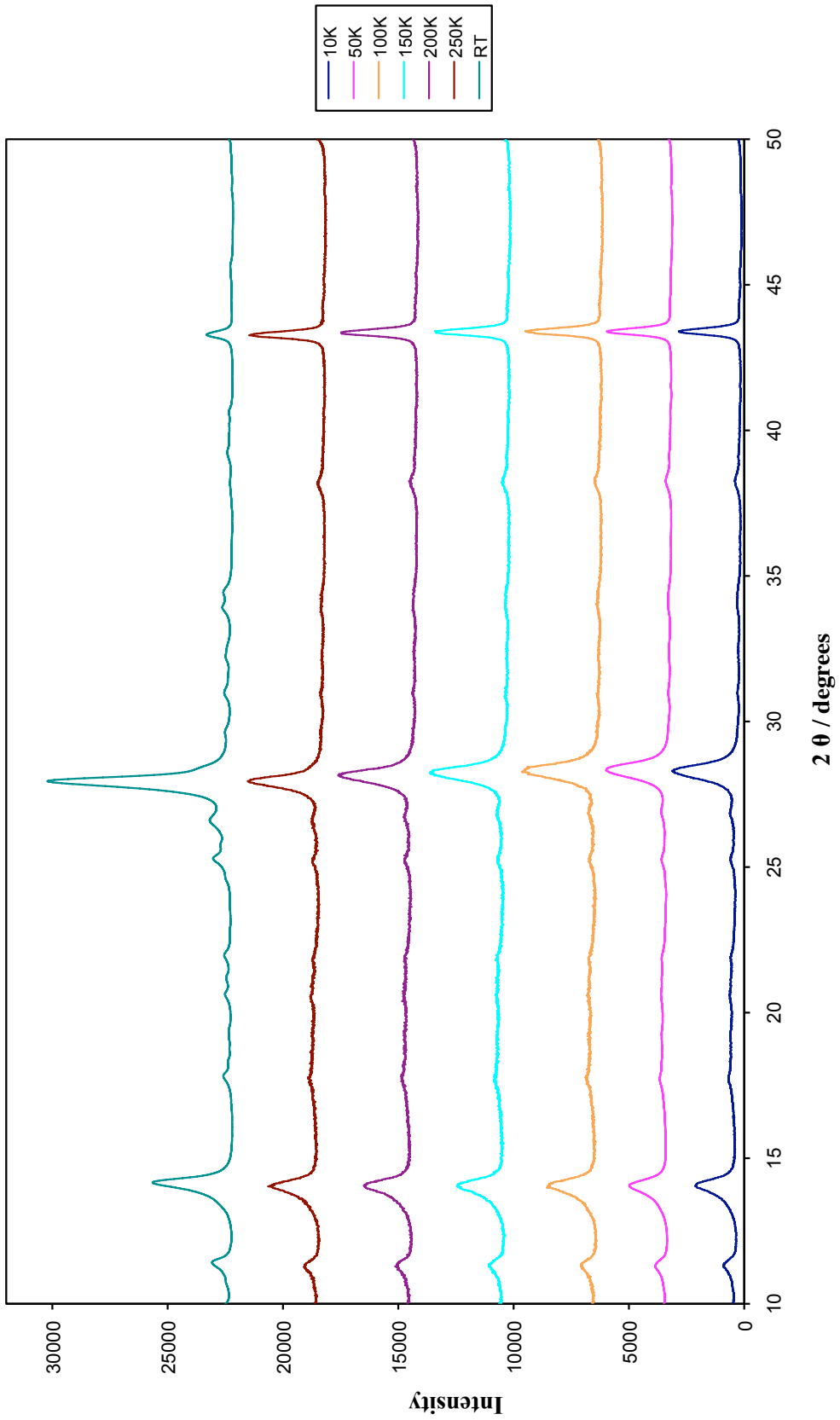

A5.2.1 Low Temperature Data

A5.2.2 Guanine Indexing Output

```
Running summary of all solutions logged so far for this dataset name,
sorted in descending order of I20 then Merit (as defined by each program)

I20  Merit    Volume   V/V1 BL IndexProg    Date     Time    Pedig     a
b        c     alpha    beta   gamma     Q(A)      Q(B)      Q(C)      Q(D)
Q(E)      Q(F)   Description (up to 80-chars, from Run-Title line)
19   17.6     584.475  1.00 P DICVOL91/log 20Mar07 11:57:30 Mon_16  20.1396
8.6592   3.6633  90.000 113.811  90.000   29.456   133.366   890.276
.000   130.755      .000  GUANINE = guanine
19   17.6     584.475  1.00 P DICVOL91/log 20Mar07 11:56:51 Mon_16  20.1396
8.6592   3.6633  90.000 113.811  90.000   29.456   133.366   890.276
.000   130.755      .000  GUANINE = guanine
19   17.5     584.306  1.00 P DICVOL91/log 20Mar07 11:57:30 Mon_27  23.0636
8.6590   3.6623  90.000 126.975  90.000   29.455   133.372  1168.179
.000   223.140      .000  GUANINE = guanine
19   17.5     584.306  1.00 P DICVOL91/log 20Mar07 11:56:51 Mon_27  23.0636
8.6590   3.6623  90.000 126.975  90.000   29.455   133.372  1168.179
.000   223.140      .000  GUANINE = guanine
19   17.2     584.308  1.00 P DICVOL91/log 20Mar07 11:57:30 Mon_11  19.5542
8.6590   3.6623  90.000 109.562  90.000   29.455   133.372   839.716
.000   105.316      .000  GUANINE = guanine
19   17.2     584.308  1.00 P DICVOL91/log 20Mar07 11:56:51 Mon_11  19.5542
8.6590   3.6623  90.000 109.562  90.000   29.455   133.372   839.716
.000   105.316      .000  GUANINE = guanine
19   16.1     586.087  1.00 P DICVOL91/log 20Mar07 11:57:30 Mon_22  21.8221
8.6579   3.6739  90.000 122.397  90.000   29.455   133.406  1039.188
.000   187.475      .000  GUANINE = guanine
19   16.1     586.087  1.00 P DICVOL91/log 20Mar07 11:56:51 Mon_22  21.8221
8.6579   3.6739  90.000 122.397  90.000   29.455   133.406  1039.188
.000   187.475      .000  GUANINE = guanine
19   16.0     586.188  1.00 P DICVOL91/log 20Mar07 11:57:30 Mon_14  19.5976
8.6579   3.6746  90.000 109.918  90.000   29.456   133.406   837.832
.000   107.037      .000  GUANINE = guanine
19   16.0     586.188  1.00 P DICVOL91/log 20Mar07 11:56:51 Mon_14  19.5976
8.6579   3.6746  90.000 109.918  90.000   29.456   133.406   837.832
.000   107.037      .000  GUANINE = guanine
19   15.7     598.235  1.02 P DICVOL91/log 20Mar07 11:57:30 Mon__6  18.7431
8.6598   3.7490  90.000 100.542  90.000   29.451   133.347   736.131
.000    53.877      .000  GUANINE = guanine
19   15.7     598.235  1.02 P DICVOL91/log 20Mar07 11:56:51 Mon__6  18.7431
8.6598   3.7490  90.000 100.542  90.000   29.451   133.347   736.131
.000    53.877      .000  GUANINE = guanine
19   15.7     598.234  1.02 P DICVOL91/log 20Mar07 11:57:30 Mon_23  21.4230
8.6598   3.7490  90.000 120.668  90.000   29.451   133.347   961.687
.000   171.681      .000  GUANINE = guanine
19   15.7     598.234  1.02 P DICVOL91/log 20Mar07 11:56:51 Mon_23  21.4230
8.6598   3.7490  90.000 120.668  90.000   29.451   133.347   961.687
.000   171.681      .000  GUANINE = guanine
19   15.7     598.233  1.02 P DICVOL91/log 20Mar07 11:57:30 Mon__7  18.8705
8.6598   3.7490  90.000 102.451  90.000   29.451   133.347   746.177
.000    63.924      .000  GUANINE = guanine
```

```
19   15.7     598.233  1.02 P DICVOL91/log 20Mar07 11:57:30 Mon_15  19.7755
8.6598   3.7490  90.000 111.284  90.000   29.451   133.347   819.465
.000   112.783      .000  GUANINE = guanine
19   15.7     598.233  1.02 P DICVOL91/log 20Mar07 11:56:51 Mon__7  18.8705
8.6598   3.7490  90.000 102.451  90.000   29.451   133.347   746.177
.000    63.924      .000  GUANINE = guanine
19   15.7     598.233  1.02 P DICVOL91/log 20Mar07 11:56:51 Mon_15  19.7755
8.6598   3.7490  90.000 111.284  90.000   29.451   133.347   819.465
.000   112.783      .000  GUANINE = guanine
19   14.4     584.677  1.00 P DICVOL91/log 20Mar07 11:57:30 Mon_26  24.0562
8.6575   3.6635  90.000 129.977  90.000   29.427   133.418  1268.841
.000   248.294      .000  GUANINE = guanine
19   14.4     584.677  1.00 P DICVOL91/log 20Mar07 11:56:51 Mon_26  24.0562
8.6575   3.6635  90.000 129.977  90.000   29.427   133.418  1268.841
.000   248.294      .000  GUANINE = guanine
19   14.1     598.419  1.02 P DICVOL91/log 20Mar07 11:57:30 Mon_17  20.0158
8.6637   3.7487  90.000 112.993  90.000   29.455   133.227   839.734
.000   122.866      .000  GUANINE = guanine
19   14.1     598.419  1.02 P DICVOL91/log 20Mar07 11:56:51 Mon_17  20.0158
8.6637   3.7487  90.000 112.993  90.000   29.455   133.227   839.734
.000   122.866      .000  GUANINE = guanine
19   13.9     584.677  1.00 P DICVOL91/log 20Mar07 11:57:30 Mon__5  18.9674
8.6575   3.6635  90.000 103.616  90.000   29.427   133.418   788.803
.000    71.733      .000  GUANINE = guanine
19   13.9     584.677  1.00 P DICVOL91/log 20Mar07 11:56:51 Mon__5  18.9674
8.6575   3.6635  90.000 103.616  90.000   29.427   133.418   788.803
.000    71.733      .000  GUANINE = guanine
19   13.9     547.453   .94 P DICVOL91/log 20Mar07 11:57:30 Mon__9   9.1369
18.4244   3.4299  90.000 108.533  90.000  133.247    29.459   945.565
.000   225.646      .000  GUANINE = guanine
19   13.9     547.453   .94 P DICVOL91/log 20Mar07 11:56:51 Mon__9   9.1369
18.4244   3.4299  90.000 108.533  90.000  133.247    29.459   945.565
.000   225.646      .000  GUANINE = guanine
19   13.9     547.452   .94 P DICVOL91/log 20Mar07 11:57:30 Mon__1   8.6790
18.4244   3.4299  90.000  93.473  90.000  133.247    29.459   853.167
.000    40.850      .000  GUANINE = guanine
19   13.9     547.452   .94 P DICVOL91/log 20Mar07 11:56:51 Mon__1   8.6790
18.4244   3.4299  90.000  93.473  90.000  133.247    29.459   853.167
.000    40.850      .000  GUANINE = guanine
19   13.9     547.450   .94 P DICVOL91/log 20Mar07 11:57:30 Mon_12   9.5234
18.4244   3.4299  90.000 114.542  90.000  133.248    29.459  1027.263
.000   307.345      .000  GUANINE = guanine
19   13.9     547.450   .94 P DICVOL91/log 20Mar07 11:56:51 Mon_12   9.5234
18.4244   3.4299  90.000 114.542  90.000  133.248    29.459  1027.263
.000   307.345      .000  GUANINE = guanine
19   13.5     549.308   .94 P DICVOL91/log 20Mar07 11:57:30 Mon_25  22.8078
8.6603   3.4423  90.000 126.110  90.000   29.453   133.332  1293.008
.000   230.017      .000  GUANINE = guanine
19   13.5     549.308   .94 P DICVOL91/log 20Mar07 11:56:51 Mon_25  22.8078
8.6603   3.4423  90.000 126.110  90.000   29.453   133.332  1293.008
.000   230.017      .000  GUANINE = guanine
```

```
19   13.3     549.308   .94 P DICVOL91/log 20Mar07 11:57:30 Mon_20  20.9644
8.6603   3.4423  90.000 118.487  90.000   29.453   133.332  1092.442
.000   171.110      .000  GUANINE = guanine
19   13.3     549.308   .94 P DICVOL91/log 20Mar07 11:56:51 Mon_20  20.9644
8.6603   3.4423  90.000 118.487  90.000   29.453   133.332  1092.442
.000   171.110      .000  GUANINE = guanine
19   13.3     549.305   .94 P DICVOL91/log 20Mar07 11:57:30 Mon__3  18.6874
8.6603   3.4423  90.000  99.594  90.000   29.453   133.332   868.034
.000    53.298      .000  GUANINE = guanine
19   13.3     549.305   .94 P DICVOL91/log 20Mar07 11:57:30 Mon_10  19.5579
8.6603   3.4423  90.000 109.588  90.000   29.453   133.332   950.787
.000   112.205      .000  GUANINE = guanine
19   13.3     549.305   .94 P DICVOL91/log 20Mar07 11:56:51 Mon__3  18.6874
8.6603   3.4423  90.000  99.594  90.000   29.453   133.332   868.034
.000    53.298      .000  GUANINE = guanine
19   13.3     549.305   .94 P DICVOL91/log 20Mar07 11:56:51 Mon_10  19.5579
8.6603   3.4423  90.000 109.588  90.000   29.453   133.332   950.787
.000   112.205      .000  GUANINE = guanine
19   12.3     580.673   .99 P DICVOL91/log 20Mar07 11:57:30 Mon__8   9.0564
18.4383   3.6383  90.000 107.103  90.000  133.467    29.414   826.969
.000   195.408      .000  GUANINE = guanine
19   12.3     580.673   .99 P DICVOL91/log 20Mar07 11:56:51 Mon__8   9.0564
18.4383   3.6383  90.000 107.103  90.000  133.467    29.414   826.969
.000   195.408      .000  GUANINE = guanine
19   12.3     580.672   .99 P DICVOL91/log 20Mar07 11:57:30 Mon_18   9.8085
18.4383   3.6383  90.000 118.056  90.000  133.468    29.414   970.030
.000   338.468      .000  GUANINE = guanine
19   12.3     580.672   .99 P DICVOL91/log 20Mar07 11:56:51 Mon_18   9.8085
18.4383   3.6383  90.000 118.056  90.000  133.468    29.414   970.030
.000   338.468      .000  GUANINE = guanine
19   12.3     549.543   .94 P DICVOL91/log 20Mar07 11:57:30 Mon_13  19.7862
8.6645   3.4423  90.000 111.376  90.000   29.457   133.203   973.215
.000   123.426      .000  GUANINE = guanine
19   12.3     549.543   .94 P DICVOL91/log 20Mar07 11:56:51 Mon_13  19.7862
8.6645   3.4423  90.000 111.376  90.000   29.457   133.203   973.215
.000   123.426      .000  GUANINE = guanine
19   12.3     549.541   .94 P DICVOL91/log 20Mar07 11:57:30 Mon__4  18.8067
8.6645   3.4423  90.000 101.563  90.000   29.457   133.203   879.249
.000    64.517      .000  GUANINE = guanine
19   12.3     549.541   .94 P DICVOL91/log 20Mar07 11:56:51 Mon__4  18.8067
8.6645   3.4423  90.000 101.563  90.000   29.457   133.203   879.249
.000    64.517      .000  GUANINE = guanine
19   12.3     549.540   .94 P DICVOL91/log 20Mar07 11:57:30 Mon__2  18.4279
8.6645   3.4423  90.000  91.018  90.000   29.457   133.203   844.189
.000     5.603      .000  GUANINE = guanine
19   12.3     549.540   .94 P DICVOL91/log 20Mar07 11:56:51 Mon__2  18.4279
8.6645   3.4423  90.000  91.018  90.000   29.457   133.203   844.189
.000     5.603      .000  GUANINE = guanine
19   12.3     549.537   .94 P DICVOL91/log 20Mar07 11:57:30 Mon_21  21.2836
8.6645   3.4423  90.000 120.039  90.000   29.457   133.203  1126.115
.000   182.347      .000  GUANINE = guanine
```

```
19   12.3     549.537   .94 P DICVOL91/log 20Mar07 11:56:51 Mon_21  21.2836
8.6645   3.4423  90.000 120.039  90.000   29.457   133.203  1126.115
.000   182.347      .000  GUANINE = guanine
19   11.8     580.719   .99 P DICVOL91/log 20Mar07 11:57:30 Mon_24  10.7076
18.4381   3.6382  90.000 126.052  90.000  133.436    29.415  1155.806
.000   462.243      .000  GUANINE = guanine
19   11.8     580.719   .99 P DICVOL91/log 20Mar07 11:56:51 Mon_24  10.7076
18.4381   3.6382  90.000 126.052  90.000  133.436    29.415  1155.806
.000   462.243      .000  GUANINE = guanine
19   11.3     616.414  1.05 P DICVOL91/log 20Mar07 11:57:30 Mon_28  22.6272
8.6589   3.8632  90.000 125.473  90.000   29.449   133.375  1010.280
.000   200.196      .000  GUANINE = guanine
19   11.3     616.414  1.05 P DICVOL91/log 20Mar07 11:56:51 Mon_28  22.6272
8.6589   3.8632  90.000 125.473  90.000   29.449   133.375  1010.280
.000   200.196      .000  GUANINE = guanine
19   11.3     549.280   .94 P DICVOL91/log 20Mar07 11:57:30 Mon_19  21.2878
8.6646   3.4407  90.000 120.060  90.000   29.458   133.200  1127.641
.000   182.589      .000  GUANINE = guanine
19   11.3     549.280   .94 P DICVOL91/log 20Mar07 11:56:51 Mon_19  21.2878
8.6646   3.4407  90.000 120.060  90.000   29.458   133.200  1127.641
.000   182.589      .000  GUANINE = guanine
19   10.69    897.414  1.54 P TAUPv3.3a    20Mar07 11:54:37 Ort__1   5.6268
8.6551  18.4272  90.000  90.000  90.000  315.8481  133.4916   29.4498
.0000     .0000     .0000 GUANINE = guanine
19    9.6     616.494  1.05 P DICVOL91/log 20Mar07 11:57:30 Mon_29  23.0976
8.6569   3.8627  90.000 127.042  90.000   29.420   133.437  1051.964
.000   211.953      .000  GUANINE = guanine
19    9.6     616.494  1.05 P DICVOL91/log 20Mar07 11:56:51 Mon_29  23.0976
8.6569   3.8627  90.000 127.042  90.000   29.420   133.437  1051.964
.000   211.953      .000  GUANINE = guanine
19    9      2092.246  3.58 P TREOR90/log  20Mar07 11:56:20 Ort__3  18.4187
17.3919   6.5314  90.000  90.000  90.000   29.4770   33.0604  234.4140
.0000     .0000     .0000 GUANINE = guanine
19    7.1    1579.847  2.70 P DICVOL91/log 20Mar07 11:57:30 Ort__1  36.8566
8.6592   4.9502  90.000  90.000  90.000    7.362   133.365   408.090
.000      .000      .000  GUANINE = guanine
19    7.1    1579.847  2.70 P DICVOL91/log 20Mar07 11:56:51 Ort__1  36.8566
8.6592   4.9502  90.000  90.000  90.000    7.362   133.365   408.090
.000      .000      .000  GUANINE = guanine
18    6      1666.431  2.85 P TREOR90/log  20Mar07 11:56:20 Ort__1  18.4411
10.4490   8.6482  90.000  90.000  90.000   29.4053   91.5905  133.7055
.0000     .0000     .0000 GUANINE = guanine
17    6      1916.376  3.28 P TREOR90/log  20Mar07 11:56:20 Ort__2  18.5137
11.9366   8.6717  90.000  90.000  90.000   29.1753   70.1837  132.9802
.0000     .0000     .0000 GUANINE = guanine
```